Spring 2017

Processing, microstructure, and mechanical properties of zirconium diboride-molybdenum disilicide ceramics and dual composite architectures

Ryan Joseph Grohsmeyer

PROCESSING, MICROSTRUCTURE, AND MECHANICAL PROPERTIES OF ZIRCONIUM DIBORIDE-MOLYBDENUM DISILICIDE CERAMICS AND DUAL COMPOSITE ARCHITECTURES

by

RYAN JOSEPH GROHSMEYER

A DISSERTATION

Presented to the Faculty of the Graduate School of the

MISSOURI UNIVERSITY OF SCIENCE AND TECHNOLOGY

In Partial Fulfillment of the Requirements for the Degree

DOCTOR OF PHILOSOPHY

in

MATERIALS SCIENCE AND ENGINEERING

2017

Submitted to:

Gregory Hilmas, Advisor
William Fahrenholtz
Jeffrey Smith
David Van Aken
Lokeswarappa Dharani

PUBLICATION DISSERTATION OPTION

This dissertation consists of the following five articles that will be submitted for publication as follows and have been formatted in the style of the journal *Ceramics International*. The manuscripts entitled, "ZrB_2-$MoSi_2$ Ceramics with Varying $MoSi_2$ Content: Part 1. Processing and Microstructure with Varying ZrB_2 Particle Size:" (Paper I, Pages 50–80), and the manuscript entitled "ZrB_2-$MoSi_2$ Ceramics with Varying $MoSi_2$ Content: Part 2. Mechanical Properties for Medium ZrB_2 Particle Size" (Paper II: Pages 81–109) are in the final stages of editing before submission to *Ceramics International* as the first two parts of a three-part series for simultaneous consideration for publication. The manuscript entitled "Densification Processes and Formation of Solid Solution Shell in ZrB_2-$MoSi_2$ Ceramics" (Paper III: Pages 110–143) is intended for submission to the *Journal of the European Ceramic Society* following further revision by the authors. The manuscript entitled "ZrB_2-$MoSi_2$ Ceramics with Varying $MoSi_2$ Content: Part 3. Mechanical Properties with Varying ZrB_2 Particle Size" (Paper IV: Pages 144–173), is under review by the authors before submission to *Ceramics International* as the third in the 3-part series. The manuscript entitled "Processing and Microstructure of ZrB_2-$MoSi_2$ Dual Composite Architectures" (Paper V: Pages 174–209) is intended for submission for publication following revision based on the recommendations of the dissertation committee and review by the authors.

ABSTRACT

This research had two objectives: characterization of processing-microstructure-mechanical property relationships of conventional ZrB_2-$MoSi_2$ ceramics at room temperature (RT) and 1500°C in air, and fabrication of ZrB_2-$MoSi_2$ dual composite architectures (DCAs) for use near 1500°C. Elastic moduli, fracture toughness, and flexure strength were measured at RT and 1500°C for 15 ZrB_2-$MoSi_2$ ceramics hot pressed using fine, medium, or coarse ZrB_2 starting powder with 5–70 vol.% $MoSi_2$, referred to as FX, MX, and CX respectively where X is the nominal $MoSi_2$ content. $MoSi_2$ decomposed during sintering, resulting in microstructures with ZrB_2 cores and $(Zr_{1-x}Mo_x)B_2$ shells via surface and grain boundary diffusion. Flexure strength at RT (700–800 MPa for FX, 560–720 MPa for MX, and 440–590 MPa for CX) was controlled by the maximum ZrB_2 grain size, and toughness (2.7–3.9 $MPa \cdot m^{½}$) did not trend with $MoSi_2$ content. At 1500°C toughness increased with $MoSi_2$ content and ZrB_2 grain size, and strength of FX and MX was controlled by oxidation damage at 1500°C. Strength of CX followed the opposite trend, with C10 exhibiting a strength of ~600 MPa.

Four ZrB_2-$MoSi_2$ DCAs were fabricated by dispersing granules of selected ZrB_2-$MoSi_2$ compositions in matrices of different ZrB_2-$MoSi_2$ compositions. Strength limitation at 1500°C by differential oxidation of granules and matrix was resolved by compositional adjustment, but microcracking due to granule-matrix CTE mismatch limited strength to ~140 MPa at RT and ~360 MPa at 1500°C. The granule-matrix interface did not deflect cracks, and the toughness at 1500°C was 6.1–6.9 $MPa \cdot m^{½}$, similar to that of conventional ZrB_2-$MoSi_2$ ceramics. CTE matching via addition of a third phase and use of a weak granule-matrix interface are recommended areas of focus for future development of high-temperature DCAs.

ACKNOWLEDGMENTS

First, I would like to thank my advisor, Dr. Gregory Hilmas, for his advice, understanding, judgment, tolerance, and support during this entire project. He enabled me to travel nationally and internationally for my research and my professional development, and did his best to see that the biggest factor limiting me in my research was myself. I would also like to thank Dr. Frederic Monteverde, who acted as my advisor while I was working in Italy and who has been a teacher, mentor, and brainstorming partner for the last four years. I would like to thank Dr. William Fahrenholtz for lending his unending advice and expertise and for trying to teach me how to write technical journal articles.

I would like to thank Dr. Jeremy Watts, Dr. Laura Silvestroni, and Mr. Andrea D'Angió for their technical advice and assistance that has been critical to the success of this project, and for their continued friendship throughout my time in Rolla and Faenza.

I would like to thank the other members of my committee: Dr. Jeffrey Smith, Dr. David Van Aken, and Dr. Lokeswarappa Dharani for giving their advice, sharing their knowledge, and teaching classes that I took, all of which allowed me to better understand my research and enabled me to perform the analyses described in this dissertation.

I would like to thank my fiancée, Alex Beall, for her constant understanding and support of everything I did for my research, for bringing me food when I got busy, for her encouragement at long distance, for moving from New York to Missouri with her goats and horses, and for always being there, even if she was across an ocean. I would also like to thank my parents, Janeen and Steve Grohsmeyer, for teaching me about science and engineering and for their support of nearly all my experiments, and I would like to thank my sister, Irene, for helping out with a lot of them. My mom deserves a special thank you for her hours of work helping to format this dissertation. I love you all very much.

I would like to thank Dr. Diletta Sciti, Dr. Laura Pienti, Mr. Simone Faille, Mr. Cesare Melandri, Mr. Daniele Dalle Fabbriche, and the undergraduate students Rachel Boillat, Michael Walden, Morgan Cornish, Andrew Schlup, and Tyler Grant for their work on this project, and all the past and present members of the UHTC group at Missouri S&T. I would like to acknowledge that funding for this project was provided by the National Science Foundation's Materials World Network program grant DMR-1209262 and by the Italian National Council of Research (CNR).

TABLE OF CONTENTS

Page

LIST OF ILLUSTRATIONS

Figure Page

SECTION

LIST OF TABLES

SECTION

1. INTRODUCTION

Advancement of leading technology in the fields of high-temperature materials processing, energy conversion, and aerospace propulsion requires structural materials with increased operating temperatures and improved high-temperature mechanical performance. The dual-scale composite architecture (DCA) design concept offers a wide range of possibilities in terms of tailored micro- and mesostructures and properties by prompting engineers to design the individual microstructures, and therefore the properties, of the components of composite materials [1]. An example of a globally isotropic DCA consists of isolated granules of a particular composition dispersed in a continuous matrix of a different composition (Figure 1.1).

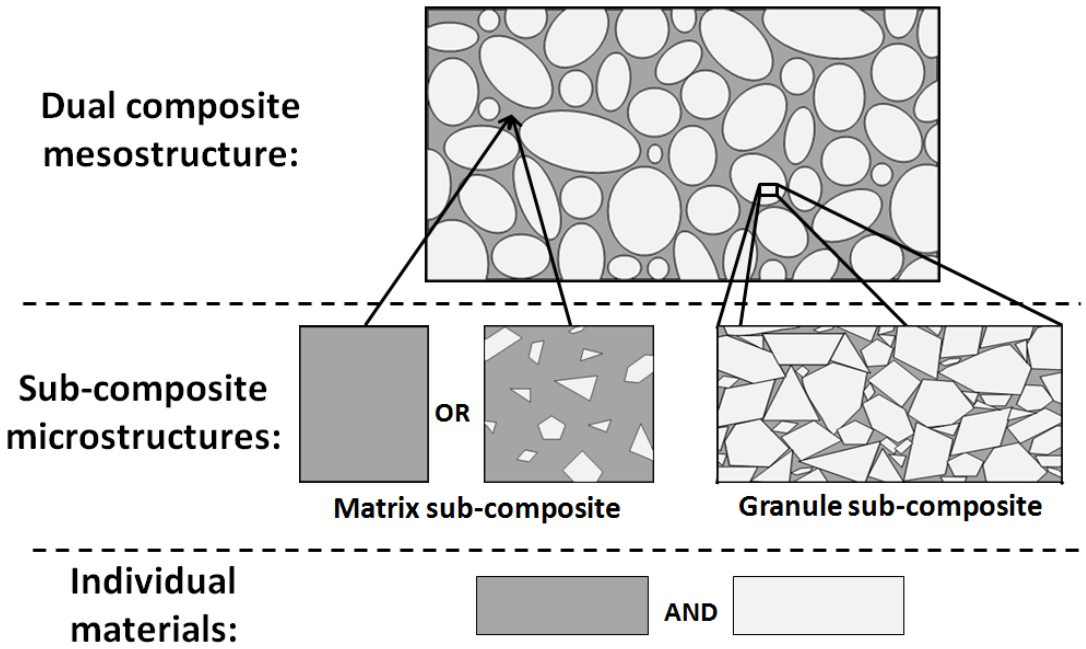

Figure 1.1. Conceptual drawing of a granule-matrix type dual composite architecture.

Previous studies have investigated highly directional ‘fibrous monolith’ type DCAs for use at elevated temperatures [2], but the study of globally isotropic granule-matrix type DCAs has been restricted to materials limited in temperature capability by melting temperature or poor oxidation resistance [3, 4]. Some WC-Co granule-matrix DCAs have been successfully applied in industry as rock drilling bits due to their ability to bypass the trade-off in fracture toughness and wear resistance that limits conventional WC-Co materials [5-9], highlighting the potential of this DCA design concept.

The component materials chosen as primary building blocks were zirconium diboride (ZrB_2) and molybdenum disilicide ($MoSi_2$) due to the reported ability of conventional ZrB_2-$MoSi_2$ ceramics to display excellent strength retention [10] and oxidation resistance [11, 12] up to the target use temperature of 1500°C and ductility due to deformation of $MoSi_2$ above its BDTT [13]. ZrB_2 is a refractory ceramic that has been the subject of in-depth study due to its combination of high melting temperature (~3245°C) [14], low electrical resistivity (10 μΩ·cm at room temperature) [15] and high thermal conductivity (>70 W/m·K up to 2000°C) [16], which aids in thermal shock resistance [17]. ZrB_2 exhibits significant strength retention and brittle mechanical failure up to at least 2300°C in Ar [18], making ZrB_2 a candidate high-temperature analog of the rigid WC particles in previous WC-Co DCAs. $MoSi_2$ has been used as heating elements in air furnaces due to its melting temperature of ~2030°C and oxidation resistance between ~800 and 1800°C via formation of a protective silica coating [19]. The ductility of $MoSi_2$ above 900–1300°C is the result of thermally-activated dislocation motion and grain boundary sliding dependent on intergranular silica content, [20] and makes $MoSi_2$ a candidate for a high-temperature analog of the ductile Co matrix in WC-Co DCAs.

Informed design of DCAs begins with sub-composite properties, as well as their processing requirements and densification behavior. Early in this research it was determined that the existing sum of processing techniques, resulting microstructures and mechanical properties in the literature was not detailed or consistent enough to allow informed DCA design decisions. Inconsistency in processing techniques, reported detail, and testing methods made direct comparisons between studies impossible, and variations in measured properties clouded overall trends. For example, ZrB_2-$MoSi_2$ ceramics in the literature have retained anywhere from ~30 and ~95% of their room-temperature flexure

strength at 1500°C [10, 21]. Several authors sought to characterize a ubiquitous diboride core-shell type morphology in ZrB_2-$MoSi_2$ microstructures, while the majority of authors did not mention the existence of these microstructural features [21, 22]. Further, fracture toughness values of ZrB_2-$MoSi_2$ ceramics had not been reported at any elevated temperature.

The purpose of this research has been two-fold: first, to establish a systematic baseline of experimental data of ZrB_2-$MoSi_2$ ceramics to advance the general understanding of these materials' processing-microstructure-property relationships to a useful level, and second, to extend the granule-matrix DCA concept to the field of high-temperature structural ceramics, and to develop an understanding of the basic design requirements of high-temperature DCAs by fabricating and testing several of the first DCAs intended for high-temperature use. This research addresses several specific questions:

1. How do the densification behavior and microstructural characteristics change as a result of varying ZrB_2 starting powder particle size, starting $MoSi_2$ content, and hot pressing temperature?
2. How does a systematic change in the starting $MoSi_2$ content for a single ZrB_2 starting powder grade influence the elastic properties, fracture toughness, and flexure strength at room temperature and at 1500°C, and what controls fracture toughness and flexure strength at room temperature and at 1500°C?
3. What is the sequence of events during the densification of ZrB_2-$MoSi_2$ ceramics, what is the composition of the $(Zr_{1-x}Mo_x)B_2$ solid solution shell structure in ZrB_2-$MoSi_2$ ceramics, and by what mechanism does it form?
4. How do the mechanical properties (elastic moduli, fracture toughness, and flexure strength) change as a function of the ZrB_2 median starting powder particle size and $MoSi_2$ content, and what factors control the mechanical properties in ZrB_2-$MoSi_2$ ceramics made with differing ZrB_2 starting powder sizes?
5. Can a granule-matrix type DCA be fabricated with ZrB_2 and $MoSi_2$ powders as starting materials, what are the mechanical properties of ZrB_2-$MoSi_2$ DCAs at room temperature and 1500°C? What are key factors to consider when designing DCAs for use at elevated temperatures?

Improved and systematic understanding of the processing-microstructure-property relationships of conventional ZrB_2-$MoSi_2$ ceramics is necessary for their eventual use in high-temperature structural applications. Adaptation of the DCA concept to the field of high-temperature materials is the first step in the development of a new variety of structural material for use in extreme environments.

2. LITERATURE REVIEW

2.1. ZIRCONIUM DIBORIDE (ZrB_2)

Due to its melting temperature of ~3250°C, ZrB_2 is a member of a group of materials classified as ultra high temperature ceramics (UHTCs), a group of borides, carbides, nitrides, and an oxide with melting temperatures above 3000°C [14, 23]. Its high melting temperature in combination with a moderate density of ~6.1 g/cm^3, and retention of strength and rigidity to above 2000°C [24–27], has made it a candidate for use in structural aerosurfaces in future hypersonic re-entry vehicles [28], as well as for molten metal crucibles, solar thermal energy absorbers [29–31] and combustion zone parts in engines [23]. ZrB_2 exhibits partially metallic atomic bonding which contributes to electrical resistivity below 10 μΩ·cm at room temperature [15] and thermal conductivity over 70 W/m·K up to 2000°C [16], which aids in thermal shock resistance. However, the tendency of ZrB_2 to exhibit brittle mechanical fracture and its susceptibility to rapid oxidation at high temperatures [32, 33] have hindered efforts to bring the material into the aforementioned applications.

2.1.1. Crystallographic, Elastic, and Thermal Properties. The properties of ZrB_2 are controlled by the nature and geometry of its chemical bonds. ZrB_2 crystallizes in the AlB_2-type hexagonal structure with P6/mmm (#191) symmetry (Figure 2.1), in which the Zr atoms form close-packed planes that alternate with sheets of covalently-bonded B in graphene-like hexagonal rings. The lattice parameters of the primitive unit cell are a = ~3.168 Å and c = ~3.530 Å (PDF 00-034-0423). B-B bonds are primarily sp^3 and sp^2 hybridized and control the a lattice parameter of the crystal structure, along with some contribution of the metallic cation radius [14]. Zr-B bonds have mixed ionic and covalent character, adding to the rigidity of the structure. Okamoto et al. measured the single-crystal elastic constants of ZrB_2 as a function of temperature, and reported a polycrystalline Young's modulus of 526 GPa, a shear modulus of 240 GPa, and a Poisson's ratio of 0.135 at room temperature [34]. Figure 2.2 shows the polycrystalline elastic moduli of ZrB_2 as calculated by Okamoto et al. from measured single-crystal values up to ~1100°C. Neuman et al. and Rhodes measured the Young's modulus of polycrystalline hot pressed ZrB_2 in four-point flexure in air up to 1600°C and in Ar up to

2100°C respectively (Figure 2.3) [18], and reported values near 400 GPa at 1100°C, about 15% lower than Okamoto's value of ~470 GPa at the same temperature.

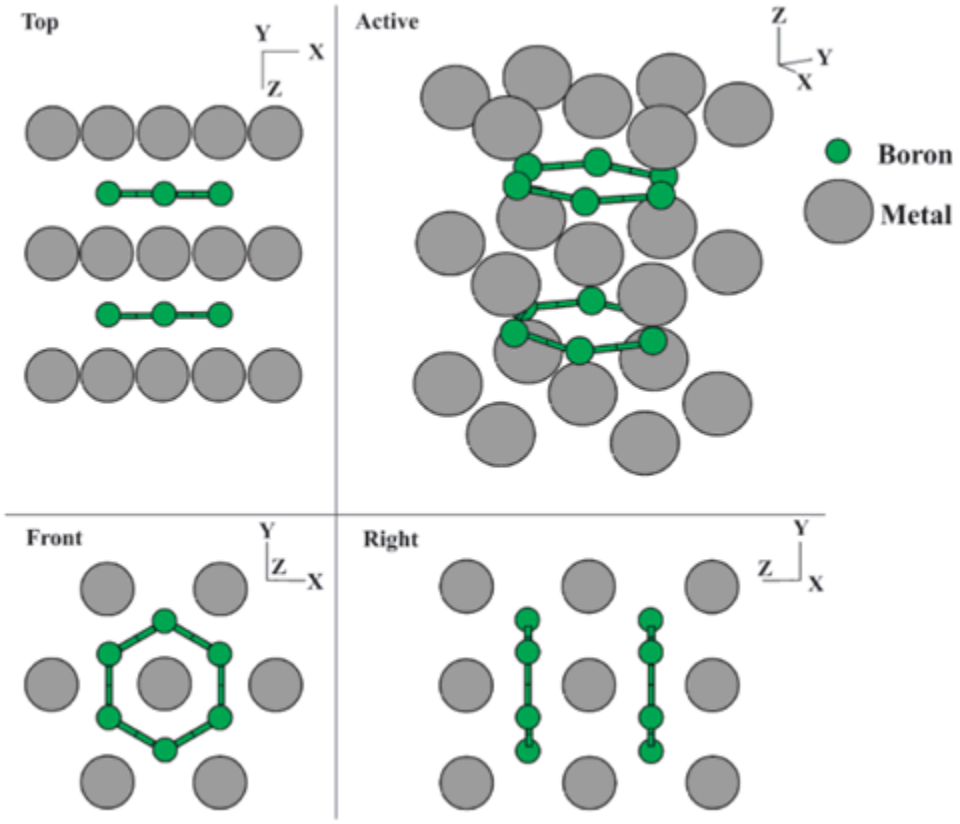

Figure 2.1. Projections of the AlB_2-type (P6/mmm, #191) crystal structure of ZrB_2. Reproduced from [14].

The covalent bonding in ZrB_2 also contributes to difficulty in sintering. Historically, ZrB_2 without sintering aids has only been densified by hot pressing at 2000°C or above under applied pressures of about 30 MPa [14]. Lonergan et al. found that grain boundary diffusion is the dominant densification mechanism in ZrB_2 below 2000°C, while lattice diffusion dominates at temperatures above 2000°C (Figure 2.4) [35]. Although recent research has made progress in synthesizing dense phase pure ZrB_2 by reactive sintering [35] or by the addition of minute amounts of sintering aids that react with impurities to form fugitive species [36, 37].

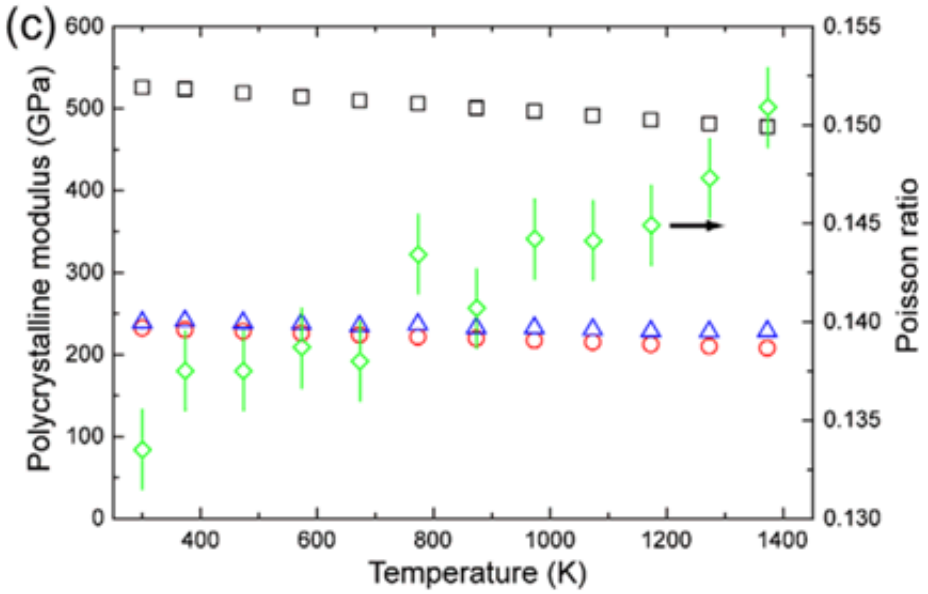

Figure 2.2. Young's (squares), shear (circles), and bulk (triangles) moduli and Poisson's ratio (diamonds) of ZrB_2 as a function of temperature. Reprinted from [34].

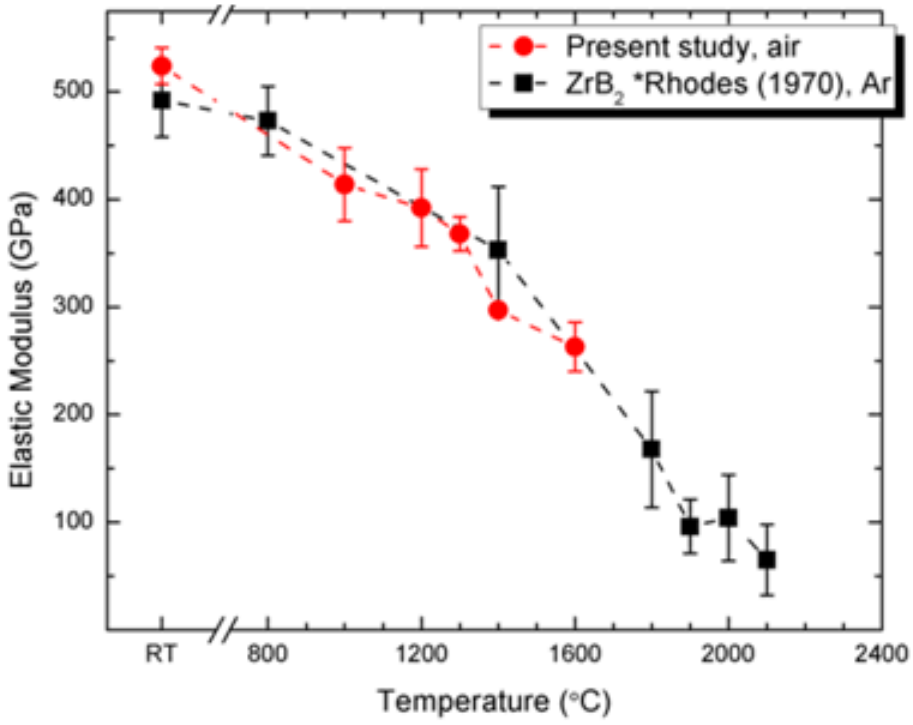

Figure 2.3. Young's modulus of ZrB_2 measured in four-point flexure as a function of temperature in air and in Ar. Measured grain size of specimens tested in air was 19.4 ± 13.0 μm. Reproduced from [18].

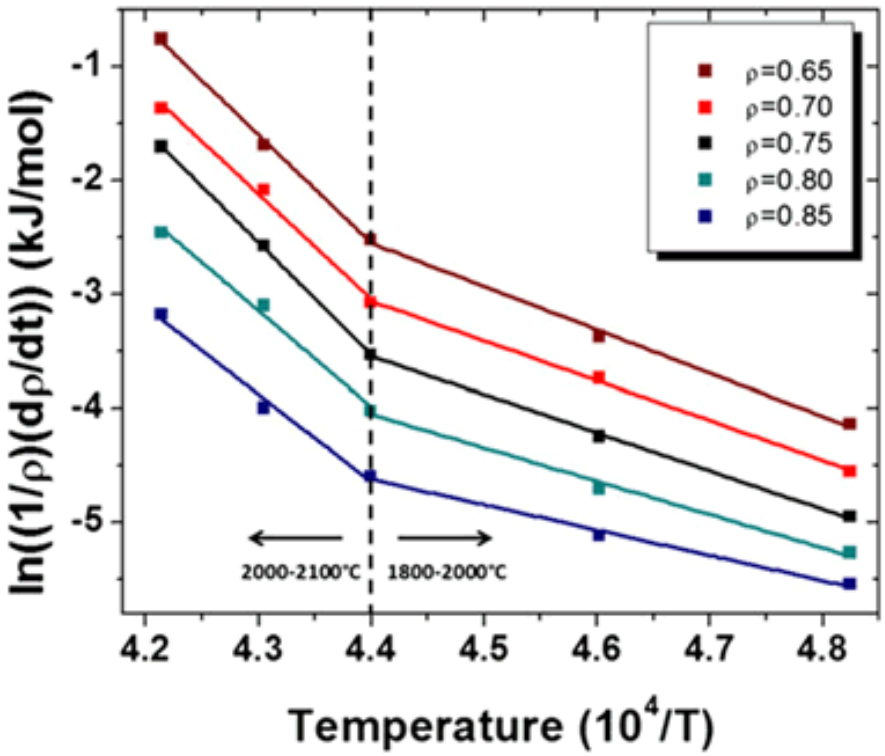

Figure 2.4. Arrhenius plot of densification rate of isothermally densified reaction hot pressed ZrB_2 as a function of inverse temperature for various densities. Inflection point indicates transition at 2000°C from grain boundary-dominated diffusion at lower temperatures to lattice-dominated diffusion above 2000°C. Reproduced from [35].

Touloukian et al. compiled data on the thermal expansion of both ZrB_2 and $MoSi_2$ as a function of temperature from over a dozen sources, and present the average relative expansions from their available sources as a function of temperature. Figure 2.5 shows the polycrystalline coefficients of thermal expansion (CTE) of ZrB_2 and $MoSi_2$ calculated from the average expansion data reported in Touloukian. The CTE of ZrB_2 increases from ~$5.2 \cdot 10^{-6}$/°C at 20°C to ~$8.9 \cdot 10^{-6}$/°C at 2000°C and can be described closely by a third order polynomial fit. The anisotropy of ZrB_2's crystal structure results in differing thermal expansion coefficients along the *a* and *c* axes. Okamoto reports CTE values of ~$6.66 \cdot 10^{-6}$/°C along the *a* axis and ~$6.93 \cdot 10^{-6}$/°C along the *c* axis in the range of 27 to 800°C, and also reports that the axial CTE values converge above ~300°C.

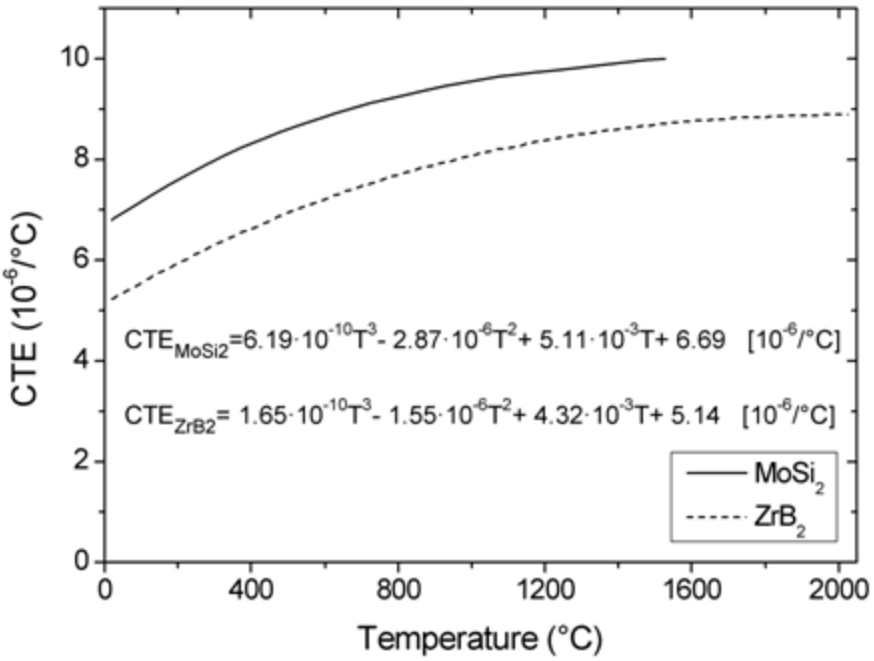

Figure 2.5. Polycrystalline coefficients of thermal expansion (CTE) of ZrB_2 and $MoSi_2$ as a function of temperature. Calculated from data in [38].

Spontaneous microcracking can occur in polycrystalline ceramics due to CTE mismatch between multiple phases (in particulate composites), crystallographic anisotropy of thermal expansion (in single-phase and particulate composites), or both. In each case, stresses accumulate during cooling due to anisotropic shrinkage. In binary particulate composites, tensile residual stresses will develop during cooling in the phase with the higher thermal expansion coefficient, while compressive residual stresses accumulate in the phase with the lower CTE. Larger grains exacerbate the anisotropic displacement that must be accommodated by neighboring grains. In a two-phase composite, a particle with a lower CTE than the surrounding matrix will generate tangential tensile stress in the surrounding matrix during cooling, which increases as the radius of the particle increases [39]. Eventually, when the strain energy becomes greater than that associated with crack propagation, spontaneous microcracks occur. Cleveland and Brandt developed an equation to predict the critical grain size for spontaneous microcracking: [40]

$$(gs)_{cr} = \left[\frac{14.4\gamma_f}{\left(E(\Delta\alpha_{\max})^2(\Delta T)^2\right)} \right] \quad (1)$$

where E is the Young's modulus, $\Delta\alpha_{max}$ is the maximum difference in crystallographic thermal expansion values, ΔT is the temperature over which stresses accumulate, and γ_f is the fracture surface energy:

$$\gamma_f = \frac{K_{Ic}\left(1-\nu^2\right)}{2E} \quad (2)$$

in which K_{Ic} is the fracture toughness of the microcracked phase, and ν is Poisson's ratio. Although this equation was developed for use in single-phase ceramics, it has been successfully applied to ZrB_2-based particulate composite systems [39]. Spontaneous microcracking has been observed in ZrB_2 ceramics with additions of SiC as a dispersed second phase [39].

2.1.2. Mechanical Behavior. The room temperature fracture toughness of polycrystalline ZrB_2 has been reported to be in the range of 1.9 to 4.8 MPa·$m^{½}$, which is similar to measured fracture toughness values of other polycrystalline engineering ceramics with similar elastic moduli, hardness, and flexure strength, such as alumina [23, 41, 42]. In alumina, fracture toughness (at crack lengths greater than the grain size) has been shown to increase with increasing grain size due to crack deflection at grain boundaries that results in a significant amount of intergranular fracture that leads to crack bridging [42]. Such a trend of toughness with grain size has not been observed in ZrB_2, which may be due to the fact that ZrB_2 exhibits primarily transgranular fracture at room temperature. Neuman et al. reported a linear increase in the fraction of ZrB_2 grains that exhibited intergranular fracture as a function of temperature in ZrB_2-30 vol.% SiC ceramics, from ~20% at room temperature to ~95% at 2200°C [25]. Increases in fracture toughness in other ceramic systems upon addition of a second particulate phase have been shown to result from the thermal residual stress state generated by a CTE mismatch between phases [43-45].

The fracture toughness of nominally pure ZrB_2 has not been investigated as a function of temperature, but the fracture toughness of ZrB_2 with 10 vol.% ZrC additions has been measured up to 2300°C (Figure 2.6) [46]. The fracture toughness of ZrB_2-10 vol.% ZrC remained between 3.4 and 5.2 $MPa \cdot m^{½}$ at all tested temperatures, but displayed maxima at 1000°C and 1800°C and minima at 1400°C and 2200°C. The decrease in toughness from 1000 to 1400C was attributed to the relaxation of CTE mismatch-related thermal residual stresses in the microstructure. Watts et al. measured the onset of thermal residual stress in ZrB_2-30 vol.% SiC at ~1400°C during cooling [47]. The increase in fracture toughness above 1400°C was attributed to stress relaxation at the crack tip due to plastic flow of ZrB_2 and ZrC, while the decrease in toughness above 1800°C was attributed to microvoid coalescence ahead of the crack tip [46].

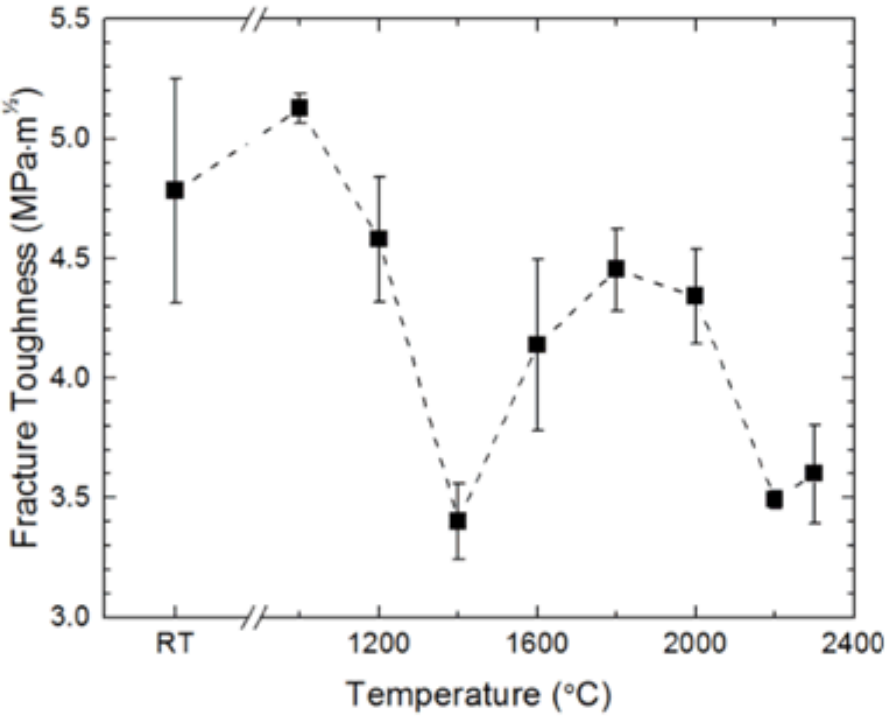

Figure 2.6. Chevron notch beam fracture toughness of ZrB2-10 vol.% ZrC tested in four-point flexure in Ar as a function of temperature. Reproduced from [46].

The flexure strength of ZrB_2 at room temperature has been reported to be in the range of 300 to 550 MPa, and reported strength values from multiple sources generally follow an inverse square relation with the grain size ($GS^{-½}$) [23]. The flexure strength of ZrB_2 as a function of temperature in Ar by Rhodes and by Neuman et al. in air and Ar is plotted in Figure 2.7 [18]. The flexure strength of ZrB_2 in air remained roughly constant up to ~1200°C, then dropped at ~1400°C due to relaxation of thermal residual stresses and continued to drop up to 1600°C. Tests in Ar show that in inert atmosphere ZrB_2 retains ~50% of its room temperature strength up to 2300°C.

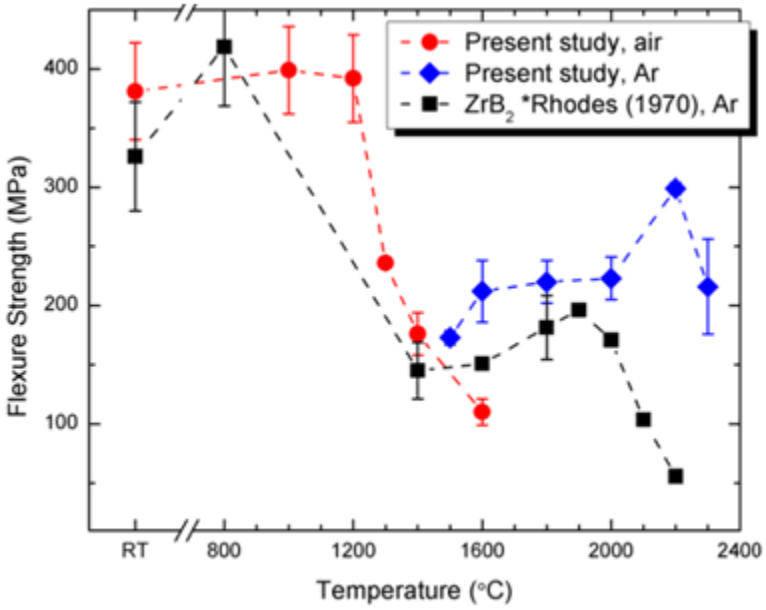

Figure 2.7. Four-point flexure strength of ZrB_2 as a function of temperature in air and in Ar. Measured grain size of specimens tested in air was 19.4 ± 13.0 μm. Reproduced from [18].

2.2. MOLYBDENUM DISILICIDE ($MoSi_2$)

Molybdenum disilicide is an intermetallic compound with a density of about 6.26 g/cm^3, a tetragonal crystal structure with I4/mmm symmetry [17, 20] (Figure 2.8a) and a melting temperature of ~2030°C [19, 48]. Its primary attributes are its relatively high melting temperature, oxidation resistance in air and oxidizing atmospheres at

temperatures up to 1800°C [48, 49], and its high-temperature ductility. Its relatively low electrical resistivity (~21.5 Ω·cm at 22°C) [48] makes it a common material for heating elements of air furnaces designed for operation in the range of 700-1800°C.

At room temperature, $MoSi_2$ is brittle, with reported fracture toughness values generally in the range of ~2.5 to 3.5 $MPa \cdot m^{½}$ [50-52]. Ductility of $MoSi_2$ at elevated temperatures has been shown to originate in slip activation of dislocations with <100>, <110>, ½<111> and ½<331> Burgers vectors (Figure 2.8, Table 2.1), as well as grain boundary sliding due to viscous flow of grain boundary SiO_2 in polycrystalline specimens [19, 50, 51]. Its brittle-to-ductile transition temperature (BDTT) has been reported as being between 900 and 1400°C, with higher BDTT temperatures reported for lower SiO_2 content materials [19, 50, 51].

Table 2.1. Slip systems observed in MoSi2 single crystals. Reproduced from [20].

Crystal orientation	Temperature (°C)	Strain rate (s^{-1})	Burgers vector	Slip plane
[001]	900–1100	10^{-5}	1/2⟨331⟩	{013}
			1/2⟨111⟩	
			⟨110⟩	
	1200–1400	10^{-5}	⟨100⟩	{001}
			⟨110⟩	
			1/2⟨111⟩	{110}
	1400–1600	10^{-4}	⟨100⟩	{001}
			⟨110⟩	
			1/2⟨111⟩	{110}
[021]	1000–1200	10^{-4} and 10^{-5}	1/2⟨111⟩	{110}
	1300–1400	10^{-4} and 10^{-5}	⟨100⟩	{001}
[771]	1000–1100	10^{-4}	1/2⟨331⟩	{013}
			1/2⟨111⟩	
			⟨110⟩	
	1000	10^{-5}	⟨100⟩	{011}
	1100–1300	10^{-5}	⟨100⟩	{011}
	1200–1300	10^{-4}	⟨100⟩	{011}

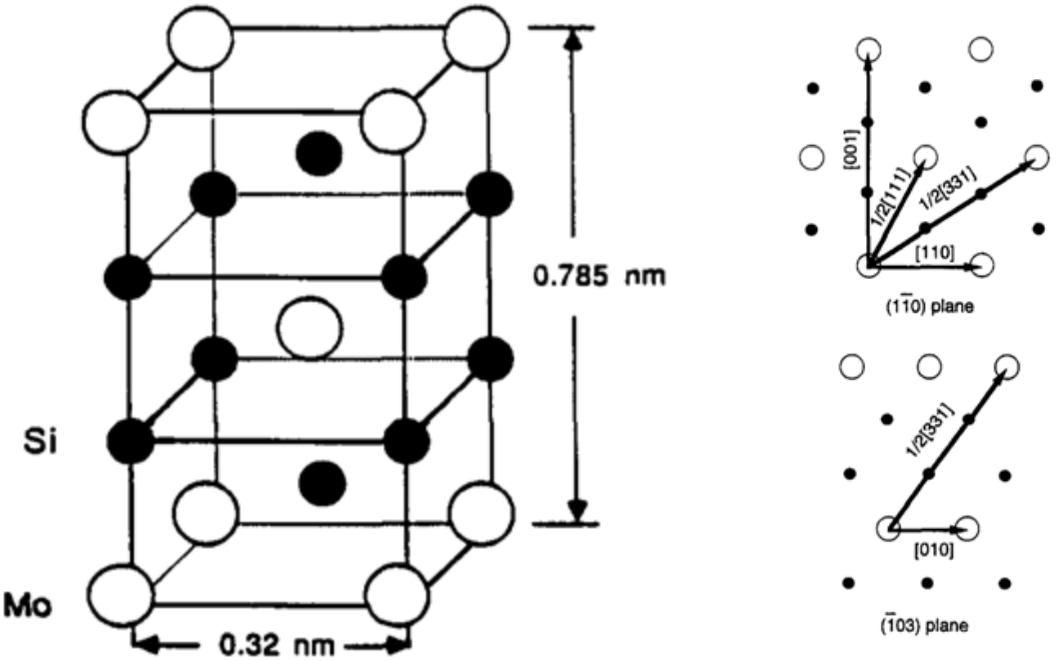

Figure 2.8. (a) $MoSi_2$ tetragonal (I4/mmm) crystal structure with unit cell dimensions; (b) illustration of Burgers vectors in $MoSi_2$ crystal. Both reproduced from [20].

SiO_2 is a common surface oxide impurity in commercial $MoSi_2$ powders due to reaction with atmospheric oxygen, and efforts have been made to process $MoSi_2$ in inert atmospheres and to remove the SiO_2 by reaction with C additions [1, 53, 54]. The elevated temperature hardness and fracture toughness of polycrystalline $MoSi_2$ have been found to depend heavily on the content of O and C [55], decreasing with increasing O content but increasing with increasing C additions [56]. Maloy et al. found that the fracture toughness of hot-pressed $MoSi_2$ with 2.8 wt.% oxygen decreased steadily from ~4 $MPa \cdot m^{½}$ at 800°C to ~0.7 $MPa \cdot m^{½}$ at 1400°C, while the fracture toughness of $MoSi_2$ with 2 wt.% C additions increased from 5.5 $MPa \cdot m^{½}$ to ~11.5 $MPa \cdot m^{½}$ over the same temperature range (Figure 2.9). The increased fracture toughness was found to be due to elimination of grain boundary SiO_2 and subsequent formation of SiC and $Mo_{\leq 5}Si_3C_{\leq 1}$ phases from reactions of SiO_2 and $MoSi_2$ with C.

Although $MoSi_2$ can display considerable ductility at elevated temperatures, its yield strength decreases sharply with increasing temperature above 1200°C, and is near 10 MPa above 1400°C for polycrystalline materials (Figure 2.10)[57, 58] and between 40

and ~240 MPa for oriented single crystals, depending on orientation (Figure 2.11) [21]. Gibbs and Petrovic showed that additions of 20 vol.% SiC whiskers increased the 0.1% strain yield strength by ~120 MPa at 1200°C and by ~10 MPa at 1500°C [58].

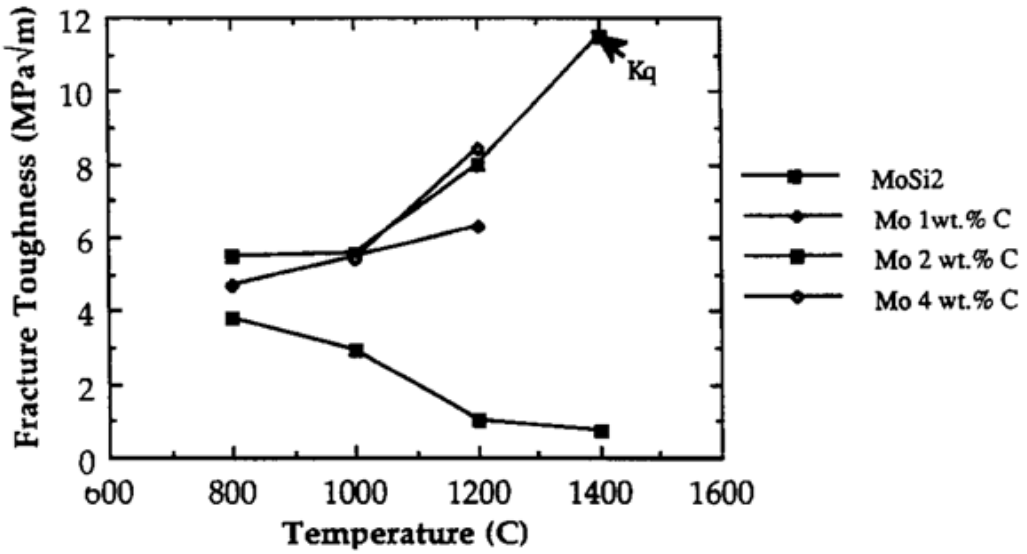

Figure 2.9. Fracture toughness of polycrystalline hot-pressed $MoSi_2$ as a function of temperature for various carbon additions. Reproduced from [20].

Due to the low activation energy required for dislocation motion, $MoSi_2$ has a propensity for creep at temperatures above 1200°C [9, 19, 51]. Sandananda et al. measured the creep rates of $MoSi_2$ at various temperatures as a function of applied stress (Figure 2.12), and showed that additions of 20 vol.% SiC whiskers decreased the creep rate between ~1200 and ~1400°C (Figure 2.13) [59]. The combination of low fracture toughness and relatively low hardness (8–10 GPa) [51, 52, 54] at room-temperature with poor creep resistance at elevated temperatures has limited its application as a stand-alone load-bearing material for either temperature regime.

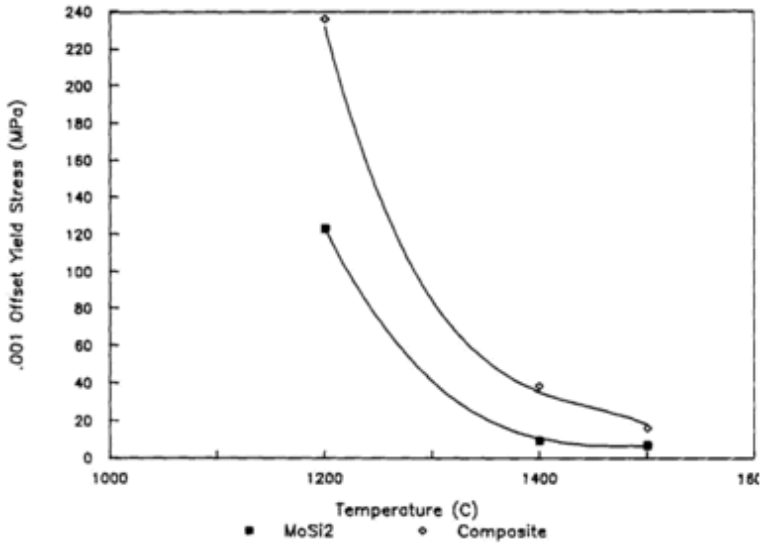

Figure 2.10. 0.1% offset yield stress as a function of temperature for polycrystalline $MoSi_2$ and a $MoSi_2$-SiC whisker composite. Measured in four-point bending, reproduced from [58].

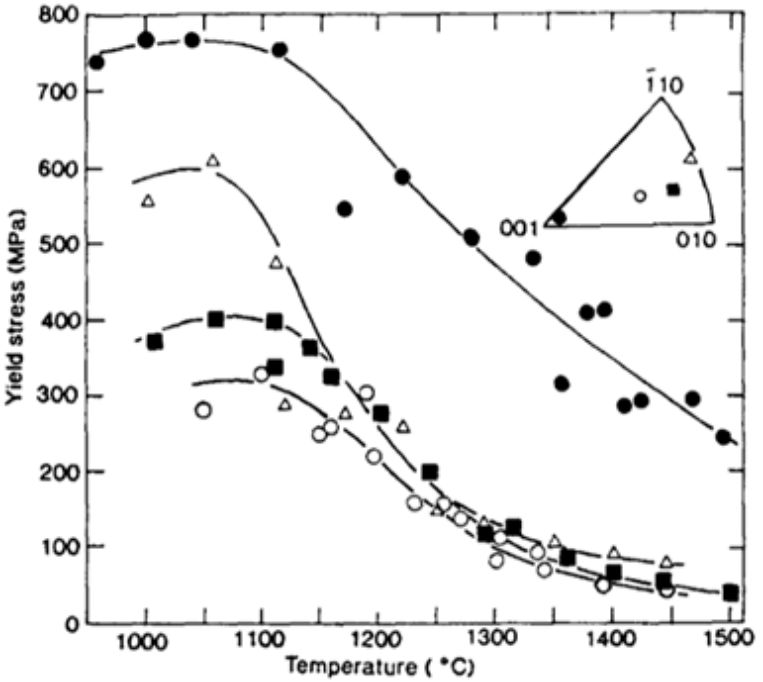

Figure 2.11. Temperature dependence of yield strength for several oriented single crystals. Reproduced from [21].

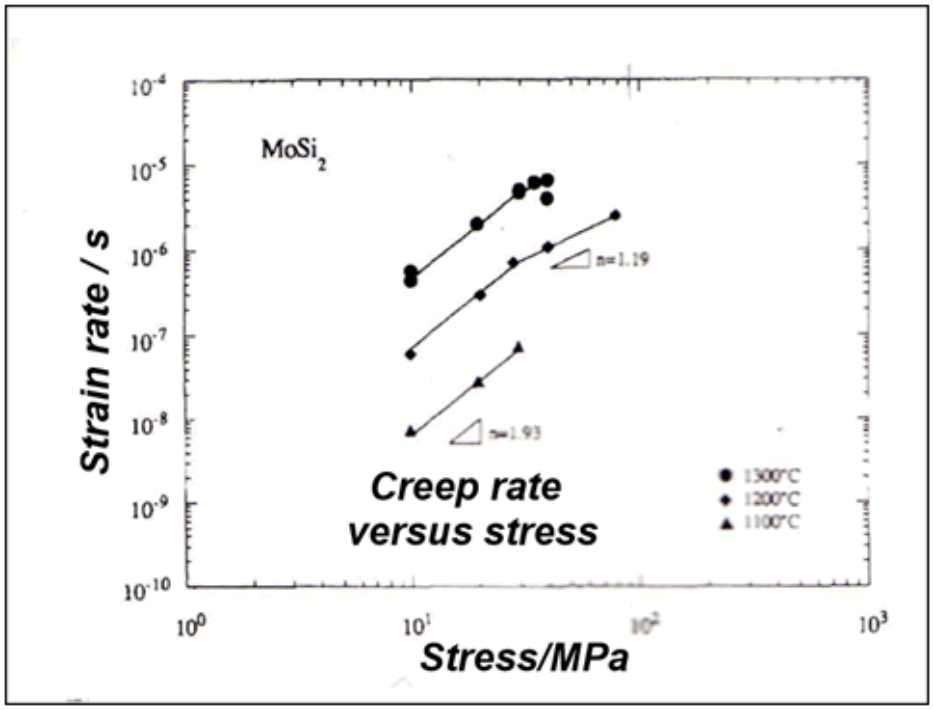

Figure 2.12. Steady state creep rates of polycrystalline $MoSi_2$ at varying temperatures as a function of applied stress. Indicated stress exponents are n = 1.19 at 1200°C above 30 MPa and n = 1.93 for all temperatures below 30 MPa. Reproduced from [19].

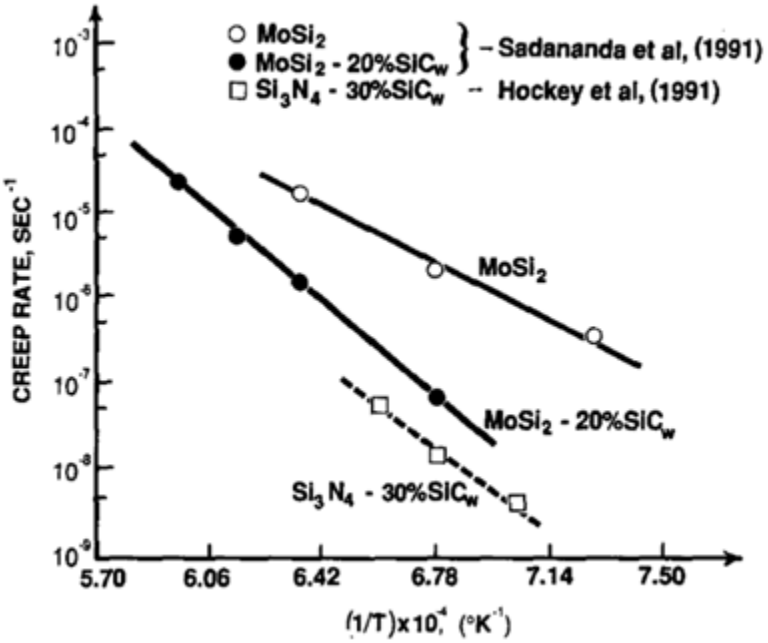

Figure 2.13. Arrhenious plot for polycrystalline $MoSi_2$ and of $MoSi_2$ and Si_3N_4 with SiC whisker additions between ~1060 and ~1480°C. Reproduced from [21].

2.3. ZIRCONIUM DIBORIDE-MOLYBDENUM DISILICIDE CERAMICS

Molybdenum disilicide ($MoSi_2$) has been studied as an additive to ZrB_2, due to its ability to perform three important functions: (1) act as a sintering aid facilitating densification of ZrB_2 by hot pressing at temperatures as low as 1750°C [10, 60, 61]; (2) improve the oxidation resistance of ZrB_2 up to ~1600˚C by forming a glassy borosilicate surface layer [62-64]; and (3) add ductility at elevated temperatures due to its brittle-to-ductile transition between 1000 and 1300˚C [57]. Additions of $MoSi_2$ also increase the flexure strength of ZrB_2 at room temperature, 1200˚C and 1500˚C in air [10, 65]. Multiple studies investigated the densification behavior of ZrB_2-$MoSi_2$ ceramics during pressureless sintering (PLS) [10], hot pressing (HP) [62, 66], reaction hot pressing (RHP) [13], and spark-plasma sintering (SPS) [60] at temperatures between 1750˚C and 1950˚C.

2.3.1. Processing and Microstructure. The morphology of the MoSi2 grains in hot pressed materials has led some authors to suspect that initial densification is assisted by deformation of the MoSi2 powder particles, their ductility allowing them to deform under applied pressure at high temperature and fill some of the space between ZrB2 grains during compaction [22]. Several authors have reported a core-shell type structure of the ZrB_2 grains in ZrB_2-$MoSi_2$ ceramics, in which a $(Zr,Mo)B_2$ solid solution shell partially or in some cases completely surrounds a ZrB_2 grain core when observed in polished sections and TEM images (Figure 2.14a) [10, 11, 22, 45, 60, 67]. This shell structure is believed to be a substitutional solid solution in which the Mo atoms replace Zr atoms on the metallic sites in the crystal lattice. Similar core-shell structures have been observed in ZrB_2 ceramics made with additions of $TaSi_2$ [11, 68, 69] and WSi_2 [11], as well as HfB_2 ceramics made with additions of $MoSi_2$ [10] and $TaSi_2$ [2, 69], and in ZrB_2-SiC ceramics with significant amounts of WC contamination from milling media wear [70]. Although only reported in a minority of the diboride literature, this type of core-shell structure has been observed in a broad enough range of diboride-based materials with transition metal additives that it may be a common characteristic and an important hint at the densification processes of this type of material that has often gone unnoticed. (Zr,Mo)B2 solid solutions are discussed in more detail in section 2.3.2. Table 2.2 presents processing details of ZrB2-MoSi2 compositions reported in the available literature for which mechanical property data is also reported.

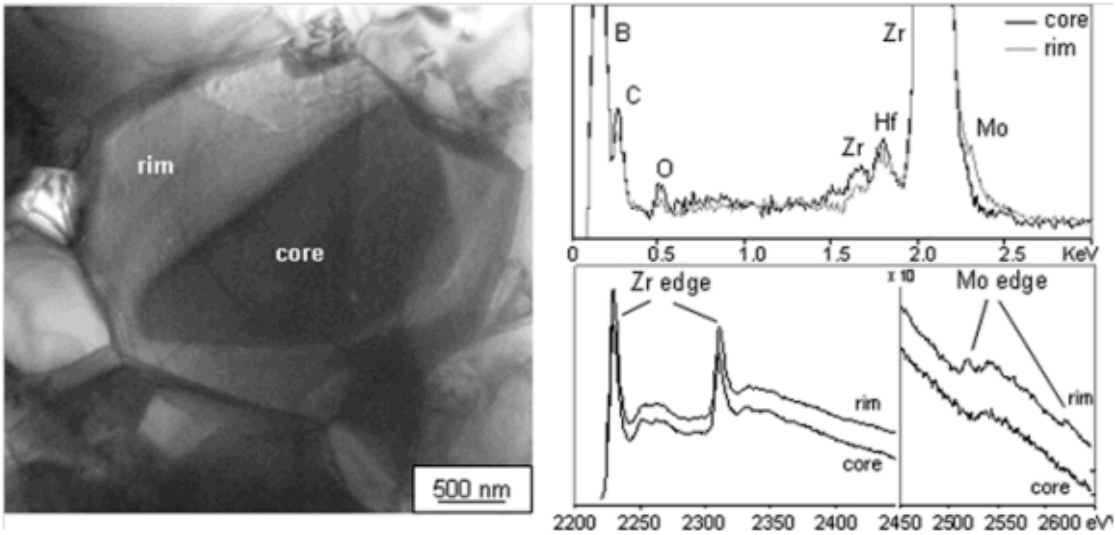

Figure 2.14. Brightfield TEM image of ZrB_2 grain core and shell in a ZrB_2-20 vol.% $MoSi_2$ ceramic, accompanied by EDS and EELS spectra of core and shell. Reproduced from [22].

The densification behavior of ZrB_2-$MoSi_2$ ceramics is complex and still not completely understood. Silvestroni et al. have proposed the only theory of densification for ZrB_2-$MoSi_2$ ceramics with an explanation of the formation of the core-shell structure, which is based on SEM and TEM observations of pressurelessly sintered (PLS) ZrB_2-$MoSi_2$ and HfB_2-$MoSi_2$ materials [10, 22]. The proposed sintering process suggests initial reactions of B_2O_3 surface oxide impurities from the starting powders with $MoSi_2$ to form MoB, Mo_5Si_3, Mo_5SiB_2, (observed in PLS ZrB_2-$MoSi_2$ in quantities of 2.7, 1, and 1 vol.%, respectively) and SiO_2. Subsequently, SiO_2 reacts with carbon from the sintering environment to form SiO(g) and CO(g) at the sintering temperature (1850°C), which escape through pores that remain open until late in the process due to the grain pinning effect of the $MoSi_2$. The study reports that SiO_2 was not observed in the PLS materials, but is a common impurity in hot pressed (HP) and spark plasma sintered (SPS) materials of the same nominal composition, suggesting that early compaction of the powder bed by applied pressure in these latter methods causes open porosity to close earlier, trapping SiO_2 species in the material. The study also notes that more rapid densification is obtained by application of pressure in HP and SPS due to the space-filling effect of deformation of $MoSi_2$ particles.

Table 2.2. Processing details of ZrB_2-$MoSi_2$ ceramics in the available literature.

Ref.	Nominal $MoSi_2$ content (vol%)	Densi-fication method	Densification T_{max} (°C)/ Dwell time (min)	Uniaxial pressure (MPa)/ atmosphere	Bulk density (g/cm^3)	Reported relative density (%)	Identified impurity phases (vol%)	ZrB_2 Avg. GS (µm)	$MoSi_2$ Avg. GS (µm)
[34]	10	HP	1900/45	32/argon	6.19	101.5	WC	-	~5
	20				6.17	100.8		-	
	30				6.29	102.6		-	
[49] [59] [57]	5*	PLS	1900/60	0/argon	-	96	*ZrC, MoB, Mo_5SiB_2, Mo_5Si_3, ZrO_2	2-3	-
	20*	PLS	1850/60	0/argon	6.07	99			-
[65]	15	HP	1750/20	30/vac.	5.98	98.1	ZrO_2	1.8	-
[54]	15	SPS	1750/7	30/vac.	6.0	97.7	SiC	1.4	-
[54]	20	HP	1800/5	30/vac.	6.01	98.1	SiO_2(~5) ZrO_2(2-3) MoB	~1.8	-
[48]	1*	SPS	1850/5	100/-	-	98	*SiO_2(1.5), SiC(0.5), ZrO_2(1)	3.8 ± 0.2	-
	3*		1750/3	100/-	-	100	*SiO_2(3), SiC(1), ZrO_2(1)	1.9 ± 0.1	-
	9*		1700/5	100/-	-	100	*SiO_2(3), SiC(1), ZrO_2(1)	1.7 ± 0.1	-
[66]	10	HP	1800/30	30/vac.	6.08	99.7	-	1.9 ± 0.6	1.8 ± 0.5
	20				6.11	99.8	-	1.6 ± 0.6	2.7 ± 0.9
	30				6.13	99.8	-	2.1 ± 0.7	2.4 ± 0.6
	40				6.13	99.7	-	1.9 ± 0.7	2.6 ± 0.8
[58]	2.3*	HP	1900/7	30/vac.	6.04	-	*SiC, ZrO_2, SiO_2	1-10	-
[67]	20	HP	1850/60	30/argon	-	95.2	-	2	2
[56]	10	RHP	1800/60	20/argon	6.101	99.9	Si (?)	-	-
	20		1800/30		6.110	99.8		1.8	
	20		1800/60		6.114	99.9		2.9	
	20		1800/120		6.115	99.9		4.6	
	30		1800/60		6.119	99.7		-	
[68]	20	HP	1800/30	30/vac.	5.8	94	SiO_2	-	-

Silvestroni et al. stress the importance of the formation of a Mo-Si-B-O liquid phase to the densification of ZrB_2-$MoSi_2$ ceramics and as the mechanism of formation of the core-shell morphology. The Mo-Si-B ternary phase diagram published by Katrych et al. reports three eutectics: the first at 1350°C between Si, $MoSi_2$, and SiB_6, the second at 1802°C between Mo_5Si_3, $MoSi_2$, and MoB, and the third at 1885°C between $MoSi_2$, Mo, and Mo_5SiB_2 (Figure 2.15) [5]. Thus, at processing temperatures between 1750 and 1950°C, one or more liquid phases can be expected. The study by Silvestroni et al. reported that the partial dissolution of the ZrB_2 phase into a Mo-Si-B-O liquid phase is supported by traces of Zr and O identified in the MoB, Mo_5Si_3, and Mo_5SiB_2 phases, and that dissolution of the diboride was followed by epitaxial reprecipitation of the $(Zr,Mo)B_2$ solid solution onto the former ZrB_2 grains during cooling.

X-ray diffraction has shown that the solid solution shell shares the P6/mmm crystal structure of the ZrB_2 core, although with slightly decreased lattice parameters (expected due to the relationship of atomic radii of Zr and Mo). Several authors have reported splitting of the characteristic ZrB_2 peaks, most easily visible at $2\theta \leq 100°$, wherein ZrB_2 peaks each have a less intense sister peak beside them at a slightly higher angle [10, 22, 45, 60]. Monteverde investigated the lattice parameter differences between core and shell [45] while Silvestroni et al. conducted TEM investigations of the interface between core and shell in ZrB_2-$MoSi_2$ [22] and ZrB_2-$TaSi_2$ [69] ceramics. TEM investigations have shown sharp interfaces between core and shell that are lined with series of dislocations, and selected area electron diffraction (SAED) has shown that associate core and shell have identical or nearly identical crystallographic orientation [22, 69]. In ZrB_2-$TaSi_2$ ceramics, the core-shell interface contained zipper-like dislocation stacking, and high-resolution TEM imaging (HRTEM) showed crystallographic alignment of core and shell, stacking faults in the shell, and both wetted and non-wetted grain boundaries between shells of different grains (Figure 2.16). HRTEM imaging of core-shell interfaces in ZrB_2-$MoSi_2$ ceramics was attempted but not successful. Silvestroni et al. proposed a complex series of densification processes for ZrB_2-$TaSi_2$ ceramics (Figure 2.17).

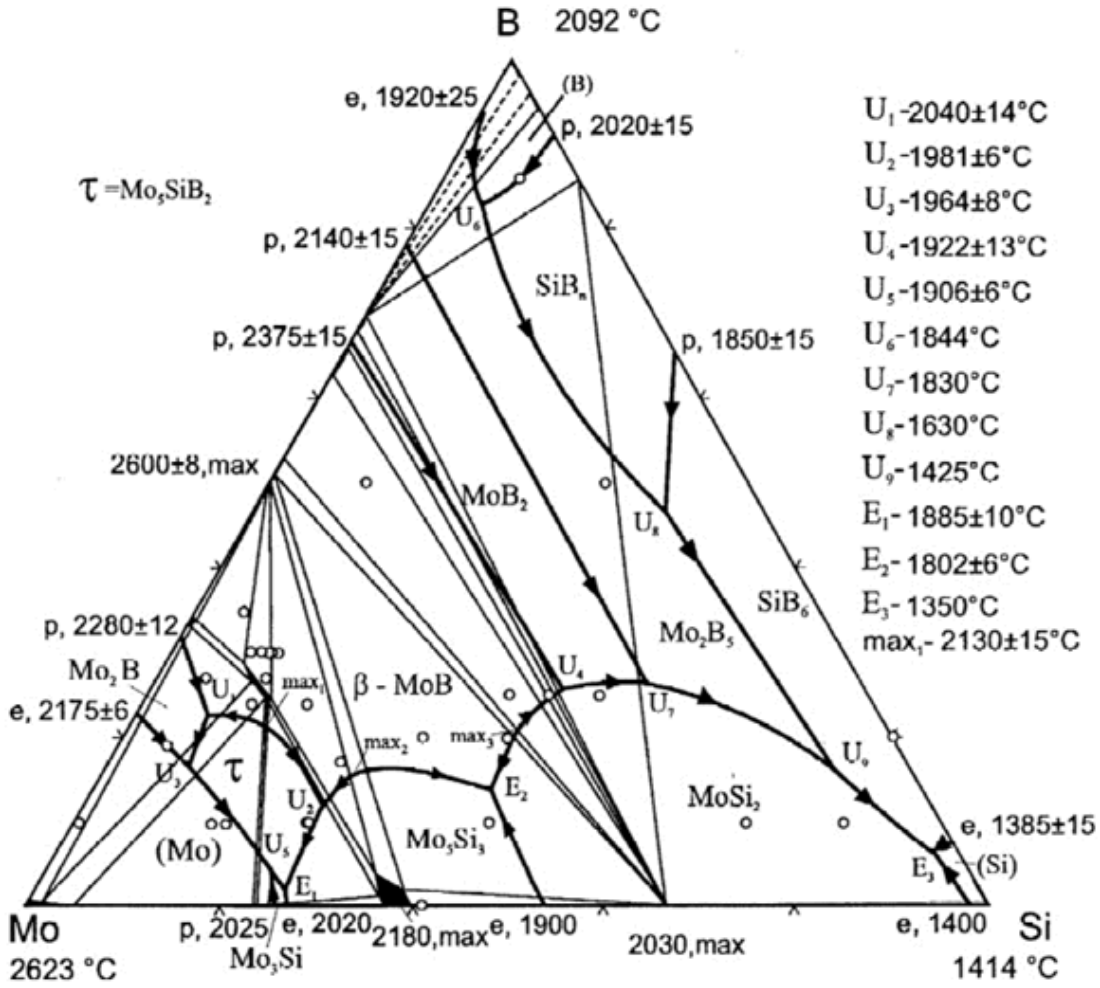

Figure 2.15. Ternary phase diagram of the Mo-Si-B system reproduced from [5].

2.3.2. Solid Solutions of Transition Metal Diborides. Solid solutions of metal diborides are not a recent discovery. In the early 1960s Kislyi et al. found that Mo powder was effective as a sintering aid for ZrB_2, and that additions of 5 and 10 mol.% Mo to ZrB_2 resulted in a single-phase, homogeneous solid solution after sintering at 2200 to 2250°C for 1.5 to 2 hours [71]. XRD showed a single set of shifted peaks. Kislyi et al. also reported the formation of a liquid phase at about 2000°C, although in a pure ZrB_2-Mo system this temperature is likely higher due to the fact that the starting ZrB_2 powder contained ~1.5 wt.% C and ~1.8 wt.% Fe. Dissolution of Mo into ZrB_2 was reported as noticeable at 1600–1700°C and above.

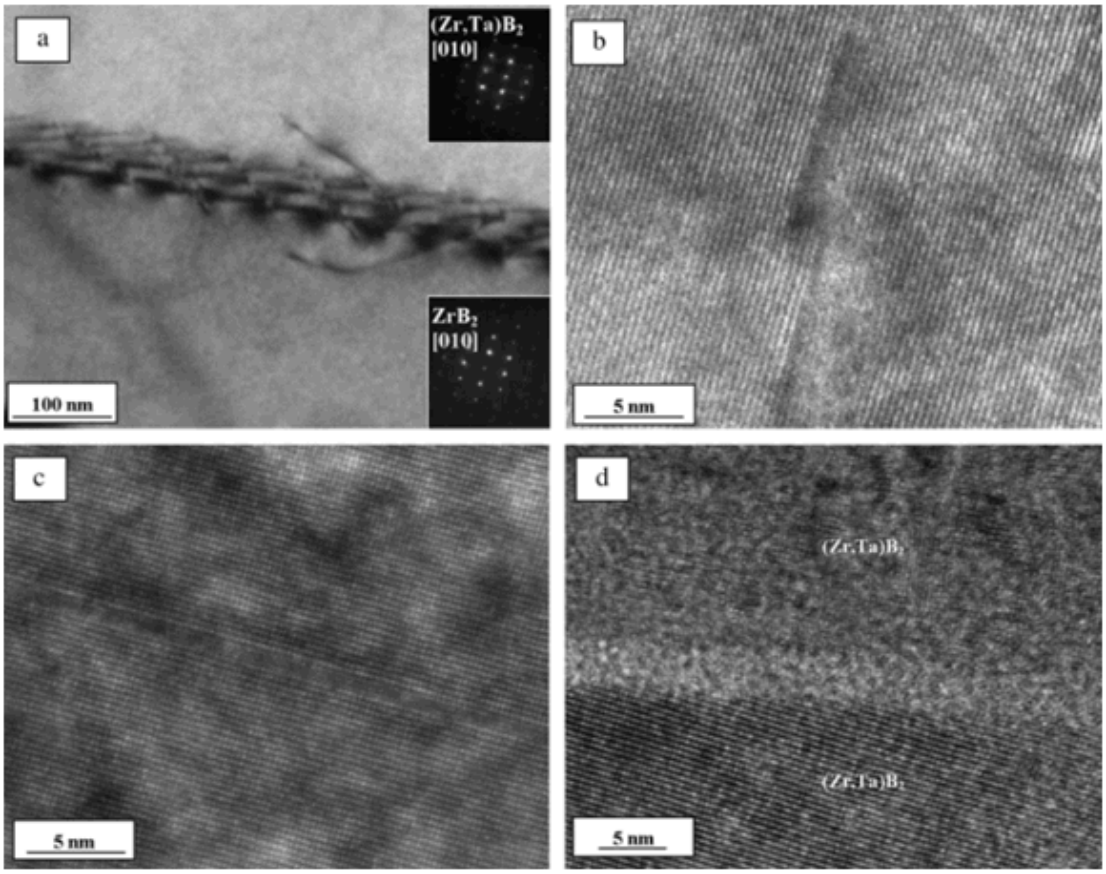

Figure 2.16. TEM images of the interface between ZrB_2 cores and $(Zr,Ta)B_2$ shells in ZrB_2-$TaSi_2$ ceramics. (a) Dislocations along the interface with SAED patterns showing crystallographic alignment, (b) core-shell interface showing low-angle grain boundary, (c) stacking faults in the $(Zr,Ta)B_2$ solid solution, and (d) example of wetted grain boundary between two adjacent $(Zr,Ta)B_2$ grains. Reproduced from [69].

Phase equilibrium data in the ZrB_2-$MoSi_2$ system are limited. Although all six of the elemental binaries have been published, only the Mo-B-Si ternary diagram is fully available (Figure 2.16) [5]. Rogl published a Zr-Mo-B ternary isothermal section at 1400°C that sheds more light on the nature of $(Zr_{1-x}Mo_x)B_2$ solid solutions (Figure 2.18) [7]. The solubility region of ZrB_2 along the Zr-B binary is ~1 at.%, which is in agreement with Rudy's reported stability range for that compound [72]. The diboride solid solubility zone maintains this small range of TM:B ratios as it extends toward a compound on the Mo-B binary labeled as Mo_2B_{5-x}, located at 68–69 at.% B. The solubility of elemental Mo in ZrB_2 is reported to be $\leq$ 2 at.% in both the Zr-Mo-B isotherm and the ZrB_2-Mo

quasibinary diagram (Figure 2.19), indicating that the exchange of Mo for Zr in the diboride has a relatively small effect on the limited stoichiometric range of TM:B ratios occupied by ZrB_2. The ZrB_2-Mo quasibinary diagram shows a eutectic temperature of ~2050°C at 47 at.% Mo, indicating that in the absence of Si, addition of Mo to ZrB_2 is not expected to result in formation of a eutectic liquid phase at commonly used processing temperatures (<2000°C) for ZrB_2-$MoSi_2$ ceramics [7].

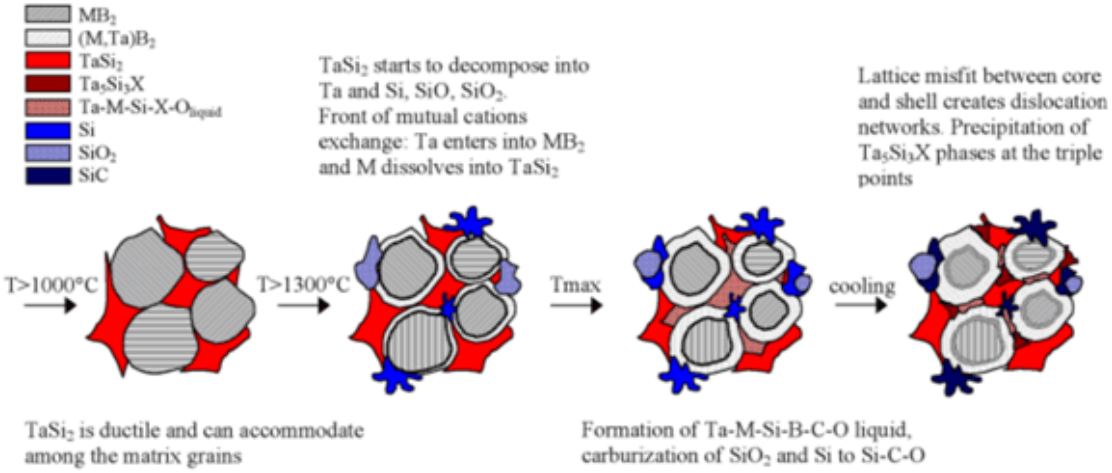

Figure 2.17. Sketch of possible densification mechanisms occurring in ZrB_2 and HfB_2 ceramics with additions of $TaSi_2$. Reproduced from [69].

In the Zr-B-Ti and Zr-B-Hf ternary systems, ZrB_2 forms complete solid solutions with the isostructural compounds TiB_2 and HfB_2 [72]. The Zr-B-Mo isotherm shows a maximum solubility of ~26 mol.% of Mo_2B_{5-x} at 1400°C. Mo_2B_5 is often reported as crystallizing in the $R\bar{3}m$ (166) structure, which is not isostructural with ZrB_2. the Mo-B binary phase diagram shows that hexagonal MoB_2 exists with P6/mmm symmetry between its eutectoid temperature of ~1517°C and its peritectic of 2375°C, above the temperature of the available Zr-B-Mo isotherm but spanning the range of densification temperatures used in the literature for ZrB_2-$MoSi_2$ ceramics (Figure 2.20) [73]. MoB_2 appears to exist as a substoichiometric compound (sometimes referred to as MoB_{2-x}) [74] [75], reaching a maximum of 66 at.% B at the peritectic temperature of Mo_2B_5

(~2140°C). The minimum B content of MoB_2 has been reported to be ~ 62 at.% B at its eutectoid temperature of 1517°C, at which it transforms into substoichiometric Mo_2B_5 (Mo_2B_{5-x}) and α-MoB upon cooling.

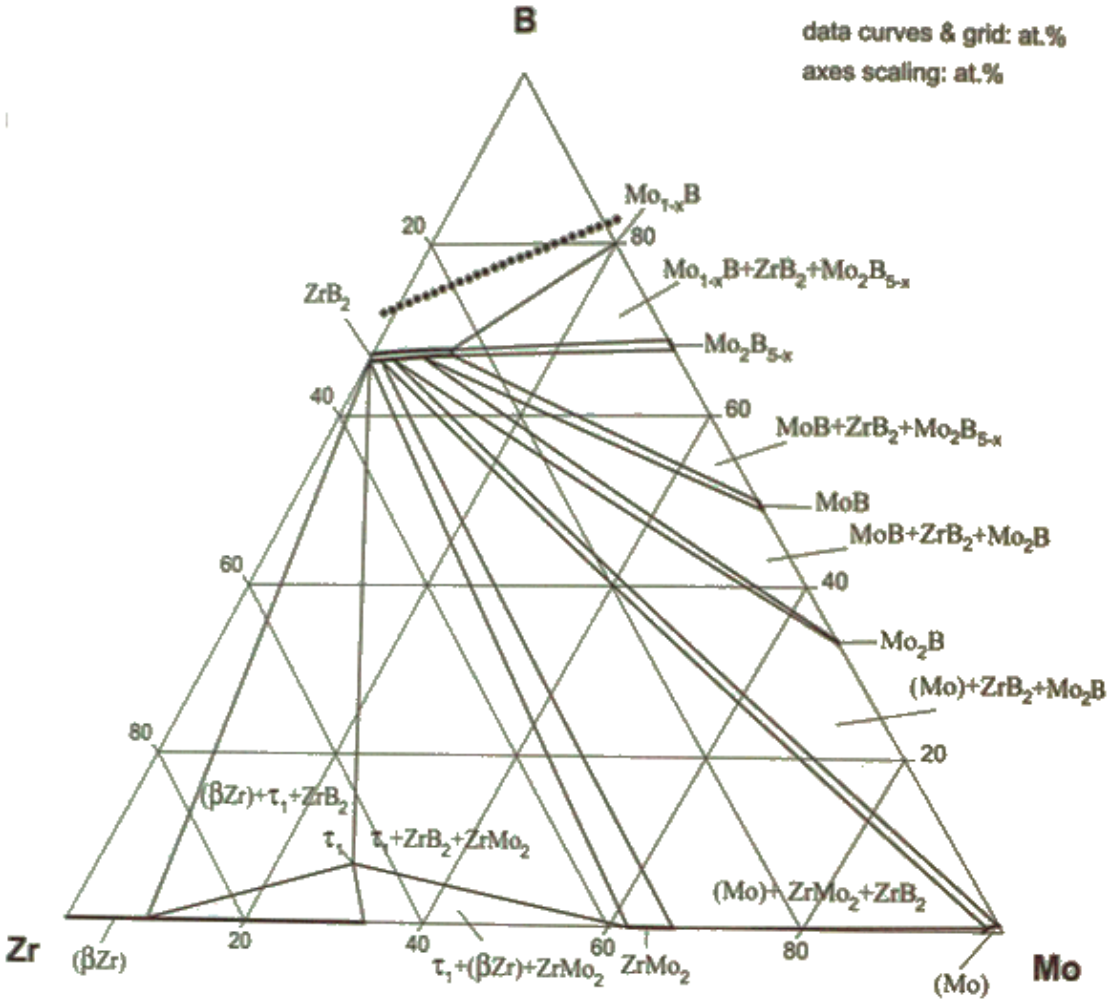

Figure 2.18. Zr-Mo-B ternary isotherm at 1400°C. Reproduced from [7].

The crystallization behavior of MoB_2 and Mo_2B_5 is complex and similarities between their crystal structures have resulted in difficulty distinguishing both phases in synthesized samples [74, 75]. Klesnar et al. reported that the stability range of Mo_2B_{5-x} may extend as low as 66 at.%, and pointed out difficulties in practical measurement of

specimen composition and determination of crystal structure after high-temperature synthesis. Kiessling first proposed the crystal structure of Mo_2B_5 to be a variation of the …AHAHAH… stacking structure of ZrB_2 [76]. This structure, which has since been characterized and supported computationally by various authors [74, 75, 77-79], consists of a stacking order …AHAKBHBKCHCK… in each unit cell, in which A, B, and C are layers of close-packed Mo atoms (B and C are shifted by (*a*/3, 2*a*/3) and (2a/3, a/3), respectively), and H and K are ring-bonded B sheets. H sheets are planar and graphene-like as in the hexagonal AlB_2-type structure, while in K sheets the B rings are buckled out of plane and have a B atom at the center of each hexagonal B ring.

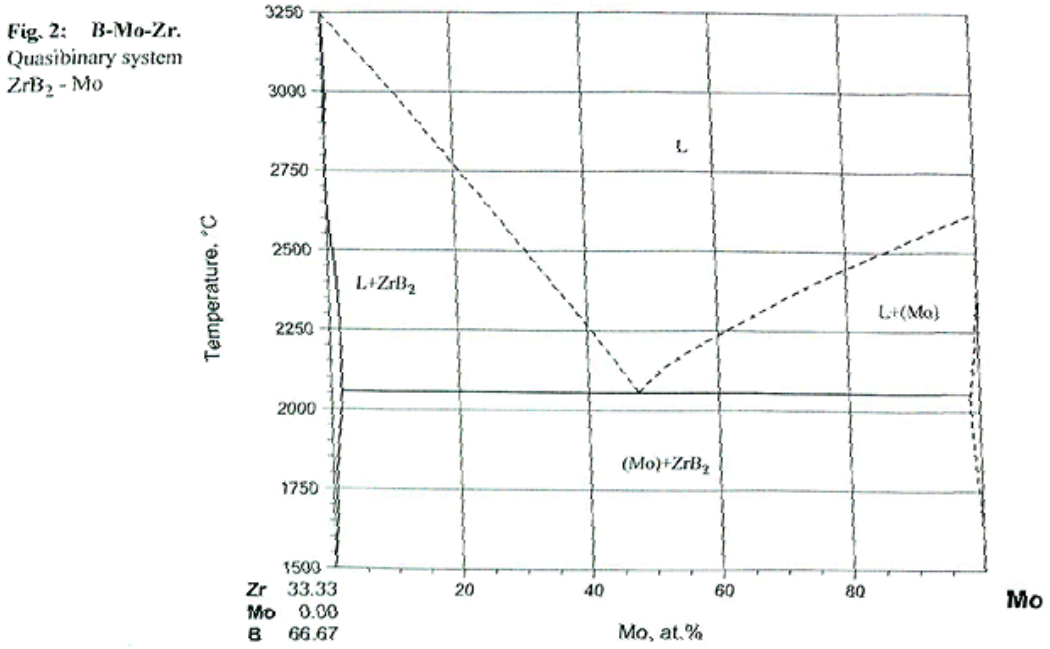

Figure 2.19. ZrB_2-Mo quasibinary phase diagram. Reproduced from [80].

McClane et al. measured the thermal conductivities of diboride solid solutions made with commercial ZrB_2 and 3 mol.% additions of Hf, Nb, W, Ti, Y, Ta, Mo, Re, V, and Cr diborides, hot pressed at 2150°C or higher to achieve homogeneous solid solutions [37, 81]. Decreases in measured thermal conductivities of solid solutions with

Hf, Nb, and Y correlated with a measured decrease in unit cell volume from that of ZrB_2, while the thermal conductivity of ZrB_2 with Ta, Re, V, and Cr diboride additions generally decreased according to the Pauling atomic radius of the solute metal atom (Figure 2.21).

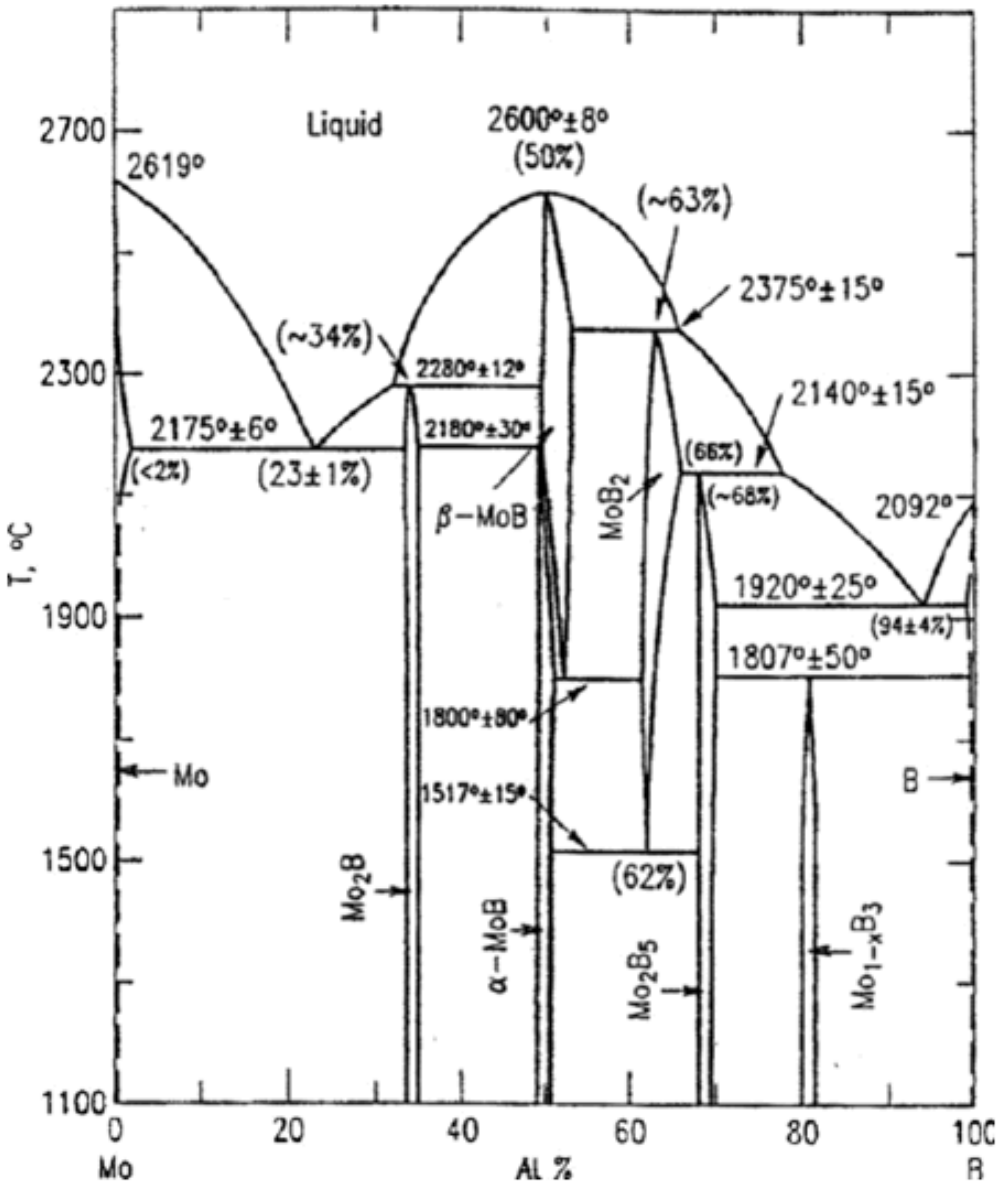

Figure 2.20. Binary phase diagram of the Mo-B system. Reproduced from [73].

However, ZrB_2 with MoB_2 additions had a thermal conductivity lower than expected based on the published atomic radius of Mo, and this was attributed to the tendency of Mo to form more complex Mo_2B_n compounds with different coordination and electronic configurations, hindering both electronic and phononic portions of thermal conductivity. Additions of W diboride had a similar effect, resulting in a thermal conductivity lower than expected.

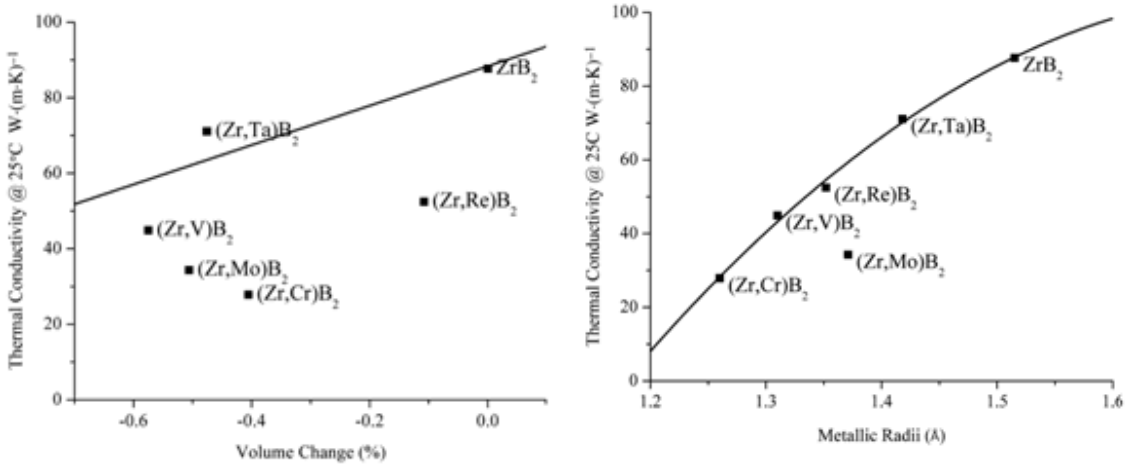

Figure 2.21. Thermal conductivity of $(Zr_{0.97}TM_{0.03})B_2$ diboride solid solutions as a function of unit cell volume change from ZrB_2 and metallic solute atom radius. Reproduced from [37].

Although Silvestroni [22], McClane [37], and others [82] have reported complete solubility of <10 mol.% MoB_2 in ZrB_2, the solubility limit of MoB_2 in ZrB_2 has not been determined. Knowledge of the solubility limit is expected to be useful in understanding the formation mechanism of the solid solution shell structures observed in ZrB_2-$MoSi_2$ ceramics in the literature by ascertaining whether the MoB_2 content of the shells is controlled by this solubility limit at the densification temperatures used. Zakharov reported a solubility of 6 to 8 wt.% (?? to ?? mol.%) MoB_2 in ZrB_2 at 1200°C [8] and, Rogl reported a solubility of ~26 mol.% at 1400°C. Post reported a single homogeneous AlB_2-type phase after arc melting a 50/50 powder mixture of ZrB_2 and MoB_2 at 2600°C, and from this assumed a complete solid solution existed at elevated temperature. There

appears to be no ZrB_2-MoB_2 pseudobinary phase diagram available. Rudy et al. published a pseudobinary diagram of the probably similar HfB_2-MoB_2 system (Figure 2.22), accompanied by measured lattice parameters of the $(Hf_{1-x}Mo_x)B_2$ solid solution diboride as a function of Mo content [3]. This diagram shows an incomplete solid solution, with the solubility limit of MoB_2 in HfB_2 increasing from ~46 mol.% at 1600°C to a maximum of ~70 mol.% at ~2378°C.

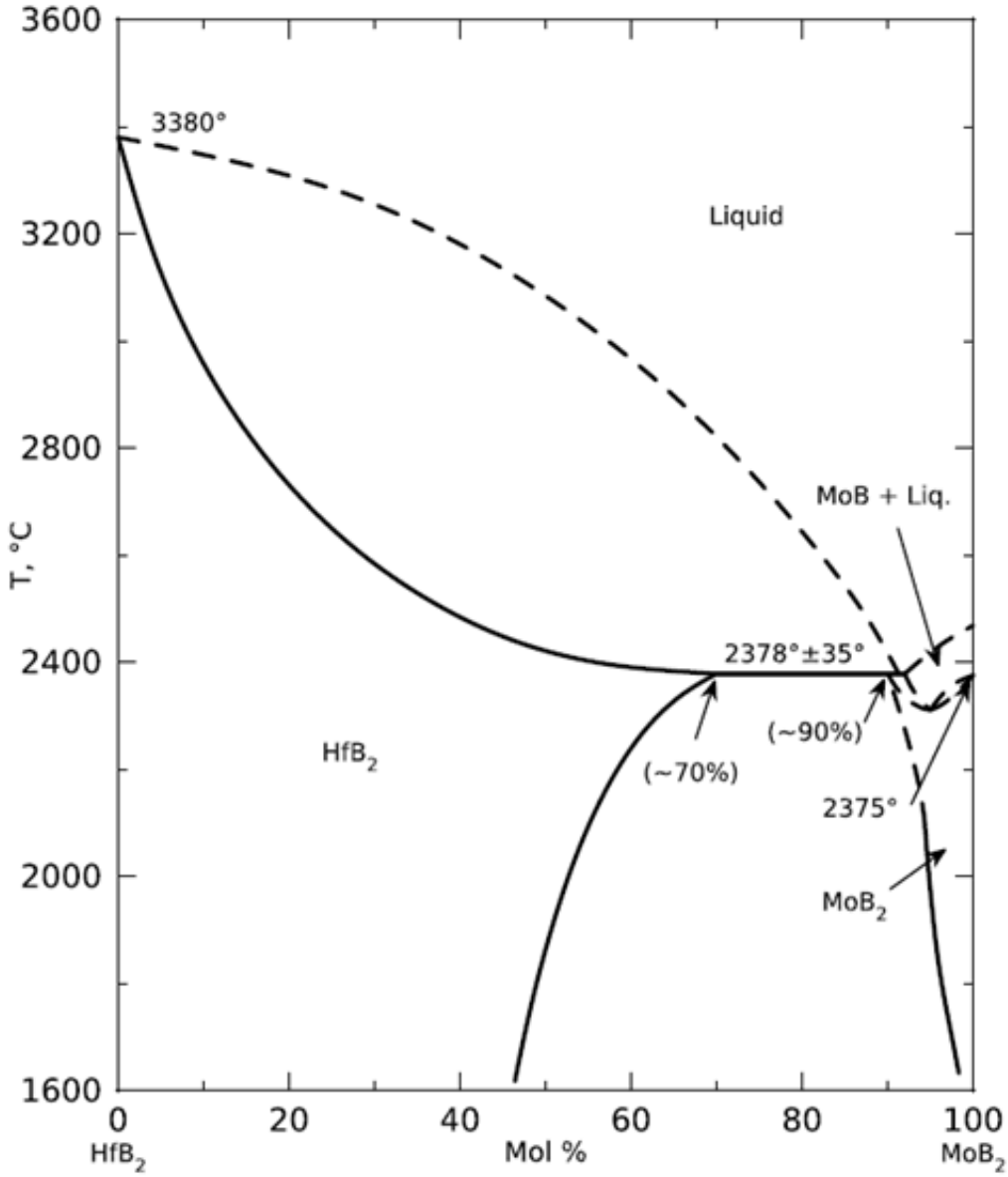

Figure 2.22. Pseudobinary of the HfB2-MoB2 system. Reproduced from [3].

Due to the similarity of ZrB_2 and HfB_2, it is likely that a ZrB_2-MoB_2 pseudobinary diagram would share characteristics with the ZrB_2-HfB_2 diagram. Because there is a greater difference in atomic radius between Mo (1.371 Å) and Zr (1.515 Å) than between Mo and Hf (1.503 Å) [83], it can be assumed that the solubility limit of MoB_2 in ZrB_2 is less than that of MoB_2 in HfB_2. In an attempt to determine the solubility limit of MoB_2 in ZrB_2 at 2150°C, Stanfield synthesized test compositions of commercial ZrB_2 with 35 and 45 mol.% MoB_2 additions, and noted homogeneous solution in both samples after hot pressing via XRD analysis [84]. Lattice parameters of (Zr,Mo)B_2 samples made by Stanfield and by McClane are plotted together in Figure 2.23a along with lattice parameters of ZrB_2 ((PDF 00-034-0423) and MoB_2 (PDF 00-006-0682). Figure 2.23b shows the unit cell volume calculated from the measured lattice parameters of each composition. It is important to note that both McClane and Stanfield used nominally identical procedures with commercial ZrB_2 and Mo powders from the same suppliers, meaning that the influence of Hf impurities in the commercial ZrB_2 is probably similar in both experiments.

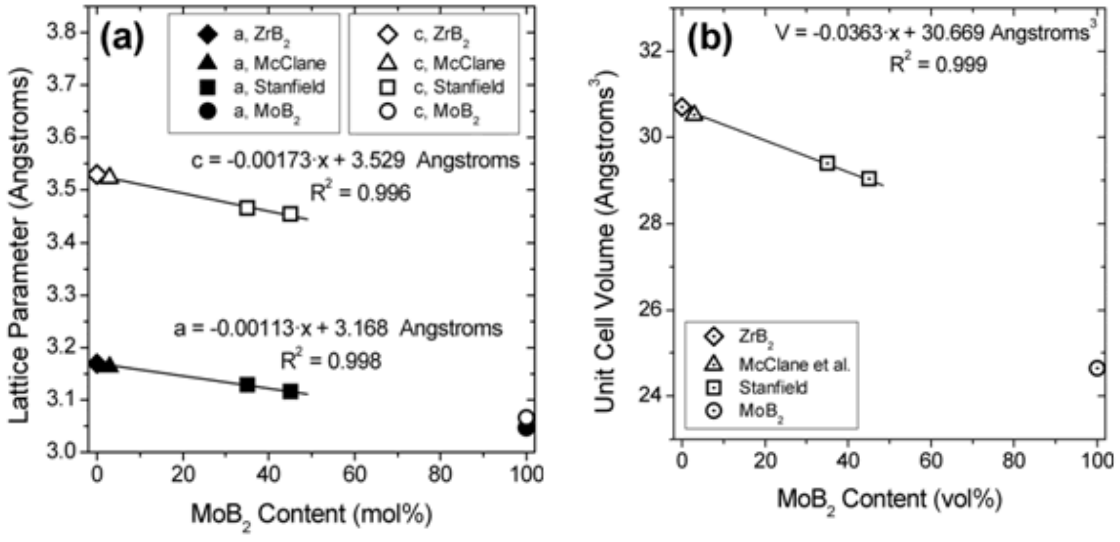

Figure 2.23. (a) Lattice parameters and (b) calculated unit cell volumes of ZrB2 (PDF 00-034-0423), MoB2 (PDF 00-006-0682), and intermediate (Zr,Mo)B2 solid solutions. [37, 84]

The trends of lattice parameter show that the *a* parameter roughly follows a linear interpolation between those of ZrB_2 and MoB_2, as would be expected by Vegard's law. However, the *c* parameter, and thus the unit cell volume, do not follow linear interpolations, supporting the supposition that the solid solubility range between ZrB_2 and MoB_2 is incomplete. Stanfield's experiments show that the solubility limit of MoB_2 in ZrB_2 is likely greater than 45 mol.% at 2150°C, and taken with data from Rogl [80], indicate that the solubility limit is likely between 26 and 45 mol.% MoB_2 in the range of densification temperatures commonly used for ZrB_2-$MoSi_2$ ceramics.

2.3.3. Mechanical Properties at Room Temperature. Several studies have examined the behavior of ZrB_2-$MoSi_2$ composites with respect to $MoSi_2$ content at room temperature [60, 62, 66], and multiple studies have compared the properties of selected compositions at room temperature and at elevated temperatures [10, 65, 67, 85]. However, data from systematic studies comparing mechanical behavior over an extended compositional range at both ambient and elevated temperature are limited. Guo et al. studied the effects of $MoSi_2$ contents from 10 to 40 vol.% on room temperature properties of hot-pressed ZrB_2 ceramics, reporting mean strength values in the range of 750 to 800 MPa for all compositions, and fracture toughness values between 2.6 and 3.7 $MPa \cdot m^{½}$ [66]. Room temperature fracture toughness values of monolithic hot pressed ZrB_2 [14, 62] and $MoSi_2$ [50-52] have been reported to be in the ranges of 3.0 to 4.2 and 2.5 to 4.0 $MPa \cdot m^{½}$, respectively. With the exception of a study by Sciti et al. [60], which reported a slight increase in fracture toughness from 2.0 to 3.3 $MPa \cdot m^{½}$ as $MoSi_2$ content increased from 1 to 9 vol.%, previous studies report toughness values in the range of 2.3 to 4.1 $MPa \cdot m^{½}$ with no overall trend in fracture toughness for $MoSi_2$ contents of 5 to 40 vol.%. [10, 62, 65-67] Guo also reported room temperature elastic moduli ranging from 490 to 448 GPa for 10 to 40 vol.% $MoSi_2$. Chamberlain et al. studied room temperature mechanical properties of hot pressed ZrB_2-$MoSi_2$ for 10 to 30 vol.% $MoSi_2$ additions, reporting flexure strength between 1000 and 1150 MPa for all compositions, and fracture toughness between 3.0 and 4.1 $MPa \cdot m^{½}$ (Chamberlain measured flexure strengths using ASTM standard A-bars, which are nominally 1.5 mm x 2 mm x 25 mm, smaller than those used in the present study) [62]. Sciti et al. measured room temperature microhardness and fracture toughness of ZrB_2-$MoSi_2$ consolidated by spark plasma

sintering for 1 to 9 vol.% $MoSi_2$ additions, reporting an increasing fracture toughness from 2.0 to 3.3 $MPa \cdot m^{½}$ with increasing $MoSi_2$ content, accompanied by an increase in microhardness from 16.5 to 18.2 GPa [60]. Table 2.3 displays the room temperature mechanical properties of ZrB_2-$MoSi_2$ ceramics reported in the available literature, and Figure 2.24 shows flexure strength of ZrB_2-$MoSi_2$ ceramics in the literature as a function of $MoSi_2$ content. Overall, neither flexure strength nor fracture toughness showed a significant trend with $MoSi_2$ content at room temperature in the literature.

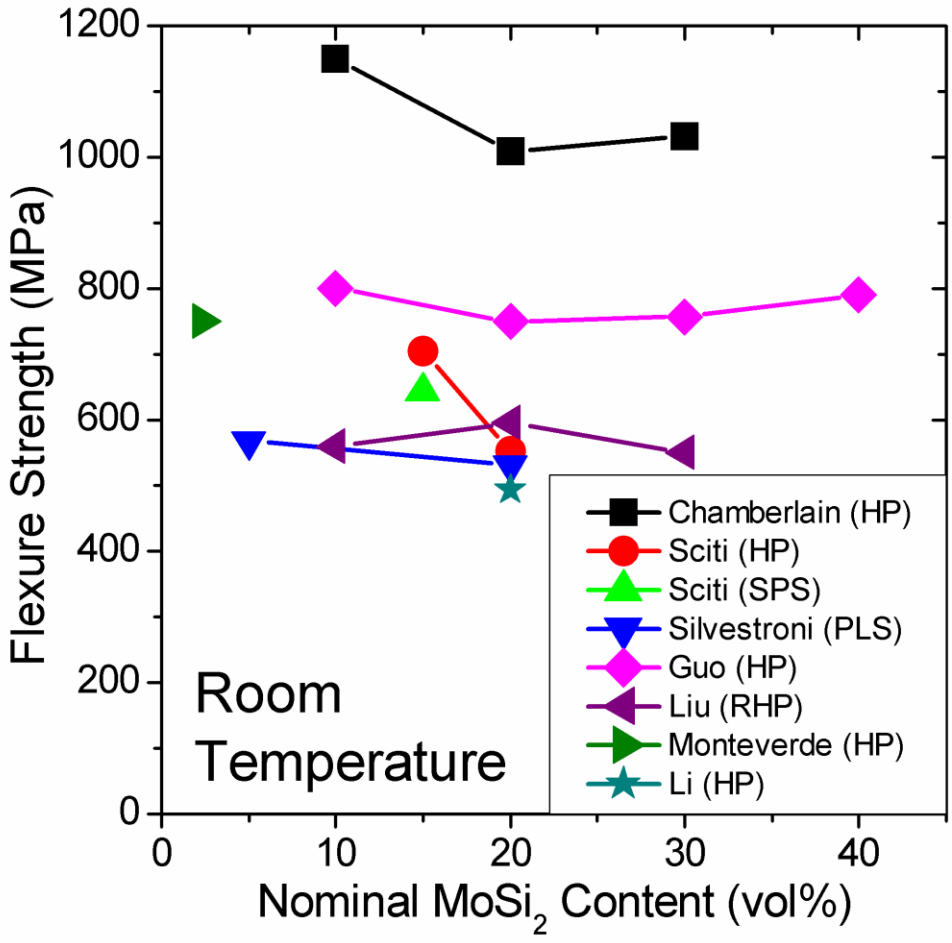

Figure 2.24. Room temperature flexure strength of ZrB_2-$MoSi_2$ ceramics as a function of $MoSi_2$ content. Gathered from the available literature [10, 13, 45, 49, 65, 66, 86].

Table 2.3. Room temperature elastic moduli, Vickers hardness, four-point flexure strength, and fracture toughness of ZrB_2-$MoSi_2$ ceramics reported in literature. Flaw size ranges were calculated for the purpose of this summary using averages and standard deviations of strength and toughness provided.

Ref.	Nominal $MoSi_2$ content (vol%)	Young's modulus (GPa)	Shear modulus (GPa)	Poisson's ratio	Vickers hardness (GPa)	Flexure strength (MPa)	Fracture toughness ($MPa \cdot m^{½}$)	Calculated flaw size (μm)
								Y = 1.99
[34]	10	516[a]	-	-	20.4 ± 2.2	1151 ± 52[e]	4.07 ± 0.4[f]	2.4 – 4.2
	20	523[a]	-	-	18.5 ± 2.7	1008 ± 137[e]	2.96 ± 0.18[f]	1.5 – 3.3
	30	494[a]	-	-	17.7 ± 1.6	1031 ± 150[e]	3.97 ± 0.42[f]	2.3 – 6.3
[49]	5	516 ± 4[b]	-	-	15.2 ± 1.0	569 ± 54	2.9 ± 0.1[g]	5.1 – 8.6
[59]	20	489 ± 4[b]	-	-	16.0 ± 0.4	531 ± 46	4.0 ± 0.6[g]	8.8 - 23
[65]	15 (HP)	531 ± 3[b]	-	-	14.9 ± 0.5	704 ± 98	-	-
[54]	15 (SPS)	479 ± 4[b]	-	-	16.2 ± 0.5	643 ± 97	2.6 ± 0.3[h]	2.4 – 7.1
[54]	20	-	-	-	15.0 ± 0.4	552 ± 336	-	-
[48]	1	-	-	-	16.5 ± 1.0	-	2.0 ± 0.2[h]	-
	3	-	-	-	18.3 ± 0.6	-	2.6 ± 0.1[h]	-
	9	-	-	-	18.2 ± 0.7	-	3.3 ± 0.5[h]	-
[66]	10	490 ± 7[c]	216 ± 3[c]	0.14 ± 0.01[c]	15.8 ± 0.7	800 ± 110[e]	3.7 ± 0.3[h]	3.5 – 8.5
	20	472 ± 6[c]	207 ± 4[c]	0.14 ± 0.01[c]	16.3 ± 0.9	748 ± 135[e]	2.8 ± 0.2[h]	2.2 – 6.0
	30	473 ± 3[c]	206 ± 1[c]	0.15 ± 0.01[c]	15.4 ± 0.7	755 ± 82[e]	2.6 ± 0.2[h]	2.1 – 4.4
	40	448 ± 4[c]	196 ± 2[c]	0.14 ± 0.01[c]	13.2 ± 0.7	790 ± 60[e]	3.1 ± 0.3[h]	2.7 – 5.5
[58]	2.3	500 ± 2[b]	-	0.12[b]	18.1 ± 0.4	750 ± 160	3.35 ± 0.27[g]	2.9 – 9.5
[67]	20	-	-	-	17.8	493[d,e]	4.25 ± 0.6[h]	14 - 24
[56]	10	-	-	-	17.5 ± 0.3	560 ± 115[d]	3.8 ± 0.4[h]	6.4 – 22
	20 (0.5 h)	-	-	-	15.4 ± 0.3	570 ± 50[d]	3.4 ± 0.6[h]	5.2 – 15
	20 (1 h)	-	-	-	15.2 ± 0.2	595 ± 50[d]	3.6 ± 0.25[h]	6.8 – 13
	20 (2 h)	-	-	-	14.8 ± 0.1	675 ± 35[d]	3.22 ± 0.2[h]	4.6 – 7.2
	30	-	-	-	14.3 ± 0.2	550 ± 60[d]	3.2 ± 0.3[h]	5.7 – 13
[68]	20	455.3[c]	-	0.11[c]	16.01	-	3.08 – 4.01[h]	-

[a]Flexure [b]Resonance [c]Pulsed-echo [d]Three-point bending [e]Polished tensile flexure surfaces [f]Indentation strength in bending [g]Chevron notch [h]Direct crack indentation method

For brittle and linear-elastic materials such as glass and ceramics, the Griffith model of fracture is often used to explain mechanical behavior. In this model, it is assumed that flexure strength is determined by a combination of the fracture toughness and stress concentrations caused by randomly distributed flaws or cracks in the material. Each specimen is assumed to fail at the flaw that produces the most severe stress concentration during testing, an assumption that is sometimes called the "weakest link" theory. The Griffith model assumes sharp crack tip small but finite tip radius of penetration depth c into the specimen surface. For a linear-elastic, homogeneous specimen of known mode-1 fracture toughness K_{Ic} and apparent strength σ,

$$c = \left(\frac{K_{Ic}}{Y \cdot \sigma} \right)^2 \tag{3}$$

where Y is a dimensionless parameter describing the severity of stress concentration due to the flaw geometry [43]. Values of Y used to represent surface flaws in ceramics specimens in bending tests include for a state of uniform tension include $2.06/\pi^{½}$ (1.16) for a semi-circular surface flaw, 1.13 for a near-surface circular flaw, and $1.12 \cdot \pi^{½}$ (1.99) for a long semi-elliptical surface crack of depth c [43, 87]. In reality for polycrystalline ceramics the critical flaw is not infinitely sharp, and does not strictly conform to ideal semi-elliptical or semi-circular shapes, and the ceramic is neither completely plasticity-free nor homogeneous at the scale of a single grain. Nevertheless, the above and similar values of Y often allow for a reasonable approximation of the stress concentration caused by real flaws in structural ceramics.

Using the measured fracture toughness and apparent flexure strength for a sample of material, the size of the critical flaws responsible for failure can be estimated using Eq. 3 by assuming an appropriate Y parameter. This estimation of the critical flaw size can be a useful first step in identification of the critical flaw population(s) by fractographic analysis. The majority of studies on ZrB_2-$MoSi_2$ ceramics in the published literature have not reported size estimates of the critical flaws responsible for failure, and to the author's knowledge no study has positively identified critical flaws in ZrB_2-$MoSi_2$ ceramics by microscopic observation. Wang and Li correlated flexure strength with

maximum observed silica inclusion size in micrographs of ZrB_2-$MoSi_2$ ceramics made by Silvestroni and Sciti [10], and proposed that silica inclusions act as the critical flaws at room temperature, 1200°C and 1500°C [88]. However, this conclusion is based on observation of polished microstructures, not direct observation of fracture surfaces, and the microstructural analysis techniques are not reported.

2.3.4. Mechanical Properties at Elevated Temperatures. Table 2.4 and Figure 2.25 display the flexure strengths of ZrB_2-$MoSi_2$ ceramics tested at elevated temperatures in air in the available literature. Silvestroni et al. measured flexure strength of pressurelessly sintered ZrB_2 with 5 and 20 vol.% $MoSi_2$ additions, and reported strength retention at elevated temperatures: room temperature strength of 569 and 531 MPa respectively were compared with strengths of 533 and 655 MPa at 1200°C, and strengths of 488 and 500 MPa at 1500°C in air [10]. The impressive retention of room temperature strength at elevated temperatures in that study was attributed to surface flaw healing by means of a glassy silica oxidation scale [10].

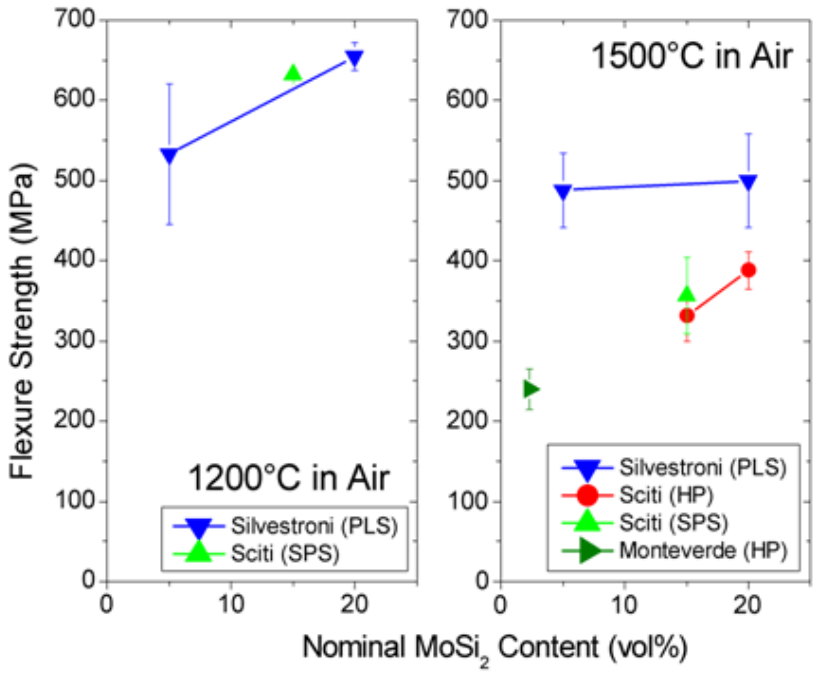

Figure 2.25. Elevated-temperature flexure strength of ZrB_2-$MoSi_2$ ceramics from the available literature.

Sciti et al. compared mechanical properties ZrB_2 with 15 to 20 vol.% $MoSi_2$ additions densified by differing sintering methods, reporting strengths in the range of 530 to 700 MPa at room temperature, 655 to 632 MPa at 1200°C in air, and strengths between 330 and 500 MPa at 1500°C in air. Monteverde compared flexure strengths of 750 MPa at room temperature with strengths of 240 MPa at 1500°C in air for ZrB_2 ceramics with 2.3 vol.% $MoSi_2$ additions, observing poor strength retention [45]. Previous studies have provided an enlightening start of the characterization of ZrB_2-$MoSi_2$ ceramics, but retention of room temperature strength to elevated temperatures has been inconsistent and more studies are required that systematically measure multiple mechanical properties at both room and elevated temperatures for broad ranges of composition.

Table 2.4. Four-point flexure strength of ZrB_2-$MoSi_2$ ceramics at elevated temperatures in air reported in literature.

Ref.	Nominal $MoSi_2$ content (vol.%)	Flexure strength 1200°C (MPa)	Flexure strength 1500°C (MPa)
[10] [67]	5	533 ± 87	488 ± 46
	20	655 ±17	500 ± 58
[85] [65]	15 (HP)	-	331 ± 31
	15 (SPS)	632 ± 5	357 ± 48
[65]	20	-	388 ± 23
[45]	2.3	-	240 ± 25

2.3.5. Oxidation Behavior at Elevated Temperatures. Surface oxidation of ZrB_2-based ceramics is known to affect mechanical properties during elevated temperature testing. The oxidation behavior of ZrB_2-$MoSi_2$ composites exhibits parabolic kinetics, forming a multilayered oxide scale [12, 63, 64, 89, 90]. Oxidation of ZrB_2-$MoSi_2$ composites involves the oxidation of both component phases. ZrB_2 is known to oxidize following Eq. (4) [64].

$$ZrB_2(s) + 2.5\ O_2(g) \rightarrow ZrO_2(s) + B_2O_3(l,g) \quad (4)$$

While liquid B_2O_3 can limit oxygen diffusion into the surface below ~1100°C, above this temperature it has a high vapor pressure and rapidly volatilizes from the surface [64, 89], allowing rapid formation of porous ZrO_2 [62]. $MoSi_2$ has been reported to oxidize according to Eq. (5) at temperatures from 1200 to 1600°C [62, 89, 90].

$$MoSi_2(s) + 3.5\ O_2(g) \rightarrow 2\ SiO_2(s) + MoO_3(l) \quad (5)$$

$MoSi_2$ has also been reported to oxidize indirectly to Mo_5Si_3, SiO_2 and MoO_3 according to Eqs. (6) and (7) [63, 65].

$$5\ MoSi_2(s) + 7\ O_2(g) \rightarrow Mo_5Si_3(s) + 7\ SiO_2(l) \quad (6)$$

$$Mo_5Si_3(s) + 10.5\ O_2(g) \rightarrow 5\ MoO_3(l) + 3\ SiO_2(l) \quad (7)$$

Formation of a continuous SiO_2 layer inhibits diffusion of oxygen through the surface scale, giving $MoSi_2$ oxidation resistance in the range of 700 to 1700°C [50]. MoO_3 has a melting temperature of 801°C, but its high vapor pressure results in its rapid evaporation below 1000°C [64, 89]. Chamberlain et al. reported that volatilization of B_2O_3 and MoO_3 species occurred above 1100°C [62]. For monolithic polycrystalline $MoSi_2$, oxidation in the range of 300 to 600°C results in formation of SiO_2, and volatile MoO_3, producing internal stresses at the grain boundaries resulting in pesting [91]. During oxidation of ZrB_2 composites with Si-containing compounds such as SiC and $MoSi_2$, a combination of these oxidation reactions has been found to produce an amorphous borosilicate surface oxide layer, with a sub-layer of porous zirconia [92]. Sciti et al. [89]. reported the presence of MoB dispersed in the porous zirconia layer after exposure to air at 1200 to 1400°C of ZrB_2 with 5 to 20 vol.% $MoSi_2$ additions, indicating the favorability of the reaction shown by Eq. (8) for ZrB_2-$MoSi_2$ composites.

$$ZrB_2(s) + 2\ MoSi_2(s) + 5\ O_2(g) \rightarrow ZrO_2(s) + 2\ MoB(s) + 4\ SiO_2(l) \quad (8)$$

The study reported that this reaction is favorable at all temperatures [89], suggesting that glassy surface oxide layers on ZrB_2-$MoSi_2$ composites may have a higher silica content

than those on ZrB_2-SiC composites. Higher silica content in the amorphous borosilicate layer is expected to contribute to higher viscosity at elevated temperatures, providing greater resistance to ablation. The favorability of Eq. (8) suggests that $MoSi_2$ may therefore be a more effective addition to ZrB_2 than SiC for purposes of oxidation resistance, due to the tendency of B to form MoB (s) instead of B_2O_3 in the presence of Mo under oxidizing conditions.

Guo et al. studied the oxidation behavior at 1500°C of ZrB_2 composites with 10, 20, and 40 vol.% $MoSi_2$ additions and reported parabolic oxidation kinetics with decreasing rates as the $MoSi_2$ content increased [12]. The oxide scale consisted of an outer silicate glassy layer atop a layer of porous zirconia, followed by an exfoliated layer of the composite substrate depleted of the silicide phase containing MoB, where cracks between exfoliated layers were filled with borosilicate glass. Sciti et al. characterized the oxidation of ZrB_2 with 5 and 20 vol.% $MoSi_2$ additions at temperatures between 700 and 1400°C for 30 h in air, and reported a similar multilayered oxide structure and the formation of a continuous silicate-based glassy outermost layer only above 1200 and 1400°C (Figure 2.26) [93].

2.4. DUAL-SCALE COMPOSITE ARCHITECTURES

Humans have made use of natural composite materials such as wood, bone, and ivory for high-performance tools and construction for thousands of years [94], Multi-phase particulate polycrystalline ceramics in the form of pottery, and fiber-reinforced ceramic matrix composites (CMCs) the form of mud bricks with straw are some of humanity's earliest intentionally engineered composite materials. Clarke proposed a systematic nomenclature for materials in this ancient tradition, which can be used to characterize two-phase composites based on the dimensional connectivity of their constituent phases (Figure 2.27) [95].

Several historically common types of two-phase composite can be described with Clarke's nomenclature, such as "0-dimensional" particles dispersed in a continuous matrix (0-3), a matrix reinforced by continuous, aligned fibers (1-3), and alternating laminate materials (2-2). Clarke's nomenclature can also be extended to refer to two 3-dimensionally continuous but interdispersed phases, such as a spinodally decomposed

solid (3-3). Logical extension of this nomenclature can also lead one to consider novel composite concepts that may not have existing (or easily fabricated) examples.

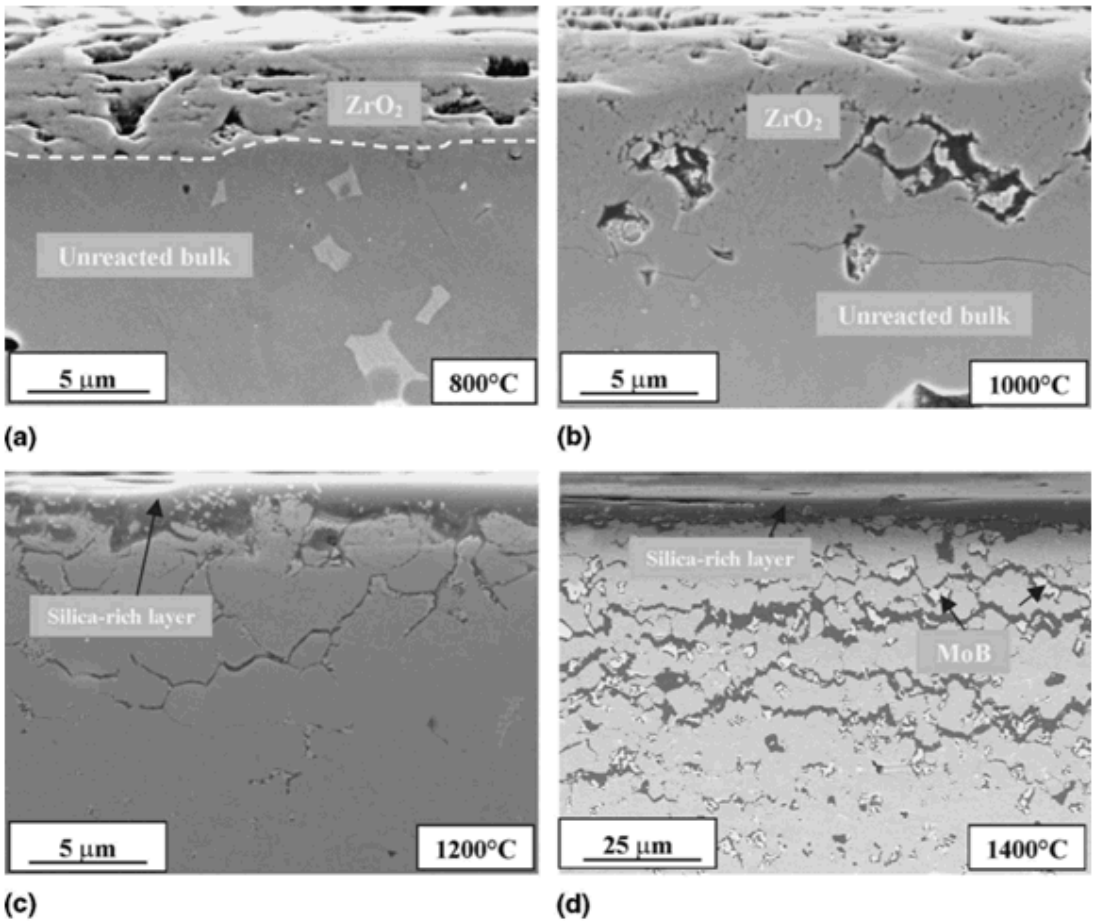

Figure 2.26. Secondary electron micrographs of polished cross sections of ZrB2-20 vol.% MoSi2 oxidized in synthetic air for 30 h at various temperatures. Note exfoliation behavior in (d). Reproduced from [89].

Clarke's nomenclature could also be extended to three-phase composites via the addition of a third number, e.g. 0-0-3 to represent two particulate phases dispersed in the same continuous matrix. Harmer et al. proposed increasing the complexity of composite materials design by engineering not only the architecture of the overall composite material, but also the individual design components by fabricating them out of engineered

composite materials on a smaller scale (Figure 2.28) [1]. This is the fundamental concept behind a dual-scale composite architecture (DCA). Mud bricks with straw could be considered a primitive form of dual composite architecture if the properties of the continuous mud matrix were intentionally adjusted by addition of another material, such as dung.

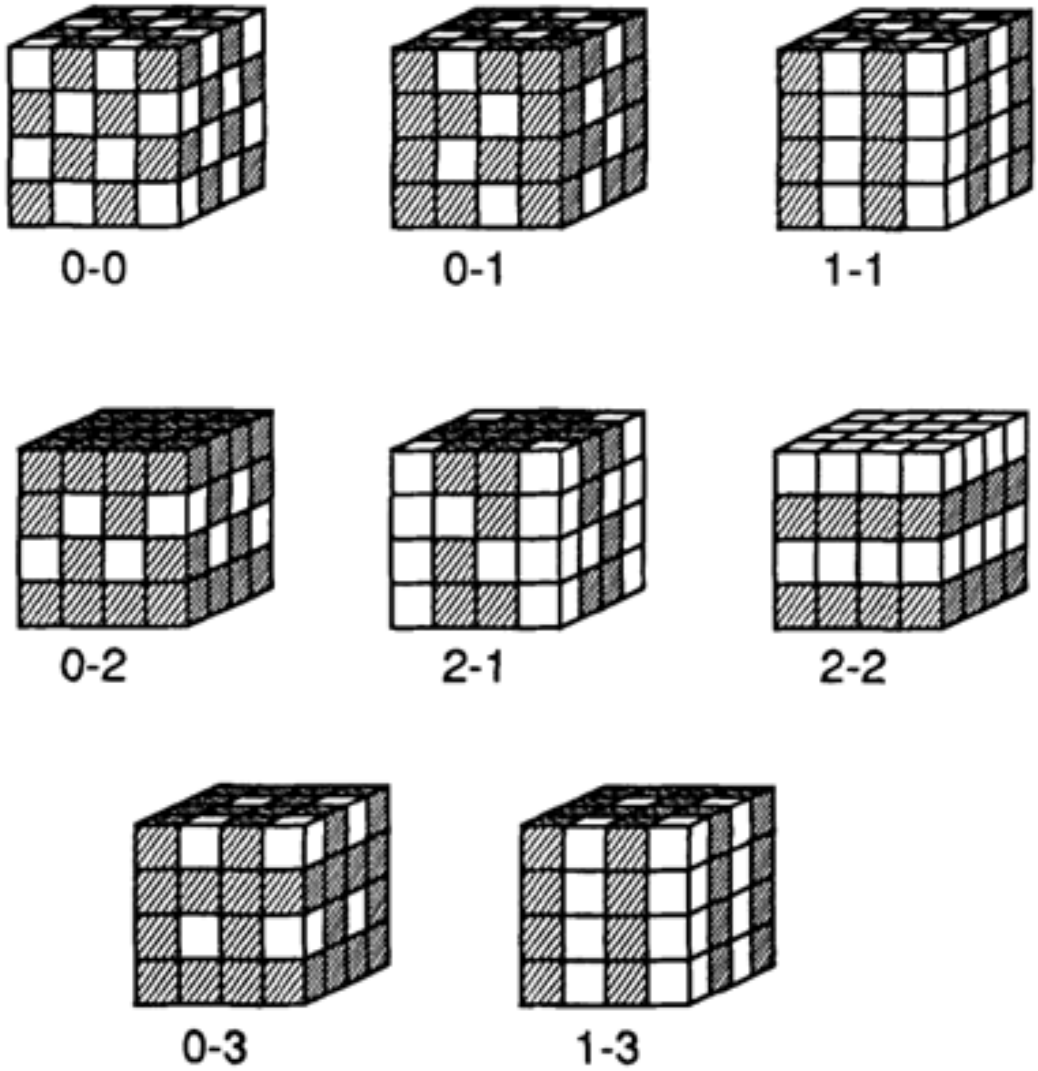

Figure 2.27. Dimensional nomenclature for two-phase composite materials proposed by Clarke. Reproduced from [95].

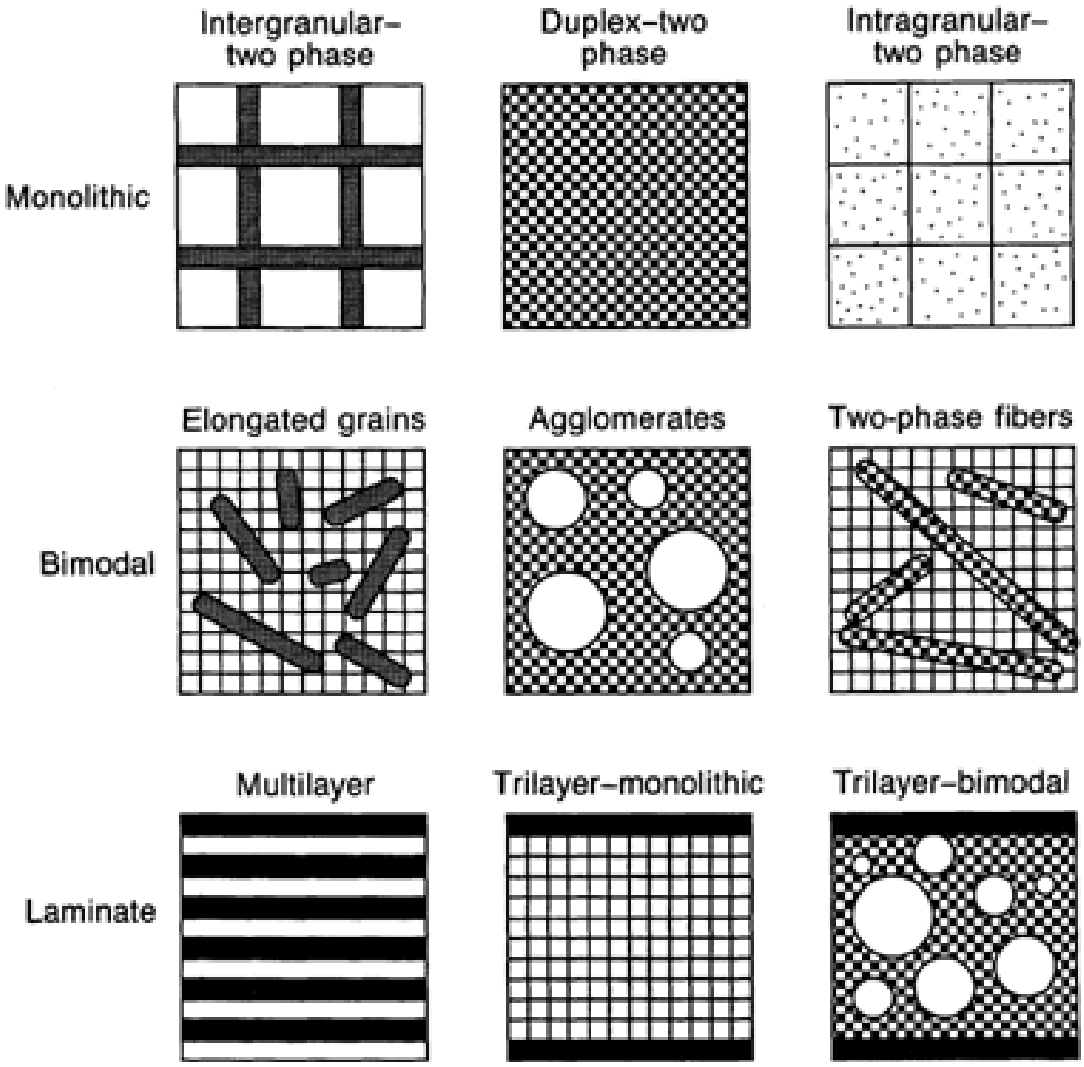

Figure 2.28. Opportunities for multi-phase microstructural engineering of dual-scale composites proposed by Harmer et al. Reproduced from [1].

The possibilities for dual composite architectures are vast, and only partially explored. The advent of metallurgical microstructural engineering has resulted in selection of intentionally designed microstructures for both utilitarian and decorative use in the form of pattern-welded steels [54]. Harmer et al. produced a basic ceramic DCA with spherical mullite granules dispersed in a matrix of 44 vol.% alumina, 56 vol.% mullite (Figure 2.29). Assuming that in the matrix both mullite and alumina are continuously connected, such a DCA could be referred to by an extension of Clarke's nomenclature in which the dispersed phase has 0-dimensional connectivity overall but is

composed of a single phase that is 3-dimensionally continuous, and the matrix that is 3-dimensionally continuous is composed of two 3-dimensionally continuous phases, thus: 0(3)-3(3-3).

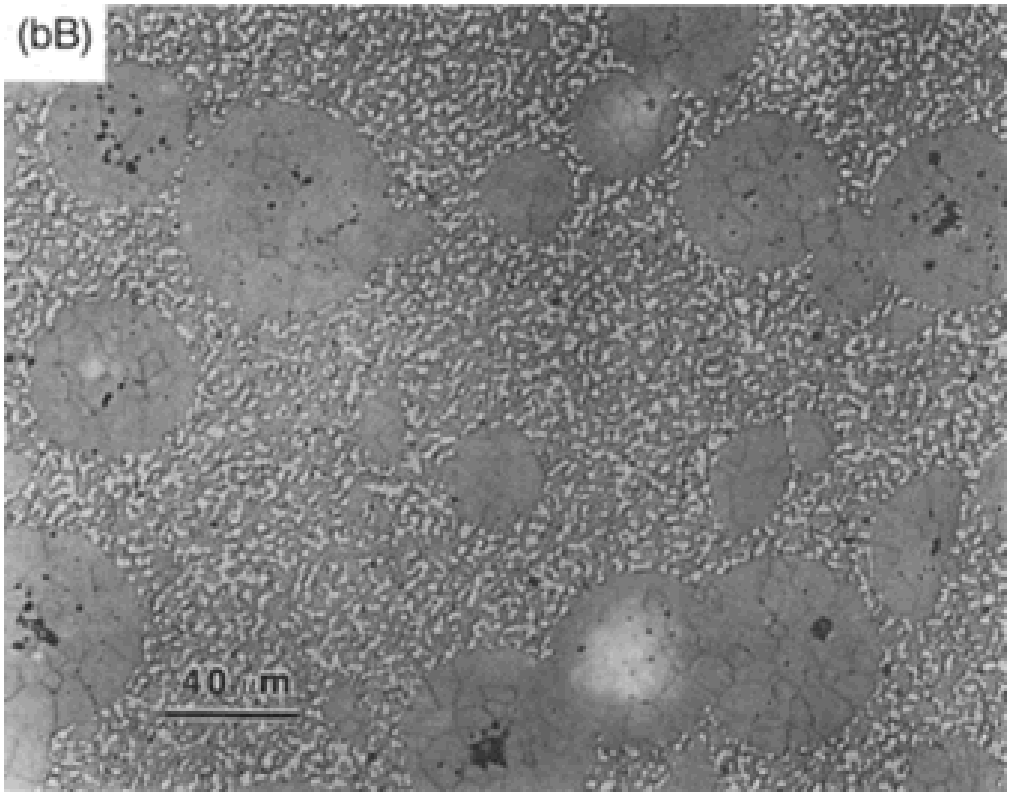

Figure 2.29. Optical micrograph of polished and etched ceramic composite comprised of 30 vol.% granules of mullite (dark gray) dispersed in an alumina-mullite matrix. Reproduced from [1].

Another, less globally isotropic type of DCA that has been investigated is the "fibrous monolith," in which sheathed longitudinal filaments (made of a multi-phase particulate ceramic composite such as ZrB_2-30 vol.% SiC) are stacked in parallel and sintered such that the sheath material (made of a multi-phase composite such as graphite with 15 vol.% dispersed ZrB_2) becomes a continuous matrix between the filaments [2]. Such a material could be termed a 1(0-3)-3(0-3) composite (Figure 2.30).

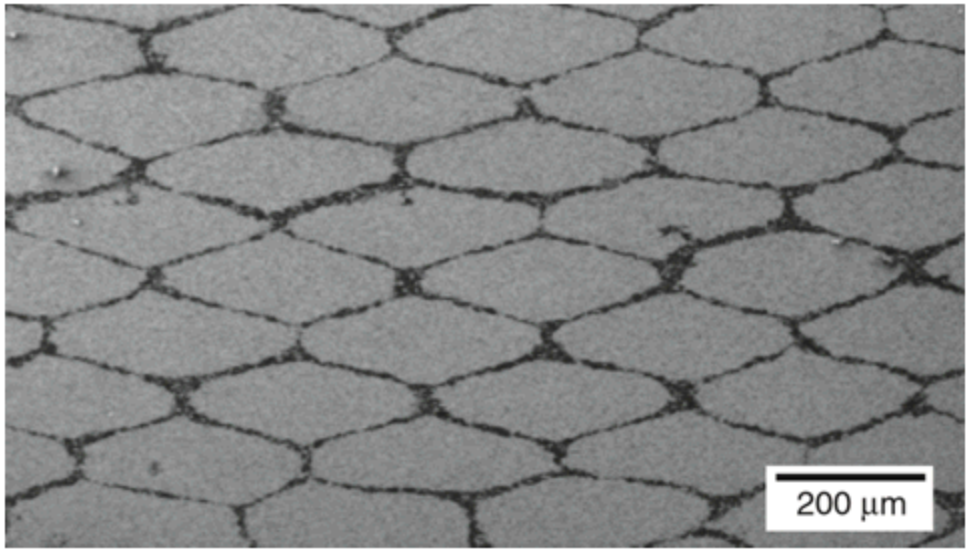

Figure 2.30. Scanning electron microscopy micrograph showing hot pressed fibrous monolith architecture consisting of ZrB_2-30 vol.% SiC cells (light) and graphite-15% ZrB_2 cell boundaries (dark), sectioned orthogonal to the filament long axis. Reproduced from [2].

The benefits of such dual-scale composite design in terms of mechanical properties have not been completely explored but could in principle be adjusted to fit the requirements of a multitude of applications. This is one of the most interesting aspects of the DCA concept. In the case of the fibrous monolith above, the primary advantages were non-catastrophic mechanical failure and an increase in thermal shock resistance to ~250% of that of the monolithic ZrB_2-30 vol.%SiC cell material via entrapment of cracks in the graphite-rich boundary material. The associated disadvantages are increased processing complexity and a ~50% decrease in room temperature flexure strength from the monolithic ZrB_2-30 vol.% SiC cell material. One of the most beneficial industrial applications of the DCA concept has been in the field of Co-cemented WC materials for wear-resistant teeth of rock drilling bits for the oil industry. Basic single-scale WC-Co composites consist of hard WC grains dispersed in a continuous matrix of more ductile Co metal (generally between 10 and 40 vol.%), which imparts fracture toughness to the otherwise brittle WC. The system exhibits a trade-off in desirable properties: when the Co content is increased to increase the fracture toughness there is a simultaneous decrease in wear-resistance. This trade-off was successfully sidestepped by substituting

conventional WC-Co cermets with 0(0-3)-3(3)-type WC-Co DCAs in which wear-resistant WC-Co granules with a low Co content were dispersed in a matrix of Co (or Co with small amounts of dispersed WC) [5-7, 96, 97]. Figure 2.31(a) shows the granule microstructure and Figure 2.31(b) shows the overall DCA mesostructure, while Figure 2.32 illustrates the trade-off relationship of conventional WC-Co materials and the combinations of wear resistance and fracture toughness attained by the DCA materials.

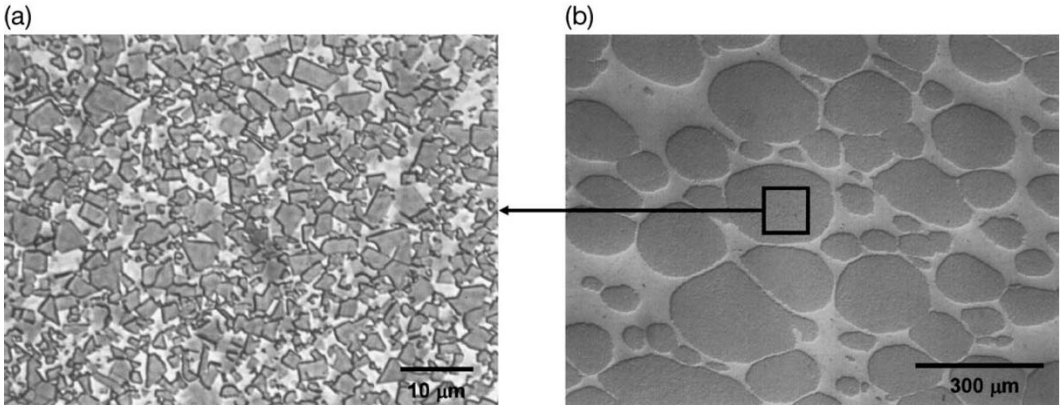

Figure 2.31. Microstructures of (a) conventional WC-Co comprising DC granules, (b) DC WC-Co granules in a Co matrix. Reproduced from [71].

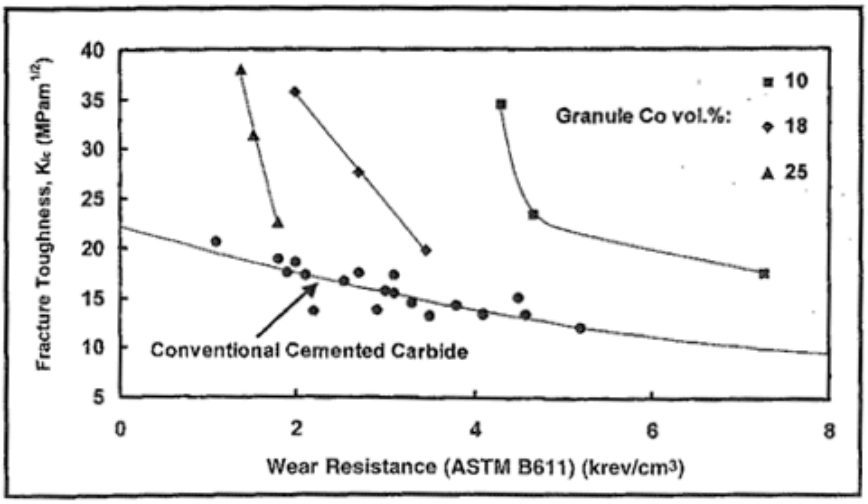

Figure 2.32. Fracture toughness as a function of wear resistance for conventional WC-Co materials and three WC-Co/Co dual composites as published by Deng et al. Reproduced from [96].

The simultaneous increase of fracture toughness and wear resistance compared to conventional WC-Co materials was due to the ability of the ductile Co matrix to both arrest and bridge cracks that initiated in near-surface granules, thus preventing catastrophic brittle failure of the part while allowing the granules to contain more WC for increased wear resistance. Crack arrest and bridging was demonstrated in the behavior of a fatigue crack in a WC-Co/Co DCA in four-point flexure, shown in Figure 2.33 [97]. Deng experimented with differing granule sizes in the same volume fraction of matrix [96], while Deng et al. experimented with variations in the volume fraction of the Co matrix [5].

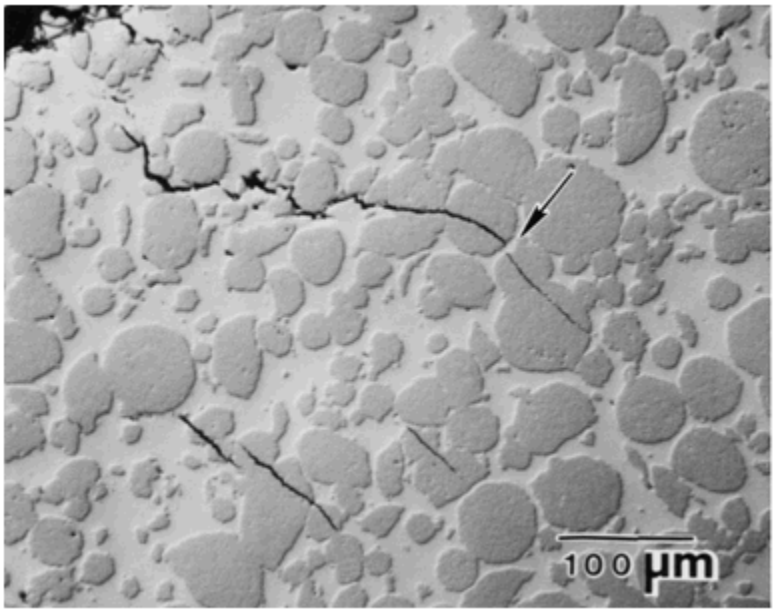

Figure 2.33. Optical micrograph of a surface-initiated fatigue crack within WC-Co/Co dual composite material after 1,000,000 cycles. The sample was fatigued under 3.5/35 kN bending force. Reproduced from [97].

The granule-matrix, or 0(X)-3(X) type of DCA has two advantages over several other arrangements proposed by Harmer et al. in that it can be easier to fabricate in a greater variety of compositions than, for example, a fibrous monolith, and it is more nearly isotropic on a global scale, making it applicable to situations in which a structural

loading direction is not fixed or predictable. Peng et al. fabricated another example of a granule-matrix architecture by first making clusters of short alumina fibers via a tumbling method and then melt-infiltrating packs of fiber clusters with 6061 aluminum alloy [98]. This DCA exhibited crack deflection during notched-bar bending tests (Figure 2.34). An all-ceramic version of a granule-matrix DCA was fabricated by Bogomol et al. by dispersing ~100 μm granules of TiB_2-B_4C solidified "fibrous" eutectic in a continuous matrix of B_4C, creating what could be referred to as a 0(1-3)-3(3) DCA [3]. This DCA was reported to demonstrate higher flexure strength and indentation fracture toughness than its conventional B_4C-TiB_2 counterparts.

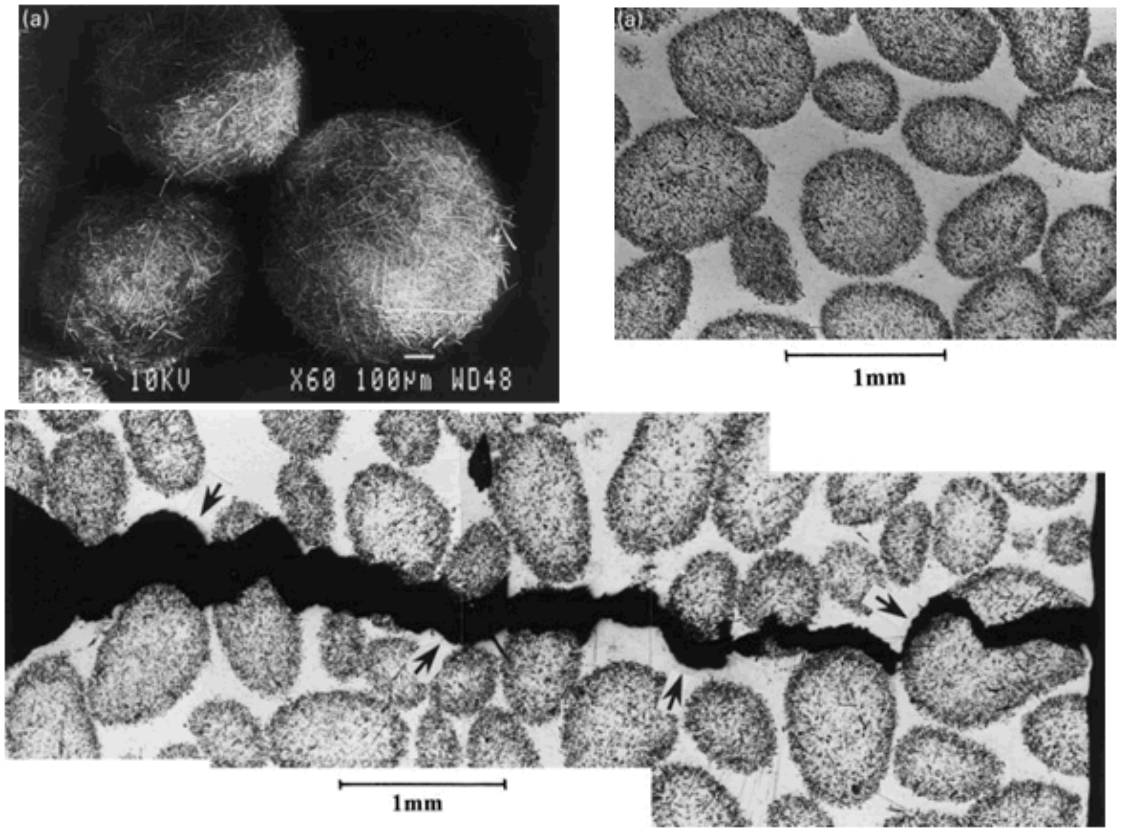

Figure 2.34. Optical and electron micrographs of an MMC with clusters of short Al_2O_3 fibers melt-infiltrated with and dispersed in 6061 Al alloy. Specimens displayed crack deflection in a notched-bar flexure test. Reproduced from [98].

Brittle ceramic materials fail catastrophically upon the initiation of unstable crack growth through the material. Thus, primary objectives in avoiding catastrophic failure of ceramic materials include crack arrest and crack deflection, in order to interrupt unstable crack growth and promote crack tip stability by either increasing the energy required to further open the crack or by changing the orientation of the crack to the direction of applied stress. Chantikul et al. showed that fracture toughness of polycrystalline alumina increased with the magnitude of crack deflection, which they demonstrated using aluminas with varying grain sizes that demonstrated intergranular fracture [42]. DCAs provide an opportunity for crack deflection on a secondary scale in ceramics, assuming cracks can be deflected at granule-matrix interfaces. He and Hutchinson developed a model to predict crack deflection at interfaces between two linear-elastic materials based on a fracture energy approach [99]. He and Hutchinson's model states that if the quotient of the fracture energy of the interface (G_{IC}) divided by the fracture energy of the material into which the crack would propagate (G_C) is below the He-Hutchinson deflection criterion curve, then crack deflection is expected. This criterion is expressed below:

$$\frac{G_{IC}}{G_C} < \frac{G_d}{G_p} \tag{9}$$

where G_d is the energy release rate of the crack if it is deflected and G_p is the energy release rate of the crack if it propagates. G_d/G_p forms the He-Hutchinson deflection criterion curve, which is expressed in more detail in Eq. (10) below:

$$\frac{G_d}{G_p} = \frac{\left[\frac{1-\beta^2}{1-\alpha^2}\right]\left[|d|^2 + |e|^2 + 2R_e(de)\right]}{c^2} \tag{10}$$

Figure 2.35 illustrates the He-Hutchinson crack deflection curves for a singly-deflected crack (top) and a doubly-deflected crack (bottom) plotted as a function of Dunder's α parameter:

$$\alpha = \frac{\frac{E_1}{1-\nu_1^2} - \frac{E_2}{1-\nu_2^2}}{\frac{E_1}{1-\nu_1^2} + \frac{E_2}{1-\nu_2^2}} \tag{11}$$

in which E_1 and E_2 are the Young's moduli and ν_1 and ν_2 are the Poisson's ratios of material 1 and material 2, respectively, as shown in the inset diagrams in Figure 2.35.

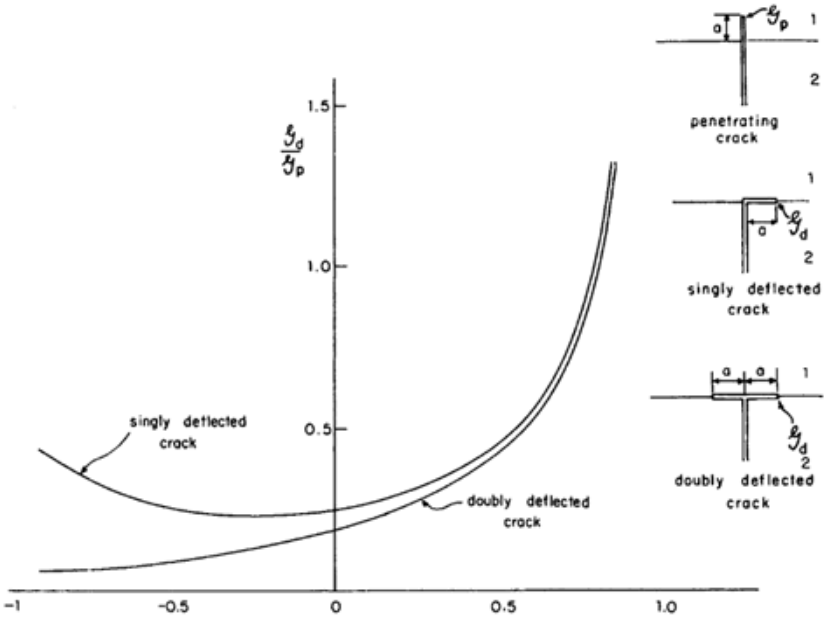

Figure 2.35. He and Hutchinson's crack deflection criterion curves plotted as a function of Dunder's α parameter (horizontal axis) for Dunder's β = 0.Reproduced from [99].

The fracture energies (G_{IC}) can be calculated using Griffith's relationship [2]:

$$G_{IC} = \frac{K_{IC}^2}{E} \tag{12}$$

where K_{IC} is the mode I fracture toughness. Zimmerman et al. successfully used He and Hutchinson's relationship to intentionally design for crack deflection in their ZrB_2-

graphite-based fibrous monolith DCA [2]. He and Hutchinson state that as a general rule of thumb for α values near zero, the fracture toughness of the interface "must be less than about one quarter of the toughness of the material across the interface if all cracks are to be deflected."

PAPER

I. ZrB_2-$MoSi_2$ CERAMICS WITH VARYING $MoSi_2$ CONTENT: PART 1. PROCESSING AND MICROSTRUCTURE WITH VARYING ZrB_2 POWDER PARTICLE SIZE

Ryan J. Grohsmeyer,[a, 1] Gregory E. Hilmas,[a, 2] Frederic Monteverde,[b]
William G. Fahrenholtz,[a] Andrea D'Angió,[b, 3] Diletta Sciti,[b] Laura Silvestroni[b]

[a] Materials Science and Engineering Department, Missouri University of Science and Technology, Rolla, MO 65409, USA

[b] National Research Council of Italy, Institute of Science and Technology for Ceramics, Faenza, 48018 RA, Italy

ABSTRACT

The densification behavior and final microstructures of hot-pressed ZrB_2-$MoSi_2$ ceramics with varying ZrB_2 starting powder particle size and $MoSi_2$ content were investigated. Fifteen different ZrB_2-$MoSi_2$ ceramics with median ZrB_2 starting powder particle sizes ranging from 2.9 to 11.7 μm and nominal $MoSi_2$ contents ranging from 5 to 70 vol.% were hot pressed at temperatures between 1750 and 1925°C. Plastic deformation of $MoSi_2$ contributed to initial densification. Decomposition of $MoSi_2$ during later stages of hot pressing was quantified by microstructural analysis and varied from ~1 to 10 vol.% $MoSi_2$. Comprehensive microstructural analysis showed that ZrB_2 grain size decreased and $MoSi_2$ cluster size increased as $MoSi_2$ content increased. Starting powders with lower impurity contents, and isothermal vacuum holds, contributed to lower oxide impurity contents in the final ceramics. A diboride core-shell structure involving $(Zr_{1-x}Mo_x)B_2$ solid solution was observed in all compositions. This study identified specific relationships between starting composition, processing conditions and final microstructure, showing how microstructure and properties could be tailored by processing to attain specific mechanical and oxidation characteristics.

---

[1] Present address: Corning Incorporated, Painted Post, NY, USA.

[2] Corresponding Author: ghilmas@mst.edu, +1-573-341-6102.

[2] Present address: University of Birmingham, Birmingham, UK.

Key Words: Hot pressing (A), Microstructure–final (B), Borides (D), Silicides (D)

1. INTRODUCTION

Zirconium diboride-based structural ceramics possess a combination of properties that makes them attractive for use in extreme environments, including melting temperatures of up to ~3250˚C, hardness in the range of 14 to 23 GPa [14, 23], maintenance of strength and rigidity in the range of 1200 to 2300°C [10, 24, 100], and chemical stability in acidic environments [101, 102]. The low electrical resistivity of ZrB_2 (6 to 23 μΩ·cm)[103, 104] contributes to its high thermal conductivity (up to ~130 W/m·K) [104], which imparts thermal shock resistance [2, 17]. Low density (6.14 g/cm^3) [18] compared to other ultra-high temperature ceramics (UHTCs) [23] makes ZrB_2 ceramics candidates for aerospace applications such as engine components and leading edges for hypersonic reentry vehicles [23, 105]. Other prospective uses include concentrated solar thermal absorbers [29-31], nuclear fuel cladding, and neutron absorbers [106]. However, the tendency of ZrB_2 to exhibit brittle mechanical fracture, and its vulnerability to rapid oxidation at high temperatures [32, 33], have hindered efforts to put the material into specific applications. Combining ZrB_2 with other phases has been shown to ameliorate these characteristics.

Molybdenum disilicide ($MoSi_2$) has been widely studied as an additive to ZrB_2, due to its ability to perform three important functions: (1) facilitate densification of ZrB_2 by pressureless sintering at 1850°C [10] and by hot pressing at temperatures as low as 1750°C [10, 60, 61]; (2) improve oxidation resistance of ZrB_2 up to ~1650˚C by forming a glassy borosilicate surface layer and solid MoB in the subsurface [11, 49, 63, 64]; and (3) add ductility at elevated temperatures due to its brittle-to-ductile transition (BDTT) upon heating between 900 and 1300˚C [57]. Multiple studies have investigated the densification behavior of ZrB_2-$MoSi_2$ ceramics at temperatures between 1750˚C and 2250˚C [23] during pressureless sintering (PLS) [10, 22, 71, 107], hot pressing (HP) [45, 62, 65, 66], reaction hot pressing (RHP) [13], and spark-plasma sintering (SPS) [60, 85]. However, no systematic studies have correlated processing methods with quantitative microstructural information over an extended compositional range.

The previous studies described above have used different starting particle sizes and different densification temperatures, but other differences among the processing methods (e.g., milling media composition and subsequent contamination, additional sintering additives, applied pressures during densification) prevent direct evaluation of the effects of processing parameters on final microstructures and properties. Silvestroni and Sciti reported pressureless sintering of ZrB_2-$MoSi_2$ ceramics with detailed microstructural analysis [10], and Silvestroni et al. provide a detailed explanation of the complex densification process, but only for a single material [22]. Guo studied densification of hot-pressed ZrB_2 ceramics with 10 to 40 vol.% $MoSi_2$ additions and reported some of the most detailed microstructural information available for such a broad compositional range, including average and maximum grain sizes of each phase, but used only one starting particle size [108, 109]. Sciti et al. compared the microstructures of ZrB_2 with 15 to 20 vol.% $MoSi_2$ densified by pressureless sintering, hot pressing, and spark plasma sintering, again with only one starting particle size. Finally, Guo reported limited decomposition of $MoSi_2$ during isothermal heat treatment at 2000°C [110], and several previous studies have reported formation of a core-shell morphology of the ZrB_2 grains in ZrB_2-$MoSi_2$ ceramics during densification [10, 45, 60, 67, 69], but these studies did not identify the roles of ZrB_2 particle size and $MoSi_2$ content on densification and microstructure development.

The purpose of the present study is to investigate the densification behavior and resulting final microstructure of hot-pressed ZrB_2-$MoSi_2$ ceramics with varying ZrB_2 starting particle size and $MoSi_2$ content. An accompanying paper discusses the mechanical properties of the compositional series processed with medium particle size ZrB_2 powder at both room temperature and at 1500°C in air, taking microstructural features into consideration.

2. EXPERIMENTAL PROCEDURE

2.1. Processing. Three commercially available ZrB_2 powders with differing median (d_{50}) particle sizes were used in this study, all supplied by H. C. Starck GmbH (Newton, MA, USA). Powder grade designations, particle size distributions, measured and reported impurities, and measured specific surface areas for the commercial powders are reported in Table I. Two grades of commercial $MoSi_2$ powder were used.

Compositions processed with the finest particle size of ZrB_2 powder were processed at CNR-ISTEC and were batched with $MoSi_2$ supplied by Sigma-Aldrich (St. Louis, MO, USA), which had a measured O content of 2.4 wt.% after preliminary ball milling. Compositions processed with the medium and coarse grades of ZrB_2 powder were processed at Missouri S&T and were batched with grade B $MoSi_2$ supplied by H.C. Starck, which had a measured O content of 1.1 wt.% and a specific surface area of 0.48 m^2/g after preliminary ball milling, and a reported Mo:Si molar ratio of 1:1.9995.

The $MoSi_2$ powders were pre-comminuted by ball milling in ethanol with ZrB_2-30 vol.% SiC media for 90 to 96 h to reduce particle size. The $MoSi_2$ slurry was dried by rotary evaporation (Rotovapor R-124, Buchi, Flawil, Switzerland) at a temperature of 80˚C under low vacuum (35 kPa residual air pressure) at 75 rpm. The pre-milled $MoSi_2$ powder was batched with the ZrB_2 powder in 5, 10, 20, 30, 40, 50, and 70 vol.% quantities. Compositions are designated FX, MX, and CX where F indicates fine, M indicates medium, and C indicates coarse ZrB_2 powders, and X is the nominal $MoSi_2$ content in vol.%. ZrB_2 and $MoSi_2$ powders were mixed by ball milling using ZrB_2-30 vol.% SiC media for 24 h (only F50 was ball milled with ZrO_2 media) in anhydrous denatured ethanol (compositions made with the fine ZrB_2 powder were mixed in absolute ethanol), and dried using rotary evaporation. The dried powders were passed through a 60 mesh screen in preparation for hot-pressing.

The sieved powders were loaded into a graphite die lined with BN-coated graphite foil. The majority of the die was made from low-expansion graphite (ET-10, nominal linear coefficient of thermal expansion (CTE) of 3.8×10^{-8}/K, Ibiden Co. Ltd., Gifu, Japan), but spacers of higher expansion graphite (ACF-10Q, nominal CTE 7.6×10^{-8}/K, Entegris, Inc., Billerica, MA, USA) were used in contact with the powder compact during hot pressing to more closely match the CTE values of the densified ceramic. MX and CX powders were uniaxially pressed at room temperature at ~2.5 MPa in the graphite die prior to hot pressing, while FX powders were uniaxially pressed at ~2.5 MPa using a steel die to produce a pellet that was then loaded into the graphite hot pressing die.

The maximum hot pressing temperature required for full densification decreased as ZrB_2 particle size decreased and $MoSi_2$ content increased. Hot pressing temperatures were adjusted to prevent unnecessary decomposition of $MoSi_2$ and ZrB_2 grain growth,

while still achieving full density as summarized in Table II. Compositions designated FX were densified in an inductively heated furnace under vacuum (initially ~100 Pa of residual air). Powders were heated at ~25°C/min directly to a maximum densification temperature of either 1750 or 1850°C, and a uniaxial pressure of 30 MPa was applied at 1 to 1.5 MPa/s loading rate between 900 and 1000°C. Maximum hold temperature and pressure were maintained until ram travel slowed to a stop, after which the furnace power was shut off and the furnace was allowed to cool naturally (~35°C/min to 1700°C). The load was released when the temperature fell below ~1600°C. The MX and CX compositions were hot-pressed in a resistively heated graphite-element furnace (HP50-7010G, Thermal Technologies Inc., Santa Rosa, CA, USA). Powders were heated under vacuum (initially ~20 Pa residual argon) at ~30˚C/min with 1 h isothermal vacuum holds at 1450˚C and 1650˚C to remove oxide species [111, 112]. Following the isothermal hold at 1650°C, the furnace was back-filled with flowing Ar and a uniaxial pressure of 30 MPa was applied at a rate of 0.3 to 0.5 MPa/s. The furnace was heated at ~30°C/min to a maximum densification temperature between 1775 and 1925°C then held until no measurable ram travel (displacement resolution of 0.1 mm) was observed for 10 min. The furnace was allowed to cool naturally (initial cooling rate ~35°C/min down to 1700°C), and uniaxial pressure was removed when the temperature fell below 1600°C.

2.2. Characterization. Powder particle size distributions were measured by laser diffraction (Microtrac S3500, Microtrac, Inc. Montgomeryville, PA, USA), specific surface areas were measured using the Brunauer-Emmett-Teller method (BET, Nova 2000e, Quantachrome Instruments, Boynton Beach, FL, USA), and O and N contents were measured using the gas combustion method (TC500, Leco, St. Joseph, MI). Bulk density was measured using Archimedes' method with distilled water as the immersing medium, as described in ASTM C373. Theoretical density was calculated using a simple rule of mixtures (ROM) based on the nominal composition, and densities of 6.14 for ZrB_2 [24] and 6.26 g/cm^3 for $MoSi_2$ [94].

Microstructures were examined using scanning electron microscopy (SEM; Sigma, Zeiss NTS Gmbh, Germany; Helios Nano Lab 600, FEI, Eindhoven, The Netherlands; or S-4700, Hitachi, Tokyo, Japan), with simultaneous energy dispersive spectroscopy (EDS; INCA Energy 300, Oxford Instruments, Abington, UK; AZtec,

Oxford Instruments, Abington, UK). Accelerating voltages in the range of 1 to 4 keV, working distances in the range of 2.5 to 5 mm, and a through-the-lens secondary electron detector were found to provide the clearest contrast between the widest variety of microstructural features. Specimens were prepared for microscopy by diamond grinding and polishing with 3.0, 1.0 and 0.25 μm successively finer diamond slurries followed by plasma cleaning in Ar-25% O_2 shortly before insertion into the microscope chamber (model 1020 Plasma Cleaner, Fischione Instruments Inc., Export, PA, USA).

Phase content was determined by areal analysis using image analysis software (ImageJ, National Institutes of Health, Bethesda, MD, USA). Final relative densities for the purposes of calculating relative density (RD) as a function of time were calculated using the results of digital image analysis (i.e., RD = 1 – fraction of porosity). Grain sizes were determined by fitting equivalent-area ellipses. Reported grain sizes are the numerical average of the mean of the long and short axes of the fitted ellipses measured for at least 600 grains per composition.

Phase analysis and lattice parameter measurements were performed using X-ray diffraction (XRD) on polished sections (D8 Advance, Bruker Co., Billerica, MA, USA) and on powdered samples pulverized in a high-purity alumina mortar and pestle to 200 mesh (PANalytical X'pert, Phillips, Eindhoven, The Netherlands).

3. RESULTS AND DISCUSSION

Relative densities of the MX and CX powder compacts ranged from 42 to 49% at the end of the isothermal vacuum hold at 1650°C, just before application of uniaxial pressure (Fig.1). The relative densities increased sharply upon application of uniaxial pressure. The increases were higher for compositions with higher $MoSi_2$ contents and ran from ~6% of RD for M5 to ~29% of RD for C70 (Fig. 2). The increase in deformation with $MoSi_2$ content indicates that plastic deformation of $MoSi_2$ powder particles is partially responsible for initial densification of hot pressed ZrB_2-$MoSi_2$ ceramics when pressure is applied above the BDTT of $MoSi_2$.

After uniaxial pressure was applied, densification continued during ramping temperature (Fig. 1). In every case, the maximum dwell temperature was reached before final density was attained meaning that densification continued during the final

isothermal dwell. Porosity was found by image analysis on polished surfaces to constitute <0.8 vol.% of each FX composition Table III), indicating that the relative density was ≥99.2%, and that low-density phases such as SiO_2 and SiC (densities of ~2.3 and ~3.21 g/cm^3, respectively) were responsible for bulk densities below theoretical values. Porosity was found to constitute <0.1 vol.% of each MX and CX composition, indicating that the relative density was ≥99.9% for all MX and CX compositions. Densification rates varied, and the time required at the final dwell temperature to reach final density was affected by both the ZrB_2 powder particle size and the $MoSi_2$ content, with finer ZrB_2 particle size and greater $MoSi_2$ content both accelerating densification. For example, while M10 attained its final density 16 min after reaching 1875°C, C10 required almost three times as long, and did not reach final density until 45 min after reaching 1925°C. Similarly, M30 attained final density 28 min after reaching 1775°C while C30 did not reach final density until 37 min after reaching 1800°C. Increasing $MoSi_2$ contents decreased the densification time from 48 min at 1925°C for C10, to 4 min after reaching 1850°C for C40 and ~1 min after reaching 1800°C for C70.

Intergranular porosity was rarely observed, although intragranular porosity was visible in a few ZrB_2 grains. Densified microstructures were characterized by the presence of roughly polyhedral or rounded ZrB_2 grains and irregularly-shaped $MoSi_2$ grains (Figs. 3–7). The $MoSi_2$ grains often displayed acute dihedral angles. The ZrB_2 grains exhibited a core-shell type structure wherein each ZrB_2 grain core was partially surrounded by a $(Zr_{1-X}Mo_X)B_2$ solid solution (SS) shell (Fig. 3b), similar to previous reports for other ZrB_2-$MoSi_2$ ceramics [10, 60, 61, 65, 113, 114]. In compositions with ≥30 vol.% retained $MoSi_2$, the SS shells often formed necks between adjacent ZrB_2 grains, rather than surrounding ZrB_2 grain cores as in compositions with lower final $MoSi_2$ contents. In some cases, SS shells formed boundaries between ZrB_2 grains and $MoSi_2$ grains, while in other cases, ZrB_2 grain cores were directly in contact with $MoSi_2$ grains or other ZrB_2 cores. The variations in core-shell morphology in ZrB_2-$MoSi_2$ ceramics with $MoSi_2$ content provide a clue to the sintering process of diboride grains in these materials during densification and will be discussed in more detail in a future paper.

Several impurity phases were observed in the ZrB_2-$MoSi_2$ ceramics. The most abundant was SiO_2, which was observed in all compositions Table III). Typically, SiO_2

was adjacent to small ZrO_2 grains and often contained SiC crystallites, suggesting that SiC precipitated out of C-rich SiO_2 during cooling (Fig. 4, Fig. 6, circled). In addition, SiC could come from milling media wear. For FX compositions, SiO_2 content increased with increasing $MoSi_2$ content from 3.7 vol.% in F5 to 8.4 vol.% in F50, presumably due to the greater O content of the starting $MoSi_2$ powder than the ZrB_2 powder Table I). A similar set of ZrB_2-$MoSi_2$ compositions was made with the same powders as the FX series but processed with 30 min isothermal vacuum holds at 1450 and 1650°C during hot pressing. The final ceramics contained 0.4, 1.3, 3.3, and 3.5 vol.% SiO_2 in compositions with 5, 10, 20, and 30 vol.% $MoSi_2$ respectively, emphasizing the effectiveness of isothermal vacuum holds at removal of SiO_2. In comparison, MX and CX compositions contained less SiO_2 (0.4–2.6 vol.% in MX and 0.2–1.5 vol.% in CX) than FX due to the lower O contents of the starting ZrB_2 and $MoSi_2$ powders and the 60 min isothermal vacuum holds during hot pressing. A phase with an aspect ratio of ~4 to 7 was observed along some grain boundaries and identified as BN using EDS analysis. MoB was only observed in F50 (0.9 ± 0.7 vol.%) and not observed in any of the other compositions. MoB has been identified as an oxidation product of ZrB_2-$MoSi_2$ ceramics [11, 12, 42, 64, 89], and it is possible that the higher oxide content in the starting powders of F50 resulted in reactions creating MoB during hot pressing. Although Silvestroni et al. reported the presence of Mo_5Si_3 and Mo_5SiB_2 as remnants of a transient liquid phase requisite for the densification process of pressurelessly sintered ZrB_2-$MoSi_2$ ceramics [22], these phases were not observed in the present study. This, along with the fact that Silvestroni et al. did not observe SiO_2 or ZrO_2 in the pressurelessly materials, suggests differences between pressureless sintering and hot pressing. Overall, the combination of tertiary phases and porosity constituted between 5.2 and 11.3 vol.% of each FX composition, while impurities and pores combined constituted between 0.7 and 4.1 vol.% of each MX composition and between 0.4 and 2.4 vol.% of each CX composition Table III). Together, these results demonstrate that impurity contents in the final ceramics can be decreased using starting powders with higher purity and isothermal vacuum holds for removal of oxide impurities.

The final $MoSi_2$ contents of the ZrB_2-$MoSi_2$ ceramics were less than the nominal batch compositions, as determined by analyzing SEM images. Final $MoSi_2$ contents

decreased due to partial or complete decomposition of $MoSi_2$ during hot-pressing Table III, Fig. 8). In C10, which was processed for the longest time (60 min) at the highest temperature (1925°C), all $MoSi_2$ decomposed during hot pressing, and no $MoSi_2$ was detected in the final microstructure by SEM or by XRD. For all of the ceramics, Si was present in the final microstructure as $MoSi_2$, SiO_2, or SiC, but in quantities less than expected based on the initial $MoSi_2$ content, which indicates that some Si was lost during hot pressing. Some of the Si produced by $MoSi_2$ decomposition could have reacted with surface oxide impurities in the powder compacts and left the system as SiO(g)[22] or remained in the system as SiO_2. However, excess Si was exuded from the hot press die and reacted with the graphite die and graphite foil used to line the die for hot pressing. Decomposition also supplied Mo necessary for the formation of the $(Zr,Mo)B_2$ SS shell [110]. The decrease in $MoSi_2$ content from the nominal composition is consequential. For example, Si-containing phases are responsible for the formation of the protective oxide layer above 1100°C. Hence, a decrease in the overall Si content should decrease oxidation resistance. Furthermore, physical, mechanical, and thermal properties such as true density and fracture toughness also depend on the final $MoSi_2$ content.

Average and median final ZrB_2 grain sizes decreased with decreasing particle size of starting ZrB_2 powder Table IV, Fig. 9a). For example, the average ZrB_2 grain size of C20 was 3.4 ± 3.0 μm, while that of M20 was 2.1 ± 1.2 μm and that of F20 was 1.3 ± 0.8 μm. Similarly, the median ZrB_2 grain sizes were 2.5 μm for C20, 1.8 μm for M20, and 1.0 μm for F20. For every composition, median ZrB_2 grain sizes were lower than reported median starting powder particle sizes, partially because powder particle sizes are reported as volume-weighted distributions while median grain sizes are not weighted. Additionally, grain sizes were measured on polished sections, which rarely bisect grains at diameter maxima. In CX and MX, the average ZrB_2 grain size decreased continuously with increasing $MoSi_2$ content from ~4.6 μm in C10 to ~1.5 μm in C70, and from ~2.8 μm in M5 to ~2.0 μm in M30. In FX, average ZrB_2 grain size decreased from ~1.8 μm in F5 to ~1.3 μm in F20, and remained roughly constant at ~1.3 μm as nominal $MoSi_2$ content increased to 50 vol.%. The median ZrB_2 grain size followed similar trends. Decreasing ZrB_2 average and median grain sizes with increasing $MoSi_2$ content is attributed to a combination of (1) increased ZrB_2 grain pinning by $MoSi_2$ grains, (2)

decreased ZrB_2 grain growth due to lower hot-pressing temperatures used as $MoSi_2$ content increased, (3) decreased ZrB_2-ZrB_2 sintering required for densification due to greater densification provided by plastic deformation of $MoSi_2$ particles (Fig. 2), and (4) decreased solubility of ZrB_2 in the fugitive Si-based liquid, which is responsible for the dissolution of ZrB_2 grains (more frequent complete dissolution for smaller ZrB_2 grains, vs. partial dissolution for larger grains). Maximum observed ZrB_2 grain sizes were independent of $MoSi_2$ content, but increased with increasing ZrB_2 powder particle size. The largest observed ZrB_2 grains were between 5.7 and 6.5 μm in FX, between 8.8 and 9.8 μm in MX and between 15 and 30 μm in CX (Fig. 9a), similar to the d_{90} values of the respective ZrB_2 starting powders Table I). The ZrB_2 grains were elongated, with an average aspect ratio of ~2.1 ± 0.9 for CX compositions, ~1.8 ± 0.6 for MX compositions, and ~1.8 ± 0.7 for FX compositions Table IV). Overall, the characteristics of ZrB_2 grains were largely determined by the characteristics of starting powders, with the hot pressing temperature and $MoSi_2$ content playing limited roles. This behavior is not surprising due to the relatively low hot pressing temperatures used in this study. Because the room temperature flexure strength of as-ground ZrB_2-$Mosi_2$ ceramics depends on the final ZrB_2 maximum grain size [42], the flexure strength can be directly influenced by the maximum particle size of the starting ZrB_2 powder.

Differentiation of individual $MoSi_2$ grains was usually not possible, so instead the morphology of $MoSi_2$ clusters was characterized. Average $MoSi_2$ cluster size increased slightly with $MoSi_2$ content in CX, from ~2.8 μm in C20 to ~3.4 um in C40. No clear trends were observed for MX or FX compositions (Fig. 9b). Average cluster sizes were 1.8 to 2.2 μm in MX and 1.1 to 2.3 μm in FX Table IV). In contrast, the maximum $MoSi_2$ cluster size increased with increasing $MoSi_2$ content in all three series. In CX, maximum $MoSi_2$ cluster size increased from 22 μm in C20 and C30 to 35 μm in C40, while in MX maximum cluster size increased from 6 μm in M5 to 11 μm in M20, and jumped to 24 μm in M30. In FX, the maximum $MoSi_2$ cluster size increased from 5.3 μm in F5 to 12 μm in F30. At 50 and 70 vol.% $MoSi_2$, the $MoSi_2$ clusters appeared to form a continuous network. The increase of maximum $MoSi_2$ cluster size with increasing $MoSi_2$ content is likely due to the $MoSi_2$ content approaching or exceeding the percolation threshold, while

the increase in $MoSi_2$ cluster size with ZrB_2 powder particle size is likely due to the difference in percolation threshold with ZrB_2 particle size.

Powder X-ray diffraction between 20° and 90° 2θ identified only hexagonal ZrB_2 and tetragonal $MoSi_2$ in all densified compositions with the exception of C10, which exhibited only the characteristic peaks of ZrB_2 (Fig. 9). MoB, which has been previously reported in pressurelessly sintered[22] and hot-pressed ZrB_2-$MoSi_2$ ceramics [65], was not detected. In agreement with SEM analysis, Mo_5Si_3 and Mo_5SiB_2, which were reported by Silvestroni et al. in pressurelessly sintered ZrB_2-$MoSi_2$ compositions [22], were not detected by XRD. Characteristic peaks of ZrB_2 were shifted to higher diffraction angles than expected (compared to ICDD #00-034-0423) and characteristic peaks of $MoSi_2$ were observed shifted to lower diffraction angles than expected (compared to ICDD #00-041-0612), indicating residual tensile stress in the $MoSi_2$ phase and residual compressive stresses in the ZrB_2 phase due to CTE mismatch. Splitting of the ZrB_2 peaks was also observed, a phenomenon caused by the contribution of the $(Zr,Mo)B_2$ SS shell whose characteristic lattice parameters were slightly smaller than those of ZrB_2 and resulted in a corresponding sister peak of decreased intensity for each expected ZrB_2 peak at slightly higher 2θ angle [45]. These sister peaks were most obvious at diffraction angles above ~95°2θ, while at lower diffraction angles peak splitting was more difficult to resolve. At lower diffraction angles the sister peaks resulted in apparent peak broadening and acted as an additional source of apparent shifting of ZrB_2 peaks toward the "average" position of the peaks of the ZrB_2 cores and those of the SS shells. The apparent shifting or broadening of the primary ZrB_2 peaks toward higher 2θ angles due to peak splitting (and subsequent decrease of primary peak intensities) is expected to interfere with attempts at quantitative phase analysis via XRD and with calculations of residual lattice strains in the ZrB_2 phase in materials containing similar core-shell type microstructures.

Spontaneous microcracking was observed in F5, F10, F20, F30, and M20 (Figs. 3a and 4). Cracks in $MoSi_2$ appeared to originate at ZrB_2-$MoSi_2$ grain boundaries. Microcracking was presumably due to the CTE mismatch between ZrB_2 (α_a=7.08 x 10^{-6}/K, α_c=6.78 x 10^{-6}/K, for 20 to 1100°C) and $MoSi_2$ (α_a=7.94 x 10^{-6}/K, α_c=9.79 x 10^{-6}/K, for 20 to 1127°C) [115]. Watts et al. [116] reported spontaneous microcracking in

ZrB_2-SiC ceramics when SiC clusters reached a critical size. Watts' study used the analysis developed by Cleveland and Bradt for single phase ceramics[117] to estimate the critical grain size for spontaneous microcracking in two phase ZrB_2-SiC. Using lower and upper bound values for fracture toughness of 2.5 and 4.0 $MPa \cdot m^{½}$ [50, 51], a Poisson's ratio of 0.151, and a Young's modulus of 440 GPa [118], the surface energy of fracture for $MoSi_2$ was estimated to be in the range of 6.9 to 17.8 J/m^2. The critical microcracking threshold was estimated using the crystallographic CTE values with the greatest difference: 9.79 x 10^{-6}/K for the c-axis of $MoSi_2$, and 6.78 x 10^{-6}/K for the c-axis of ZrB_2 (20 to 1100°C) [115]. The Young's modulus of ZrB_2 was assumed to be 526 GPa [119] and a ΔT of 1100°C was used assuming that residual stresses only accumulated below the ductile to brittle transition temperature of $MoSi_2$ [50]. From these inputs, the critical grain size for microcracking was estimated to be between 18 and 47 μm for ZrB_2-$MoSi_2$ ceramics. This is similar to the size of $MoSi_2$ clusters (> ~20 μm) observed in M30, but this does not explain the observed microcracking in M20, where the largest $MoSi_2$ clusters were ~10 μm. Microcracking in M20 originated from ZrB_2-$MoSi_2$ grain boundaries in which the ZrB_2 grain formed the convex side of a curved interface with the concave $MoSi_2$ grain. It is likely that this geometry resulted in a higher stress concentration between ZrB_2 and $MoSi_2$ grains, resulting in a stress state favorable to spontaneous microcracking in $MoSi_2$, even though the cluster size in M20 was below the range estimated for microcracking. Use of a $MoSi_2$ powder with a finer starting particle size should decrease the percolation threshold and consequently decrease the likelihood of formation of $MoSi_2$ clusters large enough to form stress-inducing arrangements with ZrB_2 grains.

Effects of macroscopic residual stresses on the scale of the hot pressed billets were also observed in the densified ZrB_2-$MoSi_2$ ceramics. Several of the preliminary hot pressed billets broke spontaneously during wire electro discharge machining (EDM) when the wire approached the center of the billet, even though clamping forces were minimal and a non-contact cutting technique was used. Billets frequently adhered to graphite dies in instances where flashing was observed on billet edges, likely resulting in residual tensile stress in the billets during cooling due to the CTE mismatch between graphite die parts and the densified ceramic. These effects were mitigated enough to

allow for successful machining by using CTE-matched spacers during hot pressing. However, thermal annealing during cooling from the densification temperature may also reduce residual stresses and eliminate failure during machining.

4. SUMMARY

Three different series of ceramics with different median ZrB_2 particle sizes and between 5 and 70 vol.% $MoSi_2$ additions were densified by hot pressing at temperatures between 1750 and 1925°C. All compositions reached >99.2% relative density. Initial densification was attributed to plastic deformation of $MoSi_2$ when pressure was applied during hot pressing. Densification rate increased as starting ZrB_2 powder particle size decreased and $MoSi_2$ content increased. Densification was accompanied by partial or complete decomposition of $MoSi_2$ that depended on the final isothermal dwell temperature. Mo supplied by $MoSi_2$ decomposition was incorporated into $(Zr,Mo)B_2$ solid solution, and the evolved Si-based liquid exited the powder compact and was not observed in the final microstructures. The present study reports the only quantitative measurements of final $MoSi_2$ and $(Zr,Mo)B_2$ solid solution microstructural contents in ZrB_2-$MoSi_2$ ceramics. Average and maximum ZrB_2 grain size depended on characteristics of starting ZrB_2 powders, but average and median ZrB_2 grain sizes also decreased as $MoSi_2$ content due to the relatively low densification temperatures. Though average $MoSi_2$ cluster size did not change significantly with $MoSi_2$ content, maximum $MoSi_2$ cluster size increased as the $MoSi_2$ content increased. Impurity phases included SiO_2, ZrO_2, SiC, and BN, and higher purity starting powders and isothermal vacuum holds during hot pressing yielded lower impurity contents in the final microstructures.

Systematic study revealed specific relationships between starting composition, processing conditions and final microstructure in ZrB_2-$MoSi_2$ ceramics, allowing future researchers to regulate ZrB_2 grain size and content of $MoSi_2$, oxides, and SS shell in final microstructures. This ability allows control of mechanical and oxidative characteristics. Additions of ≥20 vol.% $MoSi_2$ allow densification of ZrB_2 at relatively low temperatures, meaning that both ZrB_2 grain growth and $MoSi_2$ decomposition are minimized, which would be expected to result in higher room temperature flexure strength and improved high-temperature oxidation resistance and ductility.

ACKNOWLEDGEMENTS

The authors would like to thank Daniele Dalle Fabbriche for assistance with hot pressing, Dr. Eric Bohannan for assistance with XRD, and Dr. Jeremy Watts for advice and assistance throughout the project. Funding for this project was provided by the United States' National Science Foundation Materials World Network Program through grant DMR-1209262, and by Italy's National Research Council for the project "Dual Composite Ceramics for Improved Properties."

REFERENCES

1. W. G. Fahrenholtz, G. E. Hilmas, I. G. Talmy, and J. A. Zaykoski, "Refractory Diborides of Zirconium and Hafnium," *Journal of the American Ceramic Society,* 90[5] 1347-64 (2007).

2. W. G. Fahrenholtz, E. J. Wuchina, W. E. Lee, and Y. Zhou, "Ultra-High Temperature Ceramics: Materials for Extreme Environment Applications." Wiley, (2014).

3. L. Silvestroni and D. Sciti, "Effects of $MoSi_2$ additions on the properties of Hf– and Zr–B_2 composites produced by pressureless sintering," *Scripta Materialia,* 57[2] 165-68 (2007).

4. E. W. Neuman, G. E. Hilmas, and W. G. Fahrenholtz, "Ultra-High Temperature Mechanical Properties of a Zirconium Diboride-Zirconium Carbide Ceramic," *Journal of the American Ceramic Society* 1-7 (2015).

5. E. W. Neuman, G. E. Hilmas, and W. G. Fahrenholtz, "Strength of Zirconium Diboride to 2300°C," *Journal of the American Ceramic Society,* 96[1] 47-50 (2013).

6. M. Brach, V. Medri, and A. Bellosi, "Corrosion of pressureless sintered ZrB_2–$MoSi_2$ composite in H_2SO_4 aqueous solution," *Journal of the European Ceramic Society,* 27[2-3] 1357-60 (2007).

7. V. A. S. V.O. Lavrenko, V.M. Talash, V.A. Kotenko, T.V.Khomko, "Electrochemical Oxidation of ZrB_2-$MoSi_2$ Ceramics in a 3% NaCl Solution," *Powder Metallurgy and Metal Ceramics,* 50[11-12] 749-52 (2011).

8. G. J. K. Harrington, G. E. Hilmas, and W. G. Fahrenholtz, "Effect of carbon on the thermal and electrical transport properties of zirconium diboride," *Journal of the European Ceramic Society,* 35[3] 887-96 (2015).

9. J. M. Lonergan, W. G. Fahrenholtz, and G. E. Hilmas, "Zirconium Diboride with High Thermal Conductivity," *Journal of the American Ceramic Society,* 97[6] 1689-91 (2014).

10. J. W. Zimmermann, G. E. Hilmas, and W. G. Fahrenholtz, "Thermal shock resistance of ZrB_2 and ZrB_2–30% SiC," *Materials Chemistry and Physics,* 112[1] 140-45 (2008).

11. J. W. Zimmermann, G. E. Hilmas, and W. G. Fahrenholtz, "Thermal Shock Resistance and Fracture Behavior of ZrB_2-Based Fibrous Monolith Ceramics," *Journal of the American Ceramic Society,* 92[1] 161-66 (2009).

12. E. W. Neuman, G. E. Hilmas, W. G. Fahrenholtz, and A. Dominguez-Rodriguez., "Strength of Zirconium Diboride to 2300°C," *Journal of the American Ceramic Society,* 96[1] 47-50 (2013).

13. M. M. Opeka, I. G. Talmy, and J. A. Zaykoski, "Oxidation-based materials selection for 2000°C + hypersonic aerosurfaces: Theoretical considerations and historical experience," *Journal of Materials Science,* 39 5887-904 (2004).

14. L. Mercatelli, E. Sani, D. Jafrancesco, P. Sansoni, D. Fontani, M. Meucci, S. Coraggia, L. Marconi, J. L. Sans, E. Beche, L. Silvestroni, and D. Sciti, "Ultra-refractory Diboride Ceramics for Solar Plant Receivers," *Energy Procedia,* 49 468-77 (2014).

15. E. Randich and D. D. Allred, "Chemically Vapor-Deposited ZrB_2 as a Selective Solar Absorber," *Thin Solid Films,* 83 393-98 (1981).

16. D. Sciti, L. Silvestroni, L. Mercatelli, J.-L. Sans, and E. Sani, "Suitability of ultra-refractory diboride ceramics as absorbers for solar energy applications," *Solar Energy Materials and Solar Cells,* 109 8-16 (2013).

17. N. Fuhrman and W. J. Bryan, "Element with Burnable Poison Coating," (1987).

18. S. Guo, T. Mizuguchi, M. Ikegami, and Y. Kagawa, "Oxidation behavior of ZrB_2–$MoSi_2$–SiC composites in air at 1500°C," *Ceramics International,* 37[2] 585-91 (2011).

19. W. G. Fahrenholtz, "Thermodynamic Analysis of ZrB_2-SiC Oxidation: Formation of a SiC-Depleted Region," *Journal of the American Ceramic Society,* 90[1] 143-48 (2007).

20. D. Sciti, L. Silvestroni, and M. Nygren, "Spark plasma sintering of Zr- and Hf-borides with decreasing amounts of $MoSi_2$ as sintering aid," *Journal of the European Ceramic Society,* 28[6] 1287-96 (2008).

21. L. Silvestroni, H.-J. Kleebe, S. Lauterbach, and M. Muller, "Transmission electron microscopy on Zr- and Hf-borides with $MoSi_2$ addition: Densification mechanisms," *Journal of Materials Research,* 25[5] 6 (2010).

22. L. Silvestroni, G. Meriggi, and D. Sciti, "Oxidation behavior of ZrB_2 composites doped with various transition metal silicides," *Corrosion Science,* 83 281-91 (2014).

23. A. L. Chamberlain, W. G. Fahrenholtz, and G. E. Hilmas, "Characterization of Zirconium Diboride-Molybdenum Disilicide Ceramics," *Ceramic Transactions,* 153 299-308 (2003).

24. V. O. Lavrenko, A. D. Panasyuk, O. M. Grigorev, O. V. Koroteev, and V. A. Kotenko, "High-Temperature (to 1600°C) Oxidation of ZrB_2-$MoSi_2$ Ceramics in Air," *Powder Metallurgy and Metal Ceramics,* 51[1-2] 102-07 (2012).

25. D. Sciti, M. Brach, and A. Bellosi, "Long-term oxidation behavior and mechanical strength degradation of a pressurelessly sintered ZrB_2–$MoSi_2$ ceramic," *Scripta Materialia,* 53[11] 1297-302 (2005).

26. S. R. Srinivasan, R. B. Schwarz, and J. D. Embury, "Ductile-To-Brittle Transition in $MoSi_2$," pp. 1099-104 in High-Temperature Ordered Intermetallic Alloys V. Vol. 288Edited by I. Baker, R. Darolia, J. D. Whittenberger, and M. H. Yoo.

27. L. Silvestroni, H.-J. Kleebe, S. Lauterbach, and M. Muller, "Transmission electron microscopy on Zr- and Hf- borides with $MoSi_2$ addition: Densification mechanisms," *Journal of Materials Research,* 25[5] 828-33 (2010).

28. M. A. Kuzenkova and P. S. Kislyi, "Sintering of Alloys of Zriconium Diboride with Molybdenum Disilicide," *Poroshkovaya Metallurgiya,* 9[45] 11-16 (1966).

29. P. S. Kislyi and M. A. Kuzenkova, "Gas-Impermeable Protective Thermocouple Sheaths from Zirconium Boride," *Poroshkovaya Metallurgiya,* 1[25] 32-36 (1965).

30. A. L. Chamberlain, W. G. Fahreholtz, and Hilmas, "Characterization of Zirconium Diboride-Molybdenum Disilicide Ceramics," *Ceramic Transactions,* 153 299-398 (2003).

31. S. Q. Guo, T. Nishimura, T. Mizuguchi, and Y. Kagawa, "Mechanical properties of hot-pressed ZrB_2-$MoSi_2$-SiC composites," *Journal of the European Ceramic Society,* 28 1891-98 (2008).

32. F. Monteverde, "The addition of SiC particles into a $MoSi_2$-doped ZrB_2 matrix: Effects on densification, microstructure and thermo-physical properties," *Materials Chemistry and Physics,* 113 626-33 (2009).

33. D. Sciti, F. Monteverde, S. Guicciardi, G. Pezzotti, and A. Bellosi, "Microstructure and mechanical properties of ZrB_2–$MoSi_2$ ceramic composites produced by different sintering techniques," *Materials Science and Engineering: A,* 434[1-2] 303-09 (2006).

34. H.-T. Liu, W.-W. Wu, J. Zou, D.-W. Ni, Y.-M. Kan, and G.-J. Zhang, "In situ synthesis of ZrB_2–$MoSi_2$ platelet composites: Reactive hot pressing process, microstructure and mechanical properties," *Ceramics International,* 38[6] 4751-60 (2012).

35. A. Bellosi, F. Monteverde, and D. Sciti, "Fast Densification of Ultra-High-Temperature Ceramics by Spark Plasma Sintering," *International Journal of Applied Ceramic Technology,* 3[1] 32-40 (2006).

36. S.-Q. Guo, T. Nishimura, T. Mizuguchi, and Y. Kagawa, "Mechanical properties of hot-pressed ZrB_2–$MoSi_2$–SiC composites," *Journal of the European Ceramic Society,* 28[9] 1891-98 (2008).

37. S.-Q. Guo, "Densification of ZrB_2-based composites and their mechanical and physical properties: A review," *Journal of the European Ceramic Society,* 29[6] 995-1011 (2009).

38. W.-M. Guo, Z.-G. Yang, and G.-J. Zhang, "Microstructural evolution of ZrB_2–$MoSi_2$ composites during heat treatment," *Ceramics International,* 37[7] 2931-35 (2011).

39. L. Silvestroni and D. Sciti, "Densification of ZrB_2-$TaSi_2$ and HfB_2-$TaSi_2$ Ultra-High-Temperature Ceramic Composites," *Journal of the American Ceramic Society,* 94[6] 1920-30 (2011).

40. D. Sciti, S. Guicciardi, A. Bellosi, and G. Pezzotti, "Properties of a Pressureless-Sintered ZrB_2-$MoSi_2$ Ceramic Composite," *Journal of the American Ceramic Society,* 89[7] 2320-22 (2006).

41. S. Zhu, W. G. Fahrenholtz, G. E. Hilmas, and S. C. Zhang, "Pressureless sintering of zirconium diboride using boron carbide and carbon additions," *Journal of the American Ceramic Society,* 90[11] 4 (2007).

42. S. C. Zhang, G. E. Hilmas, and W. G. Fahrenholtz, "Pressureless densification of zirconium diboride with boron carbide additions," *Journal of the American Ceramic Society,* 89[5] 7 (2006).

43. H. Mehrer, H. E. Schaefer, I. V. Belova, and G. E. Murch, "Molybdenum Disilicide - Diffusion, Defects, Diffusion Correlation, and Creep," *Defect and Diffusion Forum,* 322 107-28 (2012).

44. F. T. Monteverde, "The addition of SiC particles into a $MoSi_2$-doped ZrB_2 matrix: Effects on densification, microstructure and thermo-physical properties," *Materials Chemistry and Physics,* 113[2-3] 626-33 (2009).

45. F. Monteverde, A. Bellosi, and L. Scatteia, "Processing and properties of ultra-high temperature ceramics for space applications," *Materials Science and Engineering: A,* 485[1-2] 415-21 (2008).

46. R. J. Grohsmeyer, G. E. Hilmas, F. T. Monteverde, W. G. Fahrenholtz, and E. W. Neuman, "ZrB_2-$MoSi_2$ Ceramics with Varying $MoSi_2$ Content and ZrB_2 Powder Particle Size: Mechanical Properties of MX at Room Temperature and 1500°C in Air," *Journal of the European Ceramic Society,* TBD[TBD] TBD-TBD (2017b).

47. D. Sciti, M. Brach, and A. Bellosi, "Oxidation behavior of a pressureless sintered ZrB_2–$MoSi_2$ ceramic composite," *Journal of Materials Research,* 20[04] 922-30 (2005).

48. S.-Q. Guo, T. Mizuguchi, T. Aoyagi, T. Kimura, and Y. Kagawa, "Quantitative Electron Microprobe Characterizations of Oxidized ZrB_2 Containing $MoSi_2$ Additives," *Oxidation of Metals,* 72[5-6] 335-45 (2009).

49. Y. S. Touloukian, R. K. Kirby, E. R. Taylor, and T. Y. R Lee, "Thermophysical Properties of Matter, Thermal Expansion - Nonmetallic Solids," pp. 1786 Vol. 13. Thermophysical and Electronic Properties Information Analysis Center: Purdue University, Lafayette IN, USA, (1977).

50. J. L. Watts, G. Hilmas, W. G. Fahrenholtz, and R. Cutler, "Mechanical Characterization of ZrB_2-SiC Composites with Varying SiC Particle Sizes," *Journal of the American Ceramic Society,* 94[12] 4410-18 (2011).

51. J. J. Cleveland and R. C. Brandt, "Grain Size/Microcracking Relations for Pseudobrookite Oxides," *Journal of the American Ceramic Society,* 61[11-12] 478-81 (1978).

52. E. J. L. Y.-L. Jeng, "Review Processing of molybdenum disilicide," *Journal of Materials Science,* 29 2557-71 (1994).

53. R. Mitra, "Silicides: Processing and Mechanical Behavior," pp. 107-65. in Structural Intermetallics and Intermetallic Matrix Composites. CRC Press, 2015.

54. M. Nakamura, S. Matsumoto, and T. Hirano, "Elastic constants of $MoSi_2$ and WSi_2 single crystals," *Journal of Materials Science,* 25 5 (1990).

55. N. L. Okamoto, M. Kusakari, K. Tanaka, H. Inui, M. Yamaguchi, and S. Otani, "Temperature dependence of thermal expansion and elastic constants of single crystals of ZrB_2 and the suitability of ZrB_2 as a substrate for GaN film," *Journal of Applied Physics,* 93[1] 88 (2003).

Table I. Summary of characteristics of commercial powders used, including data measured during the present study (marked with an *) and supplied information for as-received ZrB_2, and $MoSi_2$ as-received and after pre-comminution.$MoSi_2$ from Sigma-Aldrich was combined with fine (F) ZrB_2, while $MoSi_2$ from H.C. Starck was combined with medium (M) and coarse (C) ZrB_2.

Powder	**Commercial Grade**	**Supplier**	**Particle Size d_{10}–d_{50}–d_{90} (vol. dist., μm)**	**SSA (m^2/g)**	**O (wt%)**	**Hf (wt%)**	**N (wt%)**	**Fe (wt%)**	**C (wt%)**
ZrB_2 (F)	Grade B	H. C. Starck	0.640–2.85–5.22*	1.8*	2.0	0.2	0.25	0.1	0.25
ZrB_2 (M)	Grade A		1.11–4.92–8.97*	0.76*	0.49*	1.80	0.18	0.07	0.1
ZrB_2 (C)	Coarse		2.51–11.7–30.1*	0.27*	0.16*	>0.2	0.08	-	0.19
$MoSi_2$	Grade B		1.19–4.98–8.74	0.92*	0.99*	–	0.02*	–	0.06
	milled 96 hr		1.06–3.75–7.53*	*	1.08*	–	0.02*	–	–
	as-received	Sigma-Aldrich	1.71–5.84–9.18*	–	2.06*	–	0.02*	–	–
	milled 90 hr		–	–	2.38*	–	0.02*	–	–

Table II. Summary of ZrB_2 powder characteristics, hot pressing temperature, final dwell time, and Archimedes' and observed microstructural densities (RD) for ZrB_2-$MoSi_2$ ceramics.

Comp-osition	ZrB_2 powder grade d_{10} - d_{50} - d_{90} (vol. dist., µm) specific surface area (m^2/g)	$MoSi_2$ added (vol.%)	Hot-pressing temperature (°C)	Hot-pressing dwell time (minutes)	Archimedes' density (g/cm^3)	Micro-structural RD (%)
F5*	"Fine" Grade B 0.640 – 2.85 – 5.22 1.8 m^2/g 1.30 wt.% O, 0.28 wt.% N	5	1850	22	5.97	99.96
F10*		10	1750	25	5.91	99.95
F20*		20	1750	30	6.05	99.97
F30*		30	1750	15	5.93	99.94
F50*		50	1750	13	5.89	99.27
M5	"Medium" Grade A 1.11 – 4.92 – 8.97 0.76 m^2/g 0.49 wt.% O, 0.21 wt.% N	5	1900	29	6.05	99.94
M10		10	1875	26	6.04	99.94
M20		20	1825	25	6.13	99.91
M30		30	1775	36	6.07	99.97
C10	"Coarse" Custom Batch 2.51 - 11.7 - 30.1 0.27 m^2/g 0.16 wt.% O, 0.08 wt.% N	10	1925	60	6.05	99.99
C20		20	1875	26	6.07	99.94
C30		30	1800	48	6.11	99.98
C40		40	1850	62	6.17	99.96
C50		50	1850	60	6.17	99.99
C70		70	1800	11	6.12	99.99

* Processed using $MoSi_2$ from Sigma-Aldrich and without isothermal vacuum holds during HP.

Table III. Summary of observed final phase composition and final measured oxygen content in ZrB_2-$MoSi_2$ ceramics

Com-posi-tion	Measured $MoSi_2$ (vol.%)	$(Zr,Mo)B_2$ Shell SS (vol.%)	SiO_2 (vol.%)	ZrO_2 (vol.%)	SiC (vol.%)	BN (vol.%)	Porosity (vol.%)	Oxygen (wt.%)
F5	3.1 ± 0.7	27.5 ± 2.8	3.7 ± 0.6	0.33 ± 0.19	1.0 ± 0.3	0.10 ± 0.08	0.04 ± 0.02	
F10	8.5 ± 1.0	24.9 ± 0.9	5.1 ± 1.0	0.23 ± 0.10	1.4 ± 1.5	0.14 ± 0.06	0.05 ± 0.01	
F20	17.6 ± 1.7	19.7 ± 1.6	6.1 ± 0.3	0.51 ± 0.19	1.8 ± 0.1	0.20 ± 0.03	0.03 ± 0.02	
F30	26.6 ± 2.2	N.M.	5.8 ± 1.2	1.30 ± 0.50	2.6 ± 0.1	0.08 ± 0.03	0.06 ± 0.04	
F50	45.4 ± 3.7	6.7 ± 0.7	8.4 ± 3.5	1.30 ± 1.15	0.9 ± 0.2	N.O.	0.73 ± 0.26	
M5	2.0 ± 0.8	23.2 ± 2.9	0.5 ± 0.1	0.12 ± 0.03	0.4 ± 0.2	0.28 ± 0.28	0.06 ± 0.03	0.626
M10	8.7 ± 2.0	23.2 ± 3.9	0.7 ± 0.2	0.15 ± 0.03	0.1 ± 0.1	0.12 ± 0.08	0.06 ± 0.02	1.87
M20	16.3 ± 0.7	14.4 ± 0.1	2.6 ± 0.9	0.28 ± 0.04	0.8 ± 0.2	0.30 ± 0.09	0.09 ± 0.01	1.76
M30	27.4 ± 2.7	10.0 ± 0.2	0.4 ± 0.2	0.14 ± 0.12	0.1 ± 0.1	0.09 ± 0.06	0.03 ± 0.02	2.09
C10	N.O.	23.4 ± 1.4	0.2 ± 0.1	0.72 ± 0.17	0.2 ± 0.1	N.O.	0.01 ± 0.02	
C20	18.1 ± 2.9	13.0 ± 1.6	1.0 ± 0.3	0.49 ± 0.26	0.4 ± 0.2	0.01 ± 0.01	0.06 ± 0.03	
C30	25.7 ± 0.9	10.2 ± 1.8	0.5 ± 0.3	1.6 ± 0.19	0.3 ± 0.1	N.O.	0.01 ± 0.01	
C40	34.3 ± 2.2	9.2 ± 2.3	0.5 ± 0.2	0.13 ± 0.14	0.1 ± 0.1	0.02 ± 0.01	0.04 ± 0.04	
C50	42.8 ± 3.8	5.2 ± 1.3	1.5 ± 0.9	0.08 ± 0.02	0.1 ± 0.1	0.02 ± 0.02	0.01 ± 0.01	
C70	66.9 ± 3.9	3.4 ± 0.7	0.4 ± 0.2	0.01 ± 0.02	0.0 ± 0.0	N.O.	0.01 ± 0.01	

(N.O. = not observed, N. M. = not measured but observed).
F50 contained 0.9 ± 0.7 vol.% MoB; MoB was not observed in any other composition in the present study. (N.O. = not observed, N.M. = not measured but observed)

Table IV. ZrB_2 grain size (GS), ZrB_2 aspect ratio (AR), and $MoSi_2$ cluster size (CS) for ZrB_2-$MoSi_2$ ceramics.

Compo-sition	ZrB_2 Avg. GS (μm)	ZrB_2 Median GS (μm)	ZrB_2 Max. GS (μm)	ZrB_2 Avg. AR	$MoSi_2$ Avg. CS (μm)	$MoSi_2$ Max. CS (μm)
F5	1.8 ± 0.9	1.6	5.7	1.7 ± 0.8	1.5 ± 0.7	5.3
F10	1.7 ± 0.9	1.5	6.2	1.8 ± 0.6	1.9 ± 1.0	6.4
F20	1.3 ± 0.8	1.1	5.8	1.8 ± 0.6	1.4 ± 1.0	8.1
F30	1.3 ±0.8	1.1	5.9	1.8 ± 0.6	1.1 ± 1.1	12.3
F50	1.3 ± 0.9	1.0	6.5	2.1 ± 0.9	2.3 ± 3.7	-
M5	2.8 ± 1.3	2.6	9.4	1.7 ± 0.6	1.9 ± 1.1	6.2
M10	2.7 ± 1.4	2.4	9.8	1.8 ± 0.6	1.9 ± 1.2	8.8
M20	2.1 ± 1.2	1.8	8.8	1.9 ± 0.6	1.8 ± 1.2	11
M30	2.0 ± 1.2	1.6	9.0	1.8 ± 0.6	2.2 ± 1.8	24
C10	4.6 ± 2.8	3.9	16	2.1 ± 0.9	-	-
C20	3.4 ± 3.0	2.5	30	2.1 ± 1.3	2.8 ± 2.9	22
C30	2.6 ± 2.0	1.9	18	2.0 ± 0.8	3.3 ± 2.5	22
C40	2.5 ± 1.7	2.1	15	2.1 ± 0.8	3.4 ± 3.5	35
C50	2.4 ± 2.0	1.9	17	2.1 ± 0.8	-	-
C70	1.5 ± 1.3	1.0	17	2.1 ± 1.0	-	-

Numerical averages are shown with ± one standard deviation.

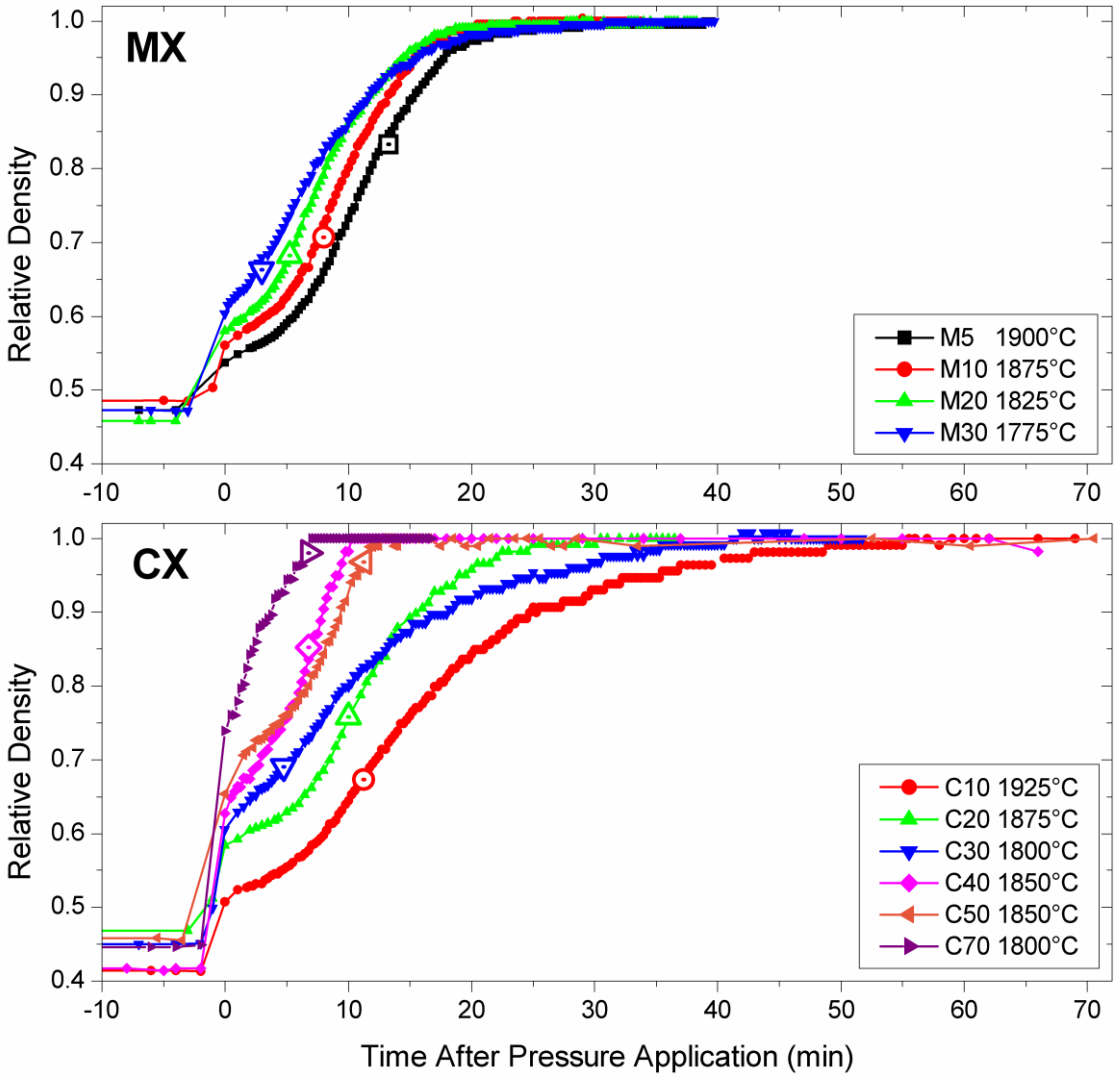

Fig. 1. Relative density of MX and CX compositions as a function of time during hot pressing. 30 MPa uniaxial pressure was fully applied at between 1621 and 1636°C in each case (shown at time = 0), after which temperature was increased.Open dotted symbols indicate when each composition reached the maximum densification temperature noted in the legend.

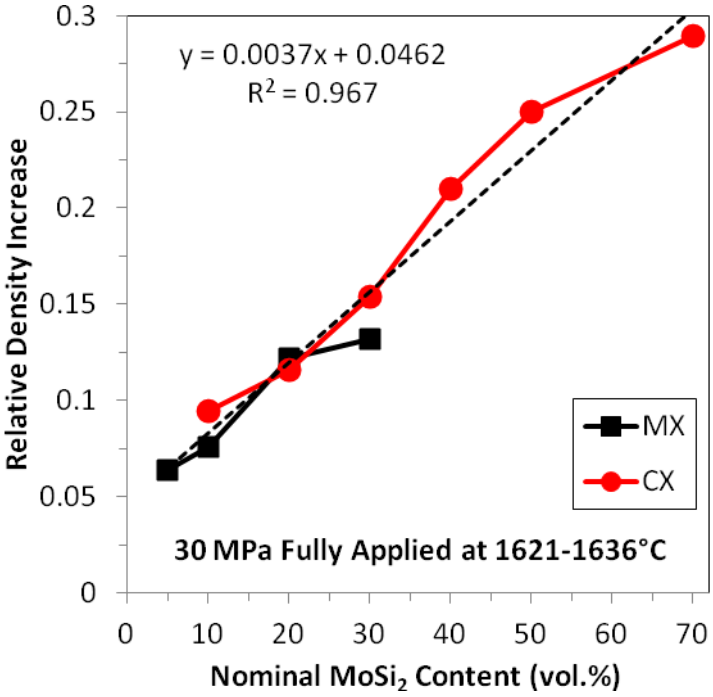

Fig. 2. Change in relative density upon full application of 30 MPa uniaxial pressure after completion of the isothermal hold at 1650°C, as a function of nominal $MoSi_2$ content.

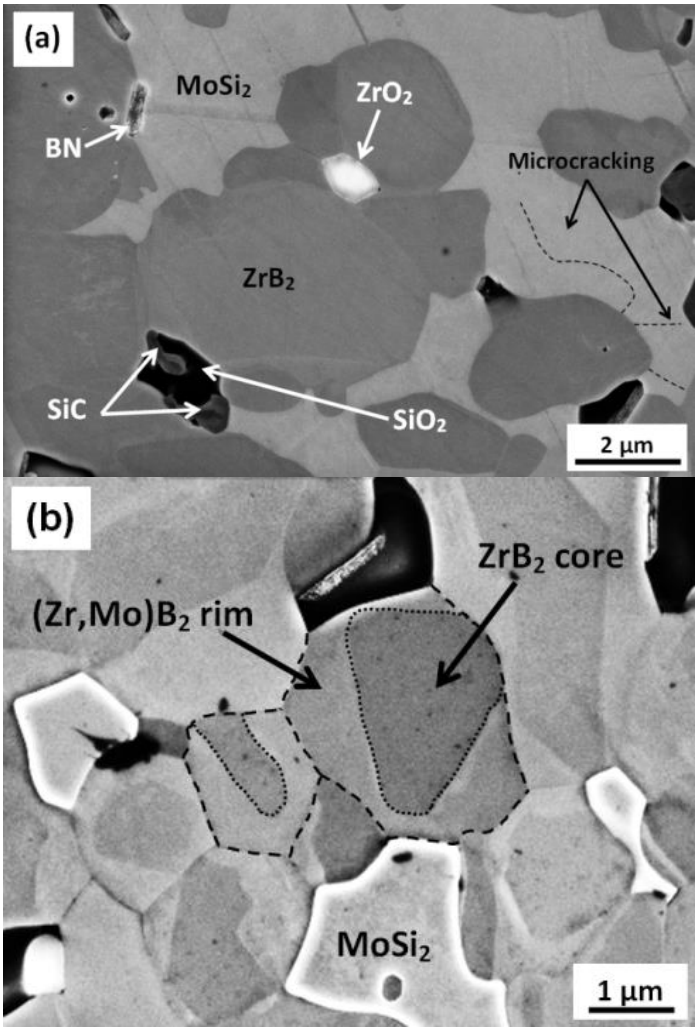

Fig. 3. Secondary electron images of typical microstructural features of the ZrB_2-$MoSi_2$ ceramics. (a) Constituent phases and microcracking (highlighted) in M20, and (b) core-shell structure of ZrB_2 grains in F20. Finely dotted lines are core-shell interface; dashed lines are ZrB_2-ZrB_2 grain boundaries.

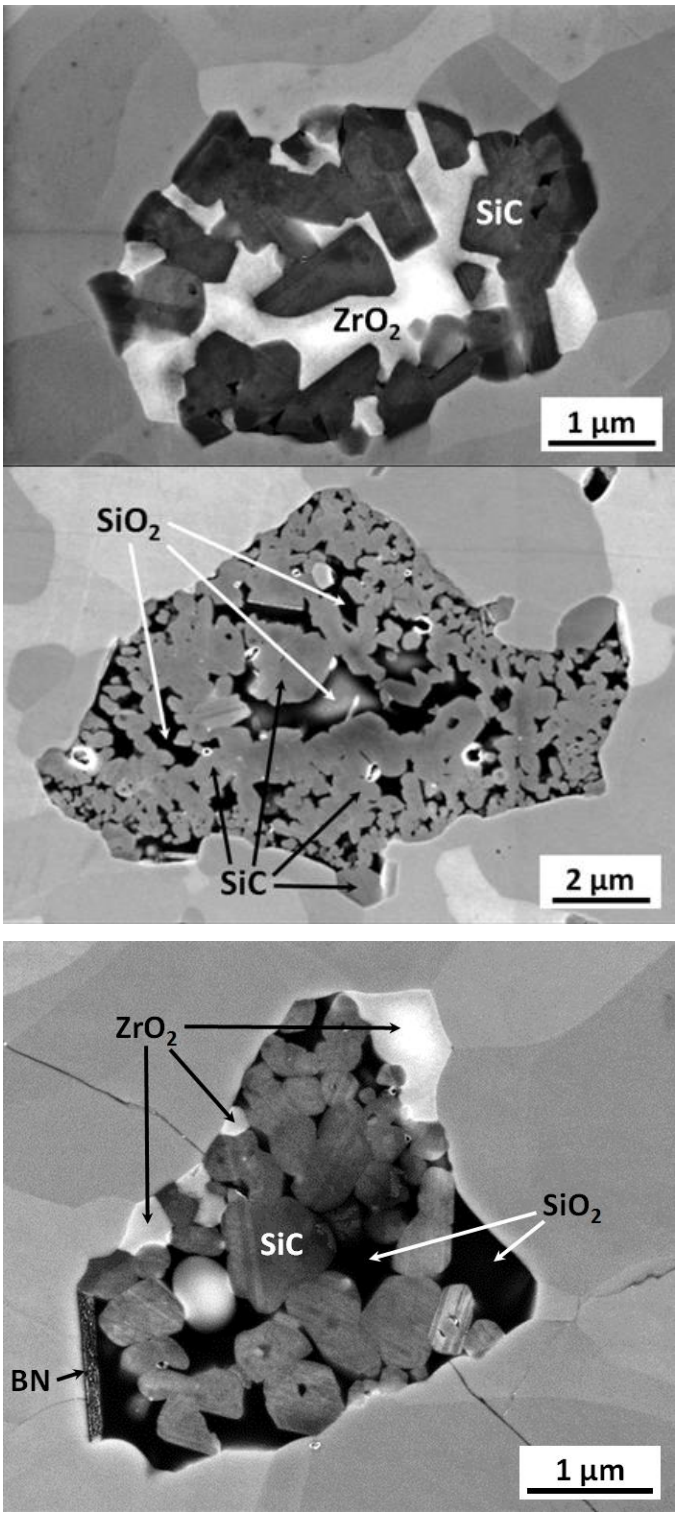

Fig. 4. Typical examples of large inclusions of clustered SiC, SiO2, ZrO2, and BN impurities observed in ZrB2-MoSi2 ceramics. Note different scales of the images.

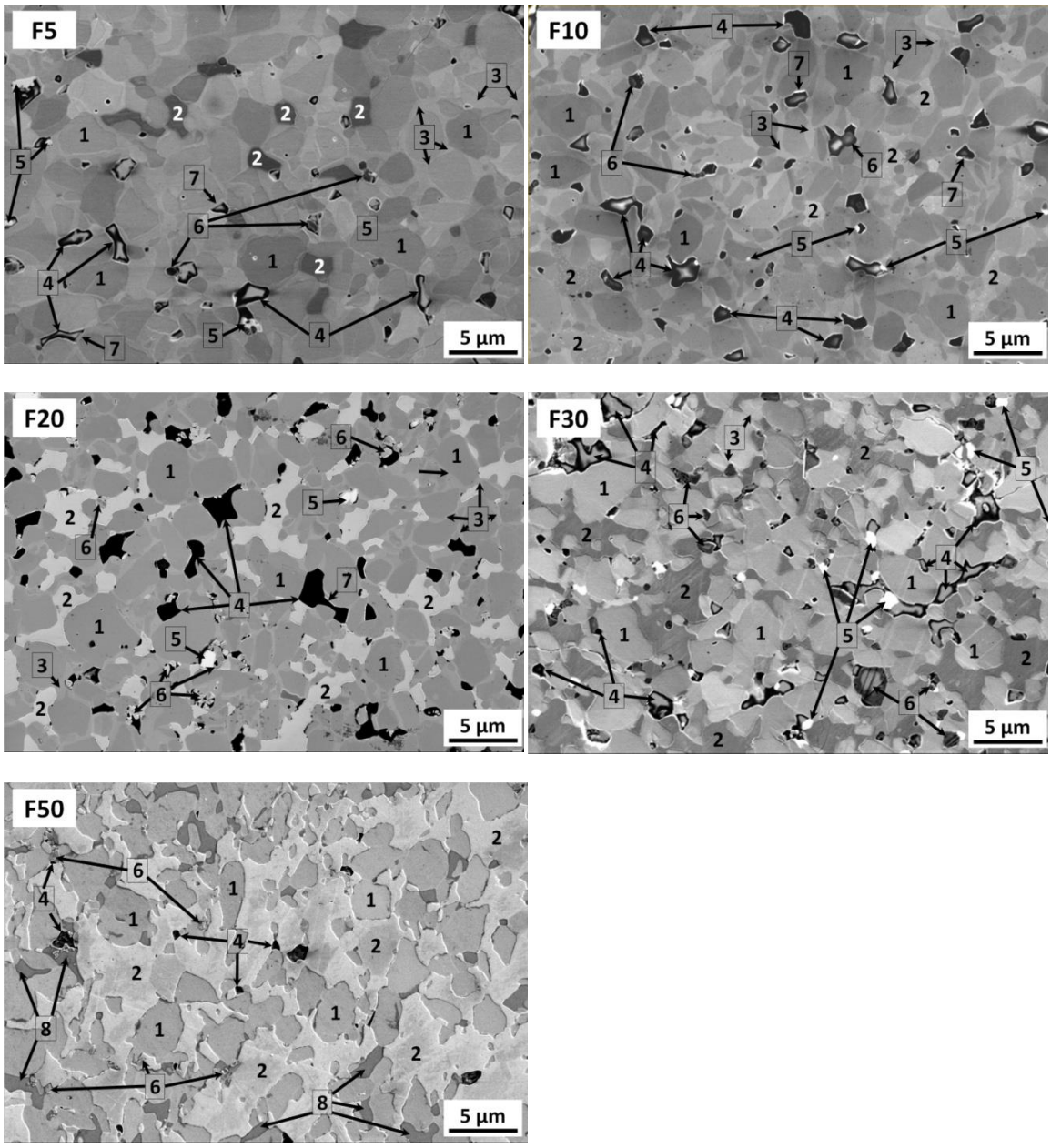

Fig. 5. Secondary electron images of the polished cross-sections of FX ZrB_2-$MoSi_2$ ceramics. Grayscale contrast of particular phases varies between images. (1): ZrB_2, (2): $MoSi_2$, (3): $(Zr,Mo)B_2$ SS shell, (4): SiO_2, (5): ZrO_2, (6): SiC, (7): BN, (8): MoB.

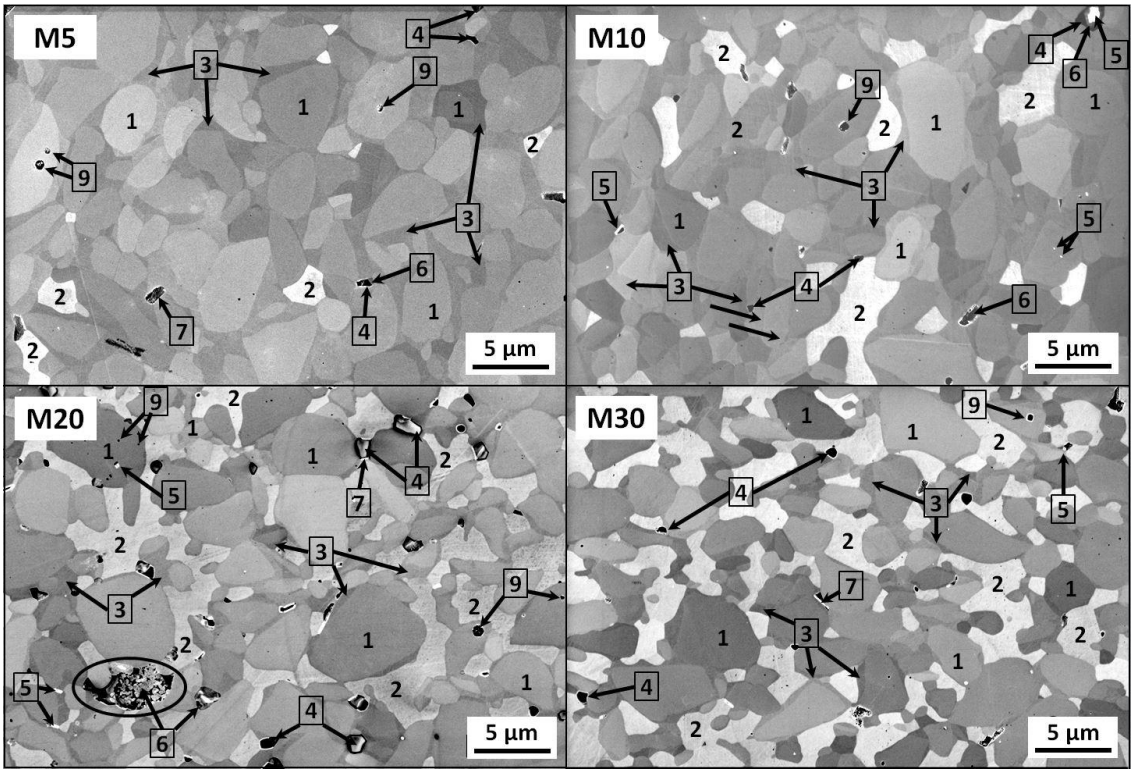

Fig. 6. Secondary electron images of the polished cross-sections of MX ZrB_2-$MoSi_2$ ceramics.The light gray phase is $MoSi_2$, the darker gray phase is ZrB_2, and the black phase is SiO_2. Circled feature in lower left of M20 is SiO_2 (black) with precipitated SiC crystals. (1): ZrB_2, (2): $MoSi_2$, (3): $(Zr,Mo)B_2$ SS shell, (4): SiO_2, (5): ZrO_2, (6): SiC, (7): BN, (9): porosity.

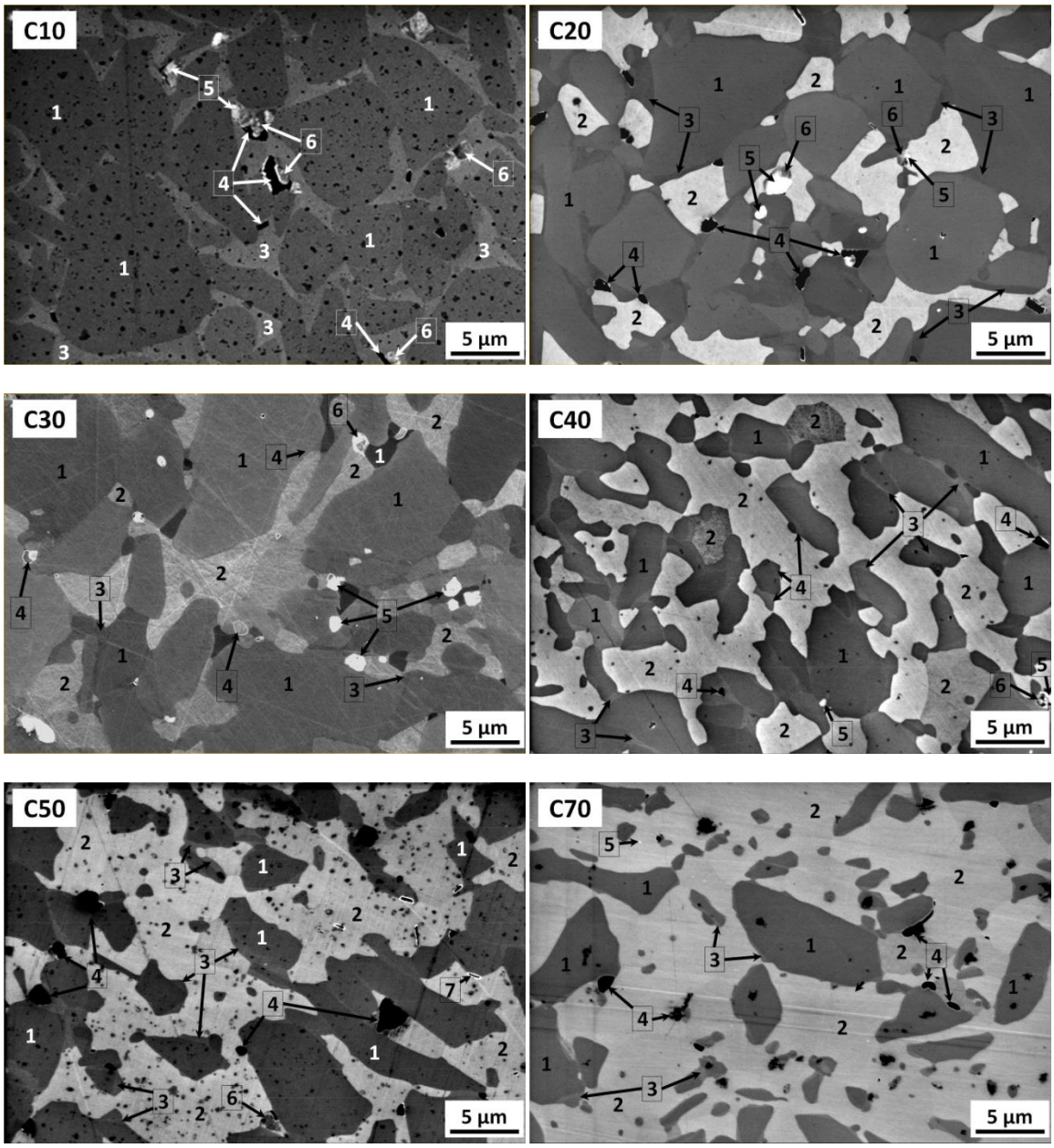

Fig. 7. Secondary electron images of the polished cross-sections of CX ZrB_2-$MoSi_2$ ceramics. Black spots on C10 and C50 are plasma cleaning artifacts. (1): ZrB_2, (2): $MoSi_2$, (3): $(Zr,Mo)B_2$ SS shell, (4): SiO_2, (5): ZrO_2, (6): SiC, (7): BN.

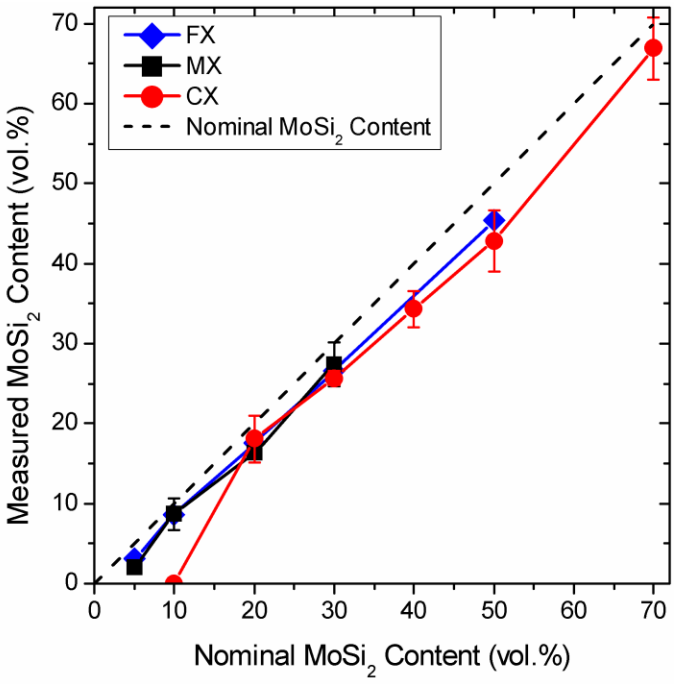

Fig. 8. Final $MoSi_2$ content in densified ceramics as measured by areal analysis on polished sections.Dotted line shows nominal $MoSi_2$ content.

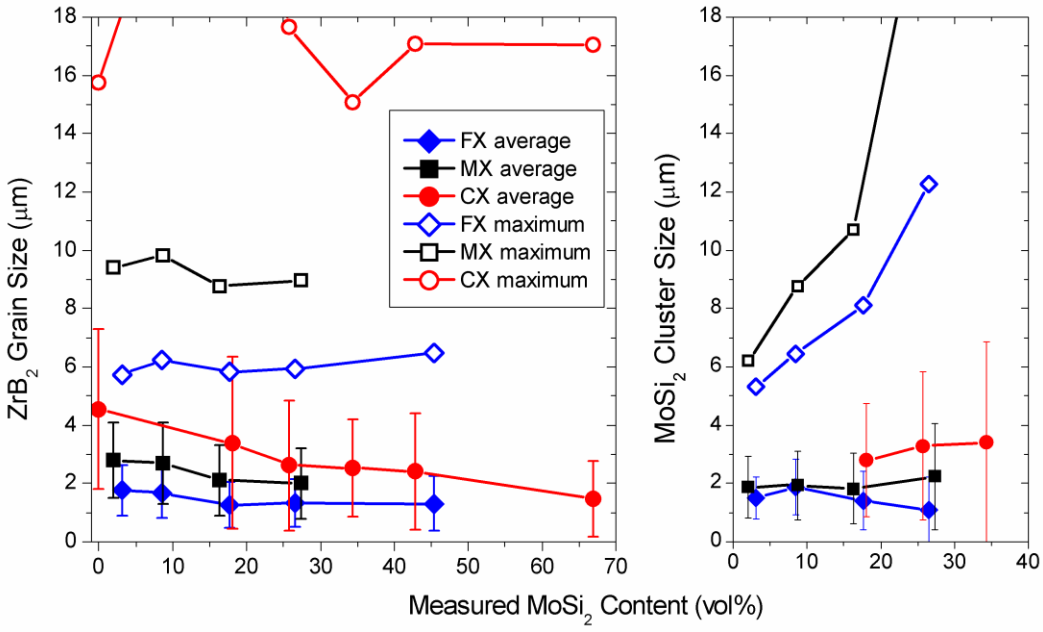

Fig. 9. Average and maximum ZrB_2 grain size and $MoSi_2$ cluster size for each series as a function of measured $MoSi_2$ content. Measured by areal analysis on polished sections and calculated by numerical average.

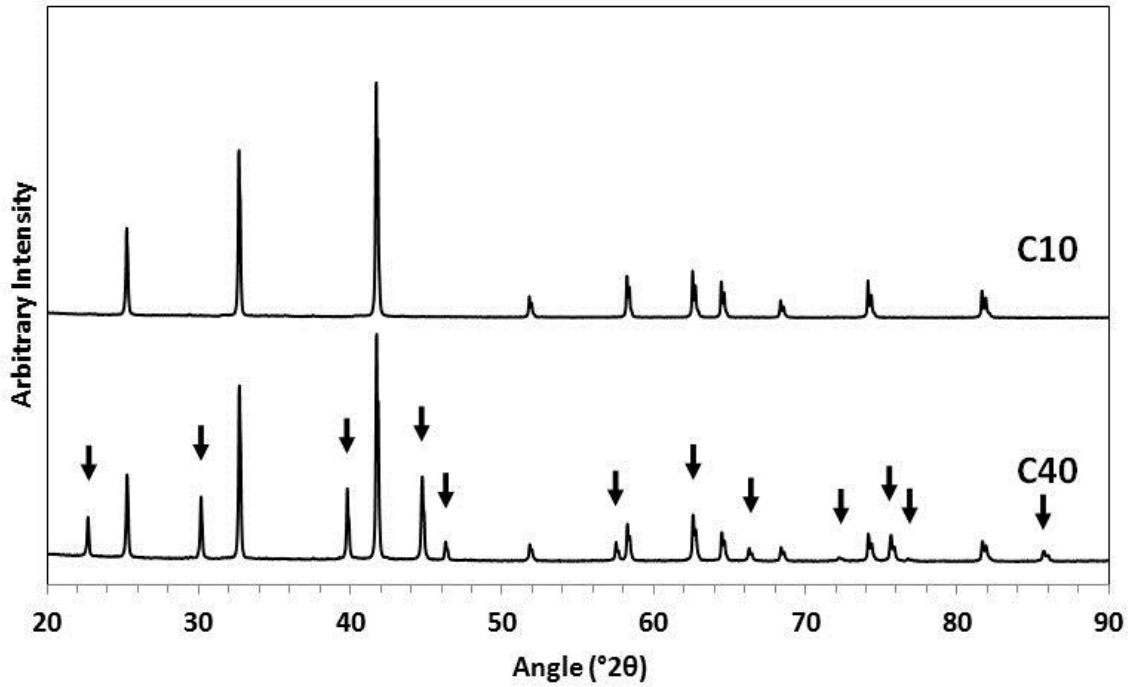

Fig. 10. Powder X-ray diffraction patterns of C10 (top) and C40 (bottom) after hot pressing and pulverizing.Vertical arrows indicate characteristic $MoSi_2$ peaks.

II. ZrB_2-$MoSi_2$ CERAMICS WITH VARYING $MoSi_2$ CONTENT: PART 2. MECHANICAL PROPERTIES FOR MEDIUM ZrB_2 PARTICLE SIZE

Ryan Grohsmeyer,[a, 3] Gregory Hilmas,[a, 4] Frédéric Monteverde,[b] William Fahrenholtz,[a] Eric Neuman[a, 5]

[a] Materials Science and Engineering Department, Missouri University of Science and Technology, Rolla, MO 65409, United States

[b] National Research Council of Italy, Institute of Science and Technology for Ceramics, Faenza, 48018 RA, Italy

ABSTRACT

Mechanical properties were measured in air at room temperature and 1500°C for ZrB_2-$MoSi_2$ ceramics with 5 to 30 vol.% $MoSi_2$ additions hot-pressed at temperatures between 1775 and 1900°C. Decomposition of $MoSi_2$ was quantified by microstructural analysis. Room temperature strength (550-720 MPa) was limited by surface grain pullout. Fracture toughness (2.8-3.8 MPa·$m^{½}$) showed no overall trend with $MoSi_2$ content. Microhardness (16.6-15.1 GPa), Young's modulus (530-470 GPa), and shear modulus (235-220 GPa) decreased, while Poisson's ratio (0.134-0.143) increased with $MoSi_2$ content. Fracture toughness at 1500°C increased from 4.1 to 5.7 MPa·$m^{½}$ as $MoSi_2$ content increased, due to high-temperature plasticity of the $MoSi_2$ that remained in the microstructure. At 1500°C, compositions with 5 and 10 vol.% $MoSi_2$ formed a porous zirconia scale, and exhibited strengths of 250 and 300 MPa. Compositions with 20 and 30 vol.% $MoSi_2$ exhibited strengths of 415 and 439 MPa due to increased toughness and formation of a protective borosilicate layer.

Key Words: High temperature mechanical properties (C), Borides (D), Silicides (D), Oxidation

---

[3] Present address: Corning Incoporated, Painted Post, NY, USA.

[4] Corresponding Author: ghilmas@mst.edu, +1-573-341-6102

[5] Present address: Sandia National Laboratories, Albuquerque, NM, USA.

1. INTRODUCTION

Zirconium diboride-based structural ceramics possess properties including melting temperatures of up to ~3250˚C,hardness in the range of 14-23 GPa [14, 23], retention of strength and elastic modulus up to 2300°C [10, 24, 100], low electrical resistivity (6-23 μΩ·cm) [16, 103], and chemical stability in acids [101, 120], which make them attractive for use in extreme environments. Applications such as aerodynamic leading edges for hypersonic reentry vehicles and high temperature engine components [23, 105], concentrated solar thermal absorbers [29-31], nuclear fuel cladding and neutron absorbers [106], and others have been suggested for ZrB_2-based materials. However, the tendency of ZrB_2 to exhibit brittle mechanical fracture and its susceptibility to rapid oxidation at high temperatures[32, 33] have hindered efforts to bring the material into the aforementioned applications. Fortunately, ZrB_2 is amenable to combination with several other phases whose additions have been shown to improve both of these characteristics.

Molybdenum disilicide ($MoSi_2$) has been studied as an additive to ZrB_2, due to its ability to perform three important functions: (1) act as a sintering aid facilitating densification of ZrB_2 by hot pressing at temperatures as low as 1750°C [10, 60, 61]; (2) improve the oxidation resistance of ZrB_2 up to ~1600˚C by forming a glassy borosilicate surface layer [62-64]; and (3) add ductility at elevated temperatures due to its brittle-to-ductile transition temperature (BDTT) upon heating to between 1000 and 1300˚C [57]. Additions of $MoSi_2$ also increase the flexure strength of ZrB_2 at room temperature, 1200˚C and 1500˚C in air [10, 65]. Additional studies have investigated mechanical properties at ambient temperature and flexure strength at elevated temperatures [10, 65]. However, fracture toughness data for the same temperature range has not been reported in the literature.

Several studies have examined the behavior of ZrB_2-$MoSi_2$ composites with respect to $MoSi_2$ content at room temperature [60, 62, 66], and multiple studies have compared the properties of selected compositions at room temperature and at elevated temperatures [10, 65, 67, 85]. However, data from systematic studies comparing mechanical behavior over an extended compositional range at both ambient and elevated temperature are limited. Guo et al. studied the effects of $MoSi_2$ contents from 10 to 40

vol.% on room temperature properties of hot-pressed ZrB_2 ceramics, reporting mean strength values in the range of 750 to 800 MPa for all compositions, and fracture toughness values between 2.6 and 3.7 $MPa \cdot m^{½}$ [66]. Guo also reported room temperature elastic moduli ranging from 490 to 448 GPa for 10 to 40 vol.% $MoSi_2$. Chamberlain et al. studied room temperature mechanical properties of hot pressed ZrB_2-$MoSi_2$ for 10 to 30 vol.% $MoSi_2$ additions, reporting flexure strength between 1000 and 1150 MPa for all compositions, and fracture toughness between 3.0 and 4.1 $MPa \cdot m^{½}$ [62]. Sciti et al. measured room temperature microhardness and fracture toughness of ZrB_2-$MoSi_2$ consolidated by spark plasma sintering for 1 to 9 vol.% $MoSi_2$ additions, reporting an increasing fracture toughness from 2.0 to 3.3 $MPa \cdot m^{½}$ with increasing $MoSi_2$ content, accompanied by an increase in microhardness from 16.5 to 18.2 GPa [60]. Silvestroni et al. measured flexure strength of pressurelessly sintered ZrB_2 with 5 and 20 vol.% $MoSi_2$ additions, and reported strength retention at elevated temperatures: room temperature strength of 569 and 531 MPa respectively were compared with strengths of 533 and 655 MPa at 1200°C, and strengths of 488 and 500 MPa at 1500°C in air [10]. Sciti et al. compared mechanical properties ZrB_2 with 15 to 20 vol.% $MoSi_2$ additions densified by differing sintering methods, reporting strengths in the range of 530 to 700 MPa at room temperature, 655 to 632 MPa at 1200°C in air, and strengths between 330 and 500 MPa at 1500°C in air. Previous studies have provided an enlightening start of the characterization of ZrB_2-$MoSi_2$ ceramics, but more studies are required that systematically measure multiple mechanical properties at both room and elevated temperatures for broad ranges of composition.

Surface oxidation of ZrB_2-based ceramics is known to affect mechanical properties during elevated temperature testing. The oxidation behavior of ZrB_2-$MoSi_2$ composites exhibits parabolic kinetics, forming a multilayered oxide scale [12, 63, 64, 89, 90]. Oxidation of ZrB_2-$MoSi_2$ composites involves the oxidation of both component phases. ZrB_2 is known to oxidize following Eq. (1) [64].

$$ZrB_2(s) + 2.5\ O_2(g) \rightarrow ZrO_2(s) + B_2O_3(l,g) \quad (1)$$

While liquid B_2O_3 can limit oxygen diffusion into the surface below ~1100°C, above this temperature it has a high vapor pressure and rapidly volatilizes from the surface [64, 89], allowing rapid formation of porous ZrO_2 [62]. $MoSi_2$ has been reported to oxidize according to Eq. (2) at temperatures from 1200 to 1600°C [62, 89, 90].

$$MoSi_2(s) + 3.5\ O_2(g) \rightarrow 2\ SiO_2(s) + MoO_3(l) \quad (2)$$

$MoSi_2$ has also been reported to oxidize indirectly to Mo_5Si_3, SiO_2 and MoO_3 according to Eqs. (3) and (4) [63, 65].

$$5\ MoSi_2(s) + 7\ O_2(g) \rightarrow Mo_5Si_3(s) + 7\ SiO_2(l) \quad (3)$$

$$Mo_5Si_3(s) + 10.5\ O_2(g) \rightarrow 5\ MoO_3(l) + 3\ SiO_2(l) \quad (4)$$

Formation of a continuous SiO_2 layer inhibits diffusion of oxygen through the surface scale, giving $MoSi_2$ oxidation resistance in the range of 700 to 1700°C [50]. MoO_3 has a melting temperature of 801°C, but its high vapor pressure results in its rapid evaporation below 1000°C [64, 89]. Chamberlain et al. reported that volatilization of B_2O_3 and MoO_3 species occurred above 1100°C [62]. For monolithic polycrystalline $MoSi_2$, oxidation in the range of 300 to 600°C results in formation of SiO_2, and volatile MoO_3, producing internal stresses at the grain boundaries resulting in pesting [91]. During oxidation of ZrB_2 composites with Si-containing compounds such as SiC and $MoSi_2$, a combination of these oxidation reactions has been found to produce an amorphous borosilicate surface oxide layer, with a sub-layer of porous zirconia [92]. Sciti et al. [89]. reported the presence of MoB dispersed in the porous zirconia layer after exposure to air at 1200 to 1400°C of ZrB_2 with 5 to 20 vol.% $MoSi_2$ additions, indicating the favorability of the reaction shown by Eq. (5) for ZrB_2-$MoSi_2$ composites.

$$ZrB_2(s) + 2\ MoSi_2(s) + 5\ O_2(g) \rightarrow ZrO_2(s) + 2\ MoB(s) + 4\ SiO_2(l) \quad (5)$$

The study reported that this reaction is favorable at all temperatures [89], suggesting that glassy surface oxide layers on ZrB_2-$MoSi_2$ composites may have a higher silica content than those on ZrB_2-SiC composites. Higher silica content in the amorphous borosilicate layer is expected to contribute to higher viscosity at elevated temperatures, providing greater resistance to ablation. The favorability of Eq. (5) suggests that $MoSi_2$ may therefore be a more effective addition to ZrB_2 than SiC for purposes of oxidation resistance, due to the tendency of B to form MoB (s) instead of B_2O_3 in the presence of Mo under oxidizing conditions.

Guo et al. studied the oxidation behavior at 1500°C of ZrB_2 composites with 10, 20, and 40 vol.% $MoSi_2$ additions and reported parabolic oxidation kinetics with decreasing rates as the $MoSi_2$ content increased [12]. The oxide scale consisted of an outer silicate glassy layer atop a layer of porous zirconia, followed by a layer of the composite substrate depleted of the silicide phase. Sciti et al. characterized the oxidation of ZrB_2 with 5 and 20 vol.% $MoSi_2$ additions at temperatures between 700 and 1400°C for 30 h in air, and reported a similar multilayered oxide structure and the formation of a continuous silicate-based glassy outermost layer only above 1200 and 1400°C [93]. Silvestroni et al. reported that formation of a silicate-based glassy layer contributed to healing of surface flaws and to strength retention at 1200 and 1500°C in air for pressurelessly sintered compositions containing 5 and 20 vol.% $MoSi_2$ [10].

The purpose of this study is to systematically investigate the mechanical properties of ZrB_2-$MoSi_2$ ceramics with $MoSi_2$ additions of 5 to 30 vol.% at room temperature and 1500°C in air. The roles of microstructure, specimen preparation, and oxidation behavior on the mechanical properties are discussed. An accompanying paper describes the processing, densification behavior, and final microstructures of three series of ZrB_2-$MoSi_2$ ceramics each processed with differing ZrB_2 starting powder particle sizes over a range of $MoSi_2$ contents. The present paper discusses the mechanical characterization of the series of compositions that was batched with the "medium" ZrB_2 starting powder particle size referred to as "MX."

2. EXPERIMENTAL PROCEDURE

2.1. Processing and Characterization. Sample compositions in the present study were batched using commercial powders (H.C. Starck, Newton, MA, USA) as reported

elsewhere [121]. The present study examines compositions batched with "medium" (grade A) ZrB_2 powder (d_{10} = 1.11 μm, d_{50} = 4.92 μm, d_{90} = 8.97 μm) mixed with pre-milled $MoSi_2$ powder in 5, 10, 20, and 30 vol.% quantities designated MX, where X is the nominal $MoSi_2$ content in vol.%. After densification by hot pressing, compositions were characterized physically and microstructurally according to the procedures described elsewhere [121].

2.2. Mechanical Testing. Young's modulus, shear modulus, and Poisson's ratio were measured by impulse excitation (MK4-I Grindosonic, J.W. Lemmens, Leuven, Belgium) based on ASTM C1259, using specimen sizes of 30 mm x 8 mm x 0.8 mm and 45 mm x 4 mm x 3 mm (length by width by thickness). Reported shear modulus and Poisson's ratio values are the average of two plate specimens. The static bend test method based on ASTM E111 was used to determine the static Young's modulus in four-point flexure testing at room temperature and 1500˚C. Microhardness was measured by Vickers' indentation based on ASTM C1327 (Zwick 3212, Zwick-Roell, Ulm, Germany), with an indentation load of 9.81 N and dwell time of 10 s. A minimum of 15 indentations per composition were measured to determine the average values.

Fracture toughness was measured at room temperature fixtures and at 1500˚C in air based on ASTM C1421 using type-A bars (nominally 45 mm x 3 mm x 4 mm) having a chevron notched beam (CNB) geometry in four-point bending. Fully articulating steel fixtures were used at room temperature, while at 1500°C fully articulating SiC fixtures were used. The chevron notches were cut with a dicing saw (Accu-cut 5200, Aremco Products, Ossining, NY, USA) with a 150 μm thick diamond wafering blade. The a_0 dimension of the chevron notch was typically between 0.3 and 0.6 mm, compared to the 0.8 ± 0.07 mm as specified by the standard. A crosshead rate of 0.018 mm/min was used at room temperature and a crosshead rate of 0.18 mm/min was used at 1500˚C. A minimum of four specimens were tested for each composition and temperature. Notch dimensions were measured using an optical microscope (KH-3000, Hirox-USA, Hackensack, NJ, or 3212, Zwick-Roell, Ulm, Germany). Fixture, specimen, and notch dimensions were adjusted for thermal expansion (α_{SiC} = 4.42·10^{-6}/K [122], α_{ZrB_2} = 7.39·10^{-6}/K, and α_{MoSi_2} = 8.39·10^{-6}/K from 20-1500°C [115]) based on a linear rule of

mixtures (ROM). Force-deflection curves that exhibited any detectable non-linearity after the maximum load was reached were considered valid.

Room-temperature flexure strength was measured according to ASTM C1161 using type-B bars (nominally 45 mm x 4 mm x 3 mm) in four-point bending with a fully articulating fixture. Flexure strength was measured at 1500˚C in air using type-B bars according to ASTM C1211 with a four-point, fully-articulating SiC fixture. A minimum of 5 specimens were tested for each composition and temperature. Bars were machined by electrical discharge machining (EDM; DS2 PartMaker, Hansvedt Industries, Rantoul, IL, USA) and finish ground with a 1200 grit diamond wheel using an automatic surface grinder (FSG-3A818, Chevalier, Santa Fe Springs, CA, USA) with a ~2.54 μm downfeed step. Corner chamfers were polished to 3 μm finish using diamond abrasives. Flexure tests were performed using a screw-driven instrumented load frame (5881, Instron SFL, Thornbury, Bristol, UK). Elevated temperature testing was performed in a $MoSi_2$ element furnace (MDS66C, Instron SFL, Thornbury, Bristol, UK). A deflectometer was used to record the center displacement of the test bars during loading. A crosshead rate of 0.5 mm/min was used at room-temperature and rates between 1 and 3 mm/min at 1500˚C. The heating rate for the high temperature tests was 10°C/min followed by an isothermal hold for 10 min to attain thermal equilibrium before testing. Specimen dimensions were adjusted for thermal expansion using the method previously described. The changes in specimen cross-section due to oxidation were neglected for calculation of flexure strength.

3. RESULTS AND DISCUSSION

3.1. Microstructural Analysis. Microstructural features are summarized here but described in more detail elsewhere [121]. The bulk density of each composition was greater than 99.9% of its theoretical value Table I) based on the fact that porosity was observed to constitute less than 0.1 vol.% (Fig. 1). The ZrB_2 grains exhibited a core-shell type structure wherein a $(Zr,Mo)B_2$ solid solution shell surrounded a ZrB_2 core similar to what has been previously reported for other ZrB_2-$MoSi_2$ ceramics [10, 60, 61, 65, 113, 114]. In addition, SiO_2, ZrO_2, SiC, and BN were observed.. Typically, tertiary phases and porosity combined constituted less than 1.4 vol.% of each composition, except for M20, which contained ~4.1 vol.%.

The $MoSi_2$ contents of the hot-pressed ceramics were less than the nominal batch compositions Table I) due to partial decomposition of $MoSi_2$ during hot-pressing, discussed elsewhere [110, 121]. Due to the variation between the nominal and retained $MoSi_2$ content in the hot-pressed ceramics, the analysis has been grouped as follows: strength and fracture toughness are discussed in nominal amounts of $MoSi_2$; Young's modulus, shear modulus, Poisson's ratio, hardness, and oxidation resistance are discussed with respect to retained $MoSi_2$ content.

The ZrB_2 grains were elongated, with an aspect ratio of ~1.8 ± 0.6 for all compositions Table I), and randomly oriented. The average ZrB_2 grain size decreased with increasing $MoSi_2$ content from ~2.8 μm in M5 to ~2.0 μm in M30. The maximum ZrB_2 grain size was ~9 μm independent of $MoSi_2$ content. Likewise, the $MoSi_2$ cluster size was ~2 μm and did not change significantly with $MoSi_2$ content. Maximum $MoSi_2$ cluster size increased from 6 μm in M5 to 11 μm in M20, but jumped to 24 μm in M30. Spontaneous microcracking was observed in M20. Cracks in $MoSi_2$ appeared to originate at ZrB_2-$MoSi_2$ grain boundaries. Microcracking was presumably due to the CTE mismatch between ZrB_2 and $MoSi_2$ and is explained in more detail elsewhere [121].

3.2. Mechanical Properties at Room Temperature. Young's modulus decreased with increasing $MoSi_2$ content from 531 GPa for M5 to 494 GPa for M30. The values fall within one standard deviation of predictions made using a linear ROM assuming a value of 526 GPa for ZrB_2 [34] and 400 GPa for $MoSi_2$, which was measured on a hot-pressed $MoSi_2$ specimen that was 97.5% dense. The value of 497 GPa for M20 falls below the ROM prediction (Fig. 2a), which is likely due to the microcracking observed in this composition. The value of 531 GPa for M5 is ~8 GPa greater than the ROM prediction for a composition with ~2 vol.% retained $MoSi_2$, however, the wide range of reported Young's modulus values for ZrB_2 suggest that this variation may not be unusual. The variation could be due to the effect of Mo in the $(Zr,Mo)B_2$ shell on the elastic properties, although no measurements of the elastic properties of $(Zr,Mo)B_2$ solid solutions have been reported to date. The formation of $(Zr,Mo)B_2$ solid solution may result in less reduction in Young's modulus due to increasing $MoSi_2$ content compared to a simple mixture of ZrB_2 and $MoSi_2$ due to the higher Young's modulus of MoB_2 (499 GPa)[123, 124] compared to $MoSi_2$. The trend of decreasing modulus with increasing

$MoSi_2$ content is in agreement with behavior of ZrB_2-$MoSi_2$ composites previously reported by Guo et al. (490 to 448 GPa, for 10 to 40 vol.% $MoSi_2$) [66], Silvestroni et al. (516 to 489 GPa, for 5 to 20 vol.% $MoSi_2$) [10], and Sciti et al. (489 to 479 GPa, for 15 to 20 vol.% $MoSi_2$) [65]. Young's modulus, shear modulus, and Poisson's ratio are shown Fig. 2 and reported in Table II. Overall, the elastic behavior of the ZrB_2-$MoSi_2$ ceramics followed expected ROM trends based on the component phases and were consistent with previously reported values, indicating that additions of $MoSi_2$ decrease the Young's and shear moduli of ZrB_2 ceramics.

Vickers microhardness decreased from 16.6 GPa for M5 to 15.1 GPa for M30 Table II). Although hardness is usually affected by microcracking, the microcracks in M20 did not appear to affect its hardness significantly. Reported microhardness values of ZrB_2-$MoSi_2$ ceramics in the range of 5 to 30 vol.% $MoSi_2$ additions range from 14.9 to 16.3 GPa [23]. The microhardness of ZrB_2 has a reported range of 14 to 23 GPa [14, 23, 125], while $MoSi_2$ has a range of 8 to 10 GPa [51, 52, 55] Radial/median cracks outlet from the corners of Vickers indents (not shown) resulted in primarily transgranular fracture with only occasional intergranular behavior and little or no crack deflection when cracks encountered $MoSi_2$ clusters, similar to what has been reported elsewhere [10]. The compositions tested in this study fell within the range of expected values based on a linear rule of mixtures from previously reported values.

At room temperature, all compositions had average fracture toughness values between 2.8 and 3.8 $MPa \cdot m^{½}$ Table II, Fig. 3). Room temperature fracture toughness values of monolithic hot pressed ZrB_2 [14, 62] and $MoSi_2$ [50-52] have been reported to be in the ranges of 3.0 to 4.2 and 2.5 to 4.0 $MPa \cdot m^{½}$, respectively. With the exception of a study by Sciti et al. [60] which reported a slight increase in fracture toughness from 2.0 to 3.3 $MPa \cdot m^{½}$ as $MoSi_2$ content increased from 1 to 9 vol.%, previous studies report toughness values in the range of 2.3 to 4.1 $MPa \cdot m^{½}$ with no overall trend in fracture toughness for $MoSi_2$ contents of 5 to 40 vol.% [10, 62, 65-67]. Roughly constant fracture toughness with respect to $MoSi_2$ content is expected, due to the similar fracture toughness values of the two pure materials, and due to the primarily transgranular fracture behavior observed at room temperature, in which $MoSi_2$ clusters do not serve to deflect cracks.

Room temperature flexure strength was in the range of 620 to 630 MPa for $MoSi_2$ additions of 5 to 10 vol.%. Although microcracking was observed in the $MoSi_2$ phase of M20, this composition had the highest strength at 723 MPa, while M30 had the lowest strength of 557 MPa (Fig. 4). Previous studies have reported flexure strengths between 500 and 720 MPa for ZrB_2-$MoSi_2$ composites in this compositional range [10, 13, 65, 85]. Guo et al. [108] and Chamberlain et al. [62] reported higher strength values, in the ranges of 750 to 800 MPa and 1000 to 1150 MPa, respectively. Guo and Chamberlain both reported room temperature flexure strength to be insensitive to $MoSi_2$ content. The relatively high strength values in those studies are probably due to a combination of smaller specimen size, polished tensile surface of the test bars, and finer grain size. The room temperature strength of the materials measured in the present study does not change with respect to $MoSi_2$ content, in agreement with previously reported studies.

The variation in strength for each composition was ~100 MPa, suggesting a range of critical flaw sizes at room temperature. Using a Griffith type analysis with a Y-parameter of 1.99 (long semi-circular surface flaw) and Eq. 10.1 in Wachtman et al. [43], the critical flaw size was in the range of 2.1 μm to 7.6 μm for M20 Table II), which had the smallest critical flaw size of the four compositions, as well as the smallest maximum ZrB_2 grain size (8.8 μm). The critical flaw size was in the range of 6 to 14 μm for M10, which had the largest calculated critical flaw size, as well as the largest maximum ZrB_2 grain size (9.8 μm). Although the maximum observed $MoSi_2$ cluster size increased from ~6 μm in M5 to ~24 μm in M30, the calculated critical flaw sizes did not appear to correlate with the maximum $MoSi_2$ cluster size, hypothesized based on previously reported behavior for ZrB_2-SiC composites in which large SiC clusters act as the strength-limiting flaw [92, 126]. The calculated flaw sizes for the MX compositions were approximately the maximum sizes of ZrB_2 grains in each composition. Fracture surfaces of ten flexure specimens were observed by SEM and found to be similar to the example shown in Fig. 5, consisting of a string or cluster of closely spaced surface flaws either on the bar's tensile surface, or more rarely at the surface of the chamfer (Fig. 5). SEM analysis indicated that ZrB_2 grain pullout occurred during machining of the test specimens resulting in surface voids which became the strength limiting flaws. Since the flaw size is on the order of the maximum ZrB_2 grain size, the intrinsic strength of the

material, as determined by the microstructure, is being measured. It is unlikely that polishing would result in increased strength of the specimens.

3.3. Toughness and Strength at 1500°C. At 1500°C, the fracture toughness increased from 4.1 MPa·m^{½} for M5 to 5.7 MPa·m^{½} for M30 Table III, Fig. 3). All compositions displayed increased fracture toughness values at 1500°C compared to room temperature. For example, the fracture toughness of M30 increased by more than a factor of two from 2.8 MPa·m^{½} at room temperature to 5.7 MPa·m^{½} at 1500°C. Above its BDTT, which is in the range of 1000°C to 1300°C, $MoSi_2$ was expected to contribute to increased fracture toughness by plastic deformation near the crack tip, relaxing concentrated stresses, and absorbing additional fracture energy. The elevated temperature fracture toughness of monolithic polycrystalline $MoSi_2$ has been found to depend heavily on the content of O and C [55]. Maloy et al. found that the fracture toughness of hot-pressed $MoSi_2$ with 2.8 wt.% oxygen decreased steadily from ~4 MPa·m^{½} at 800°C to ~0.7 MPa·m^{½} at 1400°C, while the fracture toughness of $MoSi_2$ with 2 wt.% C additions increased from 5.5 MPa·m^{½} to ~11.5 MPa·m^{½} over the same temperature range. The increased fracture toughness was determined to be due to elimination of grain boundary SiO_2 and subsequent formation of SiC and $Mo_{\leq 5}Si_3C_{\leq 1}$ phases from reactions of SiO_2 and $MoSi_2$ with C. The increase in fracture toughness from room temperature to 1500°C in ZrB_2-$MoSi_2$ is distinctly different from the decrease in fracture toughness of ZrB_2-SiC with increasing temperature that was reported by Neuman et al. [92] Similarly, ZrB_2-10 vol.% ZrC displayed a decrease in fracture toughness from 4.8 MPa·m^{½} at room temperature to 3.4 MPa·m^{½} at 1400°C [26]. The trend of increasing toughness with increases in $MoSi_2$ content at 1500°C, as well as the increase in toughness from RT to 1500°C, make this a promising system for structural applications at elevated temperatures as it suggests that ZrB_2-$MoSi_2$ ceramics become more damage tolerant at use temperatures near 1500°C. The values reported in the present study are the only elevated-temperature fracture toughness measurements of ZrB_2-$MoSi_2$ ceramics of which the authors are aware.

Flexure strength at 1500°C increased with increasing $MoSi_2$ content from 250 ± 66 MPa for M5 to 415 ± 25 MPa for M20, and 439 ± 35 MPa for M30 (Fig. 6a). The stress-strain behavior of the flexure specimens was dependent upon $MoSi_2$ content

(Fig. 6b). For example, M5 exhibited a nearly linear response, but greater $MoSi_2$ contents increased the overall ductility and caused greater deviation from linear elastic behavior. The crosshead speed was increased from 1 to 3 mm/min for M20 and M30, which resulted in more linear elastic behavior and failure. All compositions displayed lower strengths at 1500°C compared to RT, with M5 retaining ~40% of its strength while M30 retained 80% of its strength. These results demonstrate the improvement in high-temperature flexure strength due to $MoSi_2$ additions over nominally pure ZrB_2, which generally retains 40% or less of its RT flexure strength above 1400˚C in air [24]. The Young's modulus of M5 at 1500°C was measured to be 222 ± 15 GPa, with the remaining compositions excluded due to non-linearity of the stress-strain response. Sciti et al. reported flexure strengths in the range of 333 to 388 MPa at 1500°C in air for hot pressed ZrB_2 ceramics containing $MoSi_2$ additions of 15 to 20 vol.% [65]. This is in good agreement with the present study, suggesting similar failure mechanisms. However, Silvestroni et al. reported strengths of ~500 MPa at 1500°C in air for ZrB_2 ceramics containing 5 and 20 vol.% $MoSi_2$ additions [10]. Silvestroni reported that strength at 1500°C did not vary with $MoSi_2$ content, suggesting a different strength-limiting mechanism from the present study. The values reported by Silvestroni are for pressurelessly-sintered ZrB_2-$MoSi_2$ ceramics sintered at 1850°C for 1 h, having a grain size of 2.5 μm. Although the retained $MoSi_2$ contents after hot pressing are not reported, both composites were reported to contain $(Zr,Mo)B_2$ solid solution, indicating partial decomposition of $MoSi_2$. The effects of holding time at the maximum densification temperature, and the final content of shell solid solution, on the high-temperature strength of ZrB_2-$MoSi_2$ ceramics have not been systematically investigated but could be a factor that affects retained strength at elevated temperatures. ZrB_2-$MoSi_2$ ceramics in the literature, with similar processing history to those in the present study, exhibit similar strength values at 1500°C. However, the effect of densification method and dwell at maximum temperature requires further investigation.

Calculated critical flaw sizes at 1500°C Table III) are an order of magnitude larger than those at RT, suggesting a change in the critical flaw population between room temperature and 1500°C. Although non-linear behavior was observed, linear elastic behavior was assumed for critical flaw size calculations. Measured standard deviation of

strength was ~70% less at 1500°C compared to room temperature, indicating a narrower critical flaw size distribution. Unfortunately, fracture surface features were obliterated by oxidation following fracture at the test temperature, making post-test fractographic analysis impossible.

Previous research has demonstrated that oxidation induced surface damage is the strength limiting flaw at elevated temperatures in air for other ZrB_2 based ceramics [92]. Morphology of the oxide scale on the surfaces of bars tested at 1500°C was investigated to identify the strength-limiting flaws in the composites at that temperature. Two main oxidation modes were identified during SEM-EDS analysis of polished cross sections: (1) unprotective oxidation, which lacks a glassy borosilicate outer layer; and (2) protective oxidation, in which a continuous borosilicate glassy layer is formed (identified by EDS analysis). Unprotective oxidation, exemplified by M5 (Fig. 7a), consists of a thick layer of porous ZrO_2 with traces of MoB in contact with the underlying bulk ceramic.

Protective oxidation was observed for M20 and M30 (Fig. 7c and 7d, respectively) and is characterized by the presence of three layers whose thicknesses varied with composition: (1) an outer borosilicate glassy layer; (2) a porous ZrO_2 layer containing SiO_2 and traces of MoB; and (3) an inner exfoliated $MoSi_2$ depleted layer containing SiO_2 and traces of MoB. Fig. 8a schematically illustrates the observed oxidation layers (not to scale), while Fig. 8b shows the average oxide layer thicknesses for each composition. At 1500°C, layer (1) consisted of borosilicate glass generated by the oxidation of $MoSi_2$ and ZrB_2; layer (2) formed primarily from the oxidation of ZrB_2; while layer (3) formed through preferential oxidation of $MoSi_2$ into SiO_2 and gaseous MoO_3. In M5, the ~2 vol.% of $MoSi_2$ retained after hot pressing was insufficient to generate a protective borosilicate outer layer, leading to the formation of a porous zirconia layer ~120 μm thick with no $MoSi_2$ depleted region. The oxidized surface was found to contain mainly monoclinic ZrO_2 and a smaller amount of tetragonal ZrO_2. M10 exhibited a combination of protective and unprotective oxidation modes. The result was a discontinuous borosilicate outer layer and, in localized regions, round pits of porous zirconia having an average depth of ~45 μm. A further result of the round pits was an extension of the $MoSi_2$ depleted region beneath them (Fig. 7b), which gave the oxidized specimens a spotted surface appearance. Bursting of bubbles in the borosilicate glassy

layer due to subsurface formation of volatile species (e.g. MoO_3 and B_2O_3) is a possible mechanism of formation of these pits. In M20 the borosilicate protective layer was nearly continuous, with a few isolated zirconia pits which minimally affected the depth of the $MoSi_2$-depleted region. M20 formed a nearly continuous protective borosilicate layer, with few ZrO_2 pits of less than 35 μm in depth (approximately one ZrO_2 pit was observed per 4.7 cm^2 of oxidized surface area, or on average ~1.3 pits on each bar). M30 formed a continuous borosilicate layer about 5 μm thick with no pitting, a discontinuous layer of porous zirconia of similar thickness, and a $MoSi_2$ depleted region of about 30 μm. The increase in elevated temperature strength with an increase in $MoSi_2$ addition from 15 to 20 vol.% that was reported by Sciti et al., corresponds with the decrease in oxidation damage that was observed in the range of 10 to 20 vol.% $MoSi_2$ additions, although retained $MoSi_2$ contents were not reported in that study [65]. In the present study, the ~8.7 vol.% retained $MoSi_2$ in M10 was found to be insufficient to form a protective layer, but the ~16 vol.% retained $MoSi_2$ in M20 was nearly sufficient to form a continuous protective layer. Formation of a protective oxide layer is beneficial to strength retention at 1500°C, with >16 vol.% retained $MoSi_2$ necessary to form a protective borosilicate layer.

Griffith-type analysis was used to calculate the critical flaw size for the ceramics tested at 1500°C. The calculated critical flaw size range for M10 was 44 to 64 μm at 1500°C (Y=1.99). Zirconia pits at the surface of M10 extended through the total depth of the oxidation-damaged zone, up to ~70 μm beneath the outer surface of the oxide scale, extending 30 to 35 μm into the parent material. Therefore, it is suggested that the intrusion of the porous zirconia scale into the parent ZrB_2-$MoSi_2$, as pitting, is the strength limiting flaw in M10 tested at 1500°C. The calculated critical flaw size ranges were 34 to 53 μm for M20 and 30 to 63 μm for M30 (Y=1.99), similar to the range of flaw sizes calculated for M10. The depth of exfoliation in the $MoSi_2$-depleted layer was variable across the surface of individual specimens, and it is therefore expected that the porous zirconia pits or exfoliated $MoSi_2$ depleted layer act as the strength limiting flaw(s) in ZM20 at 1500°C, while variation in exfoliation depth of the $MoSi_2$-depleted layer is the strength limiting flaw for M30. The increase in flexure strength at 1500°C with increasing $MoSi_2$ content is due to the increased oxidation resistance and increased

fracture toughness. The plateau in strength from 20 to 30 vol.% $MoSi_2$ additions corresponds to a change in oxidation behavior from non-uniform oxide scale formation (5 to 20 vol.% $MoSi_2$) to uniform borosilicate glass scale formation.

4. SUMMARY

ZrB_2 ceramics with 5, 10, 20, and 30 vol.% nominal additions of $MoSi_2$ were densified by hot pressing at temperatures between 1775 and 1900°C for between 25 and 36 min. In all cases, the final ceramics retained less than the nominal $MoSi_2$ content due to decomposition of $MoSi_2$ at elevated temperature. Microstructures of all composites contained $(Zr,Mo)B_2$ solid solution forming a shell structure surrounding the cores of diboride grains. Average ZrB_2 grain size decreased from 2.8 to 2.0 μm as nominal $MoSi_2$ content increased from 5 to 30 vol.%, but maximum ZrB_2 grain size was ~9 μm for all compositions. The average $MoSi_2$ cluster size was approximately 2 μm for all compositions, but the maximum $MoSi_2$ cluster size increased from 6.2 to 24 μm as nominal $MoSi_2$ content increased from 5 to 30 vol.%.

Elastic behavior of ZrB_2-$MoSi_2$ ceramics followed expected ROM trends based on the component phases and were consistent with previously reported values, indicating that additions of $MoSi_2$ from 5 to 30 vol.% decrease the Young's modulus (531 to 494 GPa) and shear modulus (236 to 220 GPa) and increase the Poisson's ratio (0.134 to 0.142) of ZrB_2-based ceramics. Room temperature fracture toughness (2.8 to 3.8 $MPa \cdot m^{½}$) and flexure strength (557 to 723 MPa) do not trend with $MoSi_2$ content. Surface grain pull-out of ZrB_2 grains during machining was the strength-limiting flaw for ZrB_2-$MoSi_2$ ceramics at room temperature, with the critical flaw size correlating with the maximum ZrB_2 grain size. Use of finer ZrB_2 starting powders is expected to increase room temperature strength.

Both strength and fracture toughness at 1500°C of ZrB_2-$MoSi_2$ ceramics increased with increasing $MoSi_2$ content, and compositions with 20 and 30 vol.% $MoSi_2$ additions displayed ductility at 1500°C. All compositions had higher fracture toughness at 1500°C than at room temperature, and displayed an increase in fracture toughness from 4.1 to 5.7 $MPa \cdot m^{½}$ at 1500°C with increasing $MoSi_2$ content. This was attributed to increased plastic deformation near the crack tip, though further study is needed to prove this hypothesis. The trend of increasing toughness with increasing $MoSi_2$ content at

1500°C, as well as the increase in toughness from RT to 1500°C, make this a promising system for structural applications at elevated temperatures as it suggests that these ceramics become more damage tolerant at use temperatures near 1500°C. Flexure strength at 1500°C increased from 250 to 439 MPa with increasing $MoSi_2$ content due to enhanced protection from oxidation by a borosilicate glassy layer and an increase in fracture toughness due to the ductile nature of $MoSi_2$ at high temperature. The formation of a protective oxide layer was critical to retention of flexure strength at 1500°C, and at least 16 vol.% retained $MoSi_2$ was necessary to form a protective borosilicate layer. The shift in trend from increasing flexure strength from 5 to 20 vol.% $MoSi_2$ additions to a plateau near 415 to 439 MPa from 20 to 30 vol.% $MoSi_2$ additions corresponds to a change in surface oxidation behavior from unprotected to protected oxidation.

ACKNOWLEDGEMENTS

The authors would like to thank Dr. Laura Silvestroni for assistance with electron microscopy and specimen preparation, Cesare Melandri for assistance with mechanical testing and optical microscopy, Andrea D'Angio for collaboration and assistance, and Dr. Jeremy Watts and Dr. Diletta Sciti for their advice and assistance throughout the project.

FUNDING

This work was supported by the United States National Science Foundation's Materials World Network through grant DMR-1209262, and funding from National Research Council of Italy for the project, "Dual Composite Ceramics for Improved Properties."

REFERENCES

1. W. G. Fahrenholtz, G. E. Hilmas, I. G. Talmy, and J. A. Zaykoski, "Refractory Diborides of Zirconium and Hafnium," *Journal of the American Ceramic Society*, 90[5] 1347-64 (2007).

2. W. G. Fahrenholtz, E. J. Wuchina, W. E. Lee, and Y. Zhou, "Ultra-High Temperature Ceramics: Materials for Extreme Environment Applications." Wiley, (2014).

3. L. Silvestroni and D. Sciti, "Effects of $MoSi_2$ additions on the properties of Hf– and Zr–B_2 composites produced by pressureless sintering," *Scripta Materialia*, 57[2] 165-68 (2007).

4. E. W. Neuman, G. E. Hilmas, and W. G. Fahrenholtz, "Ultra-High Temperature Mechanical Properties of a Zirconium Diboride-Zirconium Carbide Ceramic," *Journal of the American Ceramic Society* 1-7 (2015).

5. E. W. Neuman, G. E. Hilmas, and W. G. Fahrenholtz, "Strength of Zirconium Diboride to 2300°C," *Journal of the American Ceramic Society,* 96[1] 47-50 (2013).

6. G. J. K. Harrington, G. E. Hilmas, and W. G. Fahrenholtz, "Effect of carbon on the thermal and electrical transport properties of zirconium diboride," *Journal of the European Ceramic Society,* 35[3] 887-96 (2015).

7. J. M. Lonergan, W. G. Fahrenholtz, G. E. Hilmas, and R. Trice, "Zirconium Diboride with High Thermal Conductivity," *Journal of the American Ceramic Society,* 97[6] 1689-91 (2014).

8. M. Brach, V. Medri, and A. Bellosi, "Corrosion of pressureless sintered ZrB_2–$MoSi_2$ composite in H_2SO_4 aqueous solution," *Journal of the European Ceramic Society,* 27[2-3] 1357-60 (2007).

9. V. O. Lavrenko, V. A. Shvets, V. M. Talash, V. A. Kotenko, and T. V. Khomko, "Electrochemical Oxidation of ZrB_2-$MoSi_2$ Ceramics in a 3% NaCl Solution," *Powder Metallurgy and Metal Ceramics,* 50[11-12] 749-52 (2011).

10. M. M. Opeka, I. G. Talmy, and J. A. Zaykoski, "Oxidation-based materials selection for 2000°C + hypersonic aerosurfaces: Theoretical considerations and historical experience," *Journal of Materials Science,* 39 5887-904 (2004).

11. L. Mercatelli, E. Sani, D. Jafrancesco, P. Sansoni, D. Fontani, M. Meucci, S. Coraggia, L. Marconi, J. L. Sans, E. Beche, L. Silvestroni, and D. Sciti, "Ultra-refractory Diboride Ceramics for Solar Plant Receivers," *Energy Procedia,* 49 468-77 (2014).

12. E. Randich and D. D. Allred, "Chemically Vapor-Deposited ZrB_2 as a Selective Solar Absorber," *Thin Solid Films,* 83 393-98 (1981).

13. D. Sciti, L. Silvestroni, L. Mercatelli, J.-L. Sans, and E. Sani, "Suitability of ultra-refractory diboride ceramics as absorbers for solar energy applications," *Solar Energy Materials and Solar Cells,* 109 8-16 (2013).

14. N. Fuhrman and W. J. Bryan, "Element with Burnable Poison Coating," U.S. Patent Number US4824634 A (1987).

15. S. Guo, T. Mizuguchi, M. Ikegami, and Y. Kagawa, "Oxidation behavior of ZrB_2–$MoSi_2$–SiC composites in air at 1500°C," *Ceramics International,* 37[2] 585-91 (2011).

16. W. G. Fahrenholtz, "Thermodynamic Analysis of ZrB_2-SiC Oxidation: Formation of a SiC-Depleted Region," *Journal of the American Ceramic Society,* 90[1] 143-48 (2007).

17. D. Sciti, L. Silvestroni, and M. Nygren, "Spark plasma sintering of Zr- and Hf-borides with decreasing amounts of $MoSi_2$ as sintering aid," *Journal of the European Ceramic Society,* 28[6] 1287-96 (2008).

18. L. Silvestroni, H.-J. Kleebe, S. Lauterbach, and M. Muller, "Transmission electron microscopy on Zr- and Hf-borides with $MoSi_2$ addition: Densification mechanisms," *Journal of Materials Research,* 25[5] 6 (2010).

19. A. L. Chamberlain, W. G. Fahreholtz, and Hilmas, "Characterization of Zirconium Diboride-Molybdenum Disilicide Ceramics," *Ceramic Transactions,* 153 299-398 (2003).

20. V. O. Lavrenko, A. D. Panasyuk, O. M. Grigorev, O. V. Koroteev, and V. A. Kotenko, "High-Temperature (to 1600°C) Oxidation of ZrB_2-$MoSi_2$ Ceramics in Air," *Powder Metallurgy and Metal Ceramics,* 51[1-2] 102-07 (2012).

21. D. Sciti, M. Brach, and A. Bellosi, "Long-term oxidation behavior and mechanical strength degradation of a pressurelessly sintered ZrB_2–$MoSi_2$ ceramic," *Scripta Materialia,* 53[11] 1297-302 (2005).

22. S. R. Srinivasan, R. B. Schwarz, and J. D. Embury, "Ductile-To-Brittle Transition in $MoSi_2$,″ pp. 1099-104 in High-Temperature Ordered Intermetallic Alloys V. Vol. 288Edited by I. Baker, R. Darolia, J. D. Whittenberger, and M. H. Yoo.

23. D. Sciti, F. Monteverde, S. Guicciardi, G. Pezzotti, and A. Bellosi, "Microstructure and mechanical properties of ZrB_2–$MoSi_2$ ceramic composites produced by different sintering techniques," *Materials Science and Engineering: A,* 434[1-2] 303-09 (2006).

24. S. Q. Guo, T. Nishimura, T. Mizuguchi, and Y. Kagawa, "Mechanical properties of hot-pressed ZrB_2-$MoSi_2$-SiC composites," *Journal of the European Ceramic Society,* 28 1891-98 (2008).

25. D. Sciti, S. Guicciardi, A. Bellosi, and G. Pezzotti, "Properties of a Pressureless-Sintered ZrB_2-$MoSi_2$ Ceramic Composite," *Journal of the American Ceramic Society,* 89[7] 2320-22 (2006).

26. A. Bellosi, F. Monteverde, and D. Sciti, "Fast Densification of Ultra-High-Temperature Ceramics by Spark Plasma Sintering," *International Journal of Applied Ceramic Technology,* 3[1] 32-40 (2006).

27. D. Sciti, M. Brach, and A. Bellosi, "Oxidation behavior of a pressureless sintered ZrB_2–$MoSi_2$ ceramic composite," *Journal of Materials Research,* 20[04] 922-30 (2005).

28. S.-Q. Guo, T. Mizuguchi, T. Aoyagi, T. Kimura, and Y. Kagawa, "Quantitative Electron Microprobe Characterizations of Oxidized ZrB_2 Containing $MoSi_2$ Additives," *Oxidation of Metals,* 72[5-6] 335-45 (2009).

29. H. T. Liu, J. Zou, D. W. Ni, J. X. Liu, and G. J. Zhang, "Anisotropy oxidation of textured ZrB_2–$MoSi_2$ ceramics," *Journal of the European Ceramic Society,* 32[12] 3469-76 (2012).

30. R. Mitra, "Silicides: Processing and Mechanical Behavior," pp. 107-65. in Structural Intermetallics and Intermetallic Matrix Composites. CRC Press, 2015.

31. K. T. Venkateswara Rao, W. O. Soboyejo, and R. O. Ritchie, "Ductile-Phase Toughening and Fatigue-Crack Growth in Nb-Reinforced Molybdenum Disilicide Intermetallic Composites," *Metallurgical Transactions A,* 23A 2249-57 (1992).

32. E. W. Neuman, G. E. Hilmas, and W. G. Fahrenholtz, "Mechanical behavior of zirconium diboride–silicon carbide ceramics at elevated temperature in air," *Journal of the European Ceramic Society,* 33[15-16] 2889-99 (2013).

33. D. Sciti, M. Brach, and A. Bellosi, "Oxidation behavior of a pressureless sintered ZrB_2–$MoSi_2$ ceramic composite," *Journal of Materials Research,* 20[4] 922-30 (2005).

34. R. J. Grohsmeyer, G. E. Hilmas, F. T. Monteverde, W. G. Fahrenholtz, A. D'Angio, D. Sciti, and L. Silvestroni, "ZrB_2-$MoSi_2$ Ceramics with Varying $MoSi_2$ Content and ZrB^2 Powder Particle Size: Processing and Microstructure," *Journal of the European Ceramic Society,* TBD[TBD] TBD (2017a).

35. R. G. Munro, "Material Properties of a Sintered α-SiC," *Journal of Physical Chemistry Reference Data,* 26[5] 9 (1997).

36. Y. S. Touloukian, R. K. Kirby, E. R. Taylor, and T. Y. R Lee, "Thermophysical Properties of Matter, Thermal Expansion - Nonmetallic Solids," pp. 1786 Vol. 13. Thermophysical and Electronic Properties Information Analysis Center: Purdue University, Lafayette IN, USA, (1977).

37. F. T. Monteverde, "The addition of SiC particles into a $MoSi_2$-doped ZrB_2 matrix: Effects on densification, microstructure and thermo-physical properties," *Materials Chemistry and Physics,* 113[2-3] 626-33 (2009).

38. F. Monteverde, A. Bellosi, and L. Scatteia, "Processing and properties of ultra-high temperature ceramics for space applications," *Materials Science and Engineering: A,* 485[1-2] 415-21 (2008).

39. W.-M. Guo, Z.-G. Yang, and G.-J. Zhang, "Microstructural evolution of ZrB_2–$MoSi_2$ composites during heat treatment," *Ceramics International,* 37[7] 2931-35 (2011).

40. N. L. Okamoto, M. Kusakari, K. Tanaka, H. Inui, and S. Otani, "Anisotropic elastic constants and thermal expansivities in monocrystal CrB_2, TiB_2, and ZrB_2," *Acta Materialia,* 58[1] 76-84 (2010).

41. I. R. Shein and A. L. Ivanovskii, "Elastic properties of mono- and polycrystalline hexagonal AlB_2-like diborides of s, p and d metals from first-principles calculations," *Journal of Physics: Condensed Matter,* 20[41] 415218 (2008).

42. P. K. Yadawa, S. K. Verma, G. Mishra, and R. R. Yadav, "Effect of Elastic Constants on the Ultrasonic Properties of Group VIB Transition Metal Diborides," *Journal of Nanotechnology & Advanced Materials,* 2[1] 1-9 (2014).

43. W. G. Fahrenholtz, G. E. Hilmas, S. Zhang, and S. Zhu, "Pressureless Sintering of Zirconium Diboride: Particle Size and Additive Effects," *Journal of the American Ceramic Society,* 91[5] 1398-404 (2008).

44. E. J. L. Y.-L. Jeng, "Review Processing of molybdenum disilicide," *Journal of Materials Science,* 29 2557-71 (1994).

45. J. J. Petrovic, "Toughening strategies for $MoSi_2$-based high temperaure structural silicides," *Intermetallics*, 8 1175-82 (2000).

46. S. Maloy, A. H. Heuer, J. Lewendowski, and J. Petrovic, "Carbon Additions to Molybdenum Disilicide: Improved High-Temperature Mechanical Properties," *Journal of the American Ceramic Society*, 74[10] 2704-06 (1991).

47. H.-T. Liu, W.-W. Wu, J. Zou, D.-W. Ni, Y.-M. Kan, and G.-J. Zhang, "In situ synthesis of ZrB_2–$MoSi_2$ platelet composites: Reactive hot pressing process, microstructure and mechanical properties," *Ceramics International*, 38[6] 4751-60 (2012).

48. S.-Q. Guo, T. Nishimura, T. Mizuguchi, and Y. Kagawa, "Mechanical properties of hot-pressed ZrB_2–$MoSi_2$–SiC composites," *Journal of the European Ceramic Society*, 28[9] 1891-98 (2008).

49. J. B. Wachtman, W. R. Cannon, and M. J. Matthewson, "Mechanical Properties of Ceramics,*"* pp. 479 2 ed. J. Wiley and Sons, Inc.: Hoboken, NJ, USA, (2009).

50. J. L. Watts, G. Hilmas, and W. G. Fahrenholtz, "Mechanical Characterization of ZrB_2-SiC Composites with Varying SiC Particle Sizes," *Journal of the American Ceramic Society*, 94[12] 4410-18 (2011).

51. E. W. Neuman, G. E. Hilmas, and W. G. Fahrenholtz, "Ultra-High Temperature Mechanical Properties of a Zirconium Diboride-Zirconium Carbide Ceramic," *Journal of the American Ceramic Society*, 99[2] 597-603 (2015).

Table I. Summary of Archimedes' bulk density, microstructural relative density, retained $MoSi_2$ content, average ZrB_2 grain size (GS), average ZrB_2 grain major elliptical axis, and cluster size (CS) for ZrB_2-$MoSi_2$ ceramics.

Com-po-sition	Bulk Density (g/cm^3)	Relative Density (%)	Measured $MoSi_2$ (vol.%)	Avg. ZrB_2 GS (μm)	ZrB_2 Major Axis (μm)	ZrB_2 Max. GS (μm)	$MoSi_2$ CS (μm)	$MoSi_2$ Max. CS (μm)
M5	6.05	99.27	2.0 ± 0.8	2.8 ± 1.3	3.5 ± 1.7	9.4	1.9 ± 1.1	6.2
M10	6.04	99.94	8.7 ± 2.0	2.7 ± 1.4	3.4 ± 1.8	9.8	1.9 ± 1.2	8.8
M20	6.13	99.91	16.3 ± 0.7	2.1 ± 1.2	2.7 ± 1.6	8.8	1.8 ± 1.2	11
M30	6.07	99.97	27.4 ± 2.7	2.0 ± 1.2	2.5 ± 1.6	9.0	2.2 ± 1.8	24

Table II. Summary of the mechanical properties of ZrB2-$MoSi_2$ ceramics at room temperature.

Composition	Young's Modulus, Dynamic (GPa)	Young's Modulus, Static (GPa)	Shear Modulus (GPa)	Poisson's Ratio	Vickers Hardness (GPa)	Flexure Strength (MPa)	Fracture Toughness ($MPa \cdot m^{1/2}$)	Calculated Flaw Size (μm)
								Y = 1.99
M5	531 ± 3	510 ± 16	236	0.134	16.6 ± 0.4	619 ± 104	3.0 ± 0.2	3.8 – 9.4
M10	518 ± 5	515 ± 7	229	0.137	16.1 ± 0.4	628 ± 125	3.8 ± 0.1	6.1 – 14
M20	497 ± 3	502 ± 8	220	0.141	16.0 ± 0.4	723 ± 88	2.9 ± 0.6	2.1 – 7.6
M30	494 ± 7	477 ± 27	220	0.142	15.1 ± 0.4	557 ± 111	2.8 ± 0.4	3.4 – 13

Table III. Summary of mechanical properties of hot-pressed ZrB_2-$MoSi_2$ ceramics at 1500°C in air.

Composition	Crosshead Speed (mm/min)	Flexure Strength (MPa)	Fracture Toughness ($MPa \cdot m^{½}$)	Calculated Flaw Size (μm)
				Y = 1.99
M5	1.0	250 ± 66	4.1 ± 0.2	40 - 136
M10	1.0	300 ± 15	4.3 ± 0.2	44 - 64
M20	3.0	415 ± 25	5.4 ± 0.3	34 - 53
M30	3.0	439 ± 35	5.7 ± 0.6	30 - 63

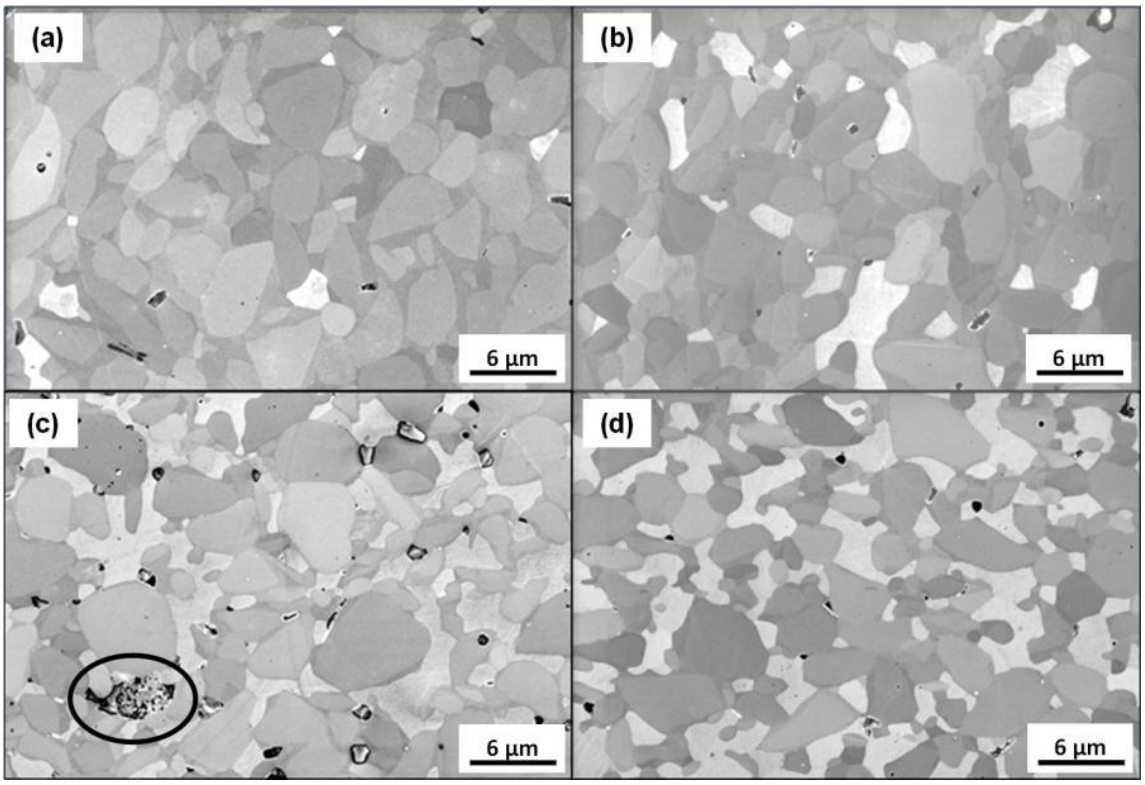

Fig. 1. Secondary electron micrographs of the polished cross-sections of the ZrB_2-$MoSi_2$ ceramics with (a)5, (b)10, (c)20, and (d)30 vol.% $MoSi_2$ additions. The light gray phase is $MoSi_2$, the darker gray phase is ZrB_2, and the black phase is SiO_2. Circled feature in lower left of (c) is SiO_2 (black) with precipitated SiC crystals.

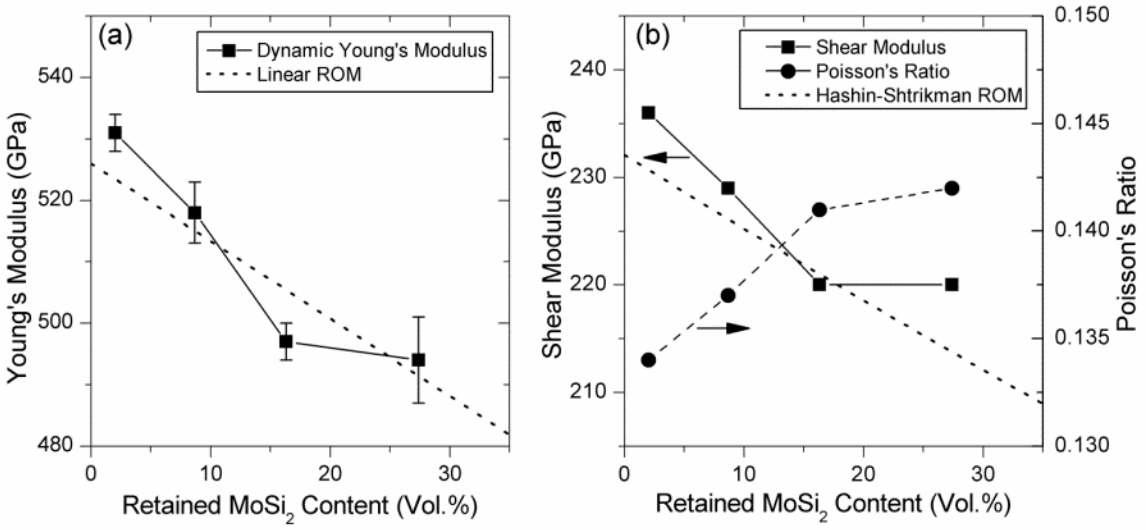

Fig. 2. Elastic moduli as a function retained $MoSi_2$ content measured by dynamic sonic resonance on flat plates and bars. (a) Measured Young's modulus compared with linear ROM from literature; (b) hear modulus and Poisson's ratio showing the average of the upper and lower bounds of the Hashin-Shtrikman model for shear modulus.

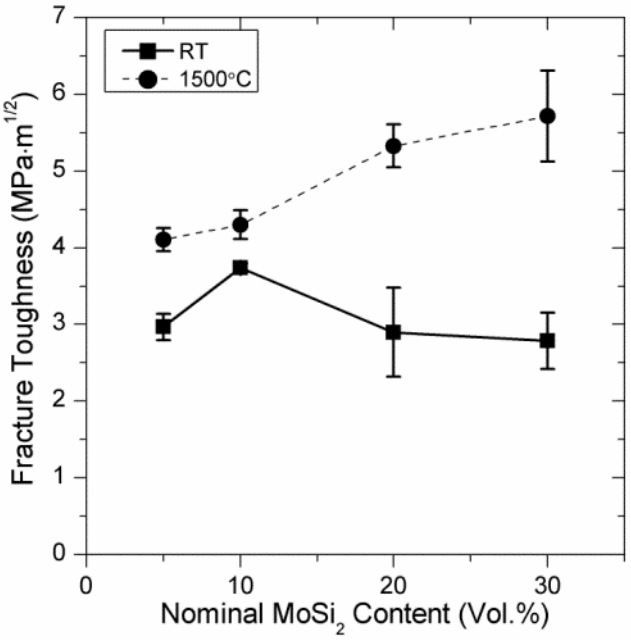

Fig. 3. Fracture toughness as a function of nominal $MoSi_2$ content at room temperature and at 1500°C in air.

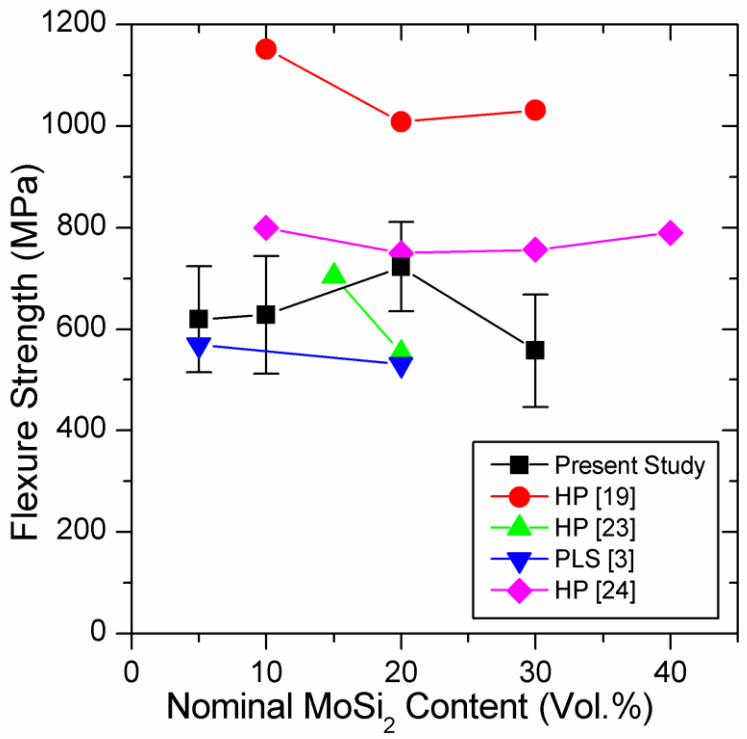

Fig. 4. Room-temperature flexure strength with respect to nominal $MoSi_2$ content for composites. Compares present study with values reported by Chamberlain et al. [62], Sciti et al. [65], Silvestroni et al. [10], and Guo et al. [66].

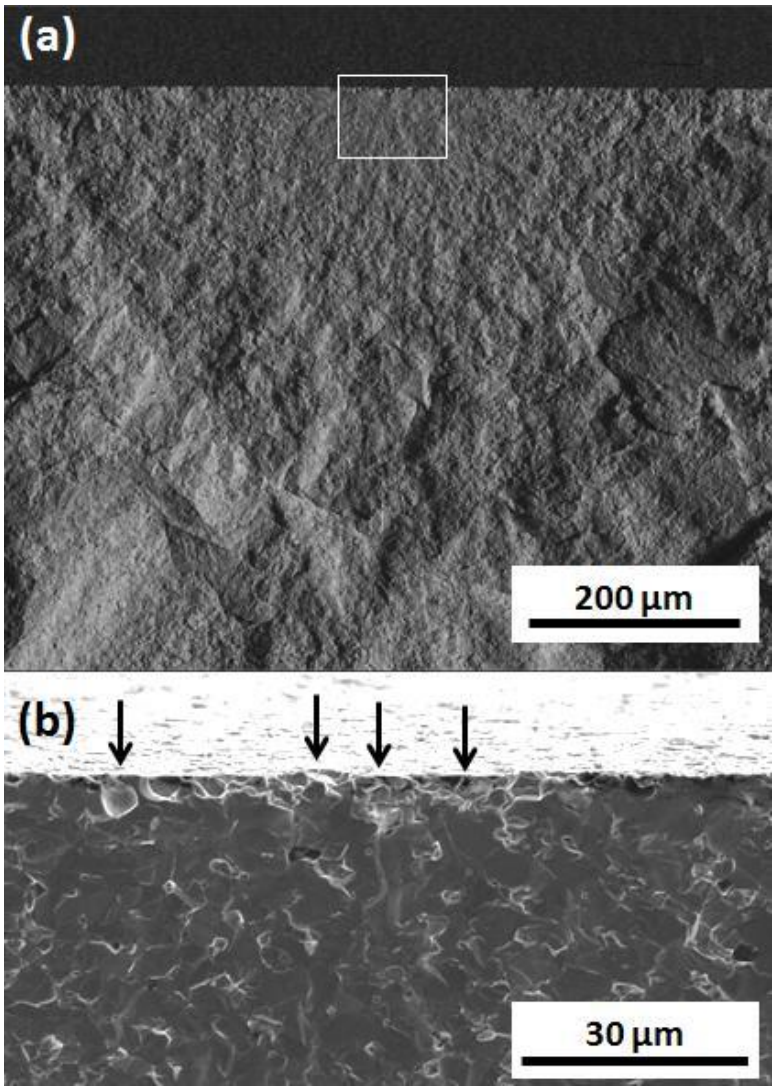

Fig. 5. Back-scattered SEM micrograph of failure origin and surface void. (a) the failure origin at the tensile surface of an M5 flexure specimen, and (b) magnified region showing surface void caused by ZrB_2 grain pull-out.

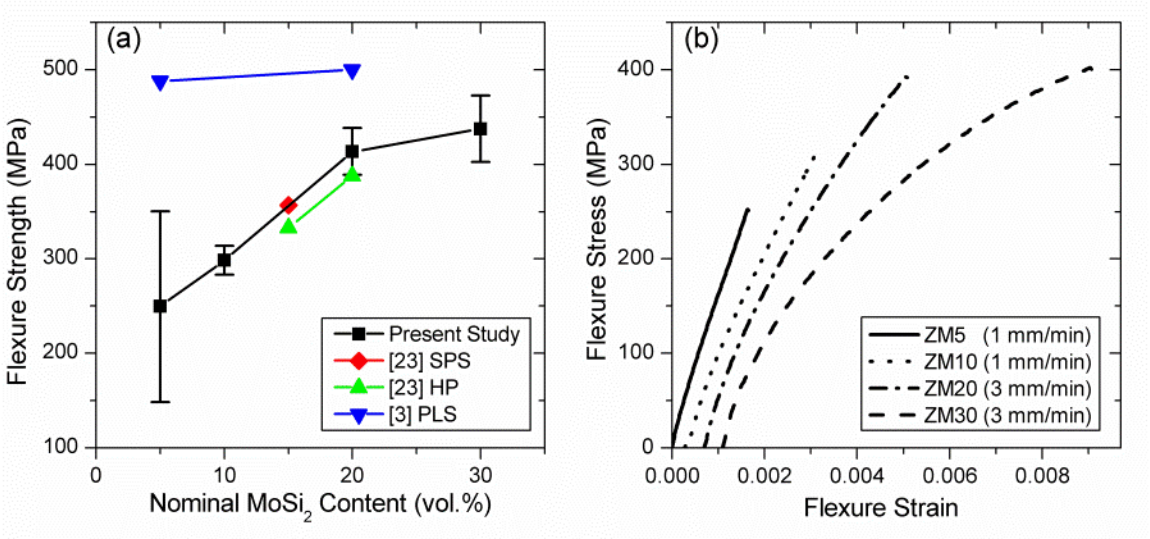

Fig. 6. (a) Flexure strength as a function of nominal $MoSi_2$ content at 1500°C [10, 65], and (b) typical stress-strain curves of specimens tested at 1500°C in air.

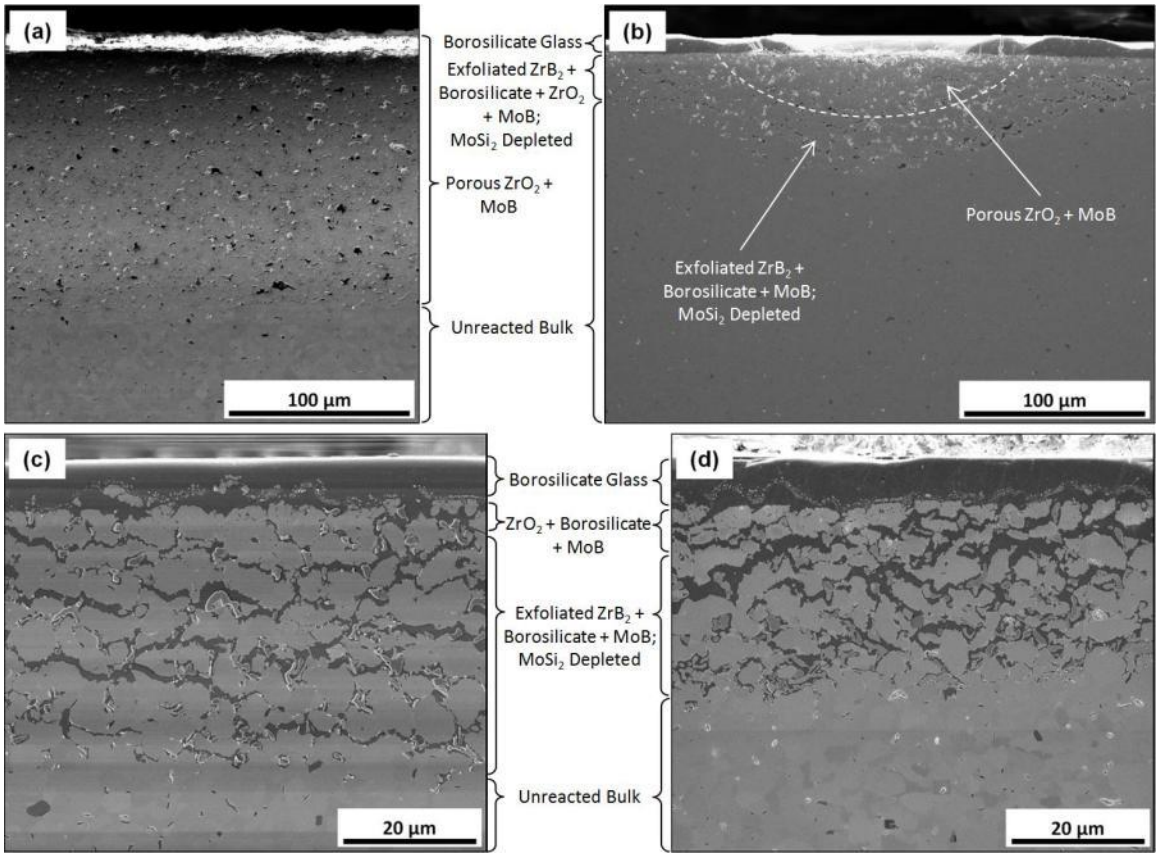

Fig. 7. SEM micrographs of polished cross sections of typical oxidation scale.(a) M5, (b) M10, (c) M20, and (d) M30 following flexure testing at 1500°C in air.

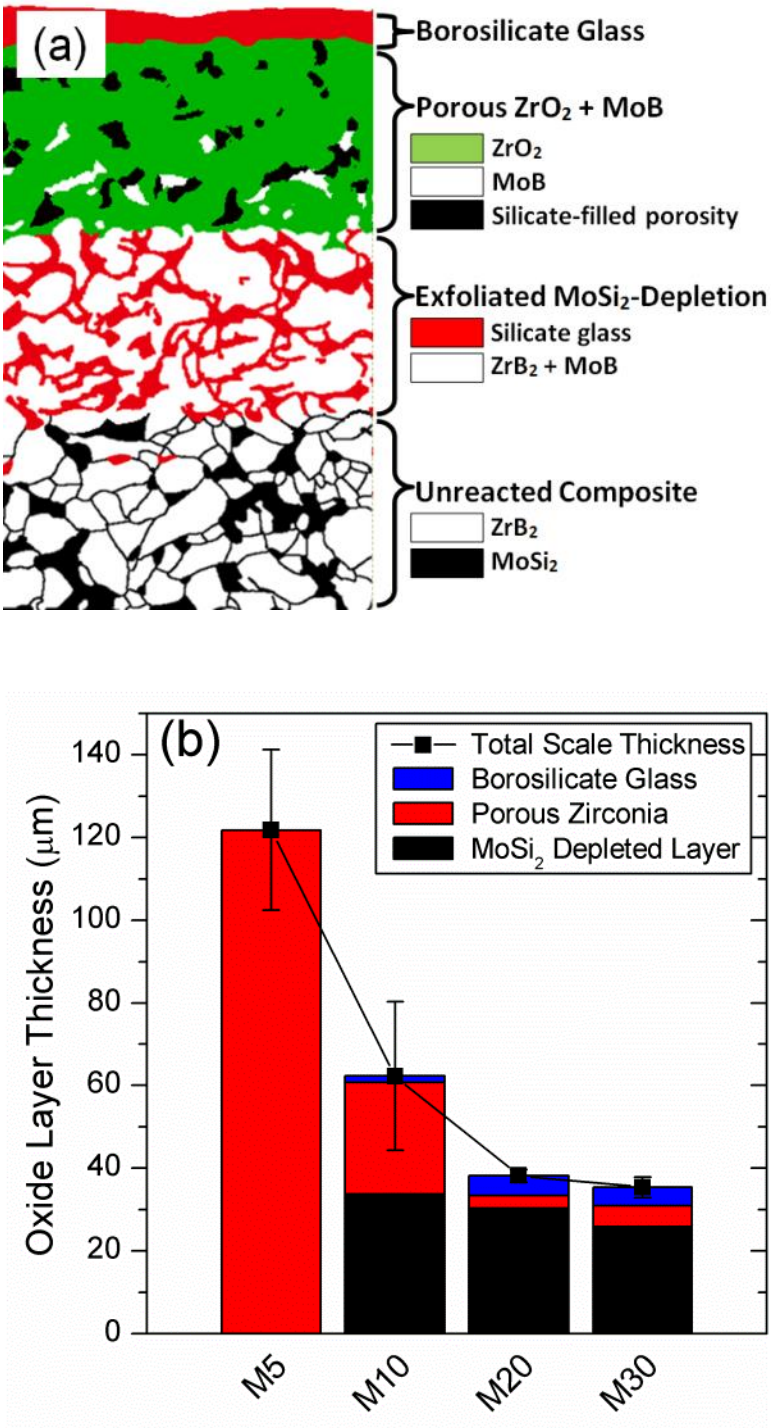

Fig. 8. Oxidation Layers. (a) Schematic, not to scale, illustrating the composition of oxidation layers formed on flexure bars during testing at 1500˚C in air. (b) Plotted thicknesses of oxide layers on individual compositions.

III. DENSIFICATION PROCESSES AND FORMATION OF SOLID SOLUTION SHELL IN ZrB_2-$MoSi_2$ CERAMICS

Ryan J. Grohsmeyer,[a, 6] Gregory E. Hilmas,[a, 7] Frederic Monteverde,[b] William G. Fahrenholtz,[a] Austin D. Stanfield[a]

[a] Materials Science and Engineering Department, Missouri University of Science and Technology, Rolla, MO 65409, USA

[b] National Research Council of Italy, Institute of Science and Technology for Ceramics, Faenza, 48018 RA, Italy

ABSTRACT

Final microstructures of fifteen hot-pressed ZrB_2-$MoSi_2$ ceramics were investigated to provide a wider understanding of densification mechanisms and formation processes of solid solution (SS) shell in ZrB_2-$MoSi_2$ ceramics. Analysis by SEM, TEM, and SAED indicated that each ZrB_2 core and its $(Zr_{1-x}Mo_x)B_2$ SS shell comprised the same monocrystalline grain, while splitting of diboride XRD peaks indicated that the widespread zones of SS shell shared the same dissolved Mo content, that the dissolved Mo is homogeneously distributed within the SS shell, and that the interfaces between the SS shell and ZrB_2 cores are sharp. Estimates of the MoB_2 content in the SS shell via XRD analysis range from 3.1 to 6.3 mol.%. Formation of the SS shell in ZrB_2-$MoSi_2$ ceramics likely occurs via the solid state mechanisms of surface and grain boundary diffusion during sintering of contacting diboride particles, during which Mo is incorporated in diffusion-deposited diboride material at particle-particle necks, assisted by mass transport through a fugitive Si-based liquid. The volume fraction of SS shell in the densified ceramics decreased with increasing $MoSi_2$ content due to the increasing densification gained via $MoSi_2$ plastic deformation and the decreasing amount of densification via ZrB_2 particle-particle sintering.

Key Words: Densification mechanism (A), Borides (D), Solid solution, Core-shell microstructure

---

[6] Present address: Corning, Incorporated, Painted Post, NY, USA.

[7] Corresponding Author: ghilmas@mst.edu, +1-573-341-6102

1. INTRODUCTION

Due to their melting temperatures of up to ~3250˚C [14], strength and rigidity up to 2300°C [10, 24, 100], chemical stability [101, 102], and thermal conductivity up to 130 W/m·K [104] resulting in thermal shock resistance [2, 17], zirconium diboride-based structural ceramics are attractive for use in extreme environments. Although pure zirconium diboride (ZrB_2) exhibits brittle mechanical fracture, and is vulnerable to rapid oxidation at high temperatures [32, 33], it is amenable to combination with other phases to ameliorate the latter characteristics.

Molybdenum disilicide ($MoSi_2$) has been studied as an additive to ZrB_2 for three main reasons. First, it acts as a sintering aid facilitating densification of ZrB_2 by pressureless sintering [10] or hot pressing at lower temperatures than otherwise possible [10, 60, 61]. Second, it forms a glassy borosilicate surface layer that improves the oxidation resistance of ZrB_2 up to ~1650˚C [11, 62-64]. Third, it enhances the ductility of ZrB_2 ceramics above its brittle-to-ductile transition temperature (BDTT) upon heating between 900 and 1300˚C [57]. While several studies have investigated the densification behavior of individual ZrB_2-$MoSi_2$ ceramics [10, 22], a systematic study of the effects of $MoSi_2$ content and ZrB_2 particle size on densification has not been reported. The choice of processing techniques and the resulting microstructures impact both the mechanical properties and oxidation behavior of ZrB_2-$MoSi_2$ ceramics, which is the motivation for a comprehensive study of the chemical processes involved in densification in the ZrB_2-$MoSi_2$ system.

Previous studies have explored the densification behavior of ZrB_2-$MoSi_2$ ceramics in the range of 1750˚C to 2250˚C [23] via pressureless sintering (PLS) [10, 22, 71, 107], hot pressing (HP) [45, 62, 65, 66], reaction hot pressing (RHP) [13], and spark-plasma sintering (SPS) [60, 85]. In some of those studies, authors have reported a core-shell type structure of the ZrB_2 grains whereby a $(Zr_{1-X},Mo_X)B_2$ solid solution shell partially or completely surrounds ZrB_2 grain cores [10, 11, 22, 45, 60, 67]. This shell structure is believed to be a substitutional solid solution (SS) of Mo for Zr on the metallic sites of ZrB_2. Similar core-shell structures have been observed in various diboride ceramics with transition metal (TM) additives. This includes ZrB_2 made with additions of $TaSi_2$ [11, 68, 69] and WSi_2 [11], additions as well as in HfB_2 made with additions of

$MoSi_2$ [10]and $TaSi_2$ [2, 69] additions, and in ZrB_2-SiC with WC added both intentionally[127] and via contamination from milling media wear [70]. Analogous core-shell structures have also been observed and characterized in TiCN-Ni cermets processed with Mo_2C additions [128]. In ZrB_2-$MoSi_2$ ceramics limited decomposition of $MoSi_2$ [110] has been suspected as the source of Mo for formation of the SS shell [10, 22, 121].

Diboride solid solutions have been studied extensively. In the 1960s, Kuzenkova and Kislyi studied pressureless sintering of ZrB_2 with Mo and $MoSi_2$ additions at 2000 to 2250°C. They reported formation of a diboride-based SS, partial vaporization of Si, and formation of a fugitive liquid phase [71, 107]. Reported solubility limits for Mo in ZrB_2 along the ZrB_2-Mo quasibinary vary from ~9 mol.% at 1200°C to ~2 mol.% at 2040°C [7] to ~10 mol.% at >2200°C [71]. Likewise, the 1400°C isothermal section for the Zr-Mo-B ternary shows a solubility limit of <2 mol.% for Mo in ZrB_2 along the ZrB_2-Mo quasibinary section, but a solubility limit of ~26 mol.% for Mo_2B_{5-x} in ZrB_2, emphasizing the importance of the TM:B ratio to solubility [7]. More recently, Guo et al. reported decomposition and migration of $MoSi_2$ in hot pressed ZrB_2 ceramics with 20 vol.% $MoSi_2$ [110]. Yan et al. investigated pressureless sintering of ZrB_2 with 20 wt.% SiC, 4 wt.% Mo, and 2 wt.% phenolic resin and reported formation of a Zr-Mo-B diboride SS after 2 h at 2250°C [6]. Sciti et al. densified ZrB_2 with 1, 3, and 9 vol.% $MoSi_2$ additions by spark plasma sintering between 1700 and 1850°C and reported formation of a $(Zr,Mo)B_2$ SS shell structure in all compositions, partial decomposition of $MoSi_2$ in compositions with 3 and 9 vol.% $MoSi_2$ additions, and complete decomposition of $MoSi_2$ in the composition with a 1 vol.% addition [60]. Monteverde analyzed microstructures of hot-pressed ZrB_2 with 2.3 vol.% $MoSi_2$ and reported a $(Zr,Mo)B_2$ SS shell structure [113]. In that study and others [10, 22, 60], peak splitting was observed in X-ray diffraction (XRD) patterns at >100° 2θ due to differences between the lattice parameters of ZrB_2 grain cores and the $(Zr,Mo)B_2$ SS shells. The peaks for grain cores remained at expected positions for ZrB_2 while the peaks of the SS shells shifted to higher angles. The lattice parameters for the shells were smaller than those of the cores due to the smaller atomic radius of Mo compared to Zr. Monteverde determined lattice parameters of both cores and SS shells as well as residual microstrains for multiple compositions [113]. Although only a minority of diboride papers report this type of core-shell morphology, it

has been observed in a broad range of diboride-based materials with group V and VI TM additives and appears to be a common characteristic of diboride + TM materials. The core-shell morphology has likely gone unreported in many studies due to the specific operating parameters that are necessary to observe the SS shell during scanning electron microscopy (SEM).

Silvestroni et al. proposed the only hypothesis for densification of ZrB_2-$MoSi_2$ ceramics that includes the formation of core-shell structures [10, 22]. The proposed mechanism includes initial reactions of $MoSi_2$ with surface oxide impurities from the starting powders to form MoB, Mo_5Si_3, Mo_5SiB_2, and SiO_2 via equations (1), (2), and (3).

$$2\ MoSi_2 + (5/2)\ O_2 + B_2O_3 \rightarrow 2\ MoB + 4\ SiO_2 \quad (1)$$

$$5\ MoSi_2 + (7/2)\ O_2 \rightarrow Mo_5Si_3 + 7\ SiO_2 \quad (2)$$

$$Mo_5Si_3 + B_2O_3 + (1/2)\ O_2 \rightarrow Mo_5SiB_2 + SiO_2 \quad (3)$$

No SiO_2 was observed in the final microstructures, indicating reaction of SiO_2 present in the starting $MoSi_2$ with carbon from the sintering atmosphere to form SiO(g) and CO(g) via equation (4) during sintering. These gases could then escape through intergranular pores that remained open until the final stage of sintering.

$$SiO_2 + C(g) \rightarrow SiO(g) + CO(g) \quad (4)$$

Silvestroni et al. postulated that a Mo-Si-B-O liquid phase led to the formation of the core-shell morphology. The Mo-Si-B ternary phase diagram contains three ternary eutectics (at 1350, 1802, and 1885°C), supporting the presence of liquid at the sintering temperature [5]. Further, they proposed that the partial dissolution of ZrB_2 into the Mo-Si-B-O liquid is supported by traces of Zr and O identified in the MoB, Mo_5Si_3, and Mo_5SiB_2 phases, and that dissolution of the diboride into the liquid is followed by epitaxial reprecipitation of the $(Zr,Mo)B_2$ SS onto the ZrB_2 grain cores, forming the shell. MoB, Mo_5Si_3, and Mo_5SiB_2 (observed in quantities of 2.7, 1.0, and 1.0 vol.%

respectively in the sintered ceramics) were retained in the final microstructure as solidified remnants of the liquid phase, out of which the $(Zr,Mo)B_2$ SS shell precipitated. Thus, presence of Mo_5Si_3, and Mo_5SiB_2 in their final microstructures served as telltale signs of the liquid-based formation mechanism of the core-shell morphology in ZrB_2-$MoSi_2$ ceramics.

Guo et al. reported decomposition of $MoSi_2$ in ZrB_2-$MoSi_2$ ceramics during post-densification heat treatments according to equation (5) [110]:

$$MoSi_2 \rightarrow Mo + 2\ Si \tag{5}$$

Si is liquid above its melting temperature of 1410°C, and according to the ternary Mo-B-Si phase diagram published by Katrych et al., a ternary eutectic at 1350°C exists at ~2.3 mol.% Mo and ~5.3 mol.% B dissolved in liquid Si [5], while at the sintering temperature used by Silvestroni et al. (1850°C) the solubilities of Mo and B in liquid Si is considerably greater.

However, the pressurelessly sintered microstructures characterized by Silvestroni et al. differed from ZrB_2-$MoSi_2$ densified by HP and SPS, in which SiO_2 is a commonly reported impurity [60, 113, 121, 129], while MoB is rare [65] and Mo_5Si_3, and Mo_5SiB_2 liquid phase remnants have not been reported in the microstructures in the literature. These results suggest differences in the sintering behavior between pressureless sintering and densification processes which include application of pressure for ZrB_2-$MoSi_2$ ceramics. While the materials analyzed by Silvestroni et al. were pressurelessly sintered for 60 min, dwell times for similar materials densified by HP and SPS have in some cases been as brief as 3 to 5 min [60, 113]. In a previous article [121] the authors reported microstructural details of fifteen ZrB_2-$MoSi_2$ ceramics densified by hot pressing, all of which contained both $(Zr,Mo)B_2$ SS shell and SiO_2 impurities in the final microstructure, and none of which contained Mo_5Si_3, and Mo_5SiB_2 liquid phase remnants. Given the apparent conflicts, further investigation is needed to clarify the role of $(Zr,Mo)B_2$ SS shell formation in ZrB_2-$MoSi_2$ ceramics.

The purpose of the present study was to investigate the densification behavior of ZrB_2-$MoSi_2$ ceramics and identify the effect of $(Zr,Mo)B_2$ SS shell formation in the

densification of hot pressed ZrB_2-$MoSi_2$ ceramics. Additional provided insight to the densification process. Processing conditions, and the resulting microstructures, for fifteen ZrB_2-$MoSi_2$ compositions are discussed elsewhere [121].

2. EXPERIMENTAL PROCEDURE

2.1. Processing. ZrB_2-$MoSi_2$ compositions were fabricated in three series according to three grades of commercial ZrB_2 starting powder (all H.C. Starck, Newton, MA, USA) with different median particle sizes and additions of 5 to 70 vol.% $MoSi_2$. All compositions were densified by hot pressing at 30 MPa uniaxial pressure at temperatures between 1750 and 1925°C. Powder particle size, purity, processing, hot pressing procedures, and characterization techniques are reported in previous work [121] and summarized in Table I. Compositions are designated as FX, MX, and CX where F indicates fine, M indicates medium, and C indicates coarse ZrB_2 powder grades, and X is the nominal $MoSi_2$ content in vol.%.

An additional experiment was conducted to determine the effect of Mo on ZrB_2 powder in the absence of Si. The medium particle size ZrB_2 powder plus 7.8 vol.% Mo metal powder (2 to 4 μm particle size, 99.95% metals basis, Cerac Inc., Milwaukee, WI, USA) was ball milled using ZrB_2 milling media and hot pressed at 1925°C for 60 min in flowing Ar under 32 MPa applied uniaxial pressure. The hot pressed powder compact was ground and polished with successively finer diamond slurries to 0.25 μm and examined by SEM. Pulverized samples were examined by powder XRD.

The chemical stability of ZrB_2- $MoSi_2$ ceramic specimens was evaluated with a post-densification heat treatment. Densified specimens were ground to orthorhombic shape and ~1.5 g pieces of C10, C20, C30, C40, C50, and C70 were placed on a graphite setter that was coated with BN spray. Specimens were heated to 1925°C in a graphite resistance furnace (HP50-7010G, Thermal Technologies Inc., Santa Rosa, CA, USA) under flowing Ar and held for 12 h. After furnace cooling, specimens were examined using optical microscopy.

The lattice parameters of ZrB_2 as a function of dissolved MoB_2 content were measured by powder XRD on specially-made samples. The fine particle size ZrB_2 powder (Grade B, H.C. Starck) was mixed with Mo metal powder (2 to 4 μm particle size, 99.95% metals basis, Cerac Inc., Milwaukee, WI, USA) and amorphous B powder

(95.0%, CRS Chemicals, Canoga Park, CA) by ball milling in acetone with ZrB_2 milling media for 24 hours. Pellets ~25 mm in diameter and 4 mm thick were hot pressed at 2150°C in following the procedure used by McClane et al. [37].

2.2. Characterization. Microstructures were examined using SEM (Sigma, Zeiss NTS Gmbh, Germany; Helios Nano Lab 600, FEI, Eindhoven, The Netherlands; or S-4700, Hitachi, Tokyo, Japan), with simultaneous energy dispersive spectroscopy (EDS; INCA Energy 300, Oxford Instruments, Abington, UK, AZtec, Oxford Instruments, Abington, UK), and electron backscatter diffraction (EBSD, Channel 5 software, Oxford Instruments, Abington, UK, with Nordlys detector). Accelerating voltages in the range of 1 to 4 keV, working distances in the range of 2.5 to 5 mm, and a through-the-lens secondary electron detector were used during SEM to image the core-shell structure. Specimens were prepared for microscopy by diamond grinding and polishing with 3.0, 1.0 and 0.25 μm successively finer diamond slurries followed by plasma cleaning (Model 1020 Plasma Cleaner, Fischione Instruments Inc., Export, PA, USA) in Ar-25% O_2 gas mixture shortly before insertion into the microscope chamber. Phase content was determined by areal analysis using manual tracing of phases combined with image analysis software (ImageJ, National Institutes of Health, Bethesda, MD, USA). The microstructure of C10 was further examined using TEM (Tecnai F20, FEI, Eindhoven, The Netherlands) with simultaneous EDS and selected area electron diffraction (SAD). A foil approximately 9 μm by 14 μm was fabricated using the focused ion beam (FIB) lift-out technique with a Ga-ion gun (Helios Nanolab 600) and W nanomanipulator needle (OmniProbe, Oxford Instruments, Abington, UK). Lattice parameter measurements were performed by XRD (D8 Advance, Bruker Co., Billerica, MA, USA or PANalytical X'pert Phillips, Eindhoven, The Netherlands) on polished sections or powdered samples pulverized in a high-purity alumina mortar and pestle to -200 mesh.

3. RESULTS AND DISCUSSION

3.1. Microstructural Analysis. Microstructural images, densification curves, final impurity and phase contents, average, median, and maximum ZrB_2 grain sizes, and average and maximum $MoSi_2$ cluster sizes of the ceramics produced for this study are reported in a previous article [121]. Examples of typical microstructures of F20, M20, and C20 are shown in Figure 1. The image of F20 was captured at 6 keV and WD = 3.8

mm, image of M20 was captured at 2 keV and WD = 2.4 mm, image of C20 was captured 1 keV and WD = 3.1 mm. Positive relief of $MoSi_2$ in F20 is due to polish/etching with colloidal silica for ~30 seconds prior to microscopy.

The densified ceramics contained less $MoSi_2$ than the nominal batch compositions Table I) due to partial or, in the case of C10, complete decomposition of $MoSi_2$ during hot-pressing (Eq. 5) [110, 121]. Complete $MoSi_2$ decomposition in a single 24 cm^3 hot-pressed billet with 10 vol.% $MoSi_2$ additions equates to the evolution of ~2.2 cm^3 of liquid Si and 9.5 g of Mo. Decomposition of $MoSi_2$ supplied Mo for formation of the $(Zr,Mo)B_2$ SS shell [110], which was observed in all compositions. Si was present in the final microstructure as $MoSi_2$, SiO_2, and SiC, but in most cases, volume fractions were less than expected based on the change in $MoSi_2$ content during hot pressing, meaning that some Si was lost from the ceramic during hot pressing. Some of this Si likely reacted with surface oxide impurities and left the system as SiO(g) according to Eqs. 1 through 4. Additional Si exited the powder bed in the liquid state and reacted with the graphite die and graphite foil used for hot pressing. A solidified Si-rich liquid was observed on graphite spacers for most compositions. In cases of decomposition of >~5 vol.% $MoSi_2$, Si was also found on the interior surfaces of the die walls and exterior surfaces of the hot pressing rams, which indicated that some Si-based liquid exited the system while porosity in the powder bed was still open, and that the powder bed should be considered an open system during densification. Subsequent XRD analysis of Si-based phases solidified on die parts after hot pressing indicated the presence of highly textured MoB among the various phases. Hence, not all Mo evolved by $MoSi_2$ decomposition was incorporated into the SS shell.

The ZrB_2 cores were compositionally distinct from the surrounding SS shells with a sharp boundary between them. In addition, the boundaries between cores and SS shells were sharp and distinct from ZrB_2-ZrB_2 grain boundaries. Figure 2 illustrates the relationships among multiple ZrB_2 grain cores, their respective shells, and triple points of ZrB_2 grains in M5 and C10. Each diboride grain contained a ZrB_2 core with its own associated $(Zr,Mo)B_2$ SS shell, which could be identified by proximity and morphology. Each core and corresponding shell also shared a contrast relationship whereby dark cores had dark shells and light cores had light shells. Contrast between different ZrB_2 grains in

SEM images on polished surfaces was due to electron tunneling differences due to differing crystallographic orientations, while contrast between a core and its associated shell was due to the difference in Mo content. The SS shells were most often observed on one or both sides of ZrB_2-ZrB_2 grain boundaries. In some cases, ZrB_2 grain cores were in direct contact with other cores at one or more points, with SS shell filling the gaps. In some cases ZrB_2 grain cores were directly in contact with adjacent $MoSi_2$ grains, while in others the SS shell was on the ZrB_2 side of the boundary between ZrB_2 and $MoSi_2$ grains. The thickness of SS shells was inconsistent and rarely completely surrounded ZrB_2 grain cores, suggesting that crystallographic orientation affects shell formation. In compositions with nominal $MoSi_2$ contents above 30 vol.%, SS shells rarely encircled grains and more often formed connective necks between adjacent ZrB_2 grains that were otherwise separated by other phases, such as $MoSi_2$ and/or SiO_2. In contrast, compositions with nominal $MoSi_2$ contents from 5 to 20 vol.%, especially in MX and FX, more often formed enveloping SS shells around ZrB_2 cores. The shift from connective necks in compositions with high $MoSi_2$ contents to shell-like structures partially surrounding rounded ZrB_2 grain cores in compositions with lower $MoSi_2$ contents hints at the formation mechanism of the SS shells. Figure 3 illustrates the change in morphology and distribution of the SS shell with respect to retained $Mosi_2$ content in selected CX microstructures ranging from 0 to ~66 vol.% retained $MoSi_2$ by showing both the unaltered microstructures, and corresponding images in which the SS shell has been manually highlighted in green.

The volume fraction of SS shell decreased as $MoSi_2$ content increased in all three compositional series Table I, Figs. 3 and 4). For example, in CX the SS shell totaled ~23 vol.% of C10, but only ~3 vol.% of C70. Similarly in FX, the SS shells totaled ~28 vol.% of F5, but only ~6 vol.% of F50. The volume fraction of SS shell also decreased with increasing ZrB_2 starting powder particle size (Fig. 4). For example, the SS shell totaled ~20 vol.% of F20, ~14 vol.% of M20, and ~13 vol.% of C20. These trends are explained in section 3.2.

Compositional characterization of SS shells by EDS in SEM was of limited use because of both the electron beam interaction volume and signal overlap of the Zr and Mo K and L spectral lines [22]. EBSD indicated a random orientation distribution of both

diboride and disilicide grains, but was not able to distinguish between diboride grain cores and the associated SS shells due to crystallographic alignment between the core and shell. Additionally, the difference between the lattice parameters of core and shell was below the resolution of the EBSD system. Thus, EBSD was not able to characterize the morphology of SS shells due to both crystallographic alignment and similarity of lattice parameters between cores and SS shells.

Investigation of C10 by TEM provided information on both composition and crystallographic orientation of grain cores and SS shells (Fig. 5). Interfaces between ZrB_2 grain cores and their associated $(Zr,Mo)B_2$ shells were clearly visible when grains were viewed on a zone axis (for the primary grain in Figs. 5a and d the zone axis was $[0\bar{1}\bar{1}]$). SAD patterns collected from the core and SS shell showed complete crystallographic alignment, in agreement with EBSD and Silvestroni et al. [22], and indicating that the core and SS shell are, for all practical purposes, a monocrystalline grain (Figs. 5b and c). An EDS line scan was made across a core-shell interface in C10. Although more Mo was detected in the SS shell (0 to 20 at.% with respect to Zr) than was detected in the core (0 to 8 at.% with respect to Zr), quantification was again affected by signal overlap of Zr and Mo spectral lines (Fig. 5e). Si was not detected in this line scan, while O and Ga (from the ion milling procedure) were detected but not included in quantification. Dislocations were visible along, and branching away from, the core-shell interface (primarily into the SS shell), suggesting that plastic strain was concentrated along the interface. High resolution TEM images (HRTEM, not shown) taken in the core and shell further illustrated the similarity of structure and orientation in the lattice fringes in each area. HRTEM imaging of the core-shell interface was attempted but was unsuccessful, because the interface was not visible when the foil was thinned enough to allow resolution of atomic fringes. Silvestroni et al. reported a similar phenomenon in ZrB_2-$MoSi_2$ ceramics, but was able to image lattice fringes and dislocation pile-up at core-shell interfaces in ZrB_2-$TaSi_2$ ceramics [69]. Lenticular features in the core were not investigated. Obvious warping of the foil specimen during final ion beam thinning indicated the presence of residual stresses in C10. Overall, observation by TEM confirmed that a core and its SS shell constitute a single grain, with distinct internal

boundary surfaces created by the sharp transition from the ZrB_2 core to the SS shell with higher Mo content.

The concentration of crystallographic dislocations observed by TEM along the core-shell interface and into the SS shell is likely due to mismatch in coefficient of thermal expansion (CTE) between cores and SS shells. The CTE of MoB_2 between 20 and 600°C has been reported to be ~6.5 x 10^{-6}/K along the *a* axis and ~9.8 x 10^{-6}/K along the *c* axis, while the CTE of ZrB_2 has been reported to be ~7.08 x 10^{-6}/K along the *a* axis and ~6.78 x 10^{-6}/K along the *c* axis (between 20 and 1100°C) [38]. Based on the pure material properties, Mo should increase the CTE of the SS shell compared to the core. Then, during cooling, the CTE mismatch would produce strain that would then be accommodated by dislocation nucleation at the core-shell interface.

Analysis of the hot pressed MX and CX ceramics by XRD provided insight into the SS shell compositions. Peak splitting was observed at angles above 95° 2θ (Fig. 6), similar to previous reports [113]. Locations of the sister peaks indicated that they represented diffraction from a volume of material with the AlB_2-type lattice structure with lattice parameters slightly less than ZrB_2, i.e., the SS shell. Refinement of both sets of peaks allowed calculation of the lattice parameters of both the ZrB_2 grain cores and SS shells. In contrast, peak shifting alone would indicate a homogeneous bulk ceramic composed entirely of a homogenized SS composition with lattice parameters shifted from those of pure ZrB_2. Likewise, peak broadening would indicate a range of lattice parameters produced by a composition gradient. In this case, splitting indicates widespread formation of discrete zones of SS with their own characteristic and consistent lattice parameters. Splitting suggests several things: (a) the many zones of (Zr,Mo)B_2 SS shell visible throughout the microstructure have the same lattice parameters and, it follows, the same dissolved Mo content; (b) the dissolved Mo concentration within the SS shell zones is homogeneous; and (c) interfaces between the SS shells and the ZrB_2 grain cores are sharp, without a composition gradient. Thus, the core-shell morphology probably did not form via a lattice diffusion mechanism such as Mo atoms diffusing into the ZrB_2 grains from grain boundaries, because this process would have resulted in a concentration gradient from the grain boundary to the core, and a diffuse boundary between the core and SS shell.

Differences in unit cell volumes obtained from cores and SS shells of the same diffraction patterns were used to estimate the quantity of Mo in the SS shells for selected compositions using a method based on Vegard's Law [130] Table II). Mo concentrations were calculated assuming metallic-site substitution and 2:1 TM:B stoichiometry, and are expressed as mol.% MoB_2. The authors are not aware of a ZrB_2-MoB_2 phase diagram, but the analogous HfB_2-MoB_2 indicates only partial SS with a maximum solubility of ~70 mol.% MoB_2 in HfB_2 at 2376°C, decreasing to ~50 mol.% at 1800°C [3]. Because Zr and Mo have a greater size difference than Hf and Mo, complete SS seems unlikely in the ZrB_2-MoB_2 binary system. Hence, a linear interpolation of the lattice parameters between ZrB_2 and MoB_2 was not expected to provide an accurate estimate of MoB_2 content in the SS shell. Instead, Mo contents were estimated using a linear interpolation between lattice parameters reported for nominally pure ZrB_2 (a = 3.16814(2) Å and c = 3.52992(5) Å) and the lattice parameters reported for ZrB_2 containing 3 mol.% MoB_2 (a = 3.16334(1) Å and c = 3.52273(4) Å) [37]. Using this method, estimates ranged from 3.1 mol.% MoB_2 for M5 to 6.3 mol.% MoB_2 for C50 Table II). The estimated quantities of MoB_2 in the SS shell did not show any obvious correlation to hot pressing temperature, hot pressing dwell time, final volume fraction of SS shell, nominal $MoSi_2$ content, or volume fraction of $MoSi_2$ decomposed during hot pressing. The lack of trends with MoB_2 content in the SS shells with amount of $MoSi_2$ decomposed suggests that the composition of the shell was not simply a function of the available supply of Mo. Further, the lack of correlation between MoB_2 content in the SS shell and hot pressing temperature suggests that the amount of MoB_2 in the SS shell is not controlled by the equilibrium solubility limit of MoB_2 in ZrB_2. The present study includes the first attempt, of which the authors are aware, to quantify the composition of the SS shell by a means other than EDS or EELS and indicates that the Mo contents of the SS shell were in the range of 3.1 to 6.3 mol.% with respect to Zr.

3.2. Clarification Studies. Mixtures of ZrB_2 and metallic Mo powders were hot pressed to study the formation mechanism of the SS shell. The compact achieved only ~75% relative density, but the $(Zr,Mo)B_2$ SS had already formed connective necks between adjacent ZrB_2 particles at this stage of densification (Fig. 7). Splitting of ZrB_2 peaks was observed by XRD, which is characteristic of the core-shell morphology.

Additional unreacted Mo was also observed by XRD, which suggests that the SS shell may form by diffusion during solid state sintering [131]. Apparently, locally available Mo atoms are transported by either surface diffusion on ZrB_2 particles or vapor transport and then incorporated as $(Zr,Mo)B_2$ SS necks at ZrB_2 particle-particle contact points. In the final microstructures, grain cores are residual ZrB_2 that did not participate in diffusion-based mass transport during sintering. The abrupt interface between the core and SS shell indicates that at 1925°C and below, the growing SS neck/shell does not appear to interact with grain cores, even after hot pressing times of up to 1 hr. If this hypothesis for formation of the SS shell is correct, it allows for direct observation of sintering progress in ZrB_2, using Mo as a traceable marker.

All known ZrB_2-based ceramics with similar core-shell structures were densified at temperatures of 1950°C or lower. In contrast, studies that have reported a homogeneous SS of Mo in ZrB_2 have been processed at temperatures of ≥2100°C [37, 71, 132]. This is consistent with the conclusion of Lonergan et al. that densification of ZrB_2 proceeded by grain boundary diffusion below 2000°C, but lattice diffusion above 2000°C [35]. Again, the developing shells represent material that has been transported during densification. Further, the decrease in SS shell content in the final microstructures as the $MoSi_2$ content increases suggests that as more densification occurs by plastic deformation of $MoSi_2$, less material transport by densification is necessary to achieve full density. This mechanism may also explain the ability of $MoSi_2$ to promote densification of ZrB_2 without significant grain growth since shell growth is uniform, which would minimize the typical mechanism whereby large grains grow by consumption of small grains. This experiment also indicates that plastic deformation of $MoSi_2$ and/or liquid phase formation also help promote densification.

A liquid phase is present during densification of ZrB_2-$MoSi_2$ ceramics even though the $(Zr,Mo)B_2$ SS shell can partially form by solid state processes. The fact that the ZrB_2-Mo powder specimen above achieved only ~75% RD while C10 attained full density under the same hot pressing conditions suggests that presence of the Si-based liquid assists in reaching full density at these temperatures. As discussed above, reaction of ZrB_2 and $MoSi_2$ results in decomposition of $MoSi_2$, evolution of Mo and Si (notionally Reaction 6), and formation of other phases such as SiO_2 and MoB.

$$ZrB_2 + MoSi_2 \rightarrow (Zr_{1-X}Mo_X)B_2 + Zr_X + Mo_{1-X} + 2\ Si\ (l) \quad (6)$$

where x is in the range of 0.02 to 0.05. Even though nominally pure $MoSi_2$ is stable up to its melting temperature of ~2030°C, heat ZrB_2-$MoSi_2$ ceramics to 1925°C after densification showed that $MoSi_2$ spontaneously decomposed in the presence of ZrB_2 at this temperature. After this test, C10 was unaffected because it retained no $MoSi_2$ after hot pressing. In the other five CX compositions, $MoSi_2$ decomposed and liquid Si was exuded from the densified specimens. The flow of Si was partially driven by the change in volume estimated for Reaction (5) to be an increase of ~28 %. Loss of Si was likely also driven by the affinity of liquid Si for graphite [133], which was used for the post-densification heat treatment. During heat treatment, the setter became coated in Si resulting in the formation of internal voids. Although C20, C30, and C40 remained intact with large internal voids, C50 and C70 crumbled upon removal from the graphite setter. Similar decomposition of $MoSi_2$ was not observed after prolonged holds at lower temperatures (e.g., 1500°C used for mechanical testing in the companion study) [42], indicating that $MoSi_2$ instability in the presence of ZrB_2 only occurs at temperatures above 1500°C. Decomposition of $MoSi_2$ was observed during hot pressing at temperatures as low as 1750°C in the FX compositions, which further narrows the window for the onset of $MoSi_2$ instability to between 1500°C and 1750°C. These results indicate that ZrB_2-$MoSi_2$ ceramics are not suited for prolonged use at temperatures in excess of 1500°C.

3.3. Densification Process. The main steps in the densification of ZrB_2-$MoSi_2$ ceramics are shown schematically in Figure 8. Initial heating of the mixed powders under vacuum results in volatilization of MoO_3, B_2O_3 and SiO_2 from particle surfaces (Fig. 8a). Volatilization of SiO_2 may include reaction with carbon from the sintering environment by Eq. (4) [22], while B_2O_3 has a high vapor pressure above 1100°C [33]. MoO_3 has a melting temperature of 801°C, but its high vapor pressure results in its rapid evaporation below 1000°C [64, 89]. Greater oxide impurity content in the FX series highlights both the importance of using starting powders with low oxide content and the effectiveness of prolonged isothermal vacuum holds for surface oxide volatilization [111, 112].

Application of uniaxial pressure above the BDTT of $MoSi_2$ causes compaction due to particle rearrangement and plastic deformation of $MoSi_2$, resulting in an increase in relative density that is proportional to the $MoSi_2$ content [121] (Fig. 8b). As temperatures exceed the threshold for Eq. (6) to become favorable, Mo and liquid Si are produced by $MoSi_2$ decomposition. Liquid Si is able to dissolve Zr, Mo, B, C, and O. Subsequent reactions between the Si-based liquid and dissolved species are expected to be at least partially responsible for formation of SiO_2, SiC, ZrO_2, and BN that were observed in the final microstructure. Excess Si-based liquid is the exuded from the powder compact through open porosity where it can react with the graphite die. The Si-based liquid may have been wicked out of the powder bed by the reactive graphite hot pressing die and graphite foil liner. If so, then lack of similar intimate contact with graphite foil during pressureless sintering may explain why Mo_5Si_2 and Mo_5SiB_2 remnants of the Si-based liquid were observed in the pressurelessly sintered ZrB_2-20 vol.% $MoSi_2$ ceramics prepared by Silvestroni et al. [22]. During exfiltration, the Si-based liquid transports dissolved species throughout the structure, providing Mo atoms for formation of the SS shell (Fig. 8e).

As temperature increases toward the final sintering temperature, decomposition of $MoSi_2$ occurs simultaneously with sintering of ZrB_2 particles via grain boundary and surface diffusion, which leads to incorporation of Mo atoms in the growing SS shells (Fig. 8c and 8d). Uneven growth of the SS shells may be due to crystallographic anisotropy. Incorporation of Mo into the developing shells clearly marks ZrB_2 that has been transported during densification (i.e., the $(Zr,Mo)B_2$ shells) in contrast to the remnants of the original, nominally pure ZrB_2 cores. Dissolution of ZrB_2 into the growth medium is driven by surface energy, which results in greater volume fractions of SS shell in the final microstructures for smaller ZrB_2 starting powder particle sizes.

At the maximum dwell temperature, densification continues, most likely by both deformation of the remaining $MoSi_2$ and growth of the Mo-rich SS shell. In compositions with low starting $MoSi_2$ contents (0 to ~30 vol.% $MoSi_2$), plastic deformation of $MoSi_2$ contributes little to densification due to its limited volume fraction. Hence, more pore volume must be filled by sintering of ZrB_2 grains, which results in higher SS shell content in final microstructures of these ceramics. As a consequence, a longer isothermal

hold time and/or higher temperatures were required to reach full density for low $MoSi_2$ additions (e.g., 45 min at 1925°C for C10) compared to compositions with higher $MoSi_2$ contents (e.g., 1 min at 1800°C for C70) [121], producing less SS shell in the latter. ZrB_2 grain cores represent material that did not actively participate in densification processes. In the final stage of sintering, closed pores are filled by diffusion-deposited SS shell, sintered $MoSi_2$, as well as SiO_2, SiC, ZrO_2 and BN (Fig. 8f).

4. SUMMARY

The microstructures of fifteen ZrB_2-$MoSi_2$ ceramics with varying ZrB_2 powder particle sizes and $MoSi_2$ volume fractions were analyzed to provide a more thorough understanding of densification and core-shell formation processes in ZrB_2-$MoSi_2$ ceramics. In general, as the $MoSi_2$ content increased, the distribution of the $(Zr,Mo)B_2$ solid solution (SS) changed from a morphology in which SS shells often nearly encircled ZrB_2 grain cores to a morphology in which SS formed connective necks between adjacent ZrB_2 grain cores that were otherwise separated by secondary phases. TEM revealed dislocation clustering along the sharp core-shell interface possibly due to a CTE mismatch between core and shell during cooling, and SAD confirmed the core and its SS shell to be part of the same diboride grain. The overall volume fraction of SS shell in the densified ceramics decreased with increasing $MoSi_2$ content due to the increasing densification gained via $MoSi_2$ plastic deformation and the decreasing amount of densification via ZrB_2 particle-particle sintering. Splitting of ZrB_2 peaks in high-angle XRD analysis suggested that the many zones of SS shell throughout the microstructure have the same content of dissolved Mo, that the dissolved Mo content is homogeneously distributed within the zones, and that the interfaces between the SS shell and the ZrB_2 grain cores do not consist of broad diffusion gradients. Estimates of the MoB_2 content in the SS shell range from 3.1 to 6.3 mol.%. $MoSi_2$ decomposition results in formation of a fugitive Si-based liquid phase, which transports dissolved Mo, B, Zr, O and C as it exfiltrates the powder compact during densification through a network of open porosity. $MoSi_2$ decomposition is likely to pose problems for future large-scale processing of ZrB_2-$MoSi_2$ ceramics due to the destructive volume increase associated with decomposition of $MoSi_2$ which would limit operating temperatures for ZrB_2-$MoSi_2$ ceramics. The $(Zr,Mo)B_2$ SS shell characteristic of ZrB_2-$MoSi_2$ ceramics likely forms via surface and

grain boundary diffusion during sintering of diboride particles assisted by mass transport through a Si-based liquid, during which Mo is incorporated in diffusion deposition of diboride material in the sintering of ZrB_2 grains.

ACKNOWLEDGEMENTS

The authors would like to thank Andrea D'Angio, Dr. Laura Silvestroni, Dr. Diletta Sciti for assistance with specimen preparation, electron microscopy and conceptual discussion, Daniele Dalle Fabbriche for his assistance with hot pressing, Dr. Eric Bohannan for assistance with XRD, and Dr. Jeremy Watts for his advice and assistance throughout the project.

FUNDING

This project was supported by the United States' National Science Foundation Materials World Network Program through grant DMR-1209262, and by Italy's National Research Council for the project "Dual Composite Ceramics for Improved Properties."

REFERENCES

1. W. G. Fahrenholtz, G. E. Hilmas, I. G. Talmy, and J. A. Zaykoski, "Refractory Diborides of Zirconium and Hafnium," *Journal of the American Ceramic Society*, 90[5] 1347-64 (2007).

2. L. Silvestroni and D. Sciti, "Effects of $MoSi_2$ additions on the properties of Hf– and Zr–B_2 composites produced by pressureless sintering," *Scripta Materialia*, 57[2] 165-68 (2007).

3. E. W. Neuman, G. E. Hilmas, and W. G. Fahrenholtz, "Ultra-High Temperature Mechanical Properties of a Zirconium Diboride-Zirconium Carbide Ceramic," *Journal of the American Ceramic Society* 1-7 (2015).

4. E. W. Neuman, G. E. Hilmas, and W. G. Fahrenholtz, "Strength of Zirconium Diboride to 2300°C," *Journal of the American Ceramic Society*, 96[1] 47-50 (2013).

5. M. Brach, V. Medri, and A. Bellosi, "Corrosion of pressureless sintered ZrB_2–$MoSi_2$ composite in H_2SO_4 aqueous solution," *Journal of the European Ceramic Society*, 27[2-3] 1357-60 (2007).

6. V. A. S. V.O. Lavrenko, V.M. Talash, V.A. Kotenko, T.V.Khomko, "Electrochemical Oxidation of ZrB2-MoSi2 Ceramics in a 3% NaCl Solution," *Powder Metallurgy and Metal Ceramics*, 50[11-12] 749-52 (2011).

7. J. M. Lonergan, W. G. Fahrenholtz, and G. E. Hilmas, "Zirconium Diboride with High Thermal Conductivity," *Journal of the American Ceramic Society*, 97[6] 1689-91 (2014).

8. J. W. Zimmermann, G. E. Hilmas, and W. G. Fahrenholtz, "Thermal shock resistance of ZrB_2 and ZrB_2–30% SiC," *Materials Chemistry and Physics*, 112[1] 140-45 (2008).

9. J. W. Zimmermann, G. E. Hilmas, and W. G. Fahrenholtz, "Thermal Shock Resistance and Fracture Behavior of ZrB_2-Based Fibrous Monolith Ceramics," *Journal of the American Ceramic Society*, 92[1] 161-66 (2009).

10. S. Guo, T. Mizuguchi, M. Ikegami, and Y. Kagawa, "Oxidation behavior of ZrB_2–$MoSi_2$–SiC composites in air at 1500°C," *Ceramics International*, 37[2] 585-91 (2011).

11. W. G. Fahrenholtz, "Thermodynamic Analysis of ZrB_2-SiC Oxidation: Formation of a SiC-Depleted Region," *Journal of the American Ceramic Society*, 90[1] 143-48 (2007).

12. D. Sciti, L. Silvestroni, and M. Nygren, "Spark plasma sintering of Zr- and Hf-borides with decreasing amounts of $MoSi_2$ as sintering aid," *Journal of the European Ceramic Society*, 28[6] 1287-96 (2008).

13. L. Silvestroni, H.-J. Kleebe, S. Lauterbach, and M. Muller, "Transmission electron microscopy on Zr- and Hf-borides with $MoSi_2$ addition: Densification mechanisms," *Journal of Materials Research*, 25[5] 6 (2010).

14. A. L. Chamberlain, W. G. Fahreholtz, and Hilmas, "Characterization of Zirconium Diboride-Molybdenum Disilicide Ceramics," *Ceramic Transactions*, 153 299-398 (2003).

15. V. O. Lavrenko, A. D. Panasyuk, O. M. Grigorev, O. V. Koroteev, and V. A. Kotenko, "High-Temperature (to 1600°C) Oxidation of ZrB_2-$MoSi_2$ Ceramics in Air," *Powder Metallurgy and Metal Ceramics*, 51[1-2] 102-07 (2012).

16. D. Sciti, M. Brach, and A. Bellosi, "Long-term oxidation behavior and mechanical strength degradation of a pressurelessly sintered ZrB_2–$MoSi_2$ ceramic," *Scripta Materialia*, 53[11] 1297-302 (2005).

17. L. Silvestroni, G. Meriggi, and D. Sciti, "Oxidation behavior of ZrB_2 composites doped with various transition metal silicides," *Corrosion Science*, 83 281-91 (2014).

18. S. R. Srinivasan, R. B. Schwarz, and J. D. Embury, "Ductile-To-Brittle Transition in $MoSi_2$," pp. 1099-104 in High-Temperature Ordered Intermetallic Alloys V. Vol. 288Edited by I. Baker, R. Darolia, J. D. Whittenberger, and M. H. Yoo.

19. L. Silvestroni, H.-J. Kleebe, S. Lauterbach, and M. Muller, "Transmission electron microscopy on Zr- and Hf- borides with $MoSi_2$ addition: Densification mechanisms," *Journal of Materials Research*, 25[5] 828-33 (2010).

20. W. G. Fahrenholtz, E. J. Wuchina, W. E. Lee, and Y. Zhou, "Ultra-high Temperature Ceramics: Materials for Extreme Environment Applications." John Wiley & Sons: Hoboken, NJ, USA, (2014).

21. M. A. Kuzenkova and P. S. Kislyi, "Sintering of Alloys of Zriconium Diboride with Molybdenum Disilicide," *Poroshkovaya Metallurgiya*, 9[45] 11-16 (1966).

22. P. S. Kislyi and M. A. Kuzenkova, "Gas-Impermeable Protective Thermocouple Sheaths from Zirconium Boride," *Poroshkovaya Metallurgiya,* 1[25] 32-36 (1965).

23. S. Q. Guo, T. Nishimura, T. Mizuguchi, and Y. Kagawa, "Mechanical properties of hot-pressed ZrB_2-$MoSi_2$-SiC composites," *Journal of the European Ceramic Society,* 28 1891-98 (2008).

24. F. Monteverde, "The addition of SiC particles into a $MoSi_2$-doped ZrB_2 matrix: Effects on densification, microstructure and thermo-physical properties," *Materials Chemistry and Physics,* 113 626-33 (2009).

25. D. Sciti, F. Monteverde, S. Guicciardi, G. Pezzotti, and A. Bellosi, "Microstructure and mechanical properties of ZrB_2–$MoSi_2$ ceramic composites produced by different sintering techniques," *Materials Science and Engineering: A,* 434[1-2] 303-09 (2006).

26. H.-T. Liu, W.-W. Wu, J. Zou, D.-W. Ni, Y.-M. Kan, and G.-J. Zhang, "In situ synthesis of ZrB_2–$MoSi_2$ platelet composites: Reactive hot pressing process, microstructure and mechanical properties," *Ceramics International,* 38[6] 4751-60 (2012).

27. A. Bellosi, F. Monteverde, and D. Sciti, "Fast Densification of Ultra-High-Temperature Ceramics by Spark Plasma Sintering," *International Journal of Applied Ceramic Technology,* 3[1] 32-40 (2006).

28. D. Sciti, S. Guicciardi, A. Bellosi, and G. Pezzotti, "Properties of a Pressureless-Sintered ZrB_2-$MoSi_2$ Ceramic Composite," *Journal of the American Ceramic Society,* 89[7] 2320-22 (2006).

29. I. G. Talmy, J. A. Zaykoski, and M. M. Opeka, "High-Temperature Chemistry and Oxidation of ZrB_2 Ceramics Containing SiC, Si_3N_4, Ta_5Si_3, and $TaSi_2$," *Journal of the American Ceramic Society,* 91[7] 2250-57 (2008).

30. L. Silvestroni and D. Sciti, "Densification of ZrB_2-$TaSi_2$ and HfB_2-$TaSi_2$ Ultra-High-Temperature Ceramic Composites," *Journal of the American Ceramic Society,* 94[6] 1920-30 (2011).

31. D. Sciti, G. Bonnefont, G. Fantozzi, and L. Silvestroni, "Spark plasma sintering of HfB_2 with low additions of silicides of molybdenum and tantalum," *Journal of the European Ceramic Society,* 30[15] 3253-58 (2010).

32. F. T. Monteverde and L. Silvestroni, "Combined Effects of WC and SiC on densification and thermo-mechanical stability of ZrB_2 ceramics," *Materials & Design,* 109[5 November] 396-407 (2016).

33. E. W. Neuman, G. E. Hilmas, and W. G. Fahrenholtz, "Elevated Temperature Strength Enhancement of ZrB_2-30 vol% SiC Ceramics by Postsintering Thermal Annealing," *Journal of the American Ceramic Society,* 99[3] 962-70 (2016).

34. T. Cutard, T. Viatte, G. Feusier, and W. Benoit, "Microstructure and High Temperature mechanical Properties of $TiC_{0.7}N_{0.3}$-Mo_2C-Ni Cermets," *Materials Science and Engineering: A,* 209 218-27 (1996).

35. W.-M. Guo, Z.-G. Yang, and G.-J. Zhang, "Microstructural evolution of ZrB_2–$MoSi_2$ composites during heat treatment," *Ceramics International,* 37[7] 2931-35 (2011).

36. R. J. Grohsmeyer, G. E. Hilmas, F. T. Monteverde, W. G. Fahrenholtz, A. D'Angio, D. Sciti, and L. Silvestroni, "ZrB_2-$MoSi_2$ Ceramics with Varying $MoSi_2$ Content and ZrB^2 Powder Particle Size: Processing and Microstructure," *Journal of the European Ceramic Society,* TBD[TBD] TBD (2017a).

37. P. Rogl, "Boron - Molybdenum - Zirconium," pp. 72-82. in Refrctory Metal Systems: Phase Diagrams, Crystallographic and Thermodynamic Data, Vol. 11E2**.** *Landolt-Bornstein - Group IV Physical Chemistry.* Edited by G. Effenberg and S. Ilyenko. Springer Berlin Heidelberg, Berlin, 2010.

38. Y. Yan, Z. Huang, S. Dong, and D. Jiang, "Pressureless Sintering of High-Density ZrB_2-SiC Ceramic Composites," *Journal of the American Ceramic Society,* 89[11] 3589-92 (2006).

39. F. T. Monteverde, "The addition of SiC particles into a $MoSi_2$-doped ZrB_2 matrix: Effects on densification, microstructure and thermo-physical properties," *Materials Chemistry and Physics,* 113[2-3] 626-33 (2009).

40. S. Katrych, A. Grytsiv, A. Bondar, P. Rogl, T. Velikanova, and M. Bohn, "Structural Materials: Metal-Silicon-Boron On the Melting Behavior of Mo-Si-B Alloys," *Journal of Alloys and Compounds,* 347 94-100 (2002).

41. M. Mallik, S. Pan, and H. Roy, "Fracture Toughness Measurement of Hot Pressed ZrB_2-$MoSi_2$ Composite," *International Journal of Current Engineering and Technology,* 3[5] 1647-52 (2013).

42. Y. S. Touloukian, R. K. Kirby, E. R. Taylor, and T. Y. R. Lee, "Thermophysical Properties of Matter, Thermal Expansion - Nonmetallic Solids,″ pp. 1786 Vol. 13. Thermophysical and Electronic Properties Information Analysis Center: Purdue University, Lafayette, IN, USA, (1977).

43. R. Jenkins and R. L. Snyder, "Introduction to X-Ray Powder Diffractometry,″ pp. 403 Vol. 138. John Wiley and Sons, Inc.: New York, (1996).

44. E. Rudy, "Ternary Phase Equilibria in Transition Metal-Boron-Carbon-Silicon Systems," pp. 585. in Compendium of Phase Diagram Data, Vol. V. Aerojet-General Corporation Technical Report, 1969.

45. D. L. McClane, W. G. Fahrenholtz, G. E. Hilmas, and D. Smith, "Thermal Properties of (Zr, TM)B_2 Solid Solutions with TM = Ta, Mo, Re, V, and Cr," *Journal of the American Ceramic Society,* 98[2] 637-44 (2015).

46. M. N. Rahaman, "Ceramic Processing and Sintering,″ pp. 875 2nd ed. Taylor and Francis Group, LLC: Boca Raton, FL, USA, (2003).

47. J. M. Lonergan, D. L. McClane, W. G. Fahrenholtz, G. E. Hilmas, and R. Orru, "Thermal Properties of Hf-Doped ZrB_2 Ceramics," *Journal of the American Ceramic Society,* 98[9] 2689-91 (2015).

48. J. M. Lonergan, W. G. Fahrenholtz, G. E. Hilmas, and W. Lee, "Sintering Mechanisms and Kinetics for Reaction Hot-Pressed ZrB_2," *Journal of the American Ceramic Society*, 98[8] 2344-51 (2015).

49. T. J. Whalen and A. T. Anderson, "Wetting of SiC, Si_3N_4, and Carbon by Si and Binary Si Alloys," *Journal of the American Ceramic Society*[Sept.-Oct.] 396-99 (1975).

50. R. J. Grohsmeyer, G. E. Hilmas, F. T. Monteverde, W. G. Fahrenholtz, and E. W. Neuman, "ZrB_2-$MoSi_2$ Ceramics with Varying $MoSi_2$ Content and ZrB_2 Powder Particle Size: Mechanical Properties of MX at Room Temperature and 1500°C in Air," *Journal of the European Ceramic Society*, TBD[TBD] TBD-TBD (2017b).

51. D. Sciti, M. Brach, and A. Bellosi, "Oxidation behavior of a pressureless sintered ZrB_2–$MoSi_2$ ceramic composite," *Journal of Materials Research*, 20[04] 922-30 (2005).

52. S. Zhu, W. G. Fahrenholtz, G. E. Hilmas, and S. C. Zhang, "Pressureless sintering of zirconium diboride using boron carbide and carbon additions," *Journal of the American Ceramic Society*, 90[11] 4 (2007).

53. S. C. Zhang, G. E. Hilmas, and W. G. Fahrenholtz, "Pressureless densification of zirconium diboride with boron carbide additions," *Journal of the American Ceramic Society*, 89[5] 7 (2006).

Table I. Summary of ZrB_2 powder characteristics, hot-pressing temperature, final dwell time, final $MoSi_2$ and SS shell contents, and relative density (RD) measured by areal analysis for ZrB_2-$MoSi_2$ ceramics.

Composition	ZrB_2 powder grade d10 - d50 - d90 (vol. avg., µm) specific surface area (m^2/g)	MoSi2 added (vol.%)	Hot-pressing temperature (°C)	Hot-pressing dwell time (minutes)	Measured $MoSi_2$ (vol.%)	$(Zr,Mo)B_2$ Shell SS (vol.%)	Microstructural RD (%)
F5*	"Fine" Grade B 0.64 – 2.85 – 5.22 1.8 m^2/g 1.30 wt.% O, 0.28 wt.% N	5	1850	22	3.1 ± 0.7	27.5 ± 2.8	99.96
F10*		10	1750	25	8.5 ± 1.0	24.9 ± 0.9	99.95
F20*		20	1750	30	17.6 ± 1.7	19.7 ± 1.6	99.97
F30*		30	1750	15	26.6 ± 2.2	N.M.	99.94
F50*		50	1750	13	45.4 ± 3.7	6.7 ± 0.7	99.27
M5	"Medium" Grade A 1.11 – 4.92 – 8.97 0.8 m^2/g 0.49 wt.% O, 0.21 wt.% N	5	1900	29	2.0 ± 0.8	23.2 ± 2.9	99.94
M10		10	1875	26	8.7 ± 2.0	23.2 ± 3.9	99.94
M20		20	1825	25	16.3 ± 0.7	14.4 ± 0.1	99.91
M30		30	1775	36	27.4 ± 2.7	10.0 ± 0.2	99.97
C10	"Coarse" Custom Batch 2.51 - 11.7 - 30.1 0.3 m^2/g 0.16 wt.% O, 0.08 wt.% N	10	1925	60	N.O.	23.4 ± 1.4	99.99
C20		20	1875	26	18.1 ± 2.9	13.0 ± 1.6	99.94
C30		30	1800	48	25.7 ± 0.9	10.2 ± 1.8	99.98
C40		40	1850	62	34.3 ± 2.2	9.2 ± 2.3	99.96
C50		50	1850	60	42.8 ± 3.8	5.2 ± 1.3	99.99
C70		70	1800	11	66.9 ± 3.9	3.4 ± 0.71	99.99

(N.O. = not observed, N.M. = not measured but observed).
* Processed using $MoSi_2$ from Sigma-Aldrich and without isothermal vacuum holds during HP.

Table II. Difference in lattice parameter between core and shell of selected compositions as measured by XRD on polished surfaces, with estimates of Mo content with respect to Zr in the SS shell.

Composition	ZrB_2 core lattice parameters		(Zr,Mo)B_2 SS (shell) lattice parameters		Volume difference (%)	Estimated MoB_2 in shell fitted to [48] (mol%)
	a (Å)	*c* (Å)	*a* (Å)	*c* (Å)		
M5	3.1683(0)	3.5296(2)	3.1649(7)	3.5240(4)	-0.37	3.1
M10	3.1687(2)	3.5300(1)	3.1626(5)	3.5208(0)	-0.64	5.4
M20	3.1678(9)	3.5294(6)	3.1620(1)	3.5216(2)	-0.59	5.0
M30	3.1676(9)	3.5288(9)	3.1640(5)	3.5236(8)	-0.38	3.2
C10	3.1681(0)	3.5293(0)	3.1627(5)	3.5206(7)	-0.58	4.9
C20	3.1678(1)	3.5293(0)	3.1618(9)	3.5223(0)	-0.57	4.8
C40	3.1678(3)	3.5293(2)	3.1615(5)	3.5231(6)	-0.57	4.8
C50	3.1678(8)	3.5293(7)	3.1613(4)	3.5175(3)	-0.75	6.3
C70	3.1668(2)	3.5272(0)	3.1636(4)	3.5204(6)	-0.39	3.3
S35	-	-	3.1295(8)	3.4656(6)	-4.19	35.0
S45	-	-	3.1162(5)	3.4532(5)	-5.35	45.0
ZrB_2 [48]	3.16814(2)	3.52992(5)	-	-	0	0
$(Zr_{0.97},Mo_{0.03})B_2$ [48]	-	-	3.16334(1)	3.52273(4)	-0.51	3

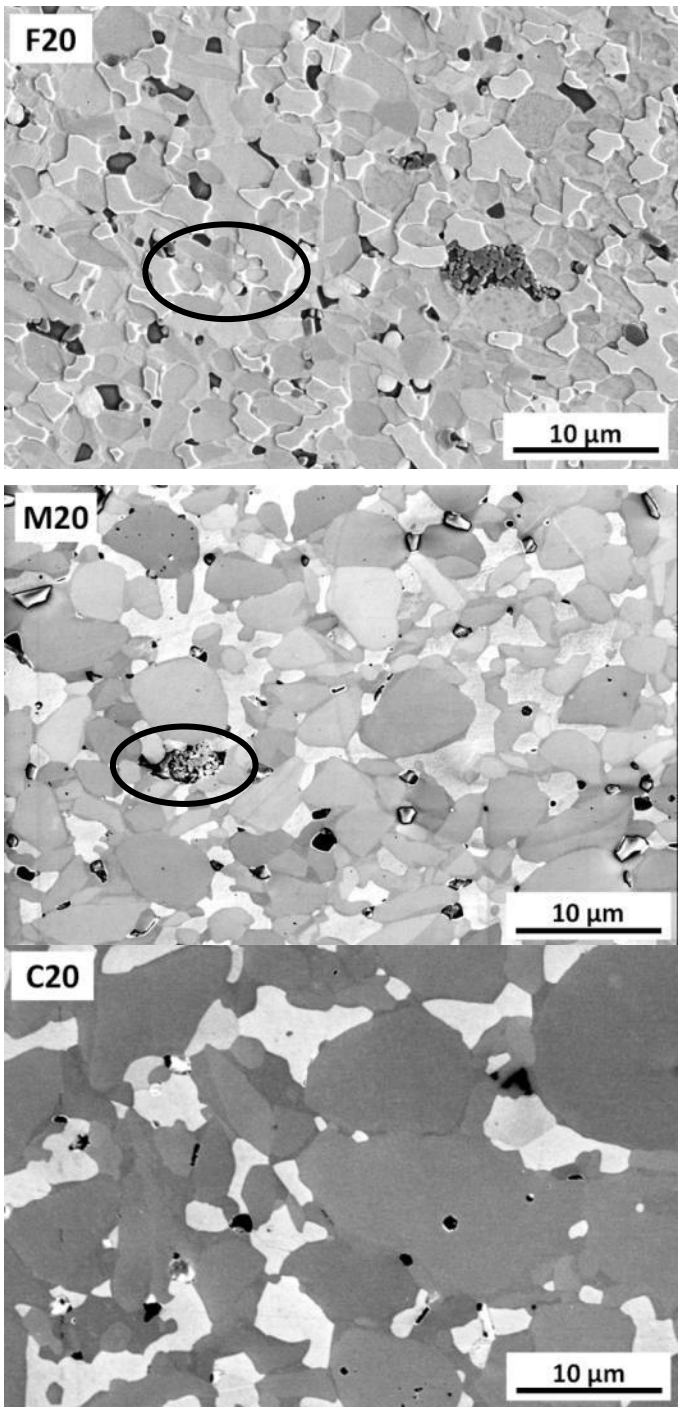

Fig. 1. Secondary electron micrographs of ZrB_2-$MoSi_2$ ceramics with 20 vol.% $MoSi_2$ additions captured using the in-lens detector. The light gray phase is $MoSi_2$, the darker gray phase is ZrB_2, and the black phase is SiO_2. Circled features in lower right of F20 and lower left of M20 is SiO_2 (black) with precipitated SiC crystals (gray) and ZrO_2 crystals (white).

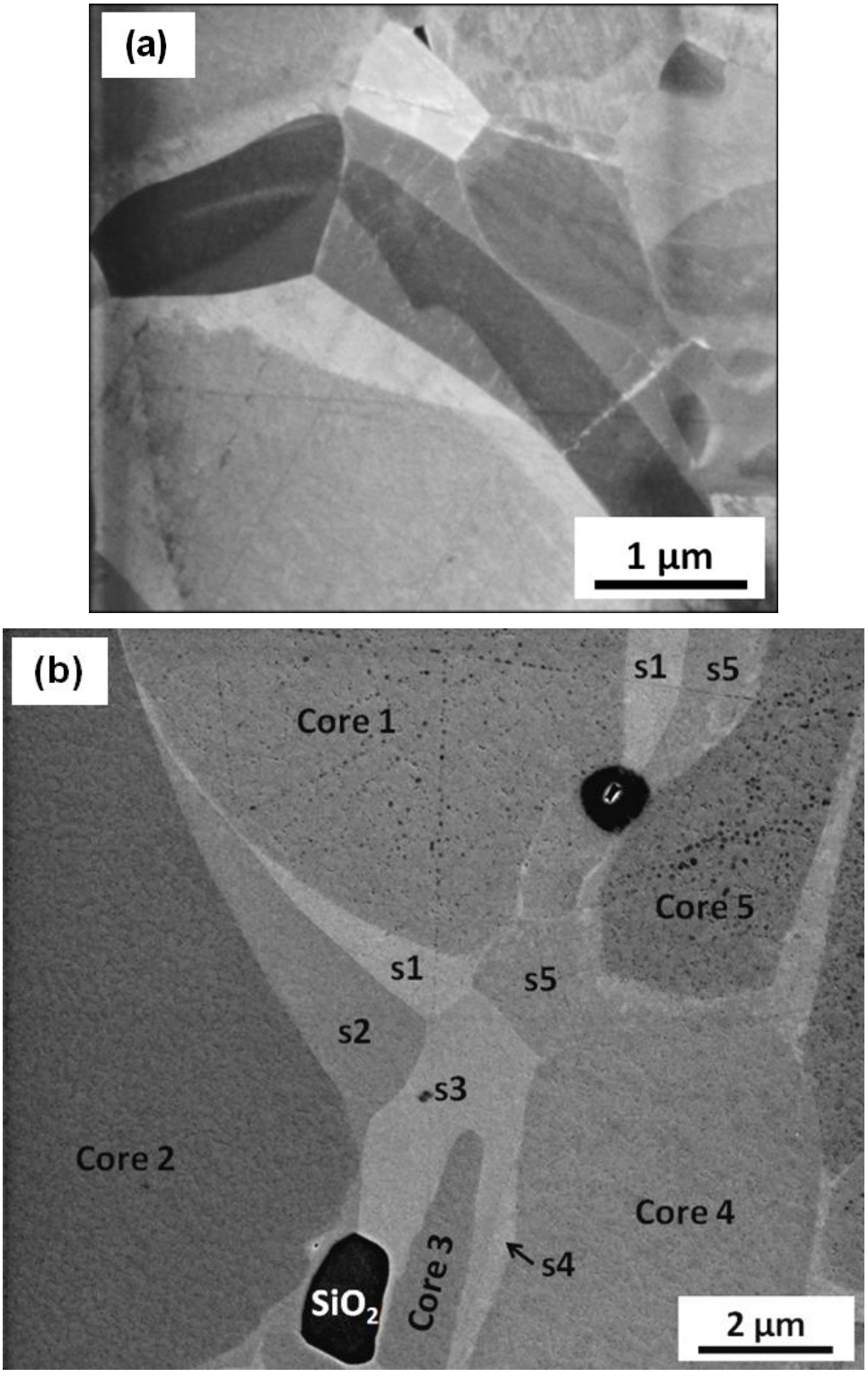

Fig. 2. Secondary electron micrographs of ZrB_2 grains.(a) a triple point of ZrB_2 grains in M5 showing the relationship of core-shell interface and grain boundaries, (b) C10 showing five ZrB_2 grain cores with corresponding shells labeled by number with the letter "s." Dark feature in upper right is a pore with solvent stain from cleaning.

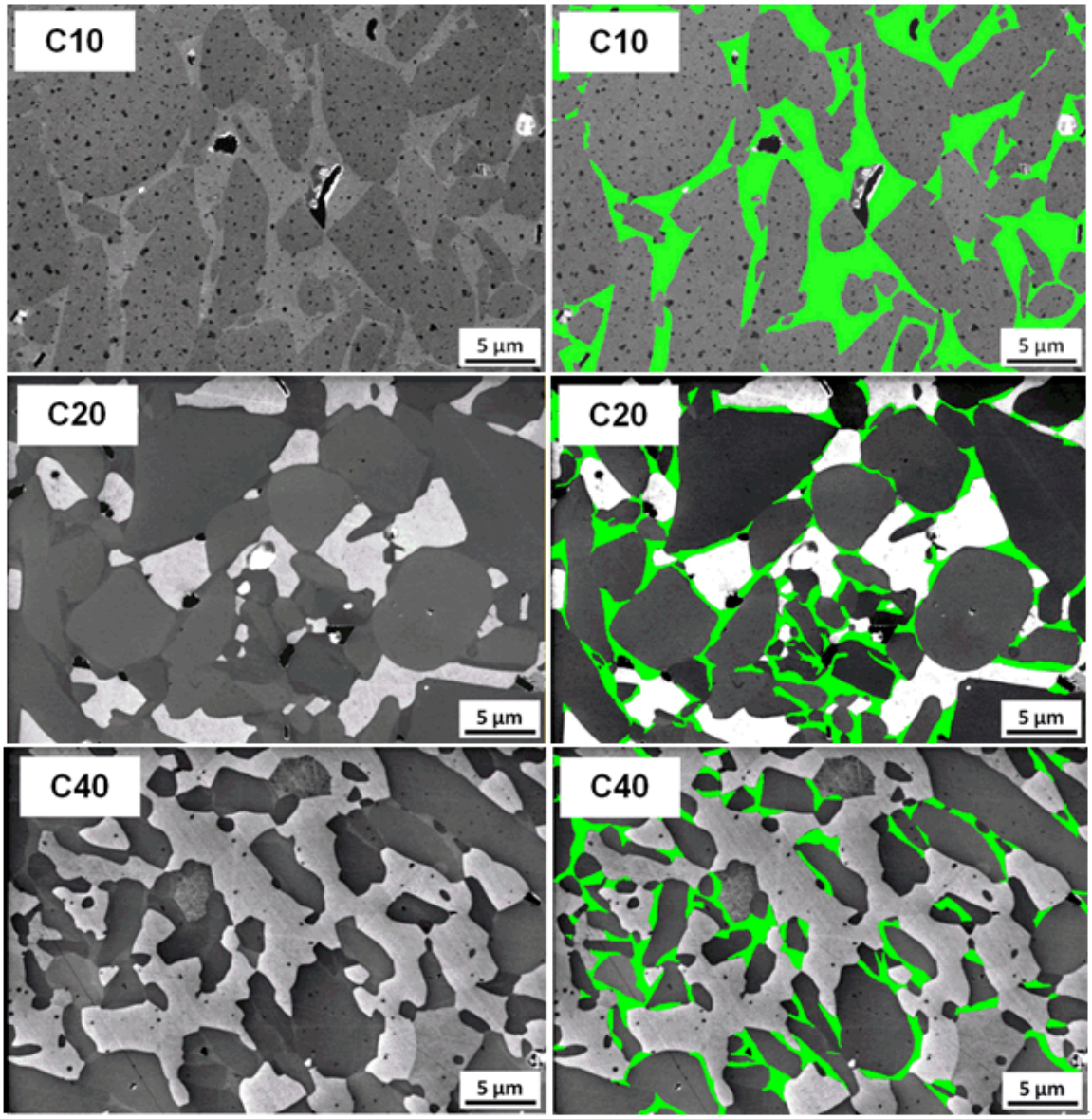

Fig. 3. Secondary electron micrographs of polished cross-sections of CX ceramics with SS shell highlighted on right.Grain boundaries are not visible in image of C10, while core-shell boundaries are visible. Black spots on C10 and C50 are plasma cleaning artifacts.

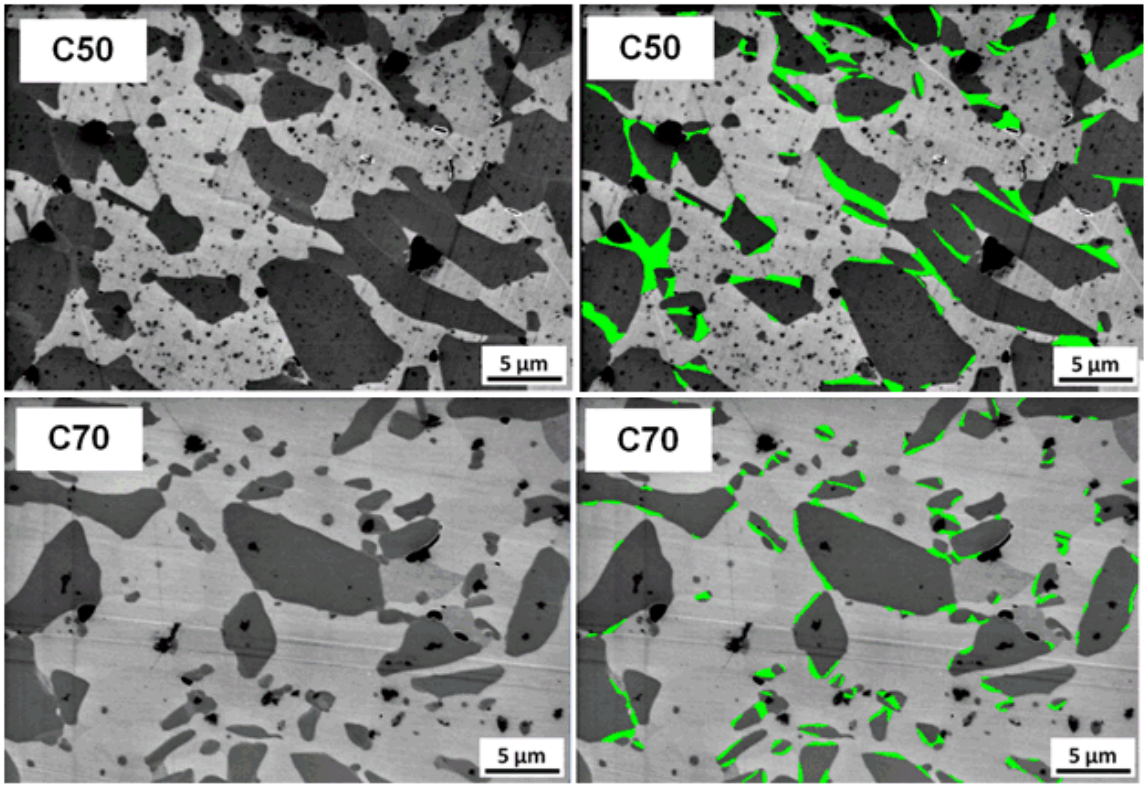

Fig. 3. (cont.) Secondary electron micrographs of polished cross-sections of CX ceramics with SS shell highlighted on right. Grain boundaries are not visible in image of C10, while core-shell boundaries are visible. Black spots on C10 and C50 are plasma cleaning artifacts.

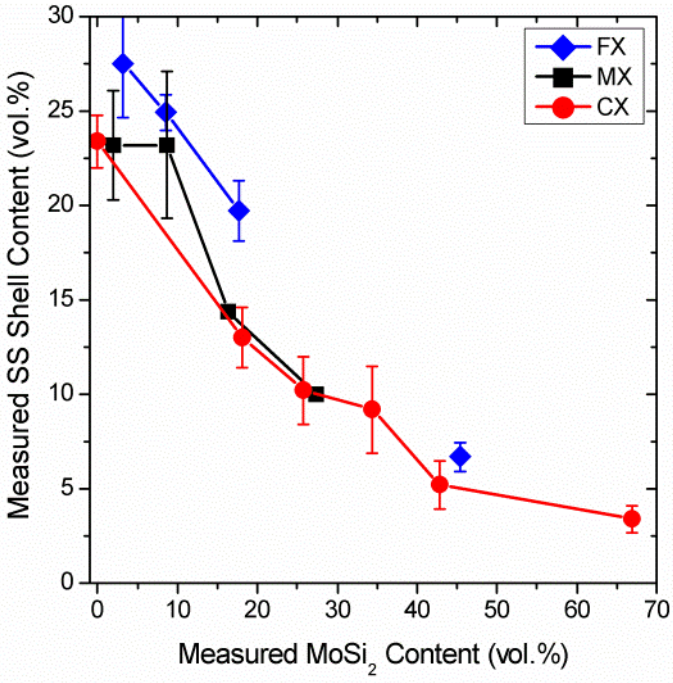

Fig. 4. SS shell content as a function of measured $MoSi_2$ content in the final microstructures.

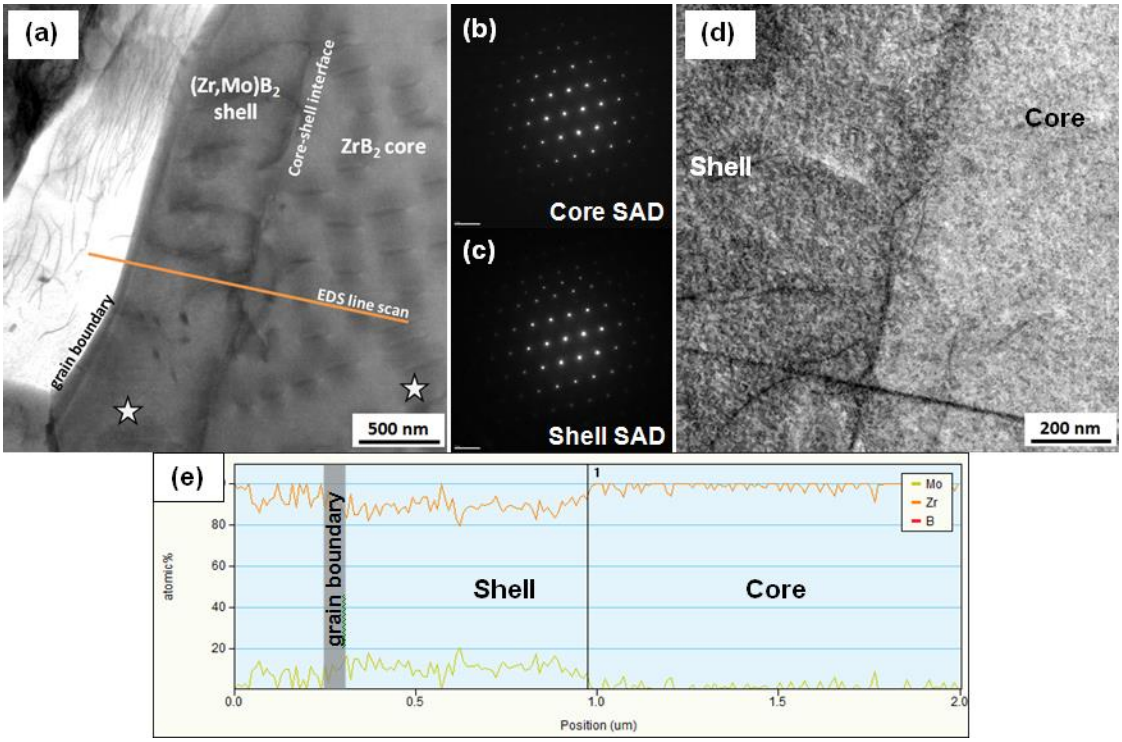

Fig. 5. TEM micrographs of C10.Images show (a) location of TEM-EDS line scan across core-shell boundary; stars indicate locations of SAD patterns from (b) ZrB_2 core, and (c) $(Zr,Mo)B_2$ SS shell on $[0\bar{1}\bar{1}]$ zone axis. (d) magnification of EDS line scan scar across core-shell interface with dislocation lines branching from interface, (e) semi-quantitative EDS line scan results showing relative concentrations of Zr & Mo in atomic %.

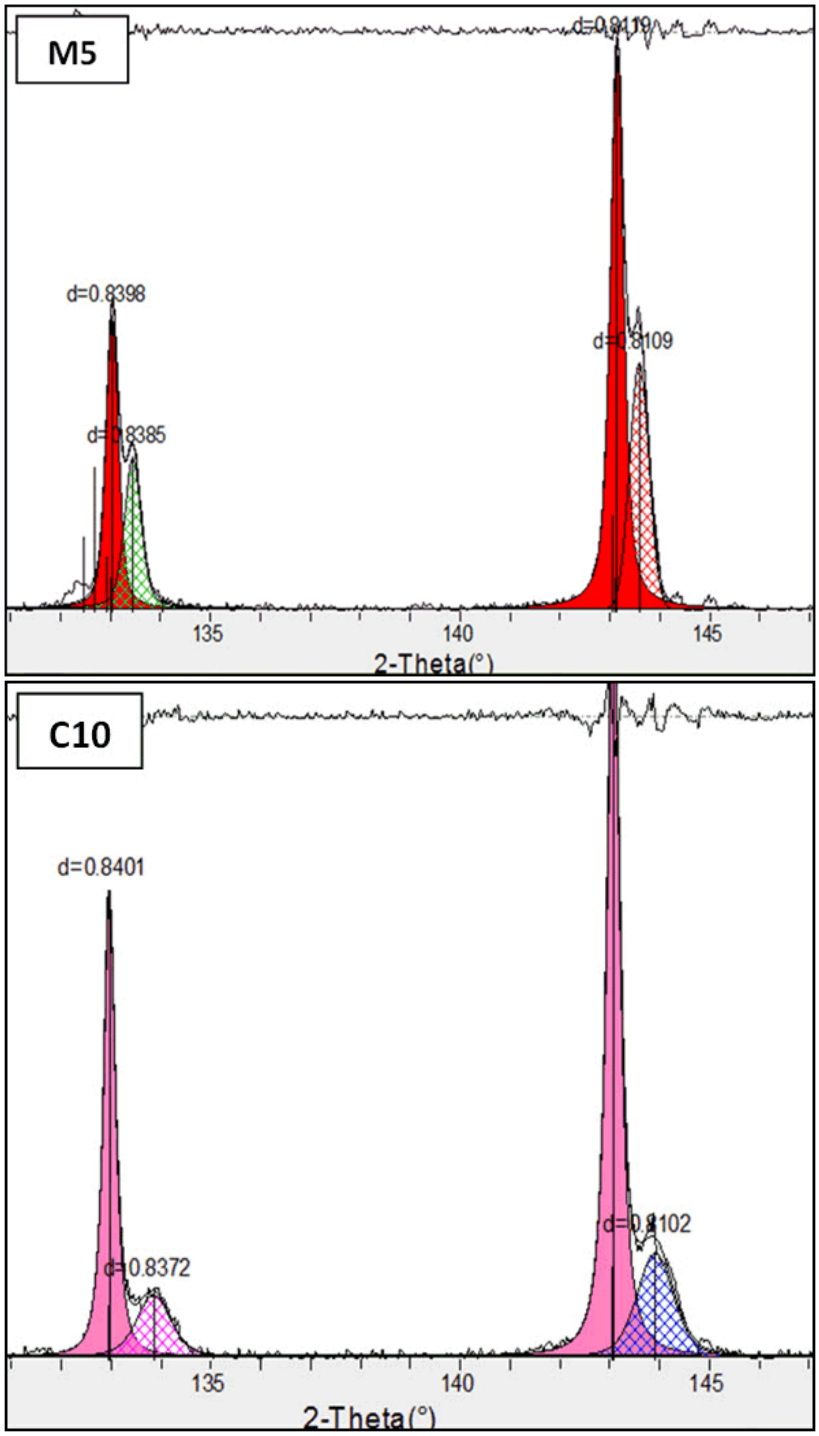

Fig. 6. High-angle segments of refined XRD patterns of M5 and C10 showing peak splitting.Solid shaded peaks represent expected peak positions for ZrB_2, and cross-hatched peaks result from discrete microstructural zones of $(Zr,Mo)B_2$ SS with their own characteristic lattice parameter in each composition.

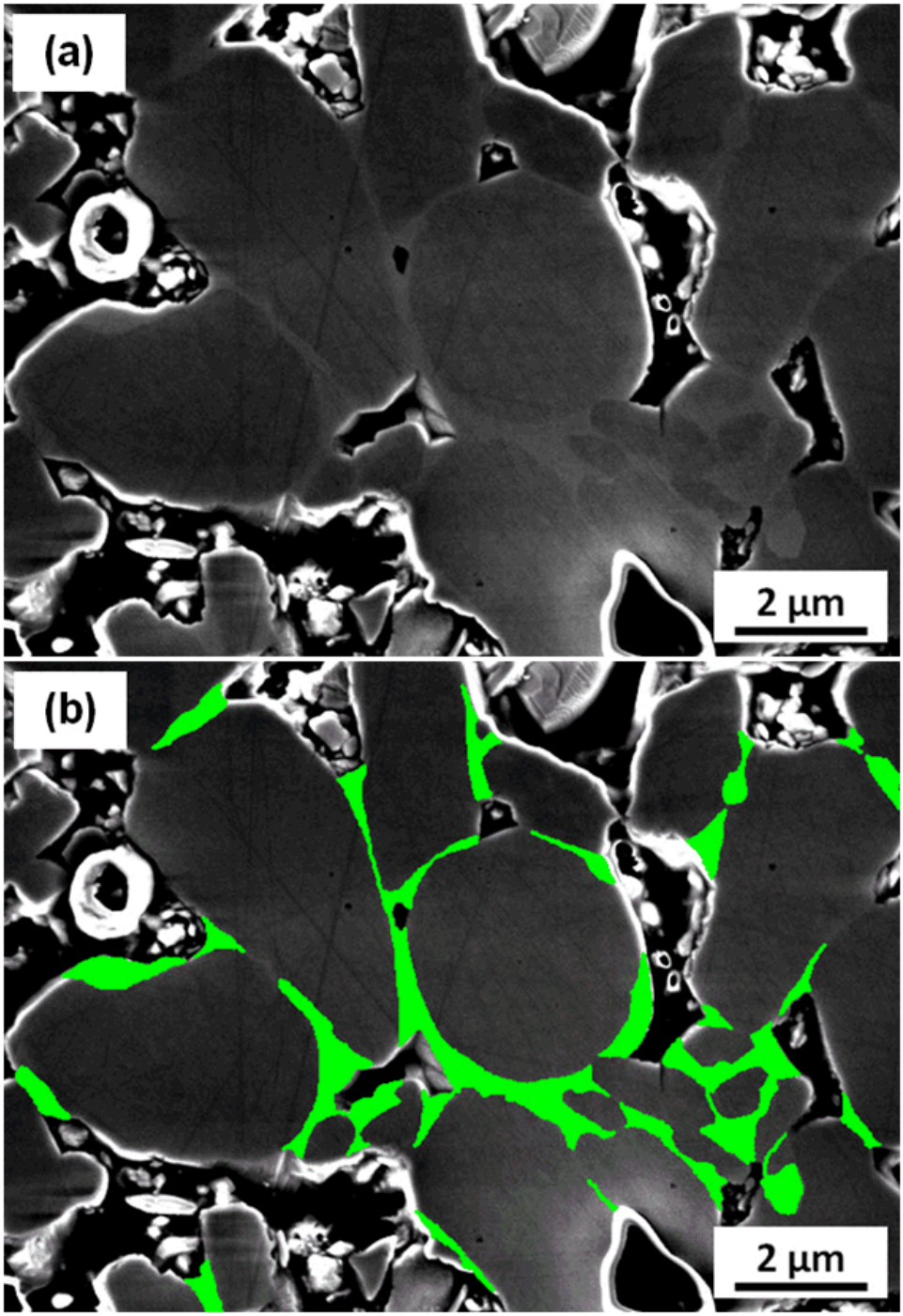

Fig. 7. Secondary electron micrographs of polished cross section of partially dense ZrB_2 with 7 vol.% Mo powder additions.Hot pressed at 1925°C for one hour at 30 MPa under flowing Ar (a) as imaged, (b) with SS shell highlighted for clarity.

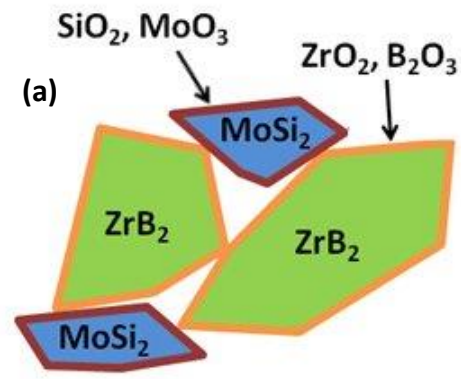

During heating and isothermal vacuum holds the oxide layers on powder particle surfaces are partially volatilized.

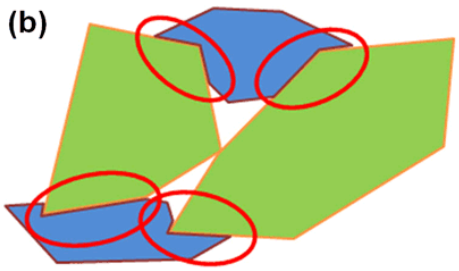

Application of uniaxial pressure in the hot press at ~1650°C causes compaction and plastic deformation of $MoSi_2$ particles, which increases the contact surface area between ZrB_2 and $MoSi_2$ particles.

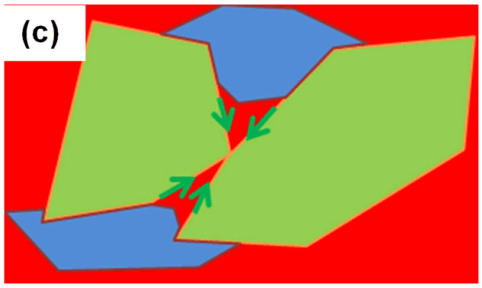

Chemical reaction of ZrB_2 with $MoSi_2$ results in partial decomposition of $MoSi_2$ and generation of a partially-wetting Si-based liquid phase. Simultaneously, sintering of ZrB_2 particles at contact points takes place via surface and grain boundary diffusion, generating $(Zr,Mo)B_2$ solid solution particle-particle necks by incorporating Mo available in Si-based liquid.

Fig. 8. Schematic illustrating the proposed densification process of ZrB_2-$MoSi_2$ ceramics during hot pressing, including formation of $(Zr,Mo)B_2$ solid solution.

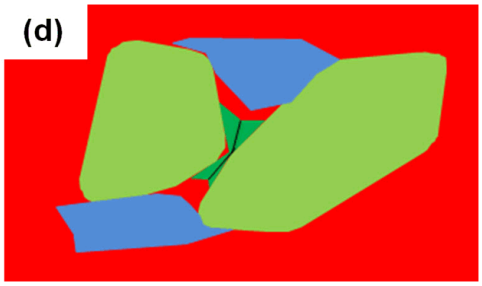

Limited amounts of Mo, Zr, B, and O dissolve in the Si-based liquid, which transports these species throughout the porous powder compact. ZrB_2 continues to sinter (forming more SS shell) and $MoSi_2$ continues to decompose, deform, and sinter, resulting in shrinkage of the powder compact.

Incomplete wetting of Si on ZrB_2 and excellent wetting of Si on graphite results in exfiltration of the Si-based liquid from the densifying powder compact as liquid is produced. Liquid exfiltration results in transport of dissolved species through and also out of the powder compact.

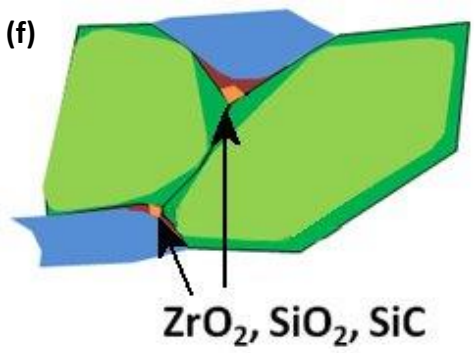

Densification proceeds via sintering of ZrB_2 and $MoSi_2$ grains. GB-dominated sintering of ZrB_2 results in continued formation of SS shell. Oxide, carbide, and nitride impurities are segregated to grain boundaries and triple points.

Fig. 8. (cont.) Schematic illustrating the proposed densification process of ZrB_2-$MoSi_2$ ceramics during hot pressing, including formation of $(Zr,Mo)B_2$ solid solution.

IV. ZrB_2-$MoSi_2$ CERAMICS WITH VARYING MoSi2 CONTENT: PART 3. MECHANICAL PROPERTIES WITH VARYING ZrB_2 PARTICLE SIZE

Ryan Grohsmeyer,[a, 8] Gregory Hilmas,[a, 9] Frederic Monteverde,[b] William Fahrenholtz,[a] Andrea D'Angió,[b, 10] Diletta Sciti,[b] Laura Silvestroni[b]

[a] Materials Science and Engineering Department, Missouri University of Science and Technology, Rolla, MO 65409, USA

[b] National Research Council of Italy, Institute of Science and Technology for Ceramics, Faenza, 48018 RA, Italy

ABSTRACT

Mechanical properties were measure in air at room temperature and 1500°C for ZrB_2-$MoSi_2$ ceramics processed with three grades of ZrB_2 starting powder with decreasing median particle sizes, and 5 to 70 vol.% $MoSi_2$ additions. Room temperature strength did not trend with $MoSi_2$ content, but increased with decreasing ZrB_2 starting particle size from 440 to 590 MPa for coarse, 560 to 720 MPa for medium and from 700 to 800 MPa for fine due to the decreasing size of critical surface flaws. Fracture toughness (2.7-3.9 MPa·$m^{½}$) showed no overall trend, while microhardness (16.9-12.2 GPa) decreased with increasing $MoSi_2$ content. Young's modulus (539-453 GPa), and shear modulus (237-194 GPa) decreased with both increasing $MoSi_2$ content and with decreasing ZrB_2 particle size. Fracture toughness at 1500°C increased from 4.1 to 8.7 MPa·$m^{½}$ as $MoSi_2$ content increased, and also increased with increasing ZrB_2 starting particle size. At 1500°C, flexure strength exhibited two different trends below ~30 vol.% $MoSi_2$, while above ~30 vol.% $MoSi_2$, flexure strength remained roughly constant at 400 to 450 MPa. Strength was controlled by oxidation damage for compositions made with fine and medium ZrB_2 and increased from between 250 and 350 MPa to ~450 MPa with increasing $MoSi_2$ content. Flexure strength of compositions made with coarse ZrB_2 powder decreased from ~600 MPa to ~450 MPa. Coarse compositions with low $MoSi_2$

---

[8] Present address: Corning Incorporated, Painted Post, NY, USA.

[9] Corresponding Author: ghilmas@mst.edu, +1-573-341-6102

[10] Present address: University of Birmingham, Birmingham, UK.

content did not appear to be controlled by oxidation damage and exhibited the highest reported strengths for the ZrB_2-$MoSi_2$ system at 1500°C in air.

Key Words: High-temperature mechanical properties (C), Borides (D), Silicides (D), Microstructure–final (B)

1. INTRODUCTION

Zirconium diboride-molybdenum disilicide (ZrB_2-$MoSi_2$) ceramics have been studied as structural materials for use in extreme environment applications that make use of their retention of strength to high temperatures [10, 23, 42, 67], oxidation resistance to >1500°C [11, 63, 89], ductility at elevated temperatures [42, 134], and resistance to corrosion in acidic environments [101, 135]. Potential applications such as concentrated solar thermal absorbers[29, 30] and aerodynamic leading edges for hypersonic reentry vehicles [49] have been proposed for ZrB_2-$MoSi_2$ ceramics.

$MoSi_2$ has been a popular additive to ZrB_2-based ceramics due to its ability to ameliorate three main disadvantages of nominally pure ZrB_2: difficulty in sintering to high relative density [23], brittle catastrophic failure even at elevated temperatures [18], and susceptibility to rapid oxidation above 1100°C [32, 33]. $MoSi_2$ acts as a sintering aid to ZrB_2, allowing densification of ZrB_2-$MoSi_2$ ceramics at temperatures as low as 1750C [60, 85, 121]. Above its brittle to ductile transition temperature (BDTT) on heating between 900 and 1300˚C [57], $MoSi_2$ imparts ductility through plastic deformation [19, 94, 136]. During oxidation at >600°C $MoSi_2$ forms a protective SiO_2 film that limits further oxidation of the $MoSi_2$ [137]. When added to ZrB_2 ceramics the presence of Si during oxidation converts the volatile B_2O_3 liquid oxide layer into a more stable borosilicate glassy protective layer [11, 12, 89], and the presence of Mo in solid solution has also been shown to improve the oxidation resistance of ZrB_2 in the absence of Si [138].

Multiple studies have investigated the dependence of benefits of $MoSi_2$ additions to ZrB_2 on the volume fraction of $MoSi_2$ added, with the majority of studies focusing on the range between 1 and 20 vol.% $MoSi_2$ additions. Multiple studies have investigated the densification of ZrB_2-$MoSi_2$ ceramics in this compositional range, and compared densification behavior, microstructure, and properties of ceramics densified by various

techniques [65]. Liu et al. used the ductility of $MoSi_2$ additions to press-forge ZrB_2-$MoSi_2$ ceramics to generate alignment of platelet-like ZrB_2 grains which resulted in anisotropic mechanical and oxidation properties [13, 134]. Two studies have reported the microstructures of ZrB_2-$MoSi_2$ ceramics up to 30 vol.% $MoSi_2$ [13, 42, 49], and Guo et al. reported comprehensive microstructural characteristics up to 40 vol.% $MoSi_2$ [66]. In recent work, the authors systematically examined the densification behavior and microstructure of ZrB_2-$MoSi_2$ ceramics with up to 70 vol.% $MoSi_2$ [121, 139], but to date the mechanical properties of these compositions have not been reported.

Similar to densification behavior, the majority of research on mechanical properties of ZrB_2-$MoSi_2$ ceramics have been conducted in the range of 1 to 20 vol.% $MoSi_2$ additions. Only four studies have reported room temperature mechanical properties between 30 and 40 vol.% $MoSi_2$ additions [66], and previous work investigated elevated temperature mechanical properties of ZrB_2-$MoSi_2$ ceramics up to 30 vol.% $MoSi_2$ additions [42]. Variations in testing and characterization methods amongst the studies makes direct comparison of results impractical, while variation in reported flexure strength at room temperature (from 490 MPa [86] to 1150 MPa[49]) and in strength retention to elevated temperatures highlights the need for further study. For example, Silvestroni and Sciti reported retention of 86% and 94% of room temperature flexure strength at 1500°C for ZrB_2 ceramics with 5 and 20 vol.% $MoSi_2$ additions, respectively, while Monteverde reported retention of only 32% of room temperature strength up to 1500°C for ZrB_2 with 2.3 vol.% $MoSi_2$ additions [45]. Furthermore, while numerous studies have reported room temperature mechanical properties of ZrB_2-$MoSi_2$ ceramics, elevated temperature mechanical properties have been reported for only ten individual ZrB_2-$MoSi_2$ compositions [10, 42, 45, 65, 67, 85].

Grain size is an important factor for structural ceramics and has been observed to impact flexure strength by influencing the critical flaw size, and fracture toughness in cases of intergranular fracture by increasing crack bridging and fracture surface area [43]. Studies have shown that in nearly phase pure ZrB_2, grain boundaries act as critical flaws and ZrB_2 grain size controls flexure strength [18], and that in ZrB_2-SiC ceramics the maximum SiC cluster size controls flexure strength [39]. Previous work has shown that in ZrB_2-$MoSi_2$ ceramics, room temperature flexure strength is dependent upon surface voids

caused by pullout of the largest ZrB_2 grains [42]. However, to date no work has systematically investigated the effects of grain size on either the room temperature or the elevated temperature mechanical properties of ZrB_2-$MoSi_2$ ceramics.

The purpose of the present study was to investigate the mechanical properties of hot-pressed ZrB_2-$MoSi_2$ ceramics with varying ZrB_2 starting powder particle size and $MoSi_2$ content at both room temperature and 1500°C in air. The roles of microstructure, specimen preparation, and oxidation behavior on the mechanical properties were examined and are discussed.

2. EXPERIMENTAL PROCEDURE

2.1. Processing and Characterization. ZrB_2-$MoSi_2$ compositions in this study were fabricated in three series based on three grades of commercial ZrB_2 starting powder (H. C. Starck, Newton, MA, USA) with different median particle sizes, and with additions of between 5 and 70 vol.% $MoSi_2$. All compositions were densified by hot pressing at 30 MPa uniaxial pressure at temperatures between 1750 and 1925°C. Powder particle size, purity, processing, hot pressing procedures, and characterization techniques are reported in previous work [121, 139] and are summarized in Table I. Compositions are designated as FX, MX, and CX where F indicates fine, M indicates medium, and C indicates coarse ZrB_2 powder grades, and X indicates the nominal $MoSi_2$ content in vol.%. After densification by hot pressing, compositions were characterized microstructurally according to procedures described elsewhere [121, 139].

2.2. Mechanical Testing. Specimen preparation and mechanical testing methods are summarized here but are described in more detail in previous work [42]. Young's modulus, shear modulus, and Poisson's ratio were measured by impulse excitation of resonant vibration based on ASTM C1259, using specimen sizes of 30 mm x 8 mm x 0.8 mm and 45 mm x 4 mm x 3 mm (length by width by thickness). The static bend test method based on ASTM E111 was used to determine the static Young's modulus in four-point bending at 1500˚C. Microhardness was measured by Vickers' indentation based on ASTM C1327 with a minimum of 15 indentations per composition.

Fracture toughness at both room temperature and at 1500˚C was measured based on ASTM C1421 using type-A bars (nominally 45 mm x 3 mm x 4 mm) having a chevron notched beam (CNB) geometry in four-point bending using fully articulating

fixtures (the notched specimens of F50 were smaller: 25 mm x 2.5 mm x 2 mm and were tested in four-point bending with a 20 mm support span and a 10 mm loading span). At room temperature, a crosshead rate of 0.02 mm/min was used for FX specimens and a rate of 0.018 mm/min was used for MX and CX specimens. At 1500°C, a crosshead rate of 0.02 mm/min was used for F50 specimens and a rate of 0.18 mm/min was used for MX and CX specimens.

Room-temperature flexure strength was measured according to ASTM C1161 using type-B bars (nominally 45 mm x 4 mm x 3 mm) in four-point bending with fully articulating fixtures. Flexure strength was measured at 1500˚C in air using type-B bars according to ASTM C1211 with a fully-articulating SiC fixture. For fracture toughness measurements, specimens of F50 were 25 mm x 2.5 mm x 2 mm and were tested on 20 mm support spans with 10 mm loading spans at both room temperature and 1500°C in air. Bars were machined by electrical discharge machining and finish ground using automatic surface grinders with resin-bonded diamond abrasive wheels. MX and CX specimens were finish ground with 1200 grit (~6 μm abrasive) grinding wheels with a ~2.5 μm downfeed step, while FX specimens were finish ground with ~48 μm abrasive wheels with 1 μm downfeed step. Corner chamfers were left as-ground on FX specimens, but were polished to 3 μm finish using diamond abrasives on MX and CX. Flexure tests were performed using screw-driven instrumented load frames (Z050, Zwick-Roell, Ulm, Germany; and 6025 and 5881, Instron SFL, Thornbury, Bristol, UK). Elevated temperature testing was performed in a $MoSi_2$ element furnace (MDS66C, Instron SFL, Thornbury, Bristol, UK). A crosshead rate of 0.5 mm/min was used for all compositions at room temperature (with the exception of F50, which was tested at 1.0 mm/min), and rates between 0.5 and 5.0 mm/min were used at 1500˚C.

3. RESULTS AND DISCUSSION

3.1. Microstructural Analysis. Microstructural features are summarized below and reported in more detail elsewhere [121, 139]. The final relative density of each composition was greater than 99.2% based on pore volume measured by microstructural analysis Table I). Decomposition of $MoSi_2$ during hot pressing resulted in final $MoSi_2$ contents that were between 1 and 10 vol.% lower than nominal batch compositions, and in the case of C10 (which was hot pressed at the highest temperature for the longest time)

all of the 10 vol.% $MoSi_2$ addition decomposed, resulting in a densified ceramic without any remaining silicide phase [121]. Final $MoSi_2$ contents are included in Table I, and due to the influence of final $MoSi_2$ content on mechanical behavior, mechanical properties are plotted with respect to measured final $MoSi_2$ content.

A portion of the Mo evolved during $MoSi_2$ decomposition was incorporated into a $(Zr_{1-x}Mo_x)B_2$ solid solution (SS) where x appears to vary from ~0.03 to ~0.06. In the densified microstructures of compositions with lower $MoSi_2$ contents, the typical diboride grain contained a ZrB_2 core partially, or in some case completely, surrounded by a SS shell such that the SS shell usually occupied one or both sides of ZrB_2-ZrB_2 grain boundaries. As final $MoSi_2$ content increased, the SS less frequently formed shells and more frequently formed connective necks between adjacent ZrB_2 grains [139]. The liquid Si that was evolved during $MoSi_2$ decomposition became a carrier of various species as it exited the powder compact through open porosity during hot pressing, in many cases significantly decreasing the final Si content of the densified ceramics, which affected their ability to form protective borosilicate glassy oxidation layers during testing at 1500°C [42].

The average ZrB_2 grain size increased with increasing starting ZrB_2 powder particle size as expected, and also decreased with increasing $MoSi_2$ content from ~1.8 μm in F5 to ~1.3 μm in F50, from ~2.8 μm in M5 to ~2.0 μm in M30, and from ~4.6 μm in C10 to ~1.5 μm in C70 Table I). The maximum observed ZrB_2 grain size was similar to the d_{90} values of starting ZrB_2 powders, increasing from between 5.7 and 6.5 μm in FX to between 8.8 and 9.8 μm in MX to between 15 and 30 μm in CX. Both average and maximum $MoSi_2$ cluster size increased with increasing $MoSi_2$ content, until in compositions with 50 and 70 vol.% $MoSi_2$ additions, $MoSi_2$ clusters appeared to be continuous throughout the microstructure.

Impurity phases in all compositions included SiO_2, ZrO_2, SiC, and BN, while MoB was observed only in F50. FX compositions contained 3.7 to 8.4 vol.% SiO_2, 3 to 7 times more SiO_2 than MX and CX compositions due to lower oxide contents of the MX and CX starting powders. Overall, the combination of tertiary phases and porosity constituted between 5.2 and 11.3 vol.% of each FX composition, while impurities and pores combined constituted between 0.7 and 4.1 vol.% of each MX composition and

between 0.4 and 2.4 vol.% of each CX composition. The range of oxides and other impurity content allowed an evaluation of the impact of impurity phases on the mechanical properties of ZrB_2- $MoSi_2$ ceramics.

3.2. Mechanical Properties at Room Temperature. Young's modulus decreased with increasing $MoSi_2$ content as expected [42] Table II, Fig. 1a). In FX, Young's modulus decreased from 481 GPa for F5 to 446 GPa for F30. In MX, Young's modulus decreased from 531 GPa for M5 to 494 GPa for M30. In CX, Young's modulus decreased from 539 GPa for C10 to 453 GPa for C70. The values roughly agree with predictions made using a linear volumetric rule of mixing (ROM) assuming a value of 526 GPa for ZrB_2 [34] and 400 GPa for $MoSi_2$ (measured on a hot-pressed $MoSi_2$ specimen that was 97.5% dense). The lower Young's modulus of the FX compositions can be partially explained by the greater content of SiO_2 and other low-modulus impurity phases. Comparing measured Young's moduli with values calculated by ROM, and using phase content measurements presented in previous work [121] (assuming Young's moduli of 526 GPa for ZrB_2 [34], 525 GPa for the SS shell with 499 GPa for MoB_2 [123, 124], 400 GPa for $MoSi_2$, 73 GPa for SiO_2 [140], 244 GPa for tetragonal ZrO_2 [141], 420 GPa for SiC [142], and 0 GPa for porosity) yields a more relevant comparison. However, even accounting for impurity content via ROM, there is an unexplained decrease in Young's modulus with decreasing ZrB_2 powder particle size: FX moduli were on average ~14 GPa lower than their ROM-predicted values, MX moduli were ~8 GPa greater than their ROM-predicted values, and CX moduli were ~16 GPa greater than their ROM-predicted values. The reason for this apparent dependence on ZrB_2 starting powder particle size is not yet fully understood. The lower moduli of FX and MX could be due to the microcracking observed in the FX compositions and in M20, although the Young's moduli of these compositions are not abnormal for ZrB_2-$MoSi_2$ ceramics with similar nominal $MoSi_2$ contents reported in the literature [23, 42]. It is possible that higher residual stresses in the CX compositions due to the presence of both larger ZrB_2 grains and $MoSi_2$ clusters resulted in an intergranular stress distribution without microcracking that promoted higher elastic moduli with increasing maximum grain size [40, 121]. Young's modulus, shear modulus, and Poisson's ratio are shown Fig. 1 and reported in Table II. With respect to $MoSi_2$ content, elastic behavior of the ZrB_2-$MoSi_2$ ceramics

followed expected ROM trends and were consistent with previously reported values, indicating that additions of $MoSi_2$ decrease the Young's and shear moduli of ZrB_2 ceramics.

Average Vickers microhardness decreased as $MoSi_2$ content increased, and did not vary significantly with starting ZrB_2 powder particle size Table II, Fig. 2). The hardness of FX decreased from 16.5 GPa for F5 to 15.3 GPa for F30, the hardness of MX decreased from 16.6 GPa for M5 to 15.1 GPa for M30, and the hardness of CX decreased from 16.9 GPa for C10 to 12.2 GPa for C70. Radial/median cracks showed primarily transgranular fracture with only occasional intergranular behavior and little or no crack deflection when cracks encountered $MoSi_2$ clusters, in agreement to what has been reported elsewhere [10]. Branching of the cracks was also observed when loads of 49 to 98 N were used. Reported microhardness values of ZrB_2-$MoSi_2$ ceramics in the range of 5 to 40 vol.% $MoSi_2$ additions ranged from 13.2 to 16.3 GPa [23, 66], the hardness of ZrB_2 has been reported to be in the range of 14 to 23 GPa [14, 23, 125], while the hardness of $MoSi_2$ has been reported to be 8 to 10 GPa [51, 52, 55] The compositions tested in this study fell within the range of expected hardness based on values previously reported in the literature for ZrB_2, $MoSi_2$, and ZrB_2- $MoSi_2$ ceramics.

At room temperature, all compositions had average fracture toughness values between 2.7 and 3.9 $MPa \cdot m^{½}$ with no clear trend of fracture toughness with respect to $MoSi_2$ content Table II, Fig. 3). Roughly constant fracture toughness with respect to $MoSi_2$ content is expected due to the similar fracture toughness values of ZrB_2 and $MoSi_2$, and due to the primarily transgranular fracture behavior observed at room temperature, in which $MoSi_2$ clusters do not serve to deflect cracks.

Room temperature flexure strength increased with decreasing ZrB_2 starting powder particle size, but showed no obvious trend with respect to $MoSi_2$ content Table II, Fig. 4). Strength was in the range of 700 to 800 MPa for FX, 560 to 720 MPa for MX, and 440 to 590 MPa for CX. Previous studies have reported flexure strengths between 500 and 720 MPa for ZrB_2-$MoSi_2$ composites in this compositional range [10, 13, 65, 85]. Guo et al. [108] and Chamberlain et al. [62] tested the flexure strength of the widest range of ZrB_2-$MoSi_2$ ceramic compositions to date, and also reported room temperature flexure strength to be insensitive to $MoSi_2$ content.

The first standard deviation in strength at room temperature for each composition was between 60 and 150 MPa, suggesting that a range of critical flaw sizes operated at room temperature. As reported in previous work [42], the critical flaw size of MX was calculated to range from 2.1 to 7.6 μm for M20 to 6.1 to 14 μm for M10. The critical flaw size of CX was calculated to range from 3.1 to 11 μm for C30 to 13 to 53 μm for C10, and the critical flaw size of F50 was calculated to be between 4.4 and 9.6 μm. The calculated critical flaw sizes did not correlate with the average ZrB_2 grain size in each composition, or with the maximum $MoSi_2$ cluster size, hypothesized based on the previously reported behavior of ZrB_2-SiC composites in which large SiC clusters act as the strength-limiting flaws [92, 126]. The calculated flaw sizes for the FX, MX, and CX compositions approximately match the maximum observed sizes of ZrB_2 grains in each composition, and correlate with the measured d_{90} of each of the ZrB_2 starting powders (5.2 μm for FX, 9.0 μm for MX, and 30 μm for CX). In previous work, fractographic analysis of broken MX flexure bars by SEM identified surface voids generated by pullout of ZrB_2 grains during surface grinding to be the critical flaws responsible for failure [42]. The correlation of maximum ZrB_2 grain size with calculated flaw sizes in FX, MX, and CX compositions supports this observation, indicating that the maximum ZrB_2 grain size, coupled with surface finishing technique(s), controls room temperature flexure strength in ZrB_2-$MoSi_2$ ceramics. The difference in wheel grit size used to finish the FX specimens vs. the MX and CX specimens did not result in larger flaws, suggesting that ZrB_2 grain pullout is the primary mechanism of material removal during surface grinding of ZrB_2-$MoSi_2$ ceramics.

Neuman et al. reported that the room temperature flexure strength of ZrB_2 was controlled by the grain size when surface cracks caused by grinding were removed from the specimens' tensile surfaces by polishing, due to the action of ZrB_2 grain boundaries as critical flaws [143]. In such a case, after polishing has reduced the surface crack size sufficiently to allow the grain boundaries to become the critical flaw and the flexure strength is thus determined by microstructural features intrinsic to the material, further reduction of the sizes of surface cracks via polishing will not serve to improve the strength beyond the intrinsic limits. Likewise, if the grain size is large enough that surface cracks caused by grinding are already small enough to allow the grain boundaries

to act as the critical flaws, then polishing would not be expected to increase the flexure strength at all. In the present study, flexure strength was strongly influenced by the maximum ZrB_2 grain size due to voids from grain pullout that acted as the critical flaws. This behavior, and the absence of observed surface zipper cracks, suggests a different material removal mechanism during surface grinding for ZrB_2-$MoSi_2$ ceramics than for nominally pure ZrB_2. It was initially assumed that polishing the flexure specimens in the present study would not increase the flexure strength due to the fact that flexure strength was already being controlled by the intrinsic maximum ZrB_2 grain size. However, this assumes that a pullout void and a grain boundary of a similarly-sized grain have the same stress-concentrating effect, which may not be the case. The two studies in the literature that report the highest room temperature flexure strengths for ZrB_2-$MoSi_2$ ceramics are also the only two studies that reported polishing the tensile surfaces of the flexure bars (Chamberlain et al. [49], σ_f 1000 to 1150 MPa, and Guo et al. [66], σ_f 750 to 800 MPa). Therefore, it is likely that surface voids left by ZrB_2 grain pullout concentrate stress more severely than ZrB_2 grain boundaries of similar size, and it is likely that the flexure strength of a ZrB_2-$MoSi_2$ ceramic with given maximum ZrB_2 grain size could be increased by polishing to remove the pullout voids.

3.3. Toughness and Strength at 1500°C. At 1500°C, fracture toughness increased with increasing $MoSi_2$ content and with increasing starting ZrB_2 powder particle size Table III, Fig. 3). The fracture toughness of MX increased from 4.1 MPa·$m^{½}$ for M5 to 4.7 MPa·$m^{½}$ for M30, and the fracture toughness of CX increased from 4.3 MPa·$m^{½}$ for C10 to 8.7 MPa·$m^{½}$ for C70. The fracture toughness of F50 at 1500°C was 5.6 MPa·$m^{½}$ while that of C50 was 7.3 MPa·$m^{½}$. Additionally, all compositions displayed increased fracture toughness at 1500°C compared to room temperature. For example, the fracture toughness of F50 increased by 50% from 3.7 MPa·$m^{½}$ at room temperature to 5.6 MPa·$m^{½}$ at 1500°C, and the fracture toughness of C70 increased by 150% from 3.5 MPa·$m^{½}$ at room temperature to 8.7 MPa·$m^{½}$ at 1500°C. The increases in fracture toughness with increasing $MoSi_2$ content, and with increasing temperature, are likely due to plastic deformation of $MoSi_2$ near the crack tip which relax concentrated stresses and absorb additional fracture energy. Optical microscopy of crack tip cross sections in unseparated toughness specimens revealed intergranular cracking and crack branching at

1500°C. Neuman et al. reported that other ZrB_2 ceramics display increasing amounts of intergranular fracture as temperature increases [143]. Fracture toughness has been observed to increase with increasing grain size due to the increased magnitude of out-of plane deflection of intergranular cracks that leads to crack bridging by grains [42, 144]. Thus, due to increased intergranular fracture observed at elevated temperatures, larger ZrB_2 grains are expected to contribute to increased fracture toughness at 1500°C. It is also likely that decreased SiO_2 content contributes to higher fracture toughness at elevated temperatures based on fracture toughness measurements of hot pressed $MoSi_2$ and $MoSi_2$-SiC materials reported in the literature [1, 54]. M5 and C10 displayed increases in fracture toughness from room temperature to 1500°C (from 3.0 to 4.1 $MPa \cdot m^{1/2}$ for M5 and from 3.1 to 4.3 $MPa \cdot m^{1/2}$ for C10), which are unlikely to be the result of plasticity on the part of $MoSi_2$ (especially in C10 since there is no $MoSi_2$ remaining) and could be due to a shift from primarily transgranular fracture at room temperature to more intergranular fracture at 1500°C. The increases of fracture toughness from room temperature to 1500°C and with increasing $MoSi_2$ content suggest that ZrB_2-$MoSi_2$ ceramics become more damage tolerant near 1500°C and make this a promising system for structural applications at elevated temperatures.

Stress-strain behavior of the flexure specimens became increasingly non-linear with increasing $MoSi_2$ content (Fig. 6). M5, and C10 exhibited linear responses, but greater $MoSi_2$ contents increased the overall ductility and caused greater deviation from linear elastic behavior during flexure testing. In order to obtain more linear-elastic behavior to failure while testing MX and CX, the crosshead speed was increased as $MoSi_2$ content increased, from 1 mm/min for M5 and C10 to 3 mm/min for M30 and 5 mm/min for C50. Despite these efforts however, the stress strain curves remained increasingly indicative of inelastic behavior as $MoSi_2$ content increased. In fact, specimens of C70 never broke at 1500°C, even when crosshead rates of 7 to 10 mm/min (corresponding to an initial strain rate of 0.113 s^{-1}) were used and center-bar deflection approached 3 mm. Thus, no flexure strength data are reported for C70 at 1500°C. The FX compositions were tested without a contact LVDT to measure strain, and so are not included in Figure 6. Due to the assumptions of small deflection and linear-elastic behavior associated with the beam bending equations used to calculate flexure strength

and strain, the reported apparent flexure strengths in Table III and Figure 5 associated with compositions that displayed significant non-linear behavior should be considered overestimates.

The Young's modulus of M5 at 1500°C in air was measured to be 222 ± 15 GPa, while the Young's modulus of C10 at 1500°C in air was measured to be 296 ± 21 GPa. All other compositions were excluded due to non-linearity of the stress-strain response. The Young's modulus of C10 is similar to the Young's moduli of nominally pure ZrB_2 (grain size ~19 μm) measured in air at 1400°C (297 ± 6 GPa) and at 1600°C (263 ± 23 GPa) reported by Neuman et al. [18], while the Young's modulus of M5 is about 25% lower. The difference between M5 and C10 of only 2 vol.% retained $MoSi_2$ is not expected to cause such a large difference in Young's modulus. Although not as linear in behavior, the other compositions displayed a similar trend of decreased rigidity with decreasing ZrB_2 powder particle size (Fig. 6), which is similar to the trend observed at room temperature of decreasing Young's modulus with ZrB_2 powder particle size. Grain boundary sliding could play a role in decreasing rigidity at 1500°C, but this trend is not yet fully understood.

Flexure strength at 1500°C followed two different trends at $MoSi_2$ contents below 30 vol.%: trend (A) in which flexure strength increased with increasing $MoSi_2$ content, and trend (B) in which flexure strength decreased with increasing $MoSi_2$ content. At $MoSi_2$ contents greater than 30 vol.%, trends A and B converge to a single trend of relatively constant flexure strength with respect to $MoSi_2$ content Table. III, Fig. 5). FX and MX both exhibited increasing strength as $MoSi_2$ content increases at 1500°C (trend A). The strength of FX increased from ~355 MPa for F5 to ~465 MPa for F20 before dropping slightly to ~425 MPa for F30 and F50. The strength of MX increased from 250 MPa for M5 to ~415 MPa for M20, and ~440 MPa for M30. CX, however, followed trend B, decreasing from ~605 MPa for C10 to 540 MPa for C20 and 445 MPa for C30. Between 30 and 50 vol.% $MoSi_2$ additions, flexure strengths of all compositions remained between 420 and 460 MPa at 1500°C. Flexure strength is discussed in two parts in the following sections: first, trend (A) of increasing flexure strength displayed by FX and MX, and second, trend (B) of decreasing flexure strength displayed by CX.

3.3.1. Trend A: Increasing Flexure Strength with Increasing $MoSi_2$ Content in FX and MX. All FX and MX compositions displayed lower strengths at 1500°C compared to RT, but the degree of strength retention at elevated temperature increased with increasing $MoSi_2$ content up to 20 to 30 vol.% $MoSi_2$ additions. In FX, retention of room temperature strength up to 1500°C ranged from ~45% for F5 and F10 to ~67% for F20, while in MX strength retention ranged from ~40% for M5 to ~80% for M30, which displayed the greatest strength retention in trend (A).

The order of magnitude increase of calculated critical flaw sizes of F50 and the MX compositions from between 2.1 and 14 μm at room temperature to between 30 and 136 μm at 1500°C Table III) indicate a change in the critical flaw population between room temperature and 1500°C in air [42]. Linear elastic behavior was assumed for critical flaw size estimation. Although the size of critical flaws increased from room temperature to 1500°C, the standard deviation in flexure strength values was ~70% less at 1500°C than at room temperature, suggesting a narrower distribution of critical flaw sizes. Unfortunately, post-fracture oxidation during cooling from the test temperature destroyed the fracture surface features making fractographic analysis impossible.

In previous work the authors identified oxidation induced surface damage as the strength limiting flaw at 1500°C in air for the MX compositions [42]. The oxidation behavior was divided via SEM-EDS analysis into two main modes: (1) unprotective oxidation, which lacks a glassy borosilicate outer layer; and (2) protective oxidation, in which a continuous borosilicate glassy layer is formed. M5 underwent unprotective oxidation, failing to form a protective borosilicate glassy layer, and forming an outer layer of porous ZrO_2 with traces of MoB in contact with the underlying bulk ceramic. M20 and M30 displayed protective oxidation, forming a continuous borosilicate glassy outer oxidation layer (beneath this was a layer of porous ZrO_2 with SiO_2 and MoB, followed by an exfoliated layer depleted of $MoSi_2$), while M10 displayed mixed protective/unprotective oxidation behavior. The transition in oxidation behavior from discontinuous to continuous borosilicate layer formation was found to be responsible for the increase in flexure strength from M5 to M30, based on calculated critical flaw size estimations that matched the size of features created by oxidation damage [42].

The flexure strength of FX at 1500°C follows the same trend as that of MX in the range of 5 to 30 vol.% $MoSi_2$ additions, which is expected due to the similarity of oxidation behavior between the FX and MX compositions, including the transition from unprotective to protective oxidation between 20 and 30 vol.% retained $MoSi_2$ content. The flexure strengths of F5, F10, and F20 were on average ~20% higher than the flexure strengths of M5, M10, and M20. The oxidation with exfoliation in the $MoSi_2$-depleted zone is related to the ZrB_2 grain size and to the dispersion of the $MoSi_2$ clusters. In such a situation, a greater number of smaller, more evenly dispersed $MoSi_2$ clusters is expected to protect more effectively against oxidation and generate less severe exfoliation. The percolation threshold for a dispersed phase decreases as the particle size of the matrix phase in which it is dispersed increases [145]. This phenomenon is evident in the larger average and maximum $MoSi_2$ clusters observed in FX compared to MX. Because the exfoliation-type oxidation observed in ZrB_2-$MoSi_2$ ceramics is a result of $MoSi_2$ depletion during oxidation, it is not unexpected that finer ZrB_2 grain size and $MoSi_2$ cluster size results in less severe exfoliation in FX than in MX. Analysis of the morphology of the oxidation scale formed on MX and FX bars during flexure testing indicates that strength in these compositions at 1500°C in air (trend (A)) is controlled by oxidation behavior. The similar strengths of M30, F30, and F50 support the conclusion that at a $MoSi_2$ content above that which is necessary to form a continuous borosilicate protective glassy layer, the oxidation behavior remains similar and flexure strength remains roughly constant.

3.3.2. Trend B: Decreasing Flexure Strength with Increasing $MoSi_2$ Content in CX. The CX compositions displayed a decrease in flexure strength as retained $MoSi_2$ content increased from ~0 to ~26 vol.% with strengths decreasing from ~605 MPa for C10 to 540 MPa for C20 and 445 MPa for C30. The strength of 604 ± 21 MPa measured for C10 is the highest flexure strength at 1500°C in air reported for any ZrB_2-$MoSi_2$ material, and is the second highest flexure strength reported for any ZrB_2-based ceramic at 1500°C in air [127]. C10 was 36% stronger at 1500°C than at room temperature. Two studies in the literature have reported similar results. In the first study, Silvestroni and Sciti discussed pressurelessly sintered ZrB_2 with 5 and 20 vol.% $MoSi_2$ additions with flexure strengths of 488 MPa and 500 MPa at 1500°C in air, retaining 86% and 94% of

their room temperature strengths, respectively [10, 67]. Both compositions were reported to have formed a protective silica scale and strength retention at 1500°C was attributed to flaw healing by this protective oxidation layer. In the second study, Monteverde and Silvestroni reported flexure strengths of ~625 MPa at room temperature and ~710 MPa at 1500°C in air for a ZrB_2 ceramic with 3 vol.% SiC and 5 vol.% WC additions, an increase in flexure strength of ~12% from room temperature to 1500°C. The latter study is particularly pertinent to the present work because its microstructure consisted of ZrB_2 grain cores surrounded by $(Zr,W)B_2$ SS shells.

However, the strength retention observed in C10 is not supported by the analysis discussed in the previous section, which identified oxidation damage as the source of critical flaws at 1500°C for similarly low $MoSi_2$ contents. C10, which displays the highest strength of any composition, retained no $MoSi_2$ after hot pressing, and did not form a protective borosilicate surface layer. Instead, the oxide layer formed on C10 is an unprotective layer of porous ZrO_2 between 120 and 160 μm thick, similar in morphology and thickness to the layer formed on M5 [42], which had the lowest strength at 1500°C of any composition in the present study. Furthermore, the average and maximum ZrB_2 grain sizes of C10 and C20 where larger, an indication that these compositions do not follow the trend of increasing strength with decreasing grain size displayed by FX and MX at 1500°C. Thus, it appears that neither oxidation damage nor grain size is the primary factor controlling strength at 1500°C in C10 and C20.

One possible explanation that has already been proposed in the literature suggests that the $(Zr,Mo)B_2$ shell solid solution may be responsible for the high strengths at elevated temperatures observed by Silvestroni and Sciti. In a computational study, Dai and Zhou used first principles density functional theory (DFT) to calculate changes to the minimum critical resolved shear stress necessary for dislocation travel in ZrB_2 for different group IV, V, and VI transition metal (TM) additives in substitutional solid solution in ZrB_2 [146]. Their results show that dislocations via the (0001) [-2110]/3 basal slip system are controlled by TM-B bonds, and that substitution of different TM atoms for Zr can facilitate nucleation of dislocations. Of the five TM additives studied in solid solution (Hf, Ta, Nb, Mo, and W), Mo and W were predicted to have the greatest effect, each decreasing the activation energy for basal dislocation nucleation by ~80% with

respect to pure ZrB_2 due to differences in the bonding characteristics of Mo and W atoms. Dai and Zhou proposed that this increased ability for limited plastic deformation in the diboride grains at elevated temperatures would increase the flaw tolerance of ZrB_2-based materials, alleviating stress at crack tips and dissipating fracture energy by limited plastic deformation. The ZrB_2-$MoSi_2$ materials studied by Silvestroni and Sciti [10, 22, 67] are specifically referenced by Dai and Zhou as possible examples of this phenomenon because they display extensive $(Zr,Mo)B_2$ SS shell as well as high strength at elevated temperatures. If this theory is correct, a comparison of the elevated-temperature mechanical properties of a ZrB_2 material with a core-shell type microstructure (such as C10) and a ZrB_2 material with a fully homogenized solid solution (such as those prepared by McClane et al. [37]) would be an interesting topic of future study.

The support of the current study's findings for Dai and Zhou's theory is inconclusive. While the two compositions that display the highest strength values at 1500°C do contain significant amounts of SS shell (~23.4 vol.% for C10 and ~13.0 vol.% for C20), other compositions that contain similar or greater amounts of SS shell (F5 with ~27.5 vol.%, F10 with ~24.9 vol.%, M5 with ~23.2 vol.% and M10 with ~23.2 vol.%) display considerably lower strengths at 1500°C, and poor strength retention from room temperature. Dai and Zhou do not discuss any trend for dislocation nucleation as a function of TM solute concentration, but it is a feasible addition to their theory that greater solute content could further facilitate dislocation nucleation. The estimates of MoB_2 content in the SS shell based on XRD lattice parameter shifts [139] are inconclusive concerning the relationship of elevated temperature strength with the MoB_2 content in the SS shell. Although the estimated MoB_2 content in the SS shell was estimated to be higher in C10 (3.4 mol.%) than that in M5 (2.2 mol.%), which correlates with the greater flexure strength of C10 compared to M5, the estimated MoB_2 contents in the SS shells of M10, M20, C40 and C50 were similar to or greater than that of C10 but are not coupled with high elevated temperature strength. In these cases, however, it should be noted that the other compositions contain more $MoSi_2$ than M5 and C10. The yield strength of $MoSi_2$ has been reported to be >10 MPa at 1500°C for polycrystalline material [57, 58] and from 40 up to ~240 MPa for oriented single crystals [21]. It is possible that failure in compositions with large maximum $MoSi_2$ cluster size could

originate in $MoSi_2$ clusters that began plastic deformation early during flexure testing and surpassed their ultimate tensile strength, although observation of diagnostic ductile void formation or cup-and-cone fracture was not possible on oxidized fracture surfaces. This subject merits more experimentation that includes a greater number of compositions with similar $MoSi_2$ contents that can be directly compared.

Finally, elevated-temperature fracture toughness values should support the theory of increased elevated-temperature strength due to dislocation nucleation in the shell, but these results are inconclusive. The elevated-temperature behavior of C10 and M5 are used for comparison in this case because they are similar in their processing, microstructure, and oxidation behavior. C10 was hot pressed for 60 minutes at 1925°C while M5 was hot pressed for 29 minutes at 1900°C, both C10 and M5 contained ~23 vol.% SS shell similar amounts of SiO_2, and they retained similar amounts of $MoSi_2$ (0 and 2 vol.% respectively) resulting in similar oxidation behavior and linear stress-strain response during flexure testing. M5 displayed the lowest fracture toughness (4.1 ± 0.2 $MPa \cdot m^{1/2}$) of any composition, and C10 displayed the second-lowest elevated-temperature fracture toughness (4.3 ± 0.5 $MPa \cdot m^{1/2}$). The primary differences are that C10 spent 60 minutes at its hot pressing temperature while M5 was held for 29 minutes, that the average grain size of C10 was ~4.6 ± 2.8 μm while the average grain size of M5 was ~2.8 ± 1.3 μm, and that C10 displayed the highest elevated-temperature strength of any composition (604 ± 34 MPa) while M5 displayed the lowest elevated-temperature strength (250 ± 66 MPa). The increase in fracture toughness of C10 and M5 from room temperature to 1500°C could be due to a shift from transgranular to intergranular fracture as mentioned in section 3.3, but another possible source of this fracture toughness increase could be high-temperature plasticity of the SS shell. In either case, however, the small difference between the elevated-temperature fracture toughness values of C10 and M5 is not likely the cause of the large difference flexure strength at 1500°C. Because strength of linear-elastic brittle materials is a function of both the fracture toughness and the flaw severity, an in-depth fractographic investigation of these two materials would aid in understanding strength retention, although in the present study this was not possible due to oxidation of the fracture surfaces. Strength and toughness testing of C10 and M5 at elevated temperatures in inert atmosphere is recommended to gain an understanding of

the origins of high strength at elevated temperatures but is outside the scope of the present study.

4. SUMMARY

Fifteen hot pressed ZrB_2-$MoSi_2$ ceramics, made from three different ZrB_2 starting powders with differing ZrB_2 median particle sizes and with $MoSi_2$ contents between 5 and 70 vol.%, were evaluated microstructurally and mechanically. The average ZrB_2 grain size increased with increasing ZrB_2 starting powder particle size and decreased with increasing $MoSi_2$ content, while maximum ZrB_2 grain size remained similar to the d_{90} of starting ZrB_2 powders but did not change with $MoSi_2$ content. All compositions experienced either partial or complete $MoSi_2$ decomposition during hot pressing, and ZrB_2 grains contained both a ZrB_2 core and $(Zr,Mo)B_2$ solid solution shell.

Elastic behavior of ZrB_2-$MoSi_2$ ceramics generally followed ROM trends based on the component phases and were consistent with previously reported values, with Young's modulus, shear modulus, and Poisson's ratio all decreasing with increasing $MoSi_2$ content in FX, MX, and CX. Interestingly, Young's modulus also decreased with decreasing ZrB_2 median powder particle size, from a range of 539 to 453 GPa for CX, to a range of 531 to 494 GPa for MX, to a range of 481 to 446 GPa for FX. Although this trend can be partially explained by higher contents of low modulus tertiary phases such as SiO_2 in compositions made with finer starting ZrB_2 powders, the behavior is not yet fully understood. Room temperature fracture toughness (2.7 to 3.9 $MPa \cdot m^{½}$) did not trend with $MoSi_2$ content or with ZrB_2 starting particle size. Room temperature flexure strength did not trend with $MoSi_2$ content but decreased with increasing ZrB_2 starting particle size from 700 to 800 MPa for FX, to 560 to 720 MPa for MX, to 440 to 590 MPa for CX. Pullout of surface ZrB_2 grains during final surface grinding caused surface voids on the order of the maximum ZrB_2 grain size, which acted as strength-limiting flaws at room temperature. Thus, decreasing the maximum ZrB_2 grain size is expected to increase the flexure strength of ZrB_2-$MoSi_2$ ceramics at room temperature.

Fracture toughness at 1500°C increased with both $MoSi_2$ content and with ZrB_2 starting particle size, from 4.1 $MPa \cdot m^{½}$ for M5 to 5.7 $MPa \cdot m^{½}$ for M30, and from 4.3 $MPa \cdot m^{½}$ for C10 to 8.7 $MPa \cdot m^{½}$ for C70. The increase of fracture toughness with increasing $MoSi_2$ content was attributed to stress relaxation at the crack tip by plastic

deformation of $MoSi_2$ clusters, while the increase in toughness with increasing ZrB_2 powder particle size was attributed to increased crack deflection and crack bridging by larger ZrB_2 grains. Flexure strength at 1500°C followed two different trends below ~30 vol.% $MoSi_2$, while at 30 vol.% and greater $MoSi_2$ contents flexure strength remained between 420 and 460 MPa for all compositions. In trend (A), flexure strength increased from 250 to 300 MPa to ~430 MPa as $MoSi_2$ content increased, due to a transition from unprotective oxidation to protective oxidation in which a continuous borosilicate glassy layer was able to form, limiting the size of oxidation damage. Although FX and MX both followed trend (A), the strength of FX was between 100 and 50 MPa higher than that of MX between 5 and 20 vol.% $MoSi_2$ additions, which was attributed to the dependence of the critical flaw size on the grain size via the morphology of the oxidation damage. In trend (B), flexure strength of CX decreased from 605 MPa for C10 to 540 MPa for 20 to 445 MPa for C30. The impressive strength of C10 and C20 is not controlled by oxidation behavior or by ZrB_2 grains size in the way that was observed in trend (A). It is possible that dissolved Mo atoms in the SS shell increased flaw tolerance by facilitating dislocation formation in the diboride, a theory that is supported by select compositions from other studies.

ACKNOWLEDGEMENTS

The authors would like to thank Daniele Dalle Fabbriche for assistance with hot pressing, Cesare Melandri for assistance with mechanical testing and optical microscopy, and Dr. Jeremy Watts for advice and assistance throughout the project.

FUNDING

This work was supported by the United States National Science Foundation's Materials World Network through grant DMR-1209262, and funding from National Research Council of Italy for the project, “Dual Composite Ceramics for Improved Properties.”

REFERENCES

1. L. Silvestroni and D. Sciti, "Effects of $MoSi_2$ additions on the properties of Hf– and Zr–B_2 composites produced by pressureless sintering," *Scripta Materialia*, 57[2] 165-68 (2007).

2. D. Sciti, S. Guicciardi, A. Bellosi, and G. Pezzotti, "Properties of a Pressureless-Sintered ZrB_2-$MoSi_2$ Ceramic Composite," *Journal of the American Ceramic Society,* 89[7] 2320-22 (2006).

3. W. G. Fahrenholtz, E. J. Wuchina, W. E. Lee, and Y. Zhou, "Ultra-high Temperature Ceramics: Materials for Extreme Environment Applications." John Wiley & Sons: Hoboken, NJ, USA, (2014).

4. R. J. Grohsmeyer, G. E. Hilmas, F. T. Monteverde, W. G. Fahrenholtz, and E. W. Neuman, "ZrB_2-$MoSi_2$ Ceramics with Varying $MoSi_2$ Content and ZrB_2 Powder Particle Size: Mechanical Properties of MX at Room Temperature and 1500°C in Air," *Journal of the European Ceramic Society,* TBD[TBD] TBD-TBD (2017b).

5. V. O. Lavrenko, A. D. Panasyuk, O. M. Grigorev, O. V. Koroteev, and V. A. Kotenko, "High-Temperature (to 1600°C) Oxidation of ZrB_2-$MoSi_2$ Ceramics in Air," *Powder Metallurgy and Metal Ceramics,* 51[1-2] 102-07 (2012).

6. L. Silvestroni, G. Meriggi, and D. Sciti, "Oxidation behavior of ZrB_2 composites doped with various transition metal silicides," *Corrosion Science,* 83 281-91 (2014).

7. D. Sciti, M. Brach, and A. Bellosi, "Oxidation behavior of a pressureless sintered ZrB_2–$MoSi_2$ ceramic composite," *Journal of Materials Research,* 20[04] 922-30 (2005).

8. H.-T. Liu, J. Zou, D.-W. Ni, J.-X. Liu, and G.-J. Zhang, "Anisotropy oxidation of textured ZrB_2–$MoSi_2$ ceramics," *Journal of the European Ceramic Society,* 32[12] 3469-76 (2012).

9. M. Brach, V. Medri, and A. Bellosi, "Corrosion of pressureless sintered ZrB_2–$MoSi_2$ composite in H_2SO_4 aqueous solution," *Journal of the European Ceramic Society,* 27[2-3] 1357-60 (2007).

10. V. O. Lavrenko, V. A. Shvets, V. M. Talash, V. A. Kotenko, and T. V. Khomko, "Electrochemical Oxidation of ZrB_2-$MoSi_2$ Ceramics in a 3% NaCl Solution," *Powder Metallurgy and Metal Ceramics,* 50[11-12] 749-53 (2012).

11. D. Sciti, L. Silvestroni, L. Mercatelli, J.-L. Sans, and E. Sani, "Suitability of ultra-refractory diboride ceramics as absorbers for solar energy applications," *Solar Energy Materials and Solar Cells,* 109 8-16 (2013).

12. L. Mercatelli, E. Sani, D. Jafrancesco, P. Sansoni, D. Fontani, M. Meucci, S. Coraggia, L. Marconi, J. L. Sans, E. Beche, L. Silvestroni, and D. Sciti, "Ultra-refractory Diboride Ceramics for Solar Plant Receivers," *Energy Procedia,* 49 468-77 (2014).

13. A. L. Chamberlain, W. G. Fahrenholtz, and G. E. Hilmas, "Characterization of Zirconium Diboride-Molybdenum Disilicide Ceramics," *Ceramic Transactions,* 153 299-308 (2003).

14. E. W. Neuman, G. E. Hilmas, W. G. Fahrenholtz, and A. Dominguez-Rodriguez., "Strength of Zirconium Diboride to 2300°C," *Journal of the American Ceramic Society,* 96[1] 47-50 (2013).

15. W. G. Fahrenholtz, "Thermodynamic Analysis of ZrB_2-SiC Oxidation: Formation of a SiC-Depleted Region," *Journal of the American Ceramic Society,* 90[1] 143-48 (2007).

16. S. Guo, T. Mizuguchi, M. Ikegami, and Y. Kagawa, "Oxidation behavior of ZrB_2–$MoSi_2$–SiC composites in air at 1500°C," *Ceramics International,* 37[2] 585-91 (2011).

17. R. J. Grohsmeyer, G. E. Hilmas, F. T. Monteverde, W. G. Fahrenholtz, A. D'Angio, D. Sciti, and L. Silvestroni, "ZrB_2-$MoSi_2$ Ceramics with Varying $MoSi_2$ Content and ZrB^2 Powder Particle Size: Processing and Microstructure," *Journal of the European Ceramic Society,* TBD[TBD] TBD (2017a).

18. A. Bellosi, F. Monteverde, and D. Sciti, "Fast Densification of Ultra-High-Temperature Ceramics by Spark Plasma Sintering," *International Journal of Applied Ceramic Technology,* 3[1] 32-40 (2006).

19. D. Sciti, L. Silvestroni, and M. Nygren, "Spark plasma sintering of Zr- and Hf-borides with decreasing amounts of $MoSi_2$ as sintering aid," *Journal of the European Ceramic Society,* 28[6] 1287-96 (2008).

20. S. R. Srinivasan, R. B. Schwarz, and J. D. Embury, "Ductile-To-Brittle Transition in $MoSi_2$," pp. 1099-104 in High-Temperature Ordered Intermetallic Alloys V. Vol. 288Edited by I. Baker, R. Darolia, J. D. Whittenberger, and M. H. Yoo.

21. D. J. Evans, S. A. Court, P. M. Hazzledine, and H. L. Fraser, "Deformation Mechanisms in the Intermetallic Compound $MoSi_2$," pp. 567-72 in High-Temperature Ordered Intermetallic Alloys V. Vol. 288Edited by I. Baker, R. Darolia, J. D. Whittenberger, and M. H. Yoo.

22. H. Mehrer, H. E. Schaefer, I. V. Belova, and G. E. Murch, "Molybdenum Disilicide - Diffusion, Defects, Diffusion Correlation, and Creep," *Defect and Diffusion Forum,* 322 107-28 (2012).

23. O. Unal, J. J. Petrovic, D. H. Carter, and T. E. Mitchell, "Dislocations and Plastic Deformation in Molybdenum Disilicide," *Journal of the American Ceramic Society,* 73[6] 1752-57 (1990).

24. Y. Q. Liu, G. Shao, and P. Tsakiropoulous, "On the Oxidation Behavior of $MoSi_2$," *Intermetallics,* 9 125-36 (2001).

25. S.-Q. Guo, T. Mizuguchi, T. Aoyagi, T. Kimura, and Y. Kagawa, "Quantitative Electron Microprobe Characterizations of Oxidized ZrB_2 Containing $MoSi_2$ Additives," *Oxidation of Metals,* 72[5-6] 335-45 (2009).

26. M. Kazemzadeh Dehdashti, W. G. Fahrenholtz, and G. E. Hilmas, "Effects of transition metals on the oxidation behavior of ZrB_2 ceramics," *Corrosion Science,* 91 224-31 (2015).

27. D. Sciti, F. Monteverde, S. Guicciardi, G. Pezzotti, and A. Bellosi, "Microstructure and mechanical properties of ZrB_2–$MoSi_2$ ceramic composites produced by different sintering techniques," *Materials Science and Engineering: A,* 434[1-2] 303-09 (2006).

28. H.-T. Liu, W.-W. Wu, J. Zou, D.-W. Ni, Y.-M. Kan, and G.-J. Zhang, "In situ synthesis of ZrB_2–$MoSi_2$ platelet composites: Reactive hot pressing process, microstructure and mechanical properties," *Ceramics International*, 38[6] 4751-60 (2012).

29. S. Q. Guo, T. Nishimura, T. Mizuguchi, and Y. Kagawa, "Mechanical properties of hot-pressed ZrB_2-$MoSi_2$-SiC composites," *Journal of the European Ceramic Society*, 28 1891-98 (2008).

30. R. J. Grohsmeyer, G. E. Hilmas, F. T. Monteverde, and W. G. Fahrenholtz, "Densification Process and Formation of Solid Solution Shell in ZrB_2-$MoSi_2$ Ceramics with Varying $MoSi_2$ Content and ZrB_2 Powder Particle Size," *Journal of the European Ceramic Society*, TBD[TBD] TBD-TBD (2017).

31. W. Li, X. Zhang, C. Hong, W. Han, and J. Han, "Microstructure and mechanical properties of zirconia-toughened ZrB_2–$MoSi_2$ composites prepared by hot-pressing," *Scripta Materialia*, 60[2] 100-03 (2009).

32. F. Monteverde, "The addition of SiC particles into a $MoSi_2$-doped ZrB_2 matrix: Effects on densification, microstructure and thermo-physical properties," *Materials Chemistry and Physics*, 113 626-33 (2009).

33. J. B. Wachtman, W. R. Cannon, and M. J. Matthewson, "Mechanical Properties of Ceramics,*"* pp. 479 2 ed. J. Wiley and Sons, Inc.: Hoboken, NJ, USA, (2009).

34. J. L. Watts, G. E. Hilmas, and W. G. Fahrenholtz, "Mechanical Characterization of ZrB_2-SiC Composites with Varying SiC Particle Sizes," *Journal of the American Ceramic Society*, 94[12] 4410-18 (2011).

35. N. L. Okamoto, M. Kusakari, K. Tanaka, H. Inui, and S. Otani, "Anisotropic elastic constants and thermal expansivities in monocrystal CrB_2, TiB_2, and ZrB_2," *Acta Materialia*, 58[1] 76-84 (2010).

36. I. R. Shein and A. L. Ivanovskii, "Elastic properties of mono- and polycrystalline hexagonal AlB_2-like diborides of s, p and d metals from first-principles calculations," *Journal of Physics: Condensed Matter*, 20[41] 415218 (2008).

37. P. K. Yadawa, S. K. Verma, G. Mishra, and R. R. Yadav, "Effect of Elastic Constants on the Ultrasonic Properties of Group VIB Transition Metal Diborides," *Journal of Nanotechnology & Advanced Materials*, 2[1] 1-9 (2014).

38. H. J. McSkimin, "Measurement of Elastic Constants at Low Temperatures by Means of Ultrasonic Waves–Data for Silicon and Germanium Single Crystals, and for Fused Silica," *Journal of Applied Physics*, 24[8] 988 (1953).

39. C. F. Smith and W. B. Crandall, "Calculated High-Temperature Elastic Constants for Zero Porosity Moniclinic Zirconia," *Journal of the American Ceramic Society*, 47[12] 624-27 (1964).

40. "ASM Engineered Materials Reverence Book,*"* 2 ed. ASM International: Materials Park, OH, USA, (1994).

41. J. J. Cleveland and R. C. Bradt, "Grain Size/Microcracking Relations for Pseudobrookite Oxides," *Journal of the American Ceramic Society,* 61[11-12] 478-81 (1978).

42. W. G. Fahrenholtz, G. E. Hilmas, I. G. Talmy, and J. A. Zaykoski, "Refractory Diborides of Zirconium and Hafnium," *Journal of the American Ceramic Society,* 90[5] 1347-64 (2007).

43. W. G. Fahrenholtz, G. E. Hilmas, S. Zhang, and S. Zhu, "Pressureless Sintering of Zirconium Diboride: Particle Size and Additive Effects," *Journal of the American Ceramic Society,* 91[5] 1398-404 (2008).

44. E. J. L. Y.-L. Jeng, "Review Processing of molybdenum disilicide," *Journal of Materials Science,* 29 2557-71 (1994).

45. J. J. Petrovic, "Toughening strategies for $MoSi_2$-based high temperaure structural silicides," *Intermetallics,* 8 1175-82 (2000).

46. S. Maloy, A. H. Heuer, J. Lewendowski, and J. Petrovic, "Carbon Additions to Molybdenum Disilicide: Improved High-Temperature Mechanical Properties," *Journal of the American Ceramic Society,* 74[10] 2704-06 (1991).

47. S.-Q. Guo, T. Nishimura, T. Mizuguchi, and Y. Kagawa, "Mechanical properties of hot-pressed ZrB_2–$MoSi_2$–SiC composites," *Journal of the European Ceramic Society,* 28[9] 1891-98 (2008).

48. A. L. Chamberlain, W. G. Fahreholtz, and Hilmas, "Characterization of Zirconium Diboride-Molybdenum Disilicide Ceramics," *Ceramic Transactions,* 153 299-398 (2003).

49. E. W. Neuman, G. E. Hilmas, and W. G. Fahrenholtz, "Mechanical behavior of zirconium diboride–silicon carbide ceramics at elevated temperature in air," *Journal of the European Ceramic Society,* 33[15-16] 2889-99 (2013).

50. J. L. Watts, G. Hilmas, and W. G. Fahrenholtz, "Mechanical Characterization of ZrB_2-SiC Composites with Varying SiC Particle Sizes," *Journal of the American Ceramic Society,* 94[12] 4410-18 (2011).

51. E. W. Neuman, "Elevated Temperature Mechanical Properties of Zirconium Diboride Based Ceramics," pp. 278. in Ceramic Engineering, Vol. Ph.D. Missouri University of Science and Technology, Rolla, MO, USA, 2014.

52. P. Chantikul, S. J. Bennison, and B. R. Lawn, "Role of Grain Size in the Strength and R-curve Properties of Alumina," *Journal of the American Ceramic Society,* 73[8] 2419-27 (1990).

53. G. Pezzotti, "On the Actual Contribution of Crack Deflection in Toughening Platelet-Reinforced Brittle-Matrix Composites," *Acta Metallurgica et Materialia,* 41[6] 1825-39 (1993).

54. S. A. Maloy, J. J. Lewandowski, and A. H. Heuer, "Effects of Carbon Additions on the High Temperature Mechanical Properties of Molybdenum Disilicide," *Materials Science and Engineering: A,* 155 159-63 (1992).

55. S. Maloy, A. H. Heuer, J. Lewandowski, and J. Petrovic, "Carbon Additions to Molybdenum Disilicide: Improved High-Temeprature Mechanical Properties," *Journal of the American Ceramic Society,* 74[10] 2704-06 (1991).

56. R. P. Kusy, "Influence of Particle Size Ratio on the Continuity of Aggregates," *Journal of Applied Physics,* 48 5301-05 (1977).

57. F. T. Monteverde and L. Silvestroni, "Combined Effects of WC and SiC on densification and thermo-mechanical stability of ZrB_2 ceramics," *Materials & Design,* 109[5 November] 396-407 (2016).

58. F.-Z. Dai and Y. Zhou, "Effects of transition metal (TM=Zr, Hf, Nb, Ta, Mo, W) elements on the shear properties of TMB_2s: A first-principles investigation," *Computational Materials Science,* 117 266-69 (2016).

59. L. Silvestroni, H.-J. Kleebe, S. Lauterbach, and M. Muller, "Transmission electron microscopy on Zr- and Hf- borides with $MoSi_2$ addition: Densification mechanisms," *Journal of Materials Research,* 25[5] 828-33 (2010).

60. D. L. McClane, W. G. Fahrenholtz, G. E. Hilmas, and D. Smith, "Thermal Properties of (Zr, TM)B_2 Solid Solutions with TM = Ta, Mo, Re, V, and Cr," *Journal of the American Ceramic Society,* 98[2] 637-44 (2015).

61. W. S. Gibbs, J. J. Petrovic, and R. E. Honnel, "SiC Whisker-$MoSi_2$ Matrix Composites," *Ceramic Engineering Science Proceedings,* 8[7-8] 645-48 (1987).

62. A. K. Vasudevan and J. J. Petrovic, "A Comparative Overview of Molybdenum Disilicide Composites," *Materials Science and Engineering: A,* 155 1-17 (1992).

Table I. Archimedes' bulk density, microstructural relative density, retained $MoSi_2$ content, average ZrB_2 grain size (GS), average ZrB_2 grain major elliptical axis, and cluster size (CS) for ZrB_2-$MoSi_2$ ceramics.

Composition	Bulk Density (g/cm^3)	Relative Density (%)	Measured $MoSi_2$ (vol.%)	$(Zr,Mo)B_2$ Shell SS (vol.%)	Avg. ZrB_2 GS (μm)	ZrB_2 Major Axis (μm)	ZrB_2 Max. GS (μm)	$MoSi_2$ CS (μm)	$MoSi_2$ Max. CS (μm)
F5	5.97	99.96	3.1 ± 0.7	27.5 ± 2.8	1.8 ± 0.9	2.2 ± 1.0	5.7	1.5 ± 0.7	5.3
F10	5.91	99.95	8.5 ± 1.0	24.9 ± 0.9	1.7 ± 0.9	2.1 ± 1.1	6.2	1.9 ± 1.0	6.4
F20	6.05	99.97	17.6 ± 1.7	19.7 ± 1.6	1.3 ± 0.8	1.6 ± 1.0	5.8	1.4 ± 1.0	8.1
F30	5.93	99.94	26.6 ± 2.2	N.M.	1.3 ± 0.8	1.7 ± 1.0	5.9	1.1 ± 1.1	12.3
F50	5.89	99.27	45.4 ± 3.7	6.7 ± 0.7	1.3 ± 0.9	1.7 ± 1.2	6.5	2.3 ± 3.7	-
M5	6.05	99.94	2.0 ± 0.8	23.2 ± 2.9	2.8 ± 1.3	3.5 ± 1.7	9.4	1.9 ± 1.1	6.2
M10	6.04	99.94	8.7 ± 2.0	23.2 ± 3.9	2.7 ± 1.4	3.4 ± 1.8	9.8	1.9 ± 1.2	8.8
M20	6.13	99.91	16.3 ± 0.7	14.4 ± 0.1	2.1 ± 1.2	2.7 ± 1.6	8.8	1.8 ± 1.2	11
M30	6.07	99.97	27.4 ± 2.7	10.0 ± 0.2	2.0 ± 1.2	2.5 ± 1.6	9.0	2.2 ± 1.8	24
C10	6.05	99.99	N.O.	23.4 ± 1.4	4.5 ± 2.8	6.0 ± 3.8	16	-	-
C20	6.07	99.94	18.1 ± 2.9	13.0 ± 1.6	3.4 ± 2.9	4.3 ± 3.7	30	2.8 ± 2.9	22
C30	6.11	99.98	25.7 ± 0.9	10.2 ± 1.8	2.6 ± 2.0	3.4 ± 2.9	18	3.3 ± 2.5	22
C40	6.17	99.96	34.3 ± 2.2	9.2 ± 2.3	2.5 ± 1.7	3.4 ± 2.4	15	3.4 ± 3.5	35
C50	6.17	99.99	42.8 ± 3.8	5.2 ± 1.3	2.4 ± 2.0	3.2 ± 2.7	17	-	-
C70	6.12	99.99	66.9 ± 3.9	3.4 ± 0.7	1.5 ± 1.3	2.0 ± 1.8	17	-	-

Averages are shown ± one standard deviation (N.O. = not observed, N.M. = not measured but observed).

Table II. Dynamic elastic properties, Vickers hardness, four-point flexure strength, chevron-notch fracture toughness, and calculated critical flaw size ranges for hot-pressed ZrB_2-$MoSi_2$ ceramics.

Composition	Young's Modulus, Dynamic (GPa)	Shear Modulus (GPa)	Poisson's Ratio	Vickers Hardness (GPa)	Flexure Strength (MPa)	Fracture Toughness (MPa·m½)	Calculated Flaw Size (μm)
							Y = 1.99
F5	481 ± 17	210**	0.145**	16.5 ± 0.2	768 ± 89	N.M.	-
F10	476 ± 2	209**	0.147**	16.2 ± 0.4	795 ± 97	N.M.	-
F20	464 ± 0.5	201**	0.161**	16 ± 0.3	701 ± 153	N.M.	-
F30	446 ± 0.5	194**	0.162**	15.3 ± 0.4	804 ± 64	N.M.	-
F50*	N.M.	N.M.	N.M.	N.M.	736 ± 85	3.7 ± 0.3	4.4–9.6
M5	531 ± 3	236	0.134	16.6 ± 0.4	619 ± 104	3.0 ± 0.2	3.8–9.4
M10	518 ± 5	229	0.137	16.1 ± 0.4	628 ± 125	3.8 ± 0.1	6.1–14
M20	497 ± 3	220	0.141	16.0 ± 0.4	723 ± 88	2.9 ± 0.6	2.1–7.6
M30	494 ± 7	220	0.142	15.1 ± 0.4	557 ± 111	2.8 ± 0.4	3.4–13
C10	539 ± 2	237	0.136	16.9 ± 0.5	445 ± 72	3.1 ± 0.4	13–53
C20	521 ± 10	227	0.141	15.4 ± 0.3	474 ± 132	3.9 ± 0.6	7.4–44
C30	504	220	0.143	15.0 ± 0.3	565 ± 66	2.7 ± 0.5	3.1–11
C40	493 ± 2	214	0.155	14.3 ± 0.6	442 ± 70	3.2 ± 0.2	8.6–20
C50	476 ± 8	210	0.150	13.5 ± 0.5	586 ± 83	3.3 ± 0.4	4.9–13
C70	453 ± 10	198	0.168	12.2 ± 0.4	576 ± 114	3.5 ± 0.6	4.3–20

*Flexure strength and fracture toughness specimens were smaller: 2 x 2.5 x 25 mm in size.

TableIII. Crosshead speeds used during flexure strength testing, mechanical properties of hot-pressed ZrB_2-$MoSi_2$ ceramics at 1500°C in air, and calculated critical flaw sizes.

Composition	Crosshead speed (mm/min)	Flexure strength (MPa)	Fracture toughness (MPa·m½)	Calculated Flaw Size (μm)
				Y = 1.99
F5	0.5	356 ± 16	N.M.	-
F10	0.5	361 ± 16	N.M.	-
F20	0.5	467 ± 64	N.M.	-
F30	0.5	427 ± 18	N.M.	-
F50*	1.0	426 ± 9	5.6 ± 0.4	37 - 53
M5	1.0	250 ± 66	4.1 ± 0.2	40 - 136
M10	1.0	299 ± 15	4.3 ± 0.2	44 - 64
M20	3.0	413 ± 25	5.4 ± 0.3	34 - 53
M30	3.0	437 ± 35	5.7 ± 0.6	30 - 63
C10	1.0	604 ± 34	4.3 ± 0.5	9 - 19
C20	1.0	541 ± 14	6.1 ± 0.1	30 - 35
C30	3.0	445 ± 28	6.6 ± 0.2	46 - 67
C40	4.0	461 ± 36	6.4 ± 0.5	34 - 66
C50	5.0	423 ± 20	7.3 ± 0.8	54 - 101
C70	7.0 to 10.0	-	8.7 ± 0.4	-

(N.M. = not measured).

* Flexure strength and fracture toughness specimens were smaller: 2 x 2.5 x 25 mm in size.

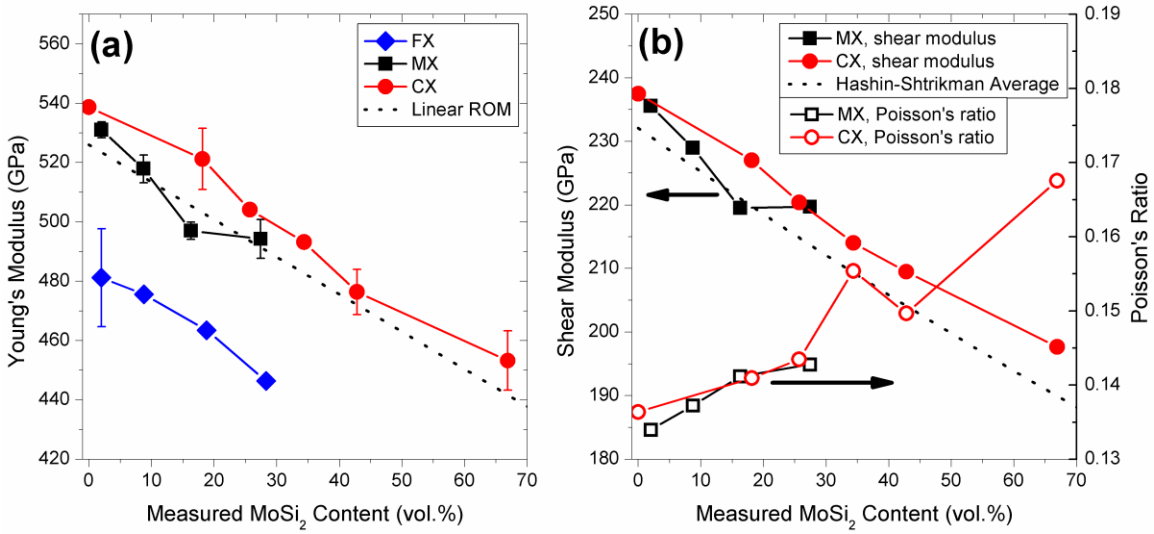

Fig. 1. Elastic moduli as a *function* of retained $MoSi_2$ content measured by dynamic sonic resonance on flat plates and bars.(a) Measured Young's modulus compared with linear ROM from literature; (b) hear modulus and Poisson's ratio showing the average of the upper and lower bounds of the Hashin-Shtrikman model for shear modulus.

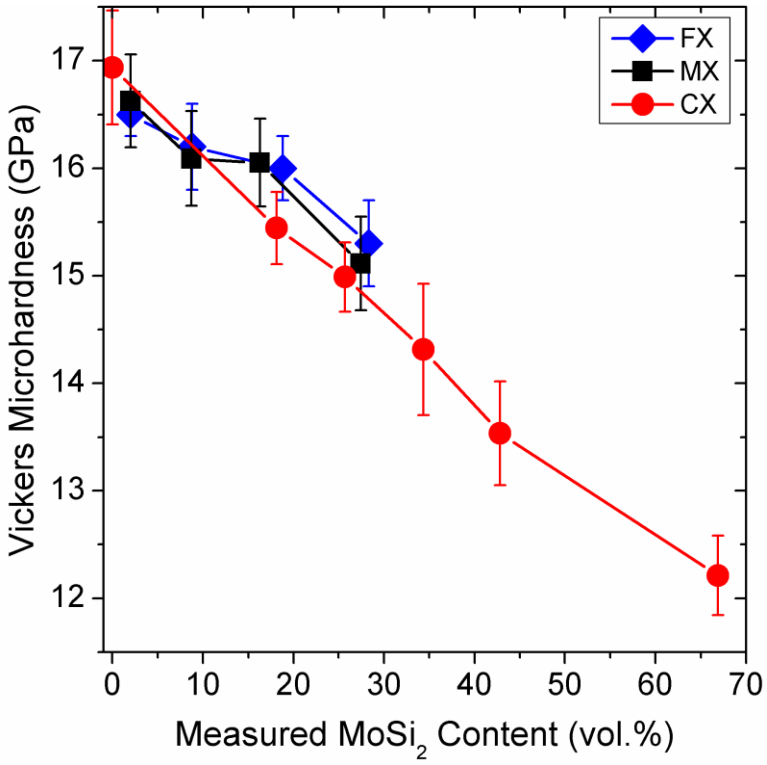

Fig. 2. Room temperature Vickers hardness as a function of measured $MoSi_2$ content.

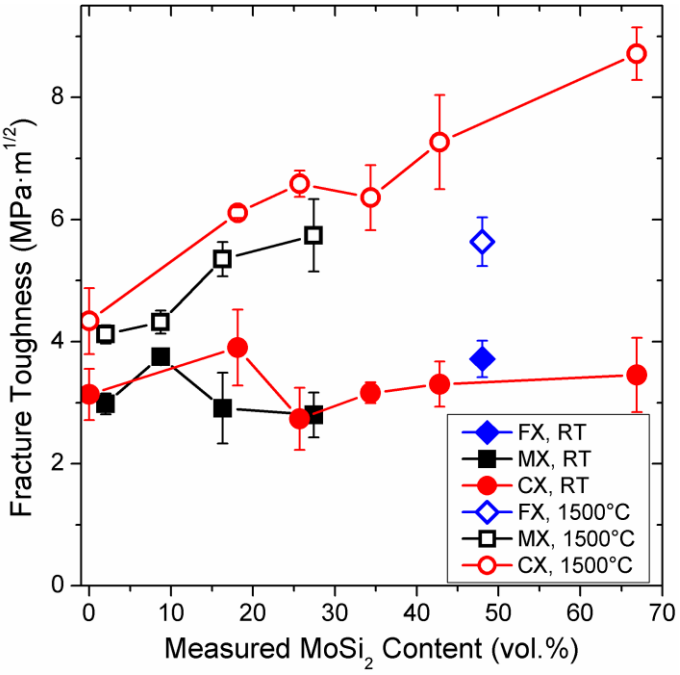

Fig. 3. Fracture toughness as a function of measured $MoSi_2$ content at room temperature and at 1500°C in air.

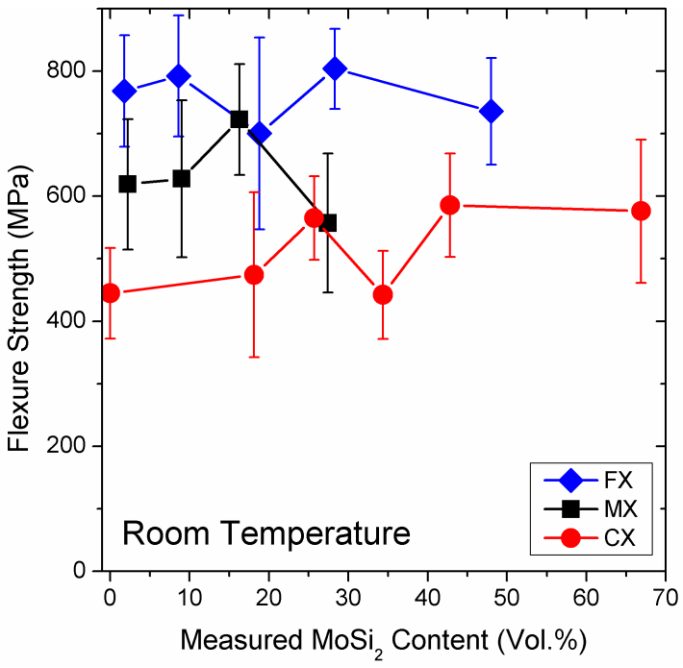

Fig. 4. Four-point flexure strength with respect to measured $MoSi_2$ content at room temperature.

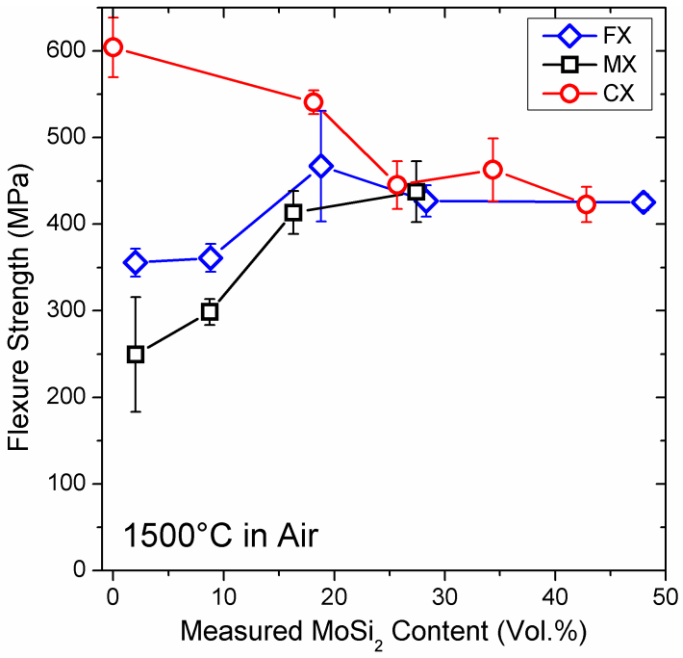

Fig. 5. Four-point flexure strength tested at 1500°C in air with respect to measured $MoSi_2$ content for composites in present study.FX and MX follow trend A (increasing flexure strength with increasing $MoSi_2$ content), and CX follows trend B (decreasing flexure strength with increasing $MoSi_2$ content).

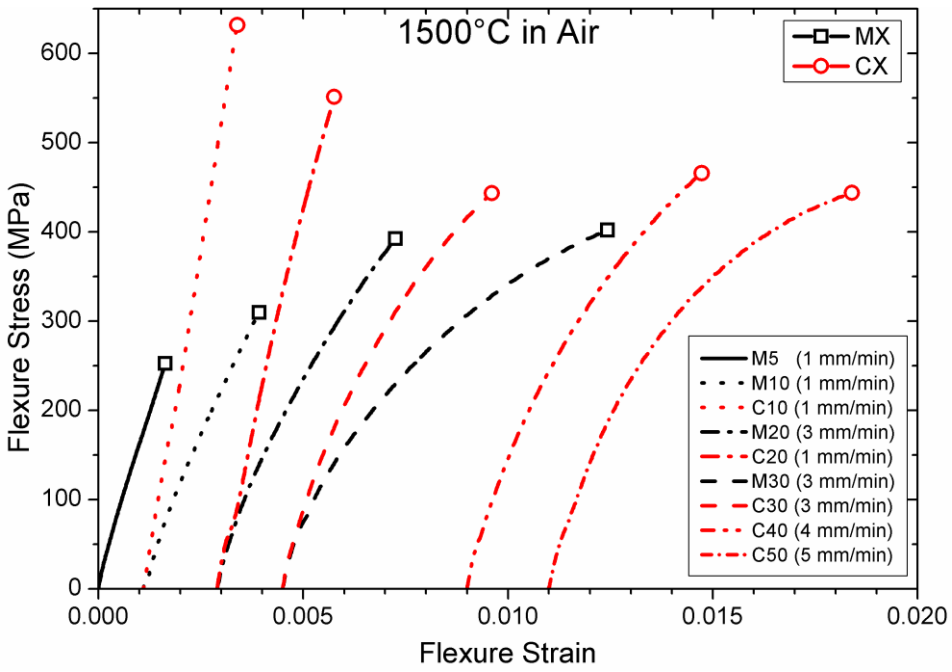

Fig. 6. Typical stress-strain curves of MX and CX specimens tested at 1500°C in air at varying crosshead rates from the present study.

V. PROCESSING OF ZrB_2-$MoSi_2$ DUAL COMPOSITE ARCHITECTURES

Ryan Grohsmeyer,[a, 11] Gregory Hilmas,[a, 12] Frederic Monteverde,[b] William Fahrenholtz[a]

[a] Materials Science and Engineering Department, Missouri University of Science and Technology, Rolla, MO 65409

[b] National Research Council of Italy, Institute of Science and Technology for Ceramics, Faenza, 48018 RA, Italy

ABSTRACT

Mechanical properties were measured at room temperature and 1500°C for ZrB_2-$MoSi_2$ dual composite architectures (DCAs) designed to increase fracture toughness of conventional ZrB_2-$MoSi_2$ ceramics without sacrificing strength at 1500°C in air. Four granule-matrix type DCAs were prepared via extrusion and hot pressing which retained defined zones (sub-composites) of differing engineered microstructure in the same bulk material. At room temperature, elastic moduli did not differ from conventional ceramics with similar overall $MoSi_2$ contents. Room temperature fracture toughness increased to 4.2 to 5.3 $MPa \cdot m^{½}$ due to crack deflection by spontaneous microcracks caused by CTE mismatch between granule and matrix sub-composites. Microcracking contributed to low room temperature flexure strengths of (~140 MPa) in all DCAs, and strengths of 320 and 360 MPa in DCA 2 and 2B at 1500°C, while the strengths of DCA 1 and 1B at 1500°C were further limited to 260 to 280 MPa by oxidation damage resulting from mismatched oxidation behavior between sub-composites. Three focus areas for future DCA development were identified: 1) resolve microcracking due to sub-composite CTE mismatch; 2) match the oxidation behavior of the sub-composites; and 3) use a discrete interface between sub-architectures to promote crack deflection.

Key Words: Dual Composite Architectures, Microstructures–final (B), Borides (D), Shaping (A)

---

[11] Present address: Corning Incorporated, Painted Post, NY, USA.

[12] Corresponding Author: ghilmas@mst.edu, +1-573-341-6102

1. INTRODUCTION

Modern technological advancement in the fields of jet propulsion, energy conversion, hypersonic flight, molten metals processing and others requires new structural materials for use in high-temperature oxidizing environments. Current material options for these applications include Ni-based superalloys, refractory metals, refractory monolithic ceramics, and fiber-reinforced ceramic matrix composites (CMCs), but each of these material families has serious drawbacks that limit their use in structural applications. Ni-based superalloys are limited by melting temperature, refractory metals by either poor oxidation resistance or high cost, monolithic ceramics by their tendency to brittle catastrophic failure, and CMCs are limited by fiber costs and complex fiber-matrix interactions. Another option for structural materials for extreme environments that offers the possibility of affordable raw materials and range of engineering design flexibility are dual composite (DC) architectures. A DC architecture is essentially a composite material on two different length scales, in which each of the large-scale composite's component materials are themselves composites with specifically engineered compositions and properties.

Peng et al. synthesized a metal-matrix composite by dispersing Al alloy-infiltrated clusters of Al_2O_3 short fibers in an Al alloy matrix, and reported crack deflection at the cluster-matrix interface [98]. Bogomol et al. prepared a ceramic DC architecture by dispersing ~100 μm particles of B_4C-TiB_2 solidified laminar eutectic composition in B_4C powder matrix and reported improved fracture toughness at room temperature [147]. The DC architectural concept has been successfully employed in the design of WC-Co cermets for room temperature rock drilling applications, allowing DC cermet materials to break away from the classic trade-off between fracture toughness and wear resistance [6, 96, 97, 148-150]. The approach involved dispersal of hard, wear-resistant WC granules with a low Co content in a continuous matrix of Co metal, which resulted in increase of both the fracture toughness and the wear resistance above those of conventional WC-Co materials with the same overall Co contents [6, 151]. These results established DC architectures as a promising new class of composite structural materials, but current DC architectures are not suited to use at elevated temperatures in oxidizing environments due to the poor oxidation resistance of the components and the melting temperatures of the

metal binders. Thus, different materials must be used for DC architectures designed for use in extreme environments.

Dual composite architectures are similar to fibrous monoliths, another alternative form of composite material that has been proposed for elevated-temperature use [2], in that their processing generally utilizes commercially available powders. But while fibrous monoliths are anisotropic 3-1 composite structures with 1-D filaments, DC architectures offer a more nearly isotropic 3-0 composite morphology, with 0-D granules dispersed in a continuous 3D matrix. In DC architectures reported in the literature, the granules have commonly been engineered to act as a hard, brittle, wear-resistant sub-composite, while the sub-composite forming the continuous matrix has been engineered to be ductile and contained little to no wear-resistant phase. The ductility of the matrix allowed the matrix to arrest cracks that propagate easily through the granules, preventing catastrophic failure of the entire part.

In terms of fracture energy, a crack will propagate if the elastic strain energy at a crack tip is greater than the energy required to create new fracture surfaces. He and Hutchinson developed a criterion for crack deflection at an interface between two elastic materials based on a consideration of fracture energy (Eq. 1)[152] stating that if the quotient of the fracture energy of the interface divided by the fracture energy of the material into which the crack is propagating is below the He-Hutchinson crack deflection curve (represented by G_d/G_p), then the crack is expected to deflect along the interface, according to

$$\frac{G_{IC}}{G_C} < \frac{G_d}{G_p} \tag{1}$$

where G_{IC} is the fracture energy of the interface, G_C is the fracture energy of the material into which the crack would propagate, G_d is the energy release rate of a deflected crack, and G_p is the energy release rate of a propagating crack. The crack deflection curve G_d/G_p was plotted by He and Hutchinson as a function of Dunder's α parameter (Eq. 2)[152] and is an asymmetric function of value ~0.25 at α=0.

$$\alpha = \frac{\frac{E_1}{1-\nu_1^2} - \frac{E_2}{1-\nu_2^2}}{\frac{E_1}{1-\nu_1^2} + \frac{E_2}{1-\nu_2^2}} \quad (2)$$

He and Hutchinson's criterion has been used to predict crack deflection in ZrB_2-based fibrous monoliths [2], and was used in the present study to predict crack deflection at granule-matrix interfaces in DC architectures at room temperature, when both sub-composites behaved in a linear-elastic fashion.

In the present study, zirconium diboride (ZrB_2) and molybdenum disilicide ($MoSi_2$) were chosen as the primary component materials out of which to fabricate the granule and matrix sub-composites. ZrB_2-$MoSi_2$ ceramics have been studied as candidate structural materials for use in extreme environments due to their retention of strength to high temperatures [10, 23, 42, 67], oxidation resistance to >1500°C [11, 63, 89], ductility at elevated temperatures [42, 134], thermal conductivity [37], and resistance to corrosion in acidic environments [101, 135]. ZrB_2 is a refractory ceramic that has been shown to exhibit high rigidity and strength up to 2300°C [18], but its low fracture toughness, resulting in brittle mechanical failure up to 2300°C [18], and its poor oxidation resistance above 1100°C [33] have limited its use. $MoSi_2$ imparts ductility through plastic deformation above its brittle to ductile transition temperature (BDTT) upon heating between 900 and 1300˚C, increasing the fracture toughness of ZrB_2 at 1500°C [19, 57, 94, 136]. $MoSi_2$ has also been shown to assist in the densification of ZrB_2 and in protecting it from oxidation via formation of a protective borosilicate glassy layer [11, 32].

The combination of ZrB_2 and $MoSi_2$ provides the opportunity to adjust the ductility, fracture toughness, and flexure strength of each sub-composite at elevated temperatures according to the relationships of these characteristics with the $MoSi_2$ content. In previous work, the trends of fracture toughness and flexure strength were systematically investigated for a range of conventional ZrB_2-$MoSi_2$ ceramics processed with 5 to 70 vol.% $MoSi_2$ additions and three commercial ZrB_2 powders with different median particle sizes. The research provided a baseline of material property data on an

array of ZrB_2-$MoSi_2$ ceramics from which candidates for granule and matrix sub-composites could be chosen [42, 121, 153]. The series of ceramics processed with coarse ZrB_2 powder (designated CX, where X represents the nominal vol.% of $MoSi_2$) contained compositions that displayed both the highest flexure strength (C10, at 604 MPa) and the highest fracture toughness (C70, at 8.7 MPa·$m^{½}$) at 1500°C. However, as fracture toughness increased with $MoSi_2$ content, flexure strength decreased, indicating a trade-off between strength and toughness with respect to $MoSi_2$ content (Fig. 1).

The purpose of the present study was to apply the dual composite architectural concept to ZrB_2-$MoSi_2$ ceramics to create a dual composite designed to increase damage tolerance. Specifically, the goal was to use the DCA concept to increase the fracture toughness while maintaining or increasing the flexure strength of conventional ZrB_2-$MoSi_2$ ceramics, specifically at elevated temperatures. A further goal was to escape the observed trade-off between flexure strength and fracture toughness in conventional ZrB_2-$MoSi_2$ ceramics and populate the area in the shaded triangle in Figure 1.

2. EXPERIMENTAL PROCEDURE

2.1. Processing and Extrusion Granulation. Compositions in the present study were batched using commercial ZrB_2 and $MoSi_2$ powders (H.C. Starck, Newton, MA, USA) as reported elsewhere [121]. The present study examines compositions batched with "coarse" ZrB_2 powder (d_{10} = 2.51 μm, d_{50} = 11.7 μm, d_{90} = 30.1 μm) mixed with grade B $MoSi_2$ powder. After pre-comminution of the $MoSi_2$ for 96 h, ZrB_2 and $MoSi_2$ powders were batched into primary architectures and mixed in ethanol by ball milling [121].

Granule compositions were mixed with nominally 45 vol.% thermoplastic polymer binder in a high-shear rheometer-mixer (C.W. Brabender Instruments, Inc., South Hackensack, NJ, USA). The polymer binder consisted of a mixture of ethylene ethyl acrylate (EEA, melt index 20, Dow Chemicals, Midland, MI, USA), isobutyl methacrylate (IBMA (B-67 resin 100%), Rohm and Haas, Philadelphia, PA, USA), and heavy mineral oil as a plasticizer (HMO, Aldrich, Milwaukee, WI), such that each total batch consisted of 55 to 57 vol.% solids, 20 to 21 vol.% EEA, 20 to 21 vol.% IBMA, and 2 to 5 vol.% HMO. The materials were mixed at 130°C at a spindle speed of 35 rpm for ~20 min, after which they were removed from the mixer, chopped, and remixed to

achieve full homogenization. The blended material was then pressed into a right circular cylinder feed rod 22 mm in diameter and 120 mm long at 130°C using a heated hydraulic press. The feed rod was loaded into a heated screw-driven press and ram extruded through a 300 μm diameter spinneret into filament at 140 to 150°C. This 300-μm-diameter filament was chopped in ~15 g batches a kitchen blender (J. Oster Manufacturing Co., WI, USA) at maximum speed in 200 mL distilled water for 200 s, resulting in cylindrical granules 300 μm in diameter with an aspect ratio of ~2:1 (Fig. 2). These granules were washed on a 60 mesh screen to remove fines and dried. After drying, the granules added to powder of the matrix composition in order to obtain nominally 50 vol.% granules and 50 vol.% matrix in the densified bulk ceramic. Granules were mixed with matrix powder by manually shaking granules and powder together in an HDPE bottle for 5 minutes. After mixing, the granule/powder mixture was poured into a graphite hot pressing die lined with BN-coated graphite foil and uniaxially pressed in the graphite die to ~2.5 MPa. The loaded die was then transferred to a retort furnace in which the polymer binder system in the granules was volatilized in flowing Ar by heating from room temperature to 600°C at a rate of 25°C/h. Finally, the graphite die was carefully removed from the retort furnace and loaded into a hot press. In order to evaluate any difference in behavior between DC architectures made with rigid granules and a ductile matrix, or ductile granules in a rigid matrix, both versions of each DC architecture were made and tested. The DC architectures with ductile granules in a rigid matrix were arbitrarily designated as “backwards” and are identified with a letter B.

2.2. Hot Pressing and Characterization. All compositions were densified by hot pressing at 1875°C and 30 MPa uniaxial pressure for approximately 60 min Table I), using intermediate isothermal vacuum holds at 1450°C and 1650°C for oxide volatilization. Hot pressing procedures are reported in previous work [121, 139].

After densification by hot pressing, compositions were characterized microstructurally according to procedures described elsewhere [121, 139]. Specimen surfaces were observed after surface grinding and after diamond polishing using a digital optical microscope (KH-3000, Hirox-USA, Hackensack, NJ), as well as with scanning electron microscopy (SEM) [121]. Final volume fractions of granules and matrix were measured by manual tracing and digital image analysis of optical micrographs. During

digital analysis, an equivalent-area ellipse was fitted to each traced granule, and the reported average diameter, aspect ratio, and major axis dimensions reported for granules are the dimensions of the fitted ellipses. Each DC architecture was analyzed in two orthogonal directions separately: first, the plane perpendicular to the direction of pressure application during hot pressing (referred to as "HP normal"), and second, planes orthogonal to the HP normal plane (referred to as "transverse"). For each DC architecture, 200 to 700 granules were analyzed on HP normal surfaces and 500 to 800 granules were analyzed on the transverse cross sectional surfaces. Final granule contents reported reflect all measurements in both HP normal and transverse directions, and the final $MoSi_2$ content of each composition were calculated assuming that the granule and matrix sub-composites retained their nominal $MoSi_2$ contents during hot pressing. The mean free path (MFP) through the matrix sub-composite was measured by randomly placing a grid of lines on micrographs and measuring at least 100 free paths through the matrix between intersections of the lines with any granule.

2.3. Mechanical Testing. Specimen preparation and mechanical testing methods are summarized here and are described in more detail in previous work [42]. Young's modulus, shear modulus, and Poisson's ratio were measured by impulse excitation of resonant vibration based on ASTM C1259, using specimen sizes of 50 mm x 15 mm x 3 mm and 45 mm x 4 mm x 3 mm (length by width by thickness).

Fracture toughness at room temperature and at 1500˚C was measured based on ASTM C1421 using type-A bars (nominally 45 mm x 3 mm x 4 mm) having a chevron notched beam (CNB) geometry in four-point bending using fully articulating fixtures. At room temperature, a crosshead rate of 0.018 mm/min was used, while at 1500°C a crosshead rate of 0.18 mm/min was used. Load and center-bar deflection data were collected at a frequency of 100 Hz. Bar specimens for both fracture toughness and flexure strength were cut out of hot pressed billets such that the force application direction during mechanical testing was parallel to the force application during hot pressing, and any anisotropy resulting from uniaxial densification during hot pressing was not investigated.

Room-temperature flexure strength was measured according to ASTM C1161 using type-B bars (nominally 45 mm x 4 mm x 3 mm) in four-point bending with fully articulating steel fixtures. Flexure strength was measured at 1500˚C in air using type-B

bars according to ASTM C1211 with a fully-articulating SiC fixture. Bars were cut by electrical discharge machining and finish ground using automatic surface grinders with resin-bonded diamond abrasive wheels [42]. Flexure tests were performed using a screw-driven instrumented load frame, and elevated temperature testing was performed in a $MoSi_2$ element furnace. A crosshead rate of 0.5 mm/min was used for all compositions at room temperature, and rates between 3.0 and 4.0 mm/min were used at 1500˚C.

3. RESULTS AND DISCUSSION

3.1. Microstructural Analysis. The granule and matrix sub-composite regions were retained in all DC architectures as discrete zones of differing composition, co-densified in the same bulk material (Figs. 3, 4, 5). Measured final bulk densities were 6.18 g/cm^3 for DCA 1 and 1B and 6.20 g/cm^3 for DCA 2 and 2B Table I), although 1 to 2 vol.% closed porosity was observed in the granules of DCA 1 (Fig. 3) and the matrix of DCA 1B. This was not unexpected, due to the fact that in previous studies the sub-composite used for the granules of DCA 1 and the matrix of DCA 1B, which contained nominally 90 vol.% coarse ZrB_2 powder and 10 vol.% $MoSi_2$ (designated C10), required a similar amount of time but at a higher temperature (1925°C) to reach full density [121]. Although this sub-composite underwent complete decomposition and loss of its $MoSi_2$ during densification individually at 1925°C [139], this was not the case in the present study, in which it was observed to contain some $MoSi_2$ after hot pressing. It is possible that the lower hot pressing temperature resulted in less $MoSi_2$ decomposition, and that the proximity of the sub-composite with 70 vol.% $MoSi_2$ additions (C70) in the DC architectures assisted in densification. For the purposes of the present discussion, the sub-composites in the DC architectures will be referred to by their designations used in previous studies that discussed their individual characterization (C10, C20, C70, Table I) [121, 139, 153], in which the letter C represents the coarse grade of ZrB_2 powder used and the following digits represent the nominal $MoSi_2$ content in volume %. Furthermore, it was assumed in the present discussion that the granule and matrix sub-composites retained their nominal $MoSi_2$ contents, although the presence of a ZrB_2 core-$(Zr,Mo)B_2$ solid solution shell structure of ZrB_2 grains in both the granules and matrix of DCA 1 indicate some decomposition of $MoSi_2$ did occur, which was expected when hot pressing

at 1875°C [139]. Figures 3a and 3b illustrate the meso- and microstructure of DCA 1 showing the relationship of the granules to the matrix.

Because of the uniaxial densification experienced during hot pressing, granules were flattened so as to appear lenticular when viewed in the transverse direction (Figs 4 and 5). The average aspect ratio of granules in the HP normal surface ranged from 1.5 ± 0.4 for DCA 1 to 2.1 ± 0.4 for DCA 1B, while the average aspect ratio of granules in the transverse surface range from 2.0 ± 0.6 for DCA 2 to 2.5 ± 0.8 for DCA 2B, and for each DC architecture the aspect ratio is greater when viewed in the transverse direction Table II). In the HP normal surface, many granule sections had elliptical and straight edges, apparently retaining shapes of the roughly cylindrical chopped granules. The average granule diameter was greater in the HP normal surface than in the transverse surface for each DC architecture, which was likely also due to the uniaxial densification during hot pressing. The average granule diameter in the HP normal surface ranged from 295 ± 115 μm in DCA 2 to 335 ± 111 μm in DCA 1, while the average granule diameter in the transverse surface ranged from 218 ± 68 μm in DCA 1B to 259 ± 83 μm in DCA 2. The maximum observed granule length was 50 to 150 μm higher in the HP normal surface for each DC architecture, and ranged from ~700 to ~1000 μm. Overall, the granule dimensions in the HP normal surface were similar to the dimensions of the chopped granules before binder burnout, indicating that the majority of densification was uniaxial, and that final granule geometry is closely controlled by the geometry of granules added to the matrix powder.

Although each DC architecture was intended to contain 50 vol.% granules and 50 vol.% matrix, the measured final granule contents do not match these nominal values Table I). DCA 1 and DCA 2 each contained ~55 vol.% granules, while DCA 1B contained ~42 vol.% granules and DCA 2 contained ~45 vol.% granules. While decomposition of $MoSi_2$ in the C70 sub-composite (which comprised the matrix in DCA 1 and 2 and the granules in DCA 1B and 2B) may be partially responsible for the apparent lack of this sub-composite in all four DC architectures, more detailed microstructural analysis of the final $MoSi_2$ contents in both granules and matrix is required to determine if this is the case. It is possible that a miscalculation of the solids loading in the polymer binder of the chopped granules resulted in differences between

nominal and measured granule contents in the DC architectures. The lower than nominal content of C70 sub-composite resulted in a lower than nominal overall $MoSi_2$ content (assuming that each sub-composite retained its nominal $MoSi_2$ content), with DCA 1 retaining ~37 vol.% $MoSi_2$, DCA 1B retaining ~35 vol.% $MoSi_2$, and DCA 2 and 2B retaining ~43 vol.% $MoSi_2$. In the following discussion, mechanical properties of the DC architectures are plotted with respect to these final overall $MoSi_2$ contents and are compared to the mechanical properties of the CX series of sub-composite compositions described in previous work, which are also plotted according to their measured final $MoSi_2$ contents [153].

Figures 3(c) and 3(d) show the interface between C10 granules and C70 matrix in DCA 1. Because the granules were added with no coating, the individual ZrB_2 and $MoSi_2$ grains at the interface between granule and matrix mesh, making the interface itself more difficult to distinguish as the magnification is increased. The average ZrB_2 grain size of individually-processed C10 (hot pressed at 1925°C) was 4.5 ± 2.8 μm, and the average grain size of individually-processed C20 (hot pressed at 1875°C, similar to the DC architectures in the present study), was 3.4 ± 2.9 μm. Thus, in DC architectures such as DCA 1 and 2 with average granule diameters between 220 and 340 μm, the granules are on average a factor of about 60 to 100 times larger than the ZrB_2 grains of which they are composed. Thermal expansion and oxidation behaviors discussed below indicate that the granules were sufficiently greater in size than their component grains to behave according to the properties of their overall ZrB_2-$MoSi_2$ sub-composite composition.

Spontaneous microcracking was observed in the C70 sub-composite in all four DC architectures, in the matrix of DCA 1 and 2, and in the granules of DCA 1B and 2B (Fig. 6), due to a mismatch in the coefficients of thermal expansion (CTE) of the granule and matrix sub-composites. Observed microcracks ranged from 50 to 500 μm in length. Cleveland and Bradt developed an equation to estimate the critical grain size required to produce spontaneous microcracking in anisotropic single-phase oxide ceramics [40]. Other studies have used Cleveland and Bradt's method to calculate the microcracking threshold of grain size in two-phase non-oxide ceramics in which the CTEs of the two phases are mismatched [39, 121]. Using polycrystalline average CTE values for ZrB_2 (6.98×10^{-6}/K, 20 to 1100°C) and $MoSi_2$ (8.56×10^{-6}/K, 20 to 1100°C) [38], overall CTE

values were calculated for the nominal granule and matrix sub-composites using the average of the upper and lower bounds given by the Rosen-Hashin rule of mixing (ROM) [154]. Using the measured average ± one standard deviation as upper and lower bounds of fracture toughness values along with Poisson's ratios and Young's moduli reported in previous work [153], the surface energy of fracture for C70 at room temperature was estimated to be in the range of 9.0 to 18.0 J/m^2. The critical granule size for microcracking in the DC architectures was calculated using the ROM values of CTE for C10 (7.13×10^{-6}/K), C20 (7.29×10^{-6}/K) and C70 (8.07×10^{-6}/K), measured Young's moduli and a ΔT of 1100°C, assuming that residual stresses began to accumulate as the densified ceramic cooled through the BDTT of $MoSi_2$ after hot pressing. With these values the critical granule size for microcracking of the C70 sub-composite was calculated to be between 250 and 500 μm in DCA 1 and 1B and between 360 and 720 μm in DCA 2 and 2B. These calculated critical granule sizes overlap the range of measured granule sizes these materials and are below the maximum observed granule sizes, indicating that microcracking should have been expected in all four DC architectures. Furthermore, it is likely that similar DC architectures made with granules that are smaller than the predicted critical size for microcracking could be manufactured without the formation of microcracks.

3.2. Mechanical Properties at Room Temperature. The Young's modulus of DCA 1 was 491 ± 3 GPa and the Young's modulus of DCA 1B was 495 GPa, in close agreement with the Young's modulus of C40 and the Young's modulus trend of the CX compositions from previous work [153], based on their final $MoSi_2$ contents Table III, Fig. 7). The Young's modulus of DCA 2 was ~490 GPa and the Young's modulus of DCA 2B was 487 ± 2 GPa, about 11 GPa higher than C50 at a similar final $MoSi_2$ content. Similarly, the shear moduli of all four DC architectures were between 212 and 214 GPa, placing those of DCA 1 and 1B close to that of C40 and those of DCA 2 and 2B about 3 GPA higher than expected for their final $MoSi_2$ content. Interestingly, the microcracking discussed above did not seem to have a deleterious effect on the elastic moduli of the DC architectures. Generally microcracking on the scale of the grain size decreases the apparent elastic moduli by decreasing the overall connectivity in the bulk [43]. It is possible that although the microcracks observed in the DC architectures are

much larger than the grain size, the total number of cracks is small and they may represent a relatively small total surface area of fracture and thus have a limited effect on the elastic moduli of the bulk material. Another possibility is that the final $MoSi_2$ contents of the DC architectures are significantly lower than those reported in Table I, which will be determined by further study.

At room temperature the fracture toughness values of the DC architectures were higher than those of the CX conventional ceramics (Fig. 8a). DCA 1 had a fracture toughness of 4.6 MPa·m^{½} and DCA 1B had a fracture toughness of 5.3 ± 0.6 MPa·m^{½}, while DCA 2 had a fracture toughness of 4.2 ± 0.4 MPa·m^{½} and DCA 2B had a fracture toughness of 4.6 ± 0.7 MPa·m^{½}. All CX conventional compositions displayed primarily transgranular fracture and had average fracture toughness values between 2.7 and 3.9 MPa·m^{½}, similar to the fracture toughness values of the nominally pure ZrB_2 and $MoSi_2$ components [153]. The increased fracture toughness of the DC architectures indicates a change in crack behavior from that of the CX conventional ceramics. DCA chevron notch bars typically exhibited multiple instances of crack arrest during testing, and fracture surfaces that separated were highly textured, with topographic features on the scale of the granules (Fig. 9). Individual conventional CX ceramics typically exhibited only one or two detectable but small instances of crack arrest during testing and their fracture surfaces were globally smooth, with texture similar to the grain size. Roughly half of the notched specimens of DCA 2 and 2B did not separate into two pieces during testing even when the load had dropped to below 5 N, and could be gently handled while remaining slightly bent after testing, indicating bridging of the crack by grains and/or granules. Although the fracture surfaces contained topographical features similar in size to the granules, it is unlikely that cracks were deflected at granule-matrix interfaces at room temperature. The fracture energies of the sub-composites are similar at room temperature (17.8 J/m^2 for C10, 29.2 J/m^2 for C20, and 26.3 J/m^2 for C70), giving values of G_{ic}/G_c of 1.47 for DCA 1, 0.68 for DCA 1B, 0.90 for DCA 2, and 1.11 for DCA 2B. At similar near-zero values of Dunder's α parameter (calculated to be ± 0.082 for DCA 1 and 1B, and ± 0.066 for DCA 2 and 2B), the value of He and Hutchinson's crack deflection criterion curve is less than the G_{ic}/G_c values for all DC architectures, between ~0.24 and ~0.26, indicating that crack deflection should not be expected at the granule-matrix

interface. The fracture surfaces contain facets of similar size to the observed microcracks, suggesting that during fracture the crack front was repeatedly deflected by the existing microcracks in the DC architectures, which likely caused momentary crack arrest observed in the force-deflection curves.

Room temperature flexure strength of the DC architectures was three to four times lower than corresponding CX conventional ceramics, with the average flexure strength of all four DC architectures falling between 136 and 143 MPa, with standard deviations between 14 and 17 MPa Table III, Fig. 10a). Fracture surfaces were similar to those of fracture toughness specimens, exhibiting topographic facets indicating crack deflection by existing microcracks, and no fracture mirror was evident (Fig. 10b). Using the average and one standard deviation in measured fracture toughness and flexure strength, a range of critical flaw sizes was calculated with a Griffith-type calculation using Y=1.99 to represent a long semi-circular surface flaw. The estimated flaw size range at room temperature varied from 150 to 430 μm for DCA 2B to 240 to 610 μm for DCA 1B, indicating that the similarly-sized microcracks discussed above are most likely the critical flaws causing failure in the DC architectures. The conventional ceramics C40 and C50 had room temperature flexure strengths of 442 and 586 MPa respectively, with calculated critical flaws sizes matching that of the maximum ZrB_2 grain sizes (between 5 and 20 μm), indicating that pullout of ZrB_2 grains during surface grinding left voids that acted as the critical flaws in those materials [42, 153]. Although the DC architectures experienced ZrB_2 grain pullout of the same nature, the presence of microcracks up to ~500 μm in size severely limited their strength at room temperature. A future DC architecture made with granule small enough to avoid spontaneous microcracking might be able to take advantage of the sub-critical residual stresses between granules and matrix to aid in crack deflection at room temperature, and without suffering the consequences of a large microcracks that are deleterious to flexure strength. Alternatively, the composition of one or both sub-composites could be adjusted by engineered addition of a third phase so as to match the overall CTE of the granules to that of the matrix. Such a phase must be compatible with the densification of ZrB_2-$MoSi_2$ ceramics, have a CTE significantly different from those of both ZrB_2 and $MoSi_2$, as well as oxidation resistance at the application temperature.

3.3. Toughness and Strength at 1500°C. At 1500°C the fracture toughness of the DC architectures was 30 to 55% higher than at room temperature, with all fracture toughness values falling between 6.1 and 6.9 MPa·$m^{½}$ Table IV). The CX conventional ceramics displayed the same trend, with C40 and C50 exhibiting fracture toughness values of 6.4 and 7.3 MPa·$m^{½}$, respectively. The increase of measured fracture toughness from room temperature to 1500°C has been attributed to a combination of increased ductility of $MoSi_2$ grains which, above their BDTT, are expected to relax stress concentration at the crack tip via plastic deformation, and crack tip branching which was exhibited by C70 when individually tested [42, 153]. At 1500°C the fracture surfaces of both chevron notch bars and flexure strength bars are flat and smooth compared to their counterparts broken at room temperature, displaying no large-scale crack deflection facets or topography similar to the granule size (Fig. 11). Above the BDTT of $MoSi_2$ and the stress relaxation threshold of ZrB_2 [155], the residual stresses responsible for microcracking at room temperature are expected to be relaxed, and thermal expansion of the C70 sub-composite during heating to the testing temperature may have partially closed the internal microcracks present at room temperature, decreasing their ability to cause crack deflection. Thus, at 1500°C the characteristics of the DC architectures expected to influence crack deflection or crack arrest are the relationships of the fracture energies of the granule and matrix sub-composites, differences in ductility, and the nature of the granule-matrix interface. Both Griffith's calculation of fracture energy and He and Hutchinson's predictions assume linear-elastic behavior, which was not the case for the sub-composites in the present study at 1500°C. The lack of a discrete interface between the granules and matrix, as shown in Figure 3c and 3d, makes deflection of cracks less likely. At the scale of a few grains, the composition of the interface approximates the composition of a ZrB_2-$MoSi_2$ conventional ceramic intermediate to the compositions of the granule and matrix sub-composites. Thus, a crack approaching the interface between a granule and matrix would not experience an abrupt change in material behavior. Furthermore, at 1500°C differences in elastic stress fields on opposite sides of the interface may be capable of relaxing via deformation of $MoSi_2$, decreasing the likelihood of crack deflection. The similarity in fracture toughness between the DC architectures and the CX ceramics of similar overall $MoSi_2$ content indicates that while the same

mechanism may be responsible for the increase in toughness of the DC architectures from room temperature to 1500°C as in the CX ceramics, the granule-matrix morphology of the DC architectures did not contribute to increased fracture toughness at 1500°C.

The flexure strength of DCA 1 and 1B increased by roughly a factor of two from room temperature to 1500°C, while the flexure strength of DCA 2 and 2B increased by factors of 2.3 and 2.6, respectively Table IV, Fig. 12a). At 1500°C the flexure strength of DCA 1 was 275 ± 25 MPa, the strength of DCA 1B was 262 ± 33 MPa, the strength of DCA 2 was 319 ± 66 MPa, and the flexure strength of DCA 2B was 359 ± 39 MPa. Fracture surfaces were oxidized but were globally smooth and did not exhibit granule-scale topography or crack deflection facets, suggesting that, as mentioned above, internal microcracks may have closed during specimen reheating to the testing temperature. Although these microcracks were identified as the critical flaws causing failure at room temperature, closing of microcracks due to thermal expansion is not likely responsible for the increase of strength from room temperature to 1500°C because crack closure does not necessarily imply rebonding of the cracked surfaces, and cracks open to the surface are expected to have oxidized internally during heating at temperatures below 600°C [156]. However, formation of a viscous borosilicate surface layer during oxidation at 1200 to 1500°C has been reported as a possible mechanism of flaw healing in ZrB_2-$MoSi_2$ ceramics [10], and this may have assisted in decreasing the severity of the stress concentration caused by surface cracks in the DC architectures and increased the strength compared to room temperature.

Calculated critical flaw sizes range from 104 to ~209 μm in DCA 1 and 1B, and from 46 to 199 μm DCA 2 and 2B, reflecting the higher strengths of the latter DC architectures. In previous work the authors identified oxidation induced surface damage as the strength limiting flaw at 1500°C in air for the MX compositions [42], and compositions with <20 vol.% $MoSi_2$ were found to be particularly vulnerable to deeply penetrating oxidation damage due to their inability to form a protective borosilicate oxide layer. This vulnerability was also evident in the C10 sub-composite in DCA 1 and 1B, in which pits of $MoSi_2$-depleted porous zirconia formed (Fig. 13). Although C10 was chosen for inclusion in DCA 1 and 1B due to its high strength and rigidity at 1500°C when tested as an individual conventional ceramic, incorporation of C10 in a DC

architecture where its oxidation behavior differed significantly from the adjacent sub-composite material (C70 forms a protective borosilicate coating) resulted in heterogeneous depth of oxidation damage penetration and post-test specimen surfaces with diagnostic white spots. Similar pits of porous zirconia were identified as the critical flaws causing failure at 1500°C in M10 in previous work, and due to their similarity in size to the calculated critical flaw size in the present study, likely played the same role in DCA 1 and 1B. DCA 2 and 2B did not form any observed zirconia pits, due to the ability of C20 to form a protective borosilicate coating, although the exfoliated region of oxidation extended more deeply into the surface of C20 than C70, resulting in a borosilicate layer of greater thickness on the C20 surfaces than on the C70 surfaces. The flexure strengths of the DC architectures were lower than those of C40 and C50, which were ~460 and ~420 MPa respectively, indicating that near-surface microcracks were likely responsible for decreasing the flexure strength of DCA 2 and 2B, while heterogeneous oxidation behavior is likely responsible for failure of DCA 1 and 1B at 1500°C.

4. SUMMARY

Four ZrB_2-$MoSi_2$ dual composite architectures (DCAs) were fabricated by dispersing extruded granules of a certain ZrB_2-$MoSi_2$ sub-composite composition in a matrix of a different ZrB_2-$MoSi_2$ sub-composite composition, with the goal of increasing fracture toughness while maintaining flexure strength of ZrB_2-$MoSi_2$ conventional ceramics at 1500°C in air. Both sub-composites in each DC architecture were co-densified in the same bulk material while maintaining discrete microstructural zones with individual compositional characteristics. The resulting microstructures of each sub-composite were similar to those of corresponding ZrB_2-$MoSi_2$ conventional ceramics processed at similar temperatures. However, mismatch between the overall coefficients of thermal expansion of the granule and matrix sub-composites resulted in spontaneous formation of 50 to 500 μm cracks in the sub-composite with the greater $MoSi_2$ content and therefore the higher CTE.

The room temperature elastic moduli of the DC architectures were not affected by these microcracks, with Young's and shear moduli matching those of corresponding ZrB_2-$MoSi_2$ conventional ceramics with the same overall $MoSi_2$ content. However, the

microcracks contributed to increased fracture toughness at room temperature via repeated crack deflection and crack tip blunting, increasing the fracture toughness from between 3.2 and 3.3 MPa·$m^{½}$ of the corresponding conventional ceramics to between 4.2 and 5.3 MPa·$m^{½}$ for the DC architectures. The microcracks had a detrimental effect on room temperature flexure strength, with surface cracks acting as critical flaws and resulting in strengths of ~140 MPa for the DC architectures, roughly 25 to 30% of the flexure strength of corresponding conventional ZrB_2-$MoSi_2$ ceramics.

Fracture toughness at 1500°C was between 6.1 and 6.9 MPa·$m^{½}$ for the DC architectures, higher than at room temperature but similar to the fracture toughness values of corresponding conventional ZrB_2-$MoSi_2$ ceramics. There was no apparent benefit of the DC architectural morphology to fracture toughness at 1500°C. Lack of detectable crack arrest or crack deflection at 1500°C was likely due to the similarity in properties of the granule and matrix sub-composites, the relaxation of elastic stresses between granules and matrix, partial closing of microcracks due to thermal expansion, and lack of a sharp interface or coating between the granules and matrix. Flexure strength at 1500°C was limited by partially-healed near-surface microcracks in DCA 2 and 2B, and by inhomogeneous oxidation behavior of the granules and matrix in DCA 1 and 1B, resulting in localized pitting of the surface due to insufficient $MoSi_2$ content in one of the two sub-composites.

The present study was not successful in breaking away from the trade-off between flexure strength and fracture toughness in ZrB_2-$MoSi_2$ ceramics at 1500°C using the DC architectural concept. However, testing and analysis combined with systematic knowledge of the ZrB_2-$MoSi_2$ sub-composites have identified three key areas of focus for future development of improved dual composite architectures for use in extreme environments: 1) resolving the issue of microcracking by either reducing the granule size or by altering the granule and matrix compositions to decrease the overall CTE mismatch; 2) matching the oxidation behavior of the granules and matrix to avoid heterogeneous surface oxidation damage; and 3) creating a discrete interface between the granules and matrix to increase the probability of crack deflection or arrest.

ACKNOWLEDGEMENTS

The authors would like to thank Morgan Cornish and Tyler Grant for assistance with extrusion and granulation, and Dr. Jeremy Watts for advice and assistance throughout the project.

FUNDING

This project was supported by the United States National Science Foundation Materials World Network through grant DMR-1209262, and funding from the National Research Council of Italy for the project, Dual Composite Ceramics for Improved Properties.

REFERENCES

1. H. X. Peng, Z. Fan, and J. R. G. Evans, "Novel MMC Microstructure with Tailored Distribution of the Reinforcing Phase," *Journal of Microscopy,* 201[2] 333-38 (2000).

2. I. Bogomol, H. Borodianska, and Y. Sakka, "A Dense and Tough (B_4C-TiB_2)-B_4C 'Composite Within a Composite' Produced by Spark Plasma Sintering," *Scripta Materialia,* 71 17-20 (2014).

3. X. Deng, "Double Cemented Carbide - A Creative Dual Composite," *The International Journal of Powder Metallurgy,* 37[8] (2001).

4. X. Deng, B. R. Patterson, K. K. Chawla, M. C. Koopman, Z. Fang, G. Lockwood, and A. Griffo, "Double Cementec Carbide - A Creative Composite Design Concept," *The International Journal of Powder Metallurgy,* 37[7] (2001).

5. Z. Fang, G. Lockwood, and A. Griffo, "A Dual Composite of WC-Co," *Metallurgical Transactions A,* 30[12] 3231-38 (1999).

6. X. Deng, B. R. Patterson, K. K. Chawla, M. C. Koopman, Z. Fang, G. Lockwood, and A. Griffo, "Mechanical Properties of a Hybrid Cemented Carbide Composite," *International Journal of Refractory Metals and Hard Materials,* 19 547-52 (2001).

7. X. Deng, B. R. Patterson, K. K. Chawla, M. C. Koopman, C. Mackin, Z. Fang, G. Lockwood, and A. Griffo, "Microstructure/Hardness Relationship in a Dual Composite," *Journal of Materials Science Letters,* 21 707-09 (2002).

8. A. Griffo, R. Brown, and K. Keshavan, "Oil and Gas Drilling Materials," *Advanced Materials and Processes,* 161[6] 59-60 (2003).

9. Z. Z. Fang, A. Griffo, B. White, G. Lockwood, D. Belnap, G. Hilmas, and J. Bitler, "Fracture Resistant Super Hard Materials and Hardmetals Composite with Functionally Designed Microstructure," *International Journal of Refractory Metals and Hard Materials,* 19 453-59 (2001).

10. J. W. Zimmermann, G. E. Hilmas, and W. G. Fahrenholtz, "Thermal Shock Resistance and Fracture Behavior of ZrB_2-Based Fibrous Monolith Ceramics," *Journal of the American Ceramic Society,* 92[1] 161-66 (2009).

11. H. Ming-Yuan and J. W. Hutchinson, "Crack Deflection at an Interface Between Dissimilar Elastic Materials," *International Journal of Solids and Structures,* 25[9] 1053-67 (1989).

12. L. Silvestroni and D. Sciti, "Effects of $MoSi_2$ additions on the properties of Hf– and Zr–B_2 composites produced by pressureless sintering," *Scripta Materialia,* 57[2] 165-68 (2007).

13. D. Sciti, S. Guicciardi, A. Bellosi, and G. Pezzotti, "Properties of a Pressureless-Sintered ZrB_2-$MoSi_2$ Ceramic Composite," *Journal of the American Ceramic Society,* 89[7] 2320-22 (2006).

14. W. G. Fahrenholtz, E. J. Wuchina, W. E. Lee, and Y. Zhou, "Ultra-high Temperature Ceramics: Materials for Extreme Environment Applications.″ John Wiley & Sons: Hoboken, NJ, USA, (2014).

15. R. J. Grohsmeyer, G. E. Hilmas, F. T. Monteverde, W. G. Fahrenholtz, and E. W. Neuman, "ZrB_2-$MoSi_2$ Ceramics with Varying $MoSi_2$ Content and ZrB_2 Powder Particle Size: Mechanical Properties of MX at Room Temperature and 1500°C in Air," *Journal of the European Ceramic Society,* TBD[TBD] TBD-TBD (2017b).

16. V. O. Lavrenko, A. D. Panasyuk, O. M. Grigorev, O. V. Koroteev, and V. A. Kotenko, "High-Temperature (to 1600°C) Oxidation of ZrB_2-$MoSi_2$ Ceramics in Air," *Powder Metallurgy and Metal Ceramics,* 51[1-2] 102-07 (2012).

17. L. Silvestroni, G. Meriggi, and D. Sciti, "Oxidation behavior of ZrB_2 composites doped with various transition metal silicides," *Corrosion Science,* 83 281-91 (2014).

18. D. Sciti, M. Brach, and A. Bellosi, "Oxidation behavior of a pressureless sintered ZrB_2–$MoSi_2$ ceramic composite," *Journal of Materials Research,* 20[04] 922-30 (2005).

19. H.-T. Liu, J. Zou, D.-W. Ni, J.-X. Liu, and G.-J. Zhang, "Anisotropy oxidation of textured ZrB_2–$MoSi_2$ ceramics," *Journal of the European Ceramic Society,* 32[12] 3469-76 (2012).

20. D. L. McClane, W. G. Fahrenholtz, G. E. Hilmas, and D. Smith, "Thermal Properties of (Zr, TM)B_2 Solid Solutions with TM = Ta, Mo, Re, V, and Cr," *Journal of the American Ceramic Society,* 98[2] 637-44 (2015).

21. M. Brach, V. Medri, and A. Bellosi, "Corrosion of pressureless sintered ZrB_2–$MoSi_2$ composite in H_2SO_4 aqueous solution," *Journal of the European Ceramic Society,* 27[2-3] 1357-60 (2007).

22. V. O. Lavrenko, V. A. Shvets, V. M. Talash, V. A. Kotenko, and T. V. Khomko, "Electrochemical Oxidation of ZrB_2-$MoSi_2$ Ceramics in a 3% NaCl Solution," *Powder Metallurgy and Metal Ceramics,* 50[11-12] 749-53 (2012).

23. E. W. Neuman, G. E. Hilmas, W. G. Fahrenholtz, and A. Dominguez-Rodriguez., "Strength of Zirconium Diboride to 2300°C," *Journal of the American Ceramic Society,* 96[1] 47-50 (2013).

24. W. G. Fahrenholtz, "Thermodynamic Analysis of ZrB_2-SiC Oxidation: Formation of a SiC-Depleted Region," *Journal of the American Ceramic Society,* 90[1] 143-48 (2007).

25. S. R. Srinivasan, R. B. Schwarz, and J. D. Embury, "Ductile-To-Brittle Transition in $MoSi_2$*,"* pp. 1099-104 in High-Temperature Ordered Intermetallic Alloys V. Vol. 288Edited by I. Baker, R. Darolia, J. D. Whittenberger, and M. H. Yoo.

26. D. J. Evans, S. A. Court, P. M. Hazzledine, and H. L. Fraser, "Deformation Mechanisms in the Intermetallic Compound $MoSi_2$*,"* pp. 567-72 in High-Temperature Ordered Intermetallic Alloys V. Vol. 288Edited by I. Baker, R. Darolia, J. D. Whittenberger, and M. H. Yoo.

27. H. Mehrer, H. E. Schaefer, I. V. Belova, and G. E. Murch, "Molybdenum Disilicide - Diffusion, Defects, Diffusion Correlation, and Creep," *Defect and Diffusion Forum,* 322 107-28 (2012).

28. O. Unal, J. J. Petrovic, D. H. Carter, and T. E. Mitchell, "Dislocations and Plastic Deformation in Molybdenum Disilicide," *Journal of the American Ceramic Society,* 73[6] 1752-57 (1990).

29. S. Guo, T. Mizuguchi, M. Ikegami, and Y. Kagawa, "Oxidation behavior of ZrB_2–$MoSi_2$–SiC composites in air at 1500°C," *Ceramics International,* 37[2] 585-91 (2011).

30. R. J. Grohsmeyer, G. E. Hilmas, F. T. Monteverde, W. G. Fahrenholtz, A. D'Angio, D. Sciti, and L. Silvestroni, "ZrB_2-$MoSi_2$ Ceramics with Varying $MoSi_2$ Content and ZrB^2 Powder Particle Size: Processing and Microstructure," *Journal of the European Ceramic Society,* TBD[TBD] TBD (2017a).

31. R. J. Grohsmeyer, G. E. Hilmas, F. T. Monteverde, W. G. Fahrenholtz, A. D'Angio, D. Sciti, and L. Silvestroni, "Mechanical Property Relationships in ZrB_2-$MoSi_2$ Ceramics with Varying $MoSi_2$ Content and ZrB_2 Powder Particle Size at Room Temperature and 1500°C in Air," *Journal of the European Ceramic Society,* TBD[TBD] TBD-TBD (2017d).

32. R. J. Grohsmeyer, G. E. Hilmas, F. T. Monteverde, and W. G. Fahrenholtz, "Densification Process and Formation of Solid Solution Shell in ZrB_2-$MoSi_2$ Ceramics with Varying $MoSi_2$ Content and ZrB_2 Powder Particle Size," *Journal of the European Ceramic Society,* TBD[TBD] TBD-TBD (2017).

33. J. J. Cleveland and R. C. Bradt, "Grain Size/Microcracking Relations for Pseudobrookite Oxides," *Journal of the American Ceramic Society,* 61[11-12] 478-81 (1978).

34. J. L. Watts, G. E. Hilmas, and W. G. Fahrenholtz, "Mechanical Characterization of ZrB_2-SiC Composites with Varying SiC Particle Sizes," *Journal of the American Ceramic Society,* 94[12] 4410-18 (2011).

35. Y. S. Touloukian, R. K. Kirby, E. R. Taylor, and T. Y. R. Lee, "Thermophysical Properties of Matter, Thermal Expansion - Nonmetallic Solids," pp. 1786 Vol. 13. Thermophysical and Electronic Properties Information Analysis Center: Purdue University, Lafayette, IN, USA, (1977).

36. B. W. Rosen and Z. Hashin, "Effective Thermal Expansion Coefficients and Specific Heats of Composite Materials," *International Journal of Engineering Science,* 8 157-73 (1970).

37. J. B. Wachtman, W. R. Cannon, and M. J. Matthewson, "Mechanical Properties of Ceramics," pp. 479 2 ed. J. Wiley and Sons, Inc.: Hoboken, NJ, USA, (2009).

38. J. Watts, G. Hilmas, W. G. Fahrenholtz, D. Brown, and B. Clausen, "Measurement of Thermal Residual Stresses in ZrB_2-SiC Composites," *Journal of the European Ceramic Society,* 31[9] 1811-20 (2011).

39. Y. Q. Liu, G. Shao, and P. Tsakiropoulos, "On the Oxidation Behavior of $MoSi_2$," *Intermetallics,* 9 125-36 (2001).

Table I. Summary microstructural content of DC architectures. Nominal $MoSi_2$ content in granules and matrix, measured granule and overall $MoSi_2$ content, and geometric bulk density and % relative density (RD) measured by microstructural analysis for ZrB_2-$MoSi_2$ DC architectures.

Specimen		Nominal $MoSi_2$ content (vol.%)	Measured granule content (vol.%)	Overall $MoSi_2$ content (vol.%)	Hot-pressing dwell time (minutes)	Geo-metric density (g/cm^3)	Microstructural RD (%)
DCA 1	Granules (C10):	10	55.4 ± 4.3	36.8 ± 2.6	55	6.18	TBD
	Matrix (C70):	70					TBD
DCA 1B	Granules (C70):	70	42.4 ± 3.0	35.4 ± 1.8	60	6.18	TBD
	Matrix (C10):	10					TBD
DCA 2	Granules (C20):	20	54.6 ± 5.1	42.7 ± 2.5	61	6.20	TBD
	Matrix (C70):	70					TBD
DCA 2B	Granules (C70):	70	45.2 ± 3.0	42.6 ± 1.5	61	6.20	TBD
	Matrix (C20):	20					TBD

Table II. Granule diameter, aspect ratio, major axis length and MFP measured on HP normal and transverse surfaces of ZrB_2-$MoSi_2$ DC architectures.

Composition		Avg. granule diameter (µm)	Avg. granule aspect ratio	Avg. granule major axis (µm)	Max. granule major axis (µm)	MFP (µm)
DCA 1	HP normal	335 ± 111	1.5 ± 0.4	403 ± 152	925	132 ± 158
	Transverse	240 ± 77	2.1 ± 0.6	324 ± 117	767	127 ± 126
DCA 1B	HP normal	300 ± 87	2.1 ± 0.4	360 ± 117	702	260 ± 220
	Transverse	218 ± 68	2.4 ± 0.7	309 ± 109	664	176 ± 173
DCA 2	HP normal	295 ± 115	1.5 ± 0.4	352 ± 154	1010	185 ± 190
	Transverse	259 ± 83	2.0 ± 0.6	343 ± 130	903	122 ± 125
DCA 2B	HP normal	306 ± 105	1.6 ± 0.7	368 ± 141	1006	281 ± 249
	Transverse	221 ± 73	2.5 ± 0.8	314 ± 117	912	124 ± 134

Table III. Room-temperature dynamic elastic moduli, four-point flexure strength, chevron notch fracture toughness values for ZrB2-$MoSi_2$ DC Architectures.

Composition	**Young's modulus (GPa)**	**Shear modulus (GPa)**	**Poisson's ratio**	**Flexure strength (MPa)**	**Fracture toughness (MPa·m½)**	**Calculated flaw size (μm)**
						Y = 1.99
DCA 1	491 ± 3	212	0.155	139 ± 14	4.6	233 – 348
DCA 1B	495	214	0.155	136 ± 17	5.3 ± 0.6	241 – 614
DCA 2	488 ± 1	214	0.143	137 ± 16	4.2 ± 0.4	190 – 431
DCA 2B	487 ± 2	213	0.143	143 ± 15	4.6 ± 0.7	154 – 433
C40	493 ± 2	214	0.155	442 ± 70	3.2 ± 0.2	8.6 – 20
C50	476 ± 8	210	0.150	586 ± 83	3.3 ± 0.4	4.9 – 13

Table IV. Crosshead speeds, flexure strength, and fracture toughness of ZrB_2-$MoSi_2$ DC architectures at 1500°C in air.

Composition	**Crosshead speed (mm/min)**	**Flexure strength (MPa)**	**Fracture toughness (MPa·m^{½})**	**Calculated flaw size (μm)**
				Y = 1.99
DCA 1	3.0	275 ± 25	6.7 ± 0.3	115 – 203
DCA 1B	3.0	262 ± 33	6.9 ± 0.9	104 – 292
DCA 2	4.0	319 ± 66	6.5 ± 0.6	59 – 199
DCA 2B	4.0	359 ± 39	6.1 ± 0.7	46 – 113
C40	4.0	461 ± 36	6.4 ± 0.5	34 – 66
C50	5.0	423 ± 20	7.3 ± 0.8	54 – 101

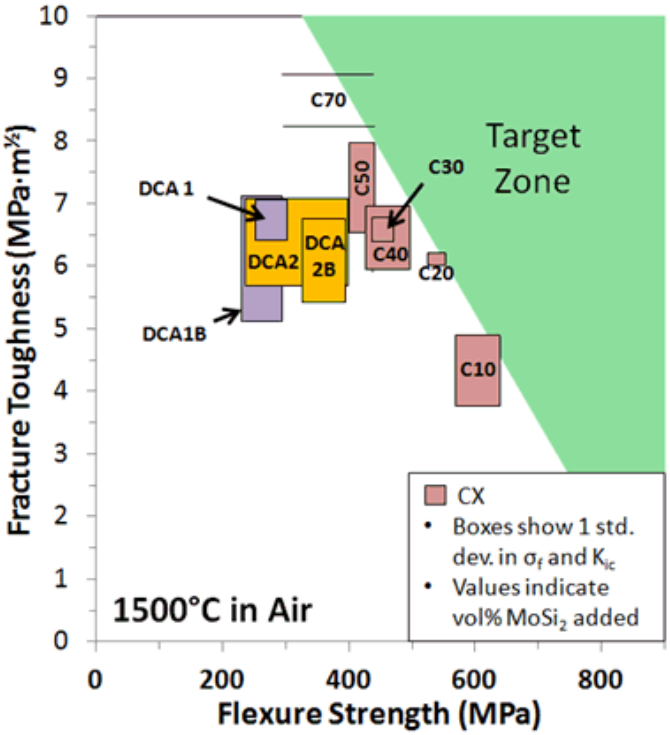

Fig. 1. Illustrative plot of the relationship of fracture toughness and four-point flexure strength measured at 1500°C in air for conventional CX ZrB_2-$MoSi_2$ ceramics from [153] and ZrB_2-$MoSi_2$ DC architectures.Flexure specimens of C70 did not break during testing due to ductile behavior, so C70 is shown at the highest calculated stress attained before the test was stopped at >2 mm of travel.

Fig.2. Extruded and chopped granules of ~55 vol.% solids loading in ~45 vol.% thermoplastic polymer, showing scarring from impact of blender blades.

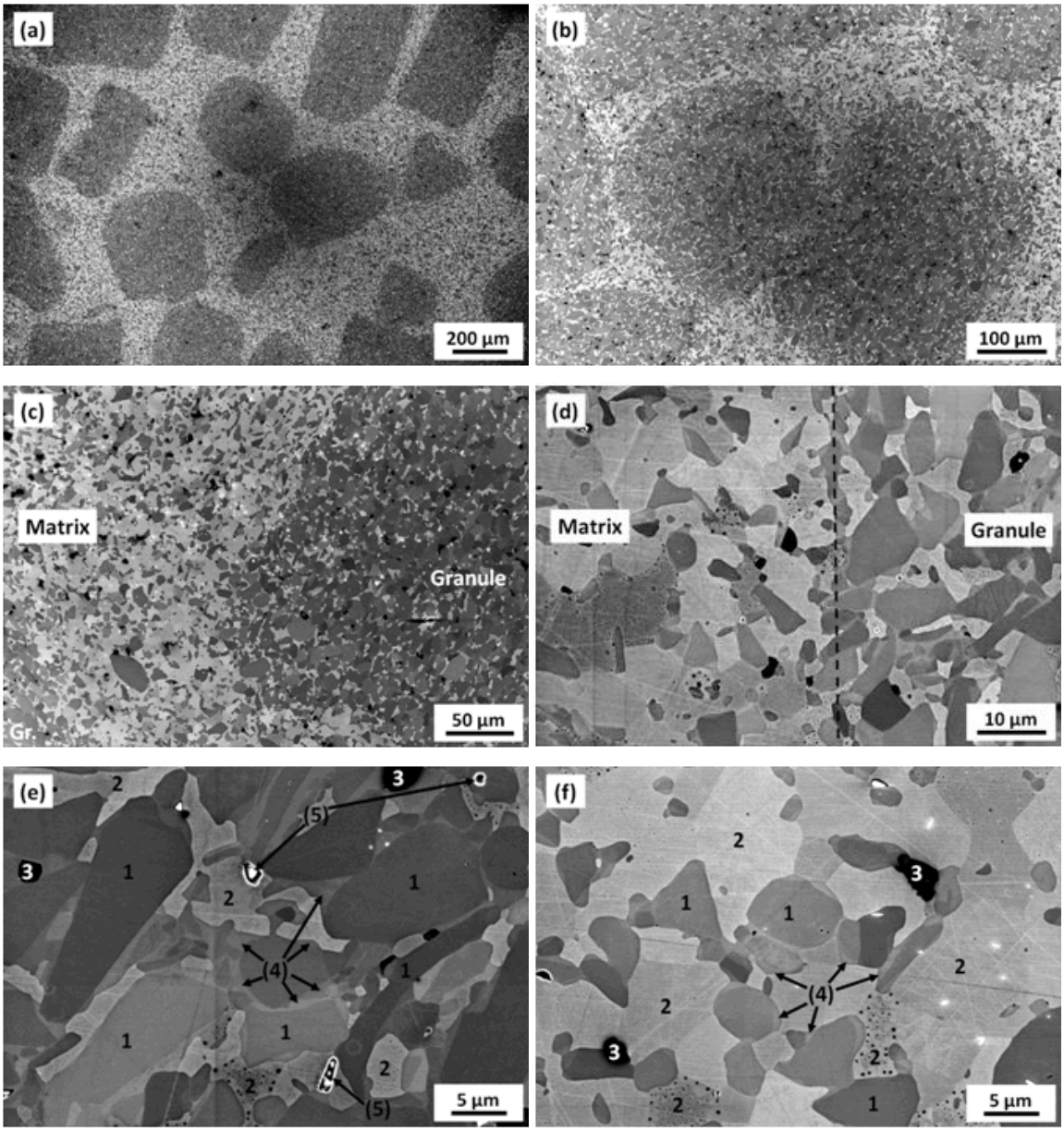

Fig. 3. Secondary electron images of DCA 1.(a) Overview of C10 granules (darker) dispersed in C70 matrix (lighter); (b) two granules in contact; (c) detail of matrix (left center) between two granules (lower left corner and right portion of image); (d) detail with dashed line approximating the granule-matrix interface; (e) detail of granule microstructure; (f) detail of matrix microstructure. In microstructures, 1=ZrB_2, 2=$MoSi_2$, 3=SiO_2, 4=$(Zr,Mo)B_2$ solid solution, 5=porosity. Darkened regions in the centers of (a) and (b) are artifacts of the microscope due to the low magnification, and dark spots visible on select $MoSi_2$ grains in (d), (e), and (f) are due to preferential etching during plasma cleaning.

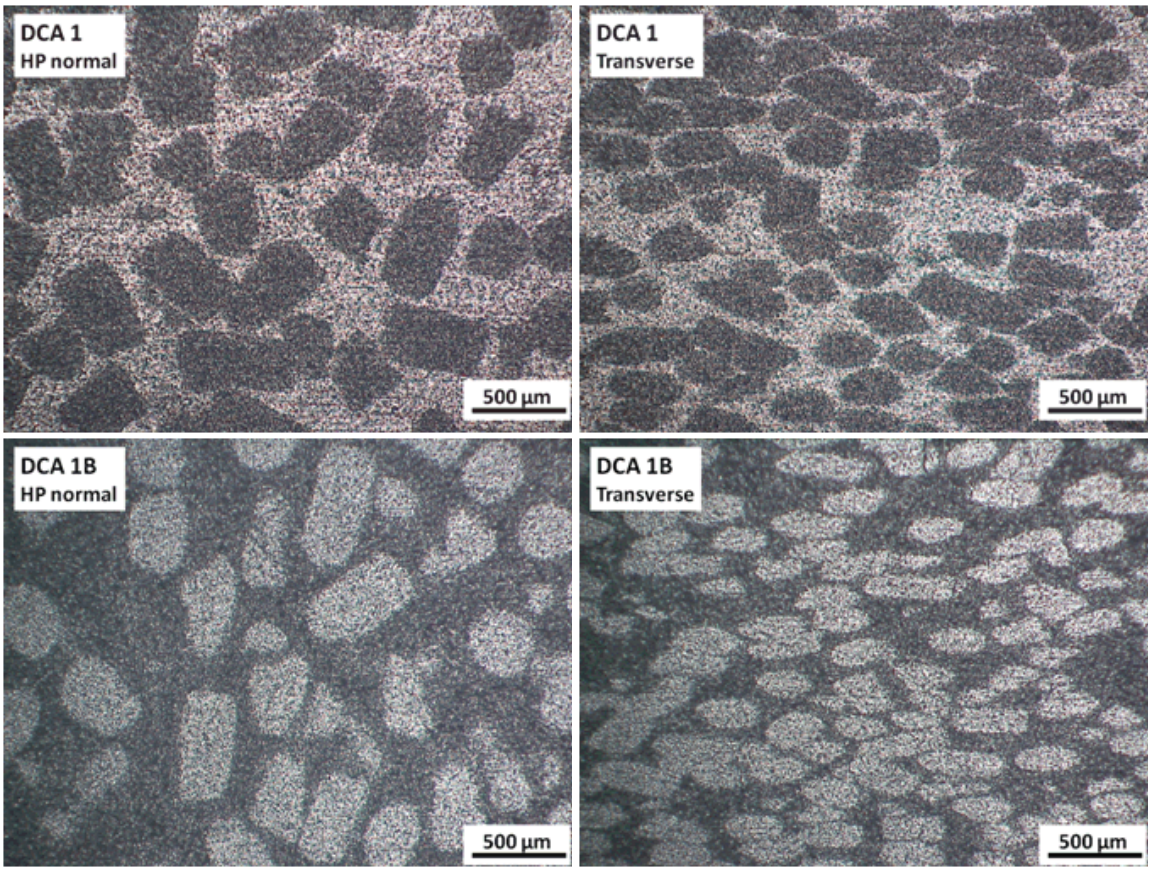

Fig. 4. Optical micrographs of DCA 1 (top) and DCA 1B (bottom) after surface grinding with 1200 grit diamond wheel.Darker gray zones are C10 sub-composite and lighter zones are C70 sub-composite. Images on left show a plane normal to the direction of force application during hot pressing and images on right the transverse direction, illustrating compaction of the granules due to uniaxial densification.

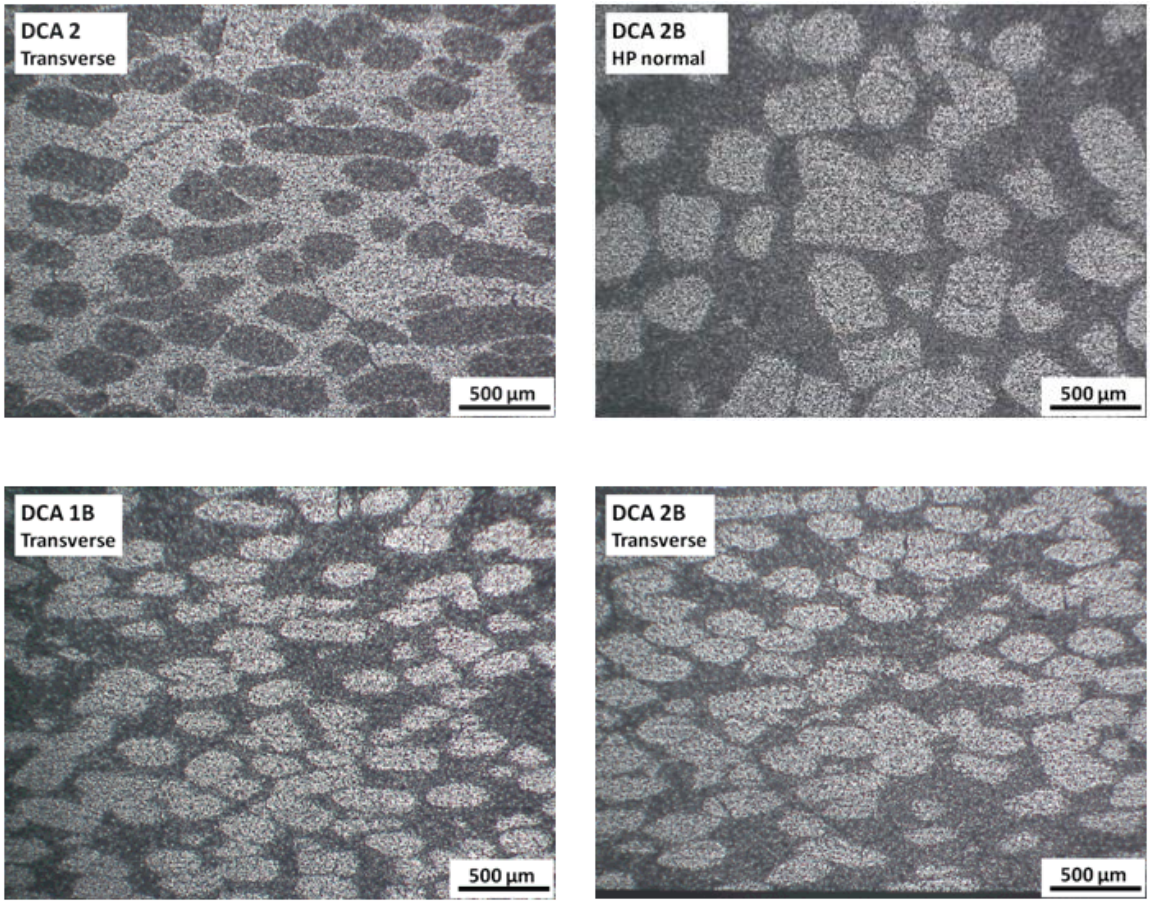

Fig. 5. Optical micrographs of DCA 2 (top) and DCA 2B (bottom) after surface grinding with 1200 grit diamond wheel.Darker gray zones are C20 sub-composite and lighter zones are C70 sub-composite. Images on left show a plane normal to the direction of force application during hot pressing and images on right the transverse direction, illustrating compaction of the granules due to uniaxial densification.

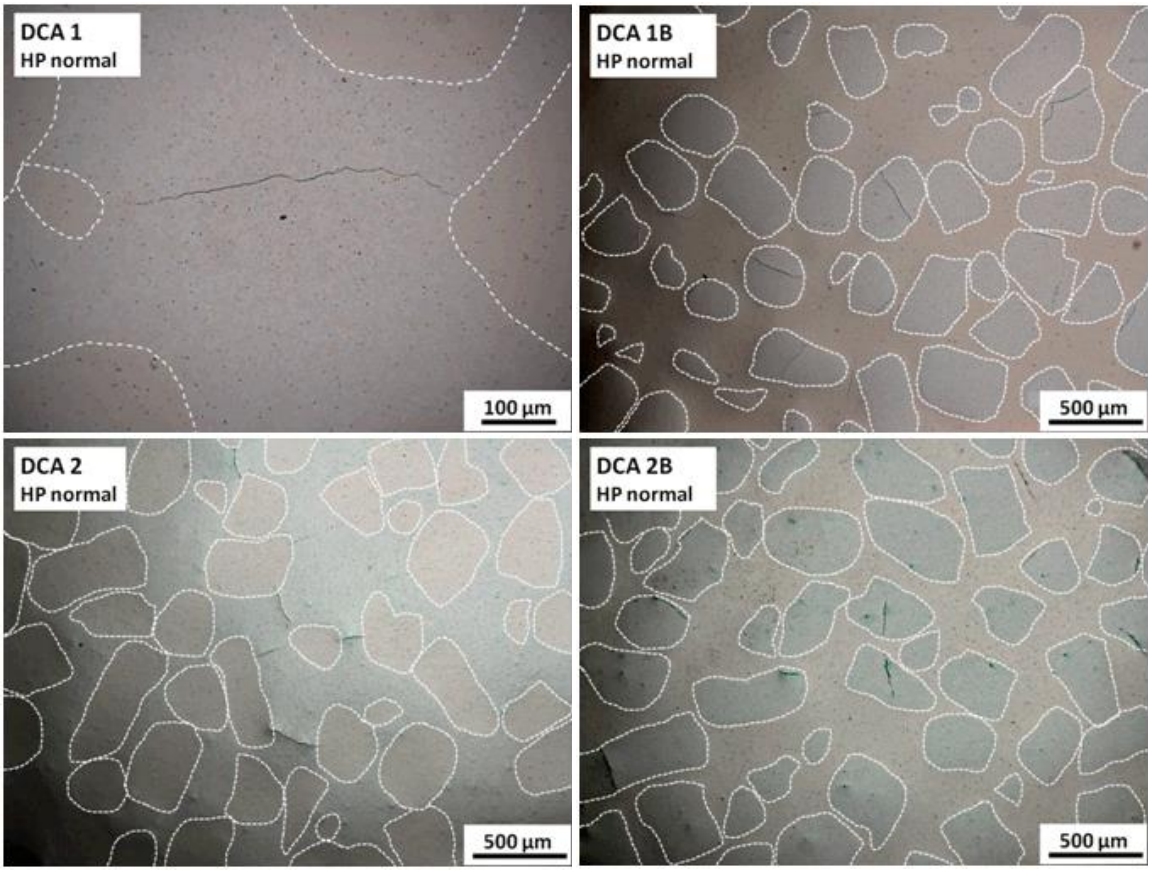

Fig. 6. Optical micrographs of polished surfaces of DC architectures illustrating spontaneous microcracking.In DCA 1: detail of a ~480 µm long crack through the C70 matrix between two C10 granules. Other images show cracking in matrix of DCA 2 and in the granules of DCA 1B and 2B.

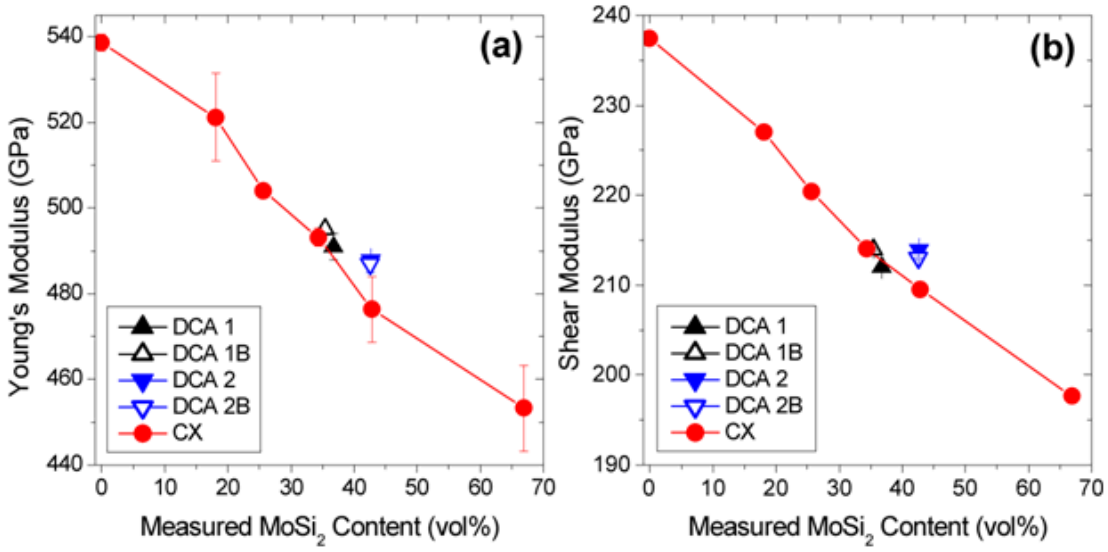

Fig. 7. Room temperature Young's modulus (a) and shear modulus (b) of DC architectures as a function of measured $MoSi_2$ content and compared with conventional CX ceramics.

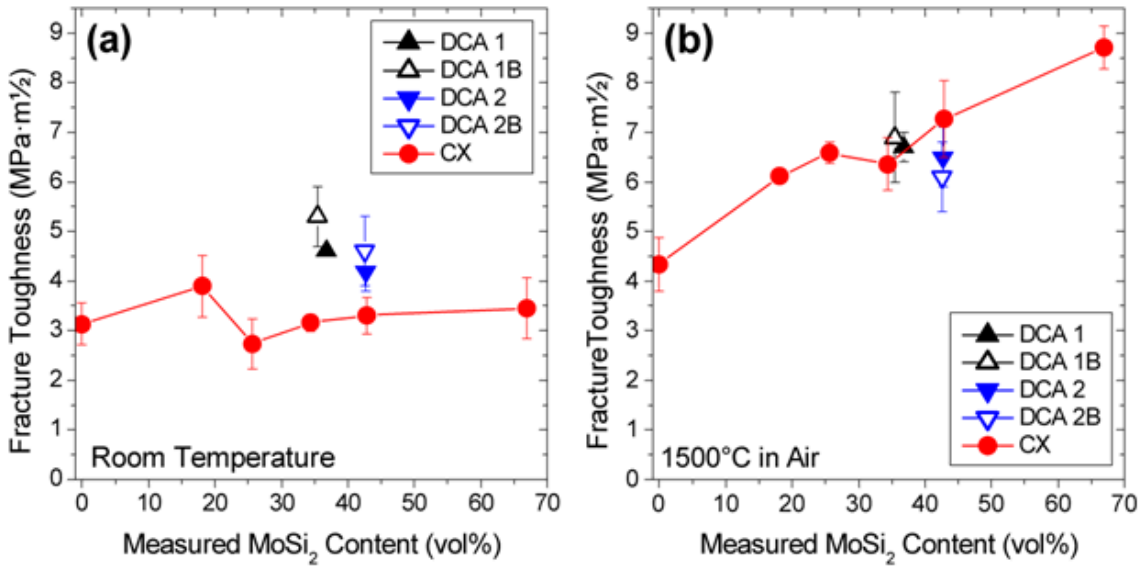

Fig. 8. Fracture toughness of DC architectures as a function of measured $MoSi_2$ content compared with conventional CX ceramics.(a) at room temperature and (b) at 1500°C in air.

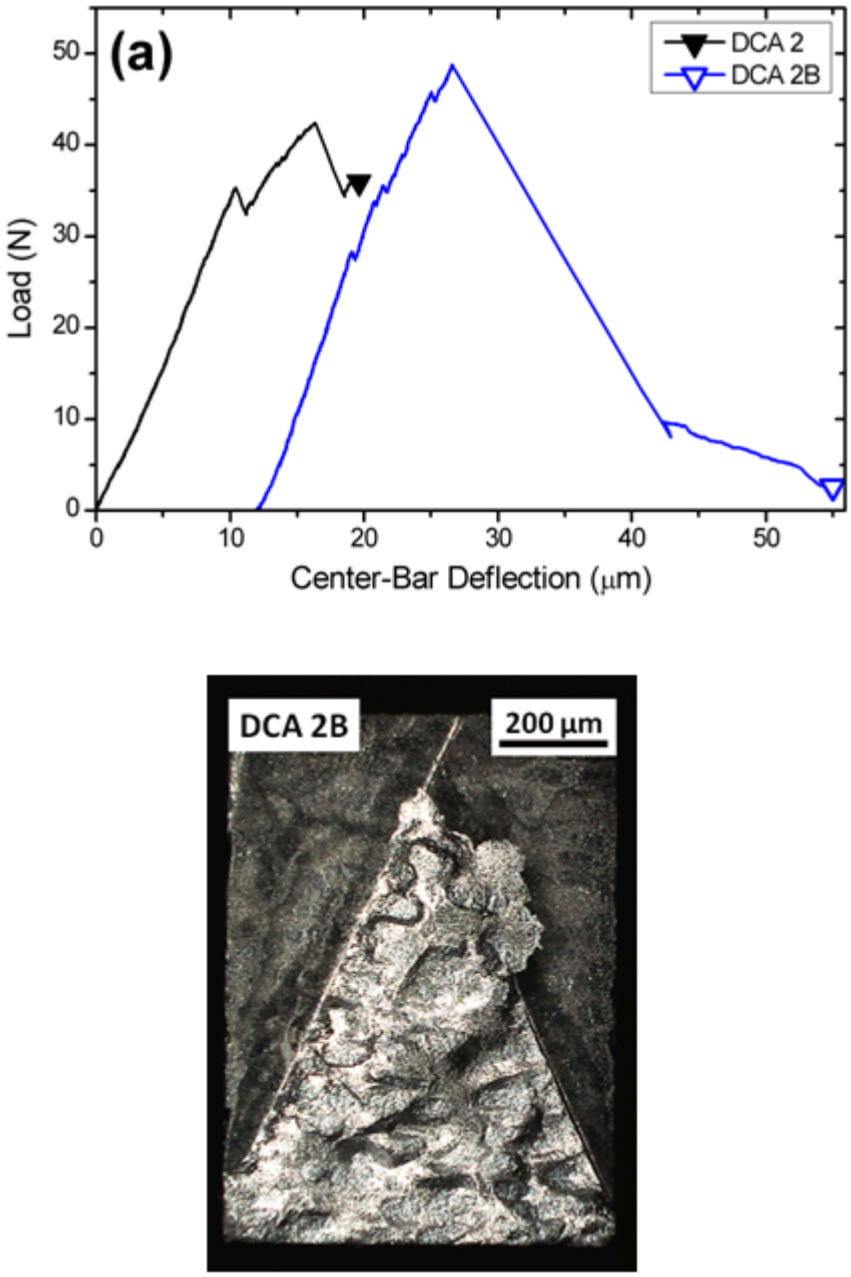

Fig. 9. Selected load vs. deflection curves and fracture surface of chevron notch specimens broken at room temperature.(a) Load vs. deflection curves of selected DCA 2 and 2B chevron notch specimens showing typical crack arrest and continued load bearing during crack growth. (b) Fracture surface of a DCA 2B specimen, showing surface topography typical of all four DC architecture compositions.

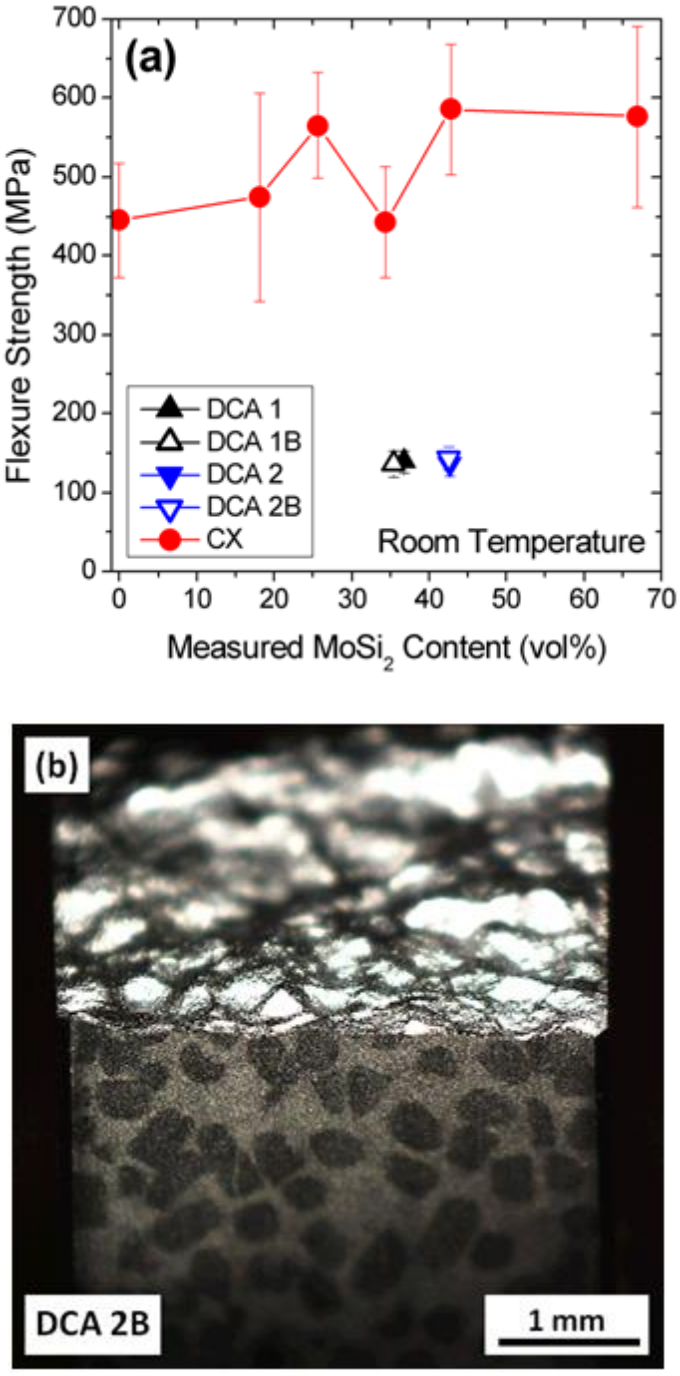

Fig. 10. Room temperature flexure strength and DCA 2B flexure fracture surface.(a) Four-point flexure strength of DC architectures and CX as a function of measured $MoSi_2$ content at room temperature; (b) optical image of a broken DCA 2B flexure bar showing the as-ground tensile surface (bottom half of image) and the topography of the fracture surface.

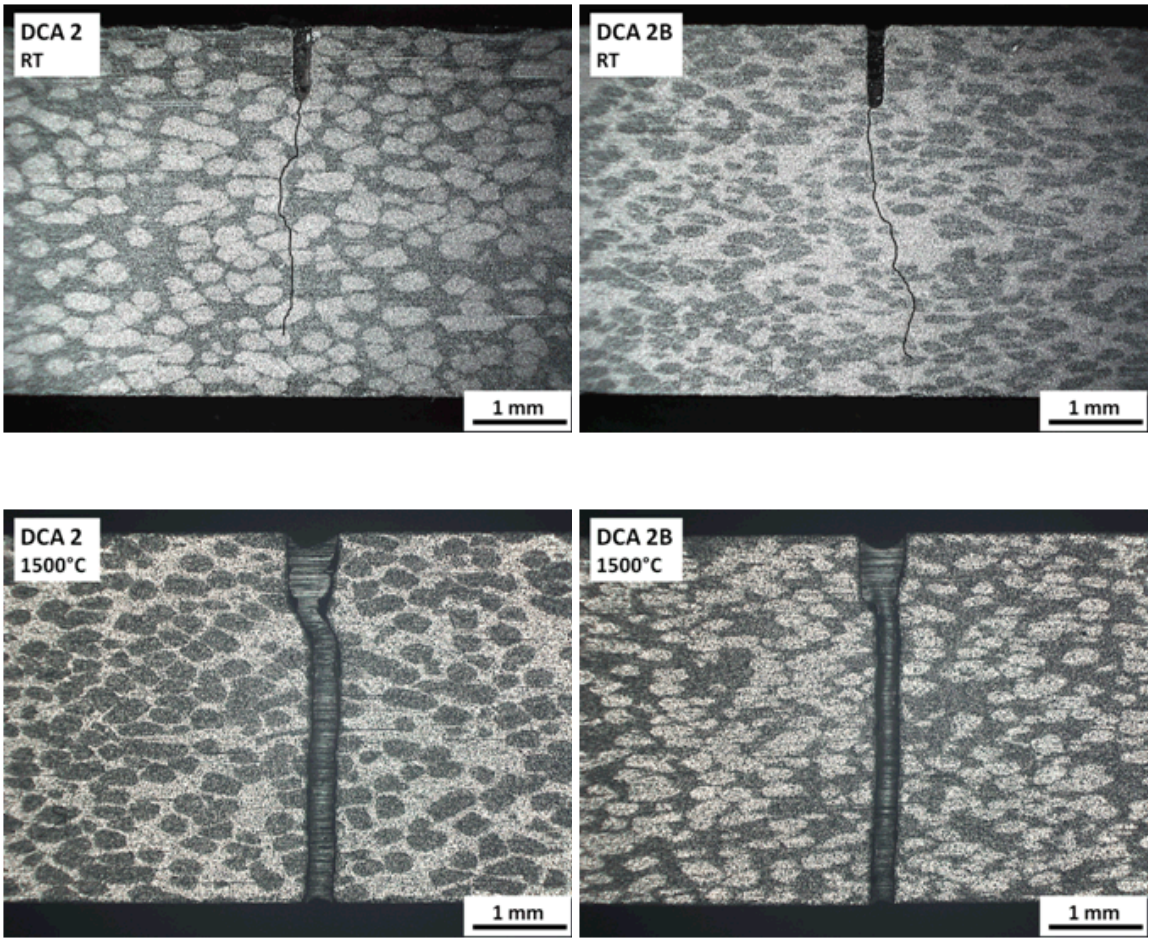

Fig. 11. Optical micrographs of surface ground cross sections of broken DCA 2 (left) and DCA 2B (right) fracture toughness specimens at room temperature and 1500°C.Images show the morphology of the crack path at room temperature in specimens that did not separate (top, with crack path artificially darkened), and at 1500°C (bottom, with mounting adhesive filling the crack between the separated specimen halves).

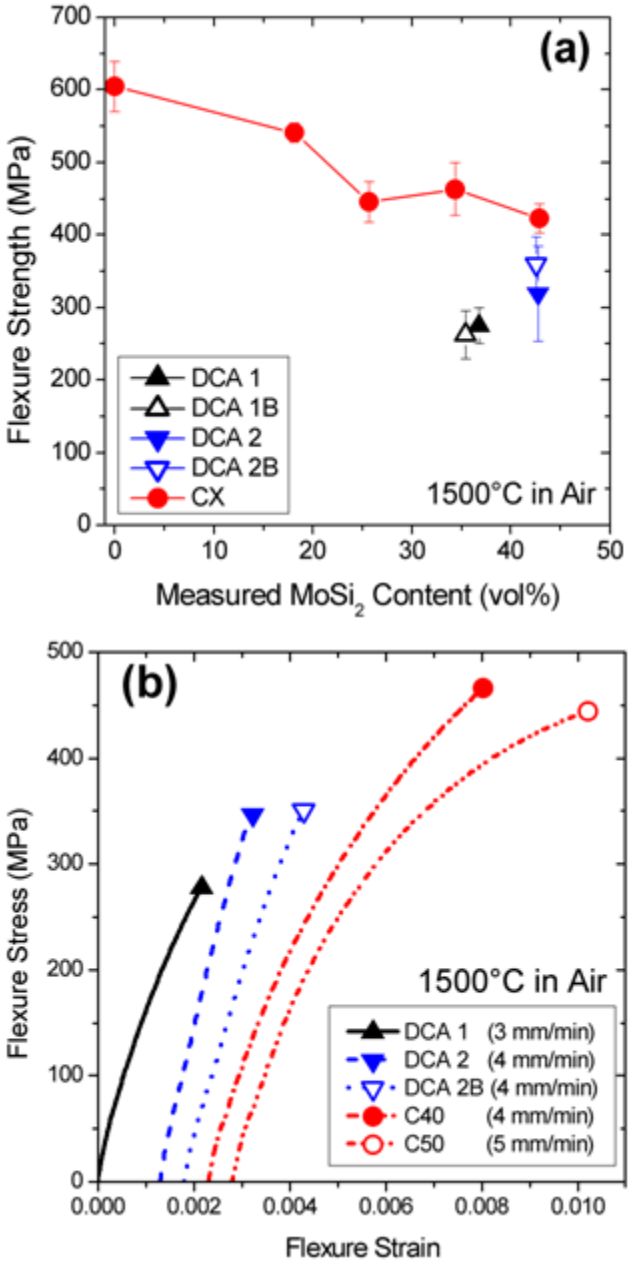

Fig. 12. Four-point flexure strength of DC architectures at 1500°C in air and typical stress-strain curves of DC architecture specimens.(a) Four-point flexure strength with respect to measured $MoSi_2$ content compared to CX from [153], (b) typical stress-strain curves of DC architecture specimens tested at varying crosshead rates compared to C40 and C50 from [153].

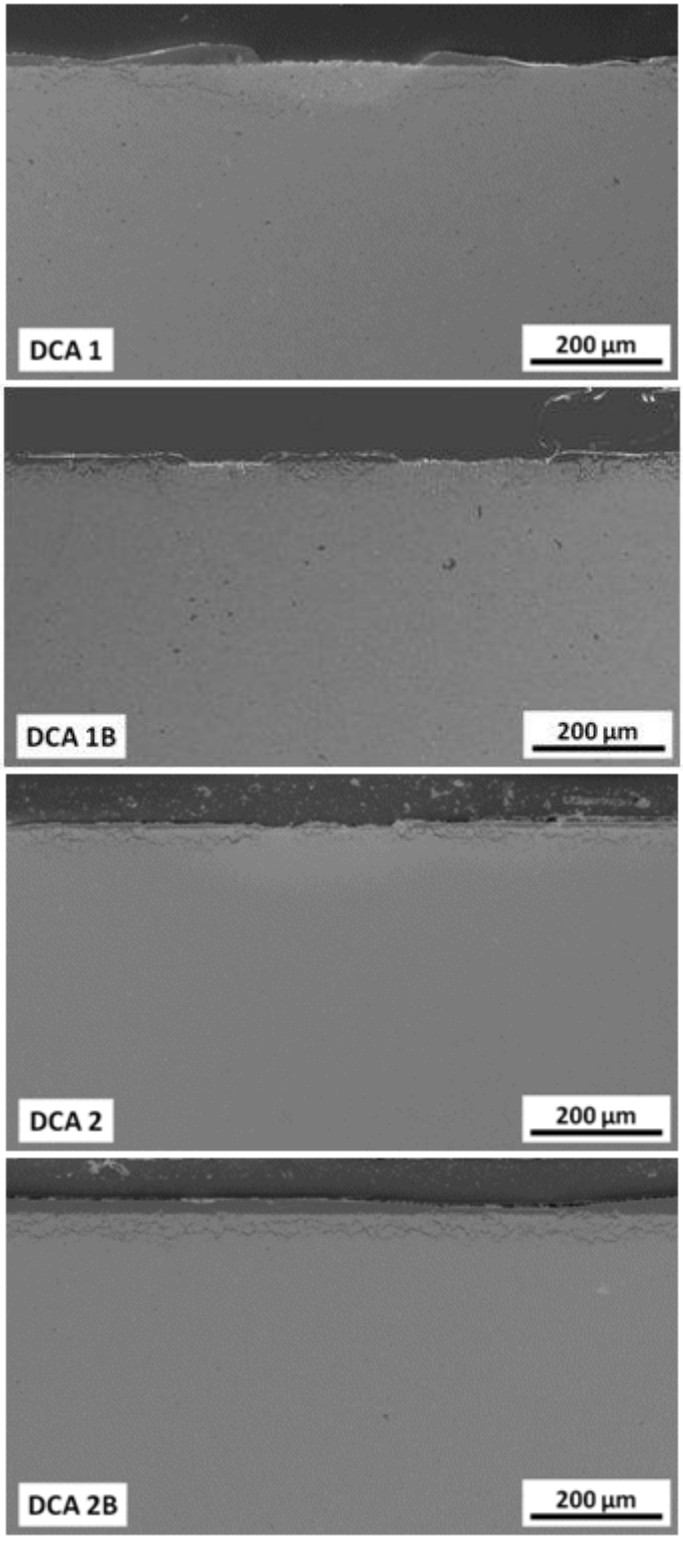

Fig. 13. Oxidation layers on flexure bars of DC architectures after testing at 1500°C in air.Images show discontinuous borosilicate glassy layer formation on DCA 1 and 1B where granule surfaces in DCA 1 and matrix surfaces in DCA 1B oxidized to form porous zirconia pits in the surface.

SECTION

3. SUMMARY AND CONCLUSIONS

The purposes of this dissertation were to (1) establish a baseline of experimental data on the processing-microstructure-property relationships of ZrB_2-$MoSi_2$ ceramics, and (2) to fabricate preliminary dual composite architectures (DCAs) for use at elevated temperatures and evaluate the evaluate basic design requirements of high-temperature DCAs. With the exceptions of the studies by Chamberlain et al., Guo, and Liu et al., studies investigating ZrB_2-$MoSi_2$ ceramics have focused on the range of compositions with ≤20 vol.% $MoSi_2$ additions at room temperature, and no studies have reported any elevated-temperature mechanical properties of ZrB_2-$MoSi_2$ ceramics with >20 vol.% $MoSi_2$ additions. Processing and testing methods have varied between studies, making direct comparison of results impossible. To date, all published work regarding DCAs has concerned materials systems that are not suitable for use at elevated temperatures in oxidizing environments, and the design criteria for such high-temperature DCAs remain unexplored. This section summarizes the results of research discussed in this dissertation intended to address the questions that describe the aims of the dissertation research, followed by several overall conclusions.

3.1. SUMMARY

1. How do the densification behavior and microstructural characteristics change as a result of varying ZrB_2 starting powder particle size, starting $MoSi_2$ content, and hot pressing temperature?

The densification behavior and final microstructures of hot-pressed ZrB_2-$MoSi_2$ ceramics with varying ZrB_2 starting powder particle size and $MoSi_2$ content were investigated. Fifteen different ZrB_2-$MoSi_2$ ceramics with median ZrB_2 starting powder particle sizes ranging from 2.9 to 11.7 μm and nominal $MoSi_2$ contents ranging from 5 to 70 vol.% were hot pressed at temperatures between 1750 and 1925°C. Plastic deformation of $MoSi_2$ upon application of uniaxial pressure contributed to initial densification. Decomposition of $MoSi_2$ during later stages of hot pressing was quantified

by microstructural analysis and varied from ~1 to 10 vol.% $MoSi_2$. Comprehensive microstructural analysis showed that ZrB_2 grain size decreased and $MoSi_2$ cluster size increased as $MoSi_2$ content increased. Starting powders with lower impurity contents and isothermal vacuum holds contributed to lower oxide impurity contents in the final ceramics. A diboride core-shell structure involving $(Zr_{1-x}Mo_x)B_2$ solid solution was observed in all compositions. This study identified specific relationships between starting composition, processing conditions and final microstructure, showing how microstructure and properties could be tailored by processing to attain specific mechanical and oxidation characteristics in future research.

2. How does a systematic change in the starting $MoSi_2$ content for a single ZrB_2 starting powder grade influence the elastic properties, fracture toughness, and flexure strength at room temperature and at 1500°C, and what controls fracture toughness and flexure strength at room temperature and at 1500°C?

Mechanical properties were measured in air at room temperature and 1500°C for ZrB_2-$MoSi_2$ ceramics with 5 to 30 vol.% $MoSi_2$ additions hot-pressed at temperatures between 1775 and 1900°C. Decomposition of $MoSi_2$ was quantified by microstructural analysis. Room temperature strength (550–720 MPa) was limited by surface grain pullout. Fracture toughness (2.8–3.8 $MPa \cdot m^{½}$) showed no overall trend with $MoSi_2$ content. Microhardness (16.6–15.1 GPa), Young's modulus (530–470 GPa), and shear modulus (235–220 GPa) decreased, while Poisson's ratio (0.134–0.143) increased with $MoSi_2$ content. Fracture toughness at 1500°C increased from 4.1 to 5.7 $MPa \cdot m^{½}$ as $MoSi_2$ content increased, due to high-temperature plasticity of the $MoSi_2$ that remained in the microstructure. At 1500°C, compositions with 5 and 10 vol.% $MoSi_2$ formed a porous zirconia scale, and exhibited strengths of 250 and 300 MPa. Compositions with 20 and 30 vol.% $MoSi_2$ exhibited strengths of 415 and 439 MPa due to increased toughness and formation of a protective borosilicate layer.

3. What is the sequence of events during the densification of ZrB_2-$MoSi_2$ ceramics, what is the composition of the $(Zr_{1-x}Mo_x)B_2$ solid solution shell structure in ZrB_2-$MoSi_2$ ceramics, and by what mechanism does it form?

Final microstructures of fifteen hot-pressed ZrB_2-$MoSi_2$ ceramics were investigated to provide a wider understanding of densification mechanisms and formation processes of solid solution (SS) shell in ZrB_2-$MoSi_2$ ceramics. Analysis by SEM, TEM, and SAED indicated that each ZrB_2 core and its $(Zr_{1-x}Mo_x)B_2$ SS shell comprised the same monocrystalline grain, while splitting of diboride XRD peaks indicated that the widespread zones of SS shell shared the same dissolved Mo content, that the dissolved Mo is homogeneously distributed within the SS shell, and that the interfaces between the SS shell and ZrB_2 cores are sharp. Estimates of the MoB_2 content in the SS shell via XRD analysis of selected compositions range from 3.1 to 6.3 mol.%. This is the first attempt of which the authors are aware to determine the composition of the SS shell via a method other than spot EDS or EELS. The SS shell characteristic of ZrB_2-$MoSi_2$ ceramics likely forms via the solid state mechanisms of surface and grain boundary diffusion during sintering of contacting diboride particles, during which Mo is incorporated in diffusion-deposited diboride material at particle-particle necks, assisted by mass transport through a fugitive Si-based liquid. The volume fraction of SS shell in the densified ceramics decreased with increasing $MoSi_2$ content due to the increasing densification gained via $MoSi_2$ plastic deformation and the decreasing amount of densification via ZrB_2 particle-particle sintering.

4. How do the mechanical properties (elastic moduli, fracture toughness, and flexure strength) change with systematic variation of the median ZrB_2 starting powder particle size, how do their trends over a range of $MoSi_2$ contents compare, and what are the factors controlling the mechanical properties in ZrB_2-$MoSi_2$ ceramics made with differing ZrB_2 starting powder sizes?

Mechanical properties were measure in air at room temperature and 1500°C for three series of ZrB_2-$MoSi_2$ ceramics processed with fine (FX), medium (MX), and coarse (CX) grades of ZrB_2 starting powder and 5 to 70 vol.% $MoSi_2$ additions. Room temperature strength increased with decreasing ZrB_2 starting particle size from 440–590 MPa for CX, 560–720 MPa for MX, and 700–800 MPa for FX due to the decreasing size of surface grain pullout voids. Fracture toughness (2.7–3.9 $MPa \cdot m^{½}$) and microhardness (16.9–12.2 GPa) showed no overall trend with ZrB_2 starting particle size. Young's

modulus (539–453 GPa), and shear modulus (237–194 GPa) decreased with decreasing ZrB_2 particle size due to impurity content and internal stresses. At 1500°C, fracture toughness increased with increasing ZrB_2 starting particle size. Above ~30 vol.% $MoSi_2$ additions, flexure strength at 1500°C remained roughly constant at 420–460 MPa. Below ~30 vol.% $MoSi_2$, strength was controlled by oxidation damage for FX and MX, increasing from 250–350 MPa to ~450 MPa with increasing $MoSi_2$ content as oxidation behavior became more protective. Flexure strength of CX showed the opposite trend, decreasing from ~600 MPa to ~450 MPa as $MoSi_2$ content increased. Strength of CX compositions with low $MoSi_2$ content did not appear to be controlled by oxidation damage and exhibited the highest reported strengths for the ZrB_2-$MoSi_2$ system at 1500°C in air. The trends of mechanical properties with respect to $MoSi_2$ content and ZrB_2 starting powder particle size reported in this study enabled informed design decisions to be made during fabrication of ZrB_2-$MoSi_2$ DCAs.

5. Can a granule-matrix type DCA be fabricated with ZrB_2 and $MoSi_2$ powders as starting materials, what are the mechanical properties of ZrB_2-$MoSi_2$ DCAs at room temperature and 1500°C and what controls those mechanical properties, what are key factors to consider when designing DCAs for use at elevated temperatures, and is the ZrB_2-$MoSi_2$ system suitable for fabrication of DCAs?

An extrusion granulation technique was developed for the fabrication of four different granule-matrix type DCAs intended for use at 1500°C from ZrB_2 and $MoSi_2$ commercial starting powders. Granulation of specific ZrB_2-$MoSi_2$ compositions was followed by dispersal of granules in matrices of different specific ZrB_2-$MoSi_2$ compositions. Mechanical properties of each DCA were measured at room temperature and 1500°C for ZrB_2-$MoSi_2$ DCAs designed to increase fracture toughness of conventional ZrB_2-$MoSi_2$ ceramics without sacrificing strength at 1500°C in air. Four granule-matrix type DCAs were prepared via extrusion and hot pressing which retained defined zones (sub-composites) of differing engineered microstructure in the same bulk material. At room temperature, elastic moduli did not differ from conventional ceramics with similar overall $MoSi_2$ contents. Room temperature fracture toughness increased to

4.2 to 5.3 MPa·$m^{½}$ due to crack deflection by spontaneous microcracks caused by CTE mismatch between granule and matrix sub-composites. Microcracking contributed to low room temperature flexure strengths of (~140 MPa) in all DCAs, and strengths of 320 and 360 MPa in DCA 2 and 2B at 1500°C, while the strengths of DCA 1 and 1B at 1500°C were further limited to 260 to 280 MPa by oxidation damage resulting from mismatched oxidation behavior between sub-composites. Three focus areas for future development of high-temperature DCAs were identified: 1) resolve microcracking due to sub-composite CTE mismatch; 2) match the oxidation behavior of the sub-composites; and 3) use a discrete interface between sub-architectures to promote crack deflection. Although not reported in the text of the current dissertation, each of these three focus areas were experimentally explored with ZrB_2-$MoSi_2$-SiC three-phase DCAs (DCAs 3, 4, and 4B) and with a ZrB_2-$MoSi_2$-SiC-BN four-phase DCA (DCA 5).

3.2. CONCLUSIONS

The work presented in the papers led the authors to several conclusions:

1. Oxide impurity contents of final microstructures can be reduced by the use of higher purity starting powders and by the use of isothermal vacuum holds during hot pressing. Due to the direct dependence of rapid early densification during application of uniaxial pressure on the $MoSi_2$ content, additions of ≥20 vol.% $MoSi_2$ allow fast densification at relatively low temperatures, minimizing both ZrB_2 grain growth and $MoSi_2$ decomposition. This is expected to result in higher room-temperature flexure strength and improved high-temperature oxidation resistance and ductility. The grain pinning effects of $MoSi_2$ on ZrB_2 grains and the minimal lattice diffusion in ZrB_2 below 2000°C likely result in flexibility in terms of the hot pressing temperatures and times used to densify ZrB_2-$MoSi_2$ ceramics without excessive grain growth.
2. Because the room-temperature flexure strength of as-ground ZrB_2-$MoSi_2$ ceramics is controlled by pullout of the largest near-surface ZrB_2 grains, the flexure strength can be improved by using ZrB_2 powder with smaller maximum particle size. In order to form a continuous protective borosilicate glassy layer and improve strength retention at 1500°C, ≥~20 vol.% $MoSi_2$ content is required in

the final microstructure. Due to decomposition of $MoSi_2$ during hot pressing, this may require a batch addition of >20 vol.% $MoSi_2$. Further, the ductility and fracture toughness of ZrB_2-$MoSi_2$ ceramics at 1500°C increases with increasing $MoSi_2$ content.

3. Due to the chemical reaction between ZrB_2 and $MoSi_2$ that results in decomposition of $MoSi_2$ at hot pressing temperatures, ZrB_2-$MoSi_2$ ceramics are not suited for use at temperatures much in excess of 1500°C. The final volume fraction of $(Zr_{1-x}Mo_x)B_2$ SS shell in ZrB_2-$MoSi_2$ ceramics can be decreased by increasing the starting $MoSi_2$ content and increased by decreasing the starting $MoSi_2$ content. Further, due to the formation of SS shell via surface and grain boundary diffusion, it is likely that the core-shell morphology can be removed by homogenizing the concentration of MoB_2 dissolved in ZrB_2 lattice by densifying or heat treating at greater than 2000°C.
4. The fracture toughness of ZrB_2-$MoSi_2$ ceramics at 1500°C can be increased slightly be increasing the ZrB_2 maximum grain size, and it can be increased by a factor of two by increasing the retained $MoSi_2$ content from 0 to ~67 vol.%. Neither grain size nor $MoSi_2$ content influence fracture toughness at room temperature due to the transgranular fracture behavior. At 1500°C, two opposing trends of flexure strength at low $MoSi_2$ contents demonstrate that we do not fully understand the factors that control strength in ZrB_2-$MoSi_2$ at 1500°C. The possible correlation of high elevated-temperature flexure strength with the SS shell morphology suggests the possibility of an as-yet unexplored strengthening mechanism related to ceramic solid solutions that deserves further study.
5. Granule-matrix type DCAs can be successfully produced with ZrB_2 and $MoSi_2$ commercial powders via simultaneous co-densification of different ZrB_2-$MoSi_2$ compositions in the same ceramic billet by hot pressing. In order to develop a ceramic DCA with favorable mechanical properties in extreme environments, the DCA must be designed with the issues of differential oxidation, crack deflection, and spontaneous microcracking in mind. In general, this leads to the conclusion that for ceramic DCAs without a ductile metal matrix at room temperature, in

order to avoid microcracking either three phases are necessary, or the granule size must be below the critical granule size for spontaneous microcracking.

In addition, several overall conclusions can be drawn from observation of the dissertation. Systematic, quantitative experimentation and microstructural analysis are critical to the observation of useful trends that may be common but not commonly observed. Unexpected and undesired results can sometimes lead to interesting discoveries, such as the complete decomposition of $MoSi_2$ in C10, which was expected to result in low flexure strength at 1500°C and instead displayed the highest reported flexure strength for any ZrB_2-$MoSi_2$ ceramic to date under those conditions.

4. SUGGESTIONS FOR FUTURE WORK

Research presented in this dissertation investigated the processing and densification, as well as the mechanical properties at room temperature and 1500°C of conventional ZrB_2-$MoSi_2$ ceramics, and fabrication, microstructure, and mechanical properties of ZrB_2-$MoSi_2$ dual composite architectures. It should be noted that before eventual application of ZrB_2-$MoSi_2$ ceramics as structural components in industrial use, extensive testing of mechanical properties as a function time at the use temperature will be required, and it is possible that the results of this testing may change the observed trends significantly. Further work on ZrB_2-$MoSi_2$-SiC and ZrB_2-$MoSi_2$-SiC-BN dual composite architectures was conducted and is not included in this dissertation. Several suggestions are presented in this section for advancement of our understanding of ZrB_2-$MoSi_2$ ceramics, and of dual composite architectures intended for use at elevated temperatures in air.

1. The morphology, volume fraction, and composition of the $(Zr,Mo)B_2$ solid solution shell in ZrB_2-$MoSi_2$ ceramics was characterized to a limited extent, but more systematic analysis is needed to understand the factors that control its composition during formation and its influence on mechanical properties at elevated temperatures. Selection of a specific composition, such as C10, for experimentation with hot pressing temperatures and dwell times, microstructural characterization via SEM and XRD, and elevated-temperature flexure tests (in Ar as well as air for determination of the effects of oxidation) should elucidate these relationships. Unfortunately, reaction of exfiltrating Si-based liquid will likely damage the hot pressing dies used for such a study if $MoSi_2$ is used. Alternative sources of solute Mo include Mo carbides and Mo borides. A key outcome of such a study should be the determination of whether the core-shell-type microstructure can be generated and maintained in ZrB_2-based materials at densification temperatures above the grain boundary-to-lattice diffusion transition of ~2000°C.

2. Additionally, investigation of the effects of WC additions on the formation of the core-shell morphology and elevated-temperature mechanical properties is recommended.

3. Fracture surface features of flexure specimens tested at 1500°C in air were destroyed after testing by continued oxidation during cooling of the furnace, making fractographic analysis impossible for high-temperature specimens. It is recommended that a flexure fixture be obtained that has a hole in the center large enough for the pieces of broken flexure specimens to fall through immediately after fracture. Cooling the specimens in an inert atmosphere such as Ar gas or liquid N_2 is expected to preserve the fracture surfaces.

4. ZrB_2-$MoSi_2$ DCAs were fabricated as a high-temperature-capable analog of WC-Co DCAs designed for room temperature use, but the ductile properties of $MoSi_2$, specifically its low yield strength, appear to have hindered its ability to arrest and bridge cracks during testing at 1500°C as Co did at room temperature. Gibbs and Petrovic showed that the yield strength of $MoSi_2$ changes quickly with temperature above 1200°C, so the dependence of mechanical behavior on yield strength could be investigated by adjusting the testing temperature in the range of 1200 to 1500°C.

5. ZrB_2 and $MoSi_2$ were chosen as primary materials for the DCAs fabricated in this study due in part to the interesting behavior exhibited these materials, but the presence of ZrB_2 in the microstructure was found to be detrimental to the oxidation resistance in all DCA sub-composites that contained it, even with additions of both $MoSi_2$ and SiC (Fig. 4.1). It was established that three phases are needed to adjust for CTE mismatch between DCA sub-composites, and it is recommended that further work toward DCAs for use at elevated temperatures in air focus on SiC-$MoSi_2$-Si_3N_4 dual composite architectures and SiC-$MoSi_2$-Si_3N_4-BN dual composite architectures. Petrovic et al. showed that 50/50vol.% $MoSi_2$-$Si3N_4$ mixtures had RT fracture toughness values of 5.5 for α-Si_3N_4 and 15 for β-Si_3N_4 [70]. Also, additions of SiC via C additions to $MoSi_2$ increased its toughness at elevated temperatures [48]. $MoSi_2$-SiC ceramics appear to have

excellent oxidation resistance (Fig. 4.1), and Vasudevan and Petrovic report that SiC and Si_3N_4 have lower oxidation rates than $MoSi_2$ at 1500°C (Fig. 4.2).

6. Several key aspects of DCA design and fabrication were not explored in the present study. One aspect is architectures other than granule-matrix, even when the fabrication methods used can be easily adapted to related architectures such as rod-matrix. Pressureless sintering of DCAs to achieve a more isotropic mesostructure was attempted but unsuccessful with ZrB_2-$MoSi_2$ ceramics.

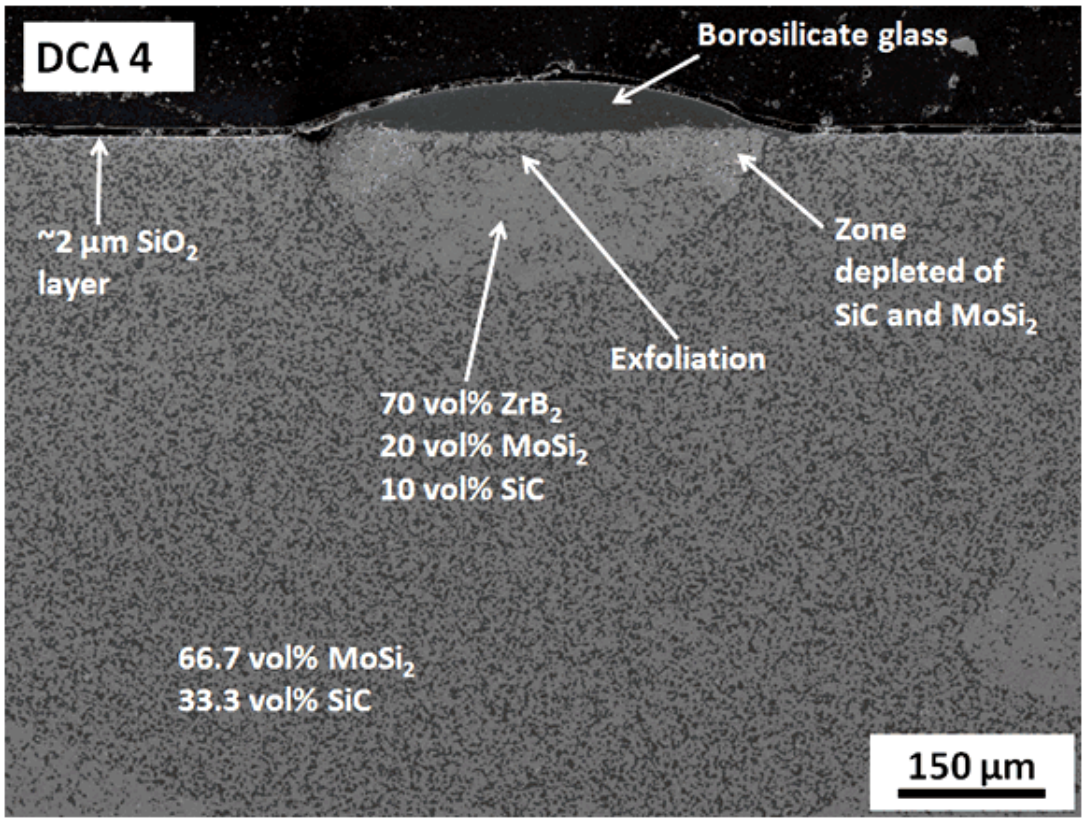

Fig. 4.1. Secondary electron micrograph of polished cross section of DCA 4 after flexure testing at 1500°C showing the difference in oxidation behavior of the ZrB_2-containing granule and the ZrB_2-free matrix.

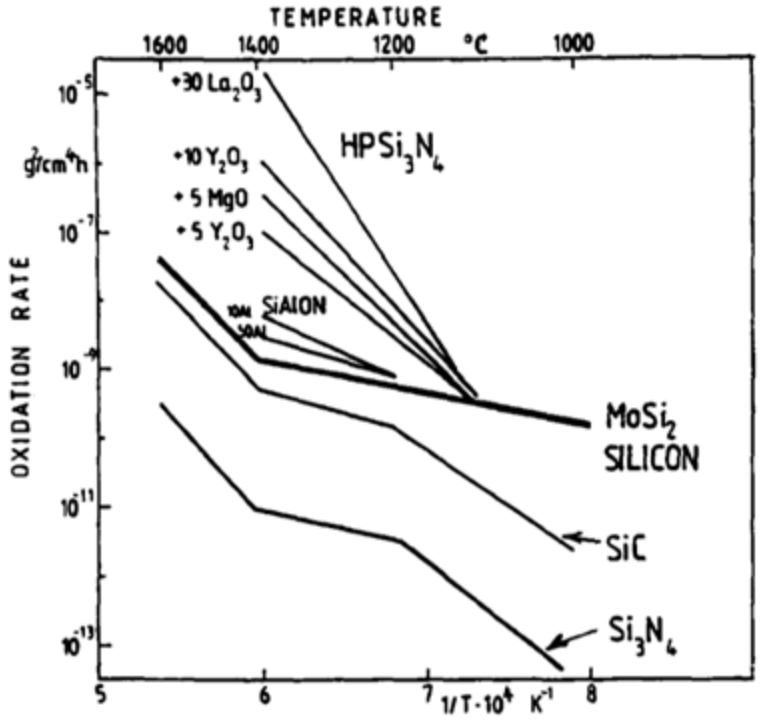

Fig. 4.2. Oxidation rates of $MoSi_2$ and selected Si-based ceramics.Reproduced from [21]
.

APPENDIX A.

INVESTIGATION OF CRYSTALLINE ANISOTROPY IN ZrB_2-$MoSi_2$ CERAMIC COMPOSITES BY ELECTRON BACKSCATTERED DIFFRACTION (EBSD)

OBJECTIVE

Ultra-high-temperature ceramics such as zirconium diboride (ZrB_2) have exceptional combinations of properties which make them candidates for use in extremely harsh mechanical, thermal, and chemical conditions. Melting points above 3000 °C, high hardness and wear resistance, high strength, electrical and thermal conductivities and excellent chemical stability support their use in applications of high-speed industrial metals machining, crucibles for liquid metals, heat shields for future hypersonic vehicles, machine bearings, and solar thermal power generation. However, because of the high degree of covalent bonding in these materials, diffusion kinetics during sintering are slow, making densification difficult. This, combined with the desire to tailor the material properties to a particular temperature/application envelope has caused various additives such as metal carbides and silicides to be used as sintering aids and property enhancers. In this case, Molybdenum disilicide ($MoSi_2$) has been added to ZrB_2 with the goal of lowering sintering temperature and increasing fracture toughness and oxidation resistance for applications near 1500 °C. This should make use of the brittle-to-ductile transition of $MoSi_2$ near 1150 °C.

Both phases in this ceramic composite have crystal structures with a unique c-axis. Zirconium diboride crystals are hexagonal P6/mmm, composed of layered sheets of hexagonally bonded boron atoms alternating with layers of zirconium atoms. $MoSi_2$ crystallizes in a tetragonal I4/mmm structure, with less well defined layers of atoms stacked in the direction of the c-axis. Material properties are structure-dependent and variations in electrical and thermal conductivities have been measured in ZrB_2 between the <100> direction and the <001> direction. Because stiffness is a fourth-rank tensor, it should also display anisotropy related to the crystal structure. Scanning electron microscopy combined with nano-indentation offer the possibility of measuring mechanical anisotropy in polycrystalline samples.

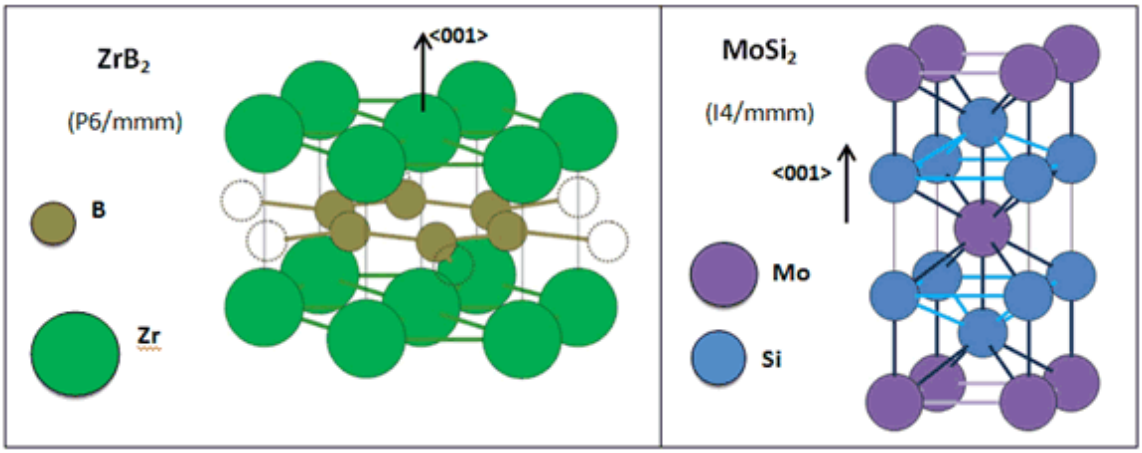

Figure 1: Illustration of the anisotropic crystal structures of ZrB_2 and $MoSi_2$.

Scanning electron microscopy, along with energy dispersive spectroscopy (EDS) and electron backscattered diffraction (EBSD) allow micron-sized grains in a ceramic composite to be imaged, identified by composition, and mapped by crystallographic orientation. Nano-indentation techniques allow mechanical data to be collected on specimen areas as small as 200 nm. The objective of this project is to use EBSD to analyze a series of nano-indentations made on ZrB_2-$MoSi_2$ composite to test for anisotropy in Young's modulus, indentation hardness, stiffness, and indenter deflection related to the crystallographic orientation of the grain that was indented.

PROCEDURE

This project was completed in two stages, one of sample preparation and indentation conducted before starting this class and one of microscopic analysis completed for this class. The first stage is outlined in summary and the second is covered in more detail.

Stage 1

Powders supplied by H.C. Starck, ZrB_2 grade A, and $MoSi_2$ grade B, were mixed in a 65%Z-35%M ratio by volume percent and ball milled in ethanol for 24 hours with milling media made of ZrB_2-30 vol.% SiC. The powder was rotary evaporated and hot

pressed at 1800°C and 30 MPa to 98.2% of relative density. The hot pressed disc was cut up with a diamond saw, and initial microscopy of polished sections showed that silica contaminants introduced as oxide present on the initial $MoSi_2$ powder comprised just over 3 vol.% of the specimen and helps to explain the difference in density from that calculated by rule of mixtures of ZrB_2, $MoSi_2$, and SiC. To help increase contrast between the Z and M phases for image analysis, the specimen was etched for 45 seconds with colloidal silica, which generated topographical differences between the phases and probably detracted from the effectiveness of the EBSD map which was performed months later.

The polished specimen was examined uncoated at the Italian National Research Council's Institute of Science and Technology for Ceramics (CNR-ISTEC) in Faenza, Italy using a Zeiss Sigma FEG SEM. EDS was used to confirm that the lighter gray phase was M, the darker gray phase was Z, and the black phases were SiO_2 pockets with SiC precipitates inside them and BN contaminants around their edges. Next, it was indented with an MTS Nano-Indenter XP indenter using a Berkovich triangular pyramidal tip. A total of 150 indents were made: 10 at 500 mN max load, 20 each at 200, 100, 50, and 10 mN, and a grid of 60 indents spaced 3 μm apart was made at 5 mN max load. 1 mN indents were attempted but the radius of the tip made the validity of these measurements questionable. During each indent, the force applied and the penetration depth were recorded approximately 5 times a second. Using these values and the value of 0.15 input for Poisson's ratio of both ZrB_2 and $MoSi_2$, the indenter software was able to calculate the Young's modulus, Berkovich hardness, displacement at maximum load and stiffness at maximum load for each indent. Next, the specimen was again investigated with the Zeiss SEM before being brought back to Rolla via Bologna, Frankfurt and Philadelphia.**Stage 2**At Missouri University of Science and Technology the specimen was observed with the help of Clarissa Wisner using the Hitachi S4700 SEM for secondary electron mode with the following operating conditions:

Table I: Operating conditions for the Hitachi S4700 SEM.

Accelerating Voltage:	1 keV
Working Distance:	3.5 mm
Detector:	Mixed
Magnification:	13,000 to 110,000 X
Tilt:	0°

The objective of this imaging session was to see if slip lines around the smallest indents could be resolved, and this attempt was successful at 60,000 and 110,000X. Successful indexing of crystalline phases by EBSD requires that the software know both the crystal structure and the precise lattice parameters of the phase. Both ZrB_2 and $MoSi_2$ already had multiple entries in the software database on the Helios, but these entries had slightly different lattice parameters listed for the phases.

In order to increase the chances of successful indexing, and because previous attempts at EBSD of ZrB_2 composites at MST had not been very successful, the lattice parameters were measured by X-ray powder diffraction with Rietveld refinement. A different sectioned piece of the same hot pressed disc that was indented was crushed in a steel anvil pulverizer and ground to -150 mesh in an alumina mortar and pestle. A rare earth magnet was used to remove the iron contaminants and the XRD scan was run from 6 to 90° 2θ in an X'Pert Pro PANalytical diffractometer with Cu Kα radiation. ZrB_2 and $MoSi_2$ were the only two detectable phases and found to be present in 68.3 and 31.7 volume percent, respectively. This is fairly close to the ZrB_2/ $MoSi_2$ ratio found in preliminary image analysis and the difference from a 65/35 ratio indicates that some of the $MoSi_2$ dissociated and formed a $(Zr,Mo)B_2$ solid solution, which has been seen in previous work by the ISTEC group in Italy. Match units for Z and M were chosen from the database in the Helios hard drive prior to mapping with lattice parameters which most closely matched the XRD lattice parameter measurements made on this specimen, and a match was chosen for ZrO_2 and SiC that fitted the suspected of those phases that was suspected to be present since no custom XRD data was available.

EBSD mapping was carried out with the Helios 600 nanolab. The specimen was mounted on an aluminum pin stub with carbon paste and dried under a warm lamp, before being scrubbed vigorously with methanol and a cotton swab, then cleaned in the plasma cleaner for five minutes immediately before loading into the specimen chamber. The pin stub was mounted to a holder on the stage that kept the specimen surface at 70° of tilt. Because the nanoindents were made near one corner of the specimen, care was taken to mount the specimen so that this corner was closest to the pole piece of the electron column so that it could be moved to 4 mm working distance.

Imaging with secondary electrons, the largest indents were found first and used to locate the indent array with the smallest indents, which were mapped for this project. After the specimen had been properly positioned, several grains were indexed as a test, but unfortunately the Kikuchi patterns were not saved. Forescatter/backscatter images were collected before and after mapping, and showed very little movement of the specimen during the approximately 48 minute scan. EBSD mapping was carried out with the following parameters:

Table II: Operating parameters for the Helios 600 nanolab during EBSD mapping.

Accelerating Voltage:	30 keV
Beam Current:	11 nA
Scope Magnification:	10,000X
Flamenco Software Magnification:	20,000X
Step Size:	0.05 μm
Grid:	265 wide x 129 h (34,185 points)
Working Distance:	4 mm

After mapping, the data were saved and the project was opened in the Project Manager with the Tango software. Using the software to do a noise reduction and to

extrapolate the wild spikes projected the indexed crystal structure to the initially non-indexed areas at amorphous pockets and grain boundaries.

The Map Composer was used to save maps of individual phases and maps in which the $MoSi_2$ was shown in shades of blue and the ZrB_2 was shown in tints of red. A crystallographic orientation map was generated which color coded the grains based on their axial orientation. Next, using the forescatter/backscatter images in which the indents could be seen, the locations of the indents were overlaid by hand on the phase identification and orientation maps. These together were used to correlate a particular indent (assigned a number by the nano-indenter) with a particular grain (assigned a number by Flamenco software), and therefore phase and orientation. This list was compared to the list of indents and phases made by visual examination immediately after indentation, and fortunately the indent numbers and phases matched up perfectly on both lists.

In order to correlate the elastic modulus, hardness, displacement and stiffness with a certain crystallographic orientation, the second Euler angle was retrieved from the data spreadsheet and matched with each indent's property measurements. Figure 2 shows why only the second Euler angle was used.

The first and third Euler angles describe a rotation around the z axis of a set of coordinates (or the c axis of a crystal's unit cell), but the second angle describes a rotation around the x (or a) axis. Therefore, the second angle determines to what degree the unique c axis of both of these crystals is misaligned from the observed polished surface of the crystal from which the Kikuchi patterns were generated. In this study, the analysis was simplified by examining only the misalignment from the c-axis of the lattice and ignored the variation between the identical a and b axes. Also, since stiffness is a fourth-rank tensor, its derived coefficient between identical a and b axes and perpendicular to a unique c axis should be isotropic within that plane.

To confirm that the software interpreted the orientation of the crystal axes in accordance with traditional Euler angle nomenclature, certain grains were selected from the orientation map that the color key showed to be rotated at close to 90° and 0° or 180° from the c axis. Grains 46, 50, 74, and 180 were chosen as examples of grains that color coding indicated were rotated close to 0°, 90°, 0°, and 90° respectively from the c axis.

The color coding and numerical values agreed, showing that a second Euler angle of 0° or 180° indicated that the indenter would have pressed parallel to the c axis. Finally, the data were plotted.

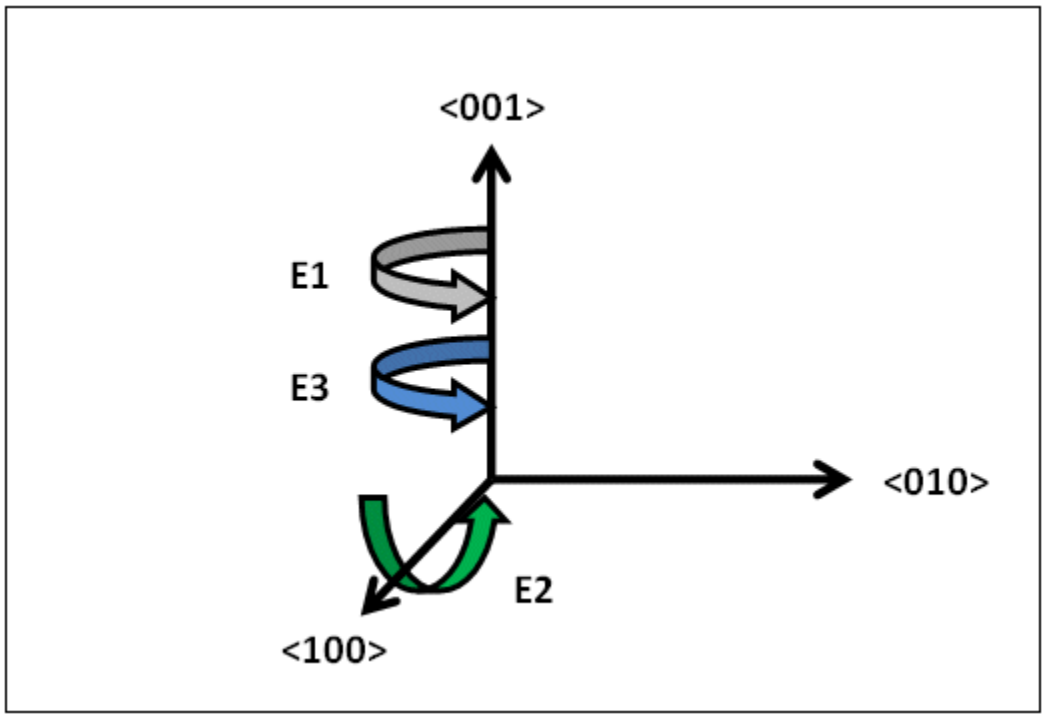

Figure 2. Illustration of Euler angle rotations of a set of orthogonal axes.**ANALYSIS**

Rietveld refinement of powder XRD showed the lattice parameters and axes angles to be the following, shown in Table III.

Table III: Lattice information from refined powder XRD.

Phase	**Structure**	**a (Å)**	**b (Å)**	**c (Å)**	**α (°)**	**β (°)**	**γ (°)**
ZrB_2	P6/mmm	3.1676	3.1676	3.5287	90.000	90.000	120.000
$MoSi_2$	I4/mmm	3.2052	3.2052	7.8497	90.000	90.000	90.000

EDS analysis of the preliminary images confirmed that the lighter gray phase is $MoSi_2$, the darker gray phase is ZrB_2, and the black phase is silica originating from the oxide scale on the $MoSi_2$ powder. This agrees with the atomic number contrast of the phases. Gray precipitates inside the silica phase were identified BN, an aerosol spray lubricant used in the laboratory, and as SiC, possibly precipitating during partial carbothermal reduction of the silica using residual carbon from the ball milling operation and carbon diffusing from the walls of the graphite die during hot pressing. Images of the nano indentations showed crystalline slip planes in the indented grains indicating that at small scales, macroscopically brittle ceramics can plastically deform to a limited extent. Brittle transgranular and intergranular cracking were also common near higher-load indents, especially those that overlap grain boundaries. Figure 3 shows a 500 mN indent overlapping both ZrB_2 and $MoSi_2$ grains.

The activated slip planes can be seen clearly as straight lines in the ZrB_2 grains and as less well-defined wavy lines in the $MoSi_2$ grains. It is very interesting to note that the slip planes in Z change orientation at grain boundaries, showing that the different crystallographic orientation does change the deformation behavior. Figure 3 is a high-resolution image of one of the 5 mN indents in ZrB_2 showing similar slip planes and indicating that slip planes still activate at very low loads. This is important for this study since the 5 mN indents were the only ones that consistently fit into single grains and did not frequently cross over grain boundaries, and so are the only ones mapped by EBSD.

The dark rectangles overlapping areas of Figure 4 are carbon deposition traces left by the beam from when different areas were imaged prior to this image capture. It is also interesting to note that researchers at ISTEC have done multiple low-load tests with their nano-indenter in fused silica and have calculated a tip radius of approximately 120 nm based on the trend of the results. It is fuzzy in this image, but the dark triangular shape at the center of the indent appears to be approximately 150 nm from corner to corner. Lower loads than 5 mN in hard ceramic materials produce indents that are too small and shallow to satisfy the criteria for a valid indent, which assumes a perfectly sharp indenter tip.

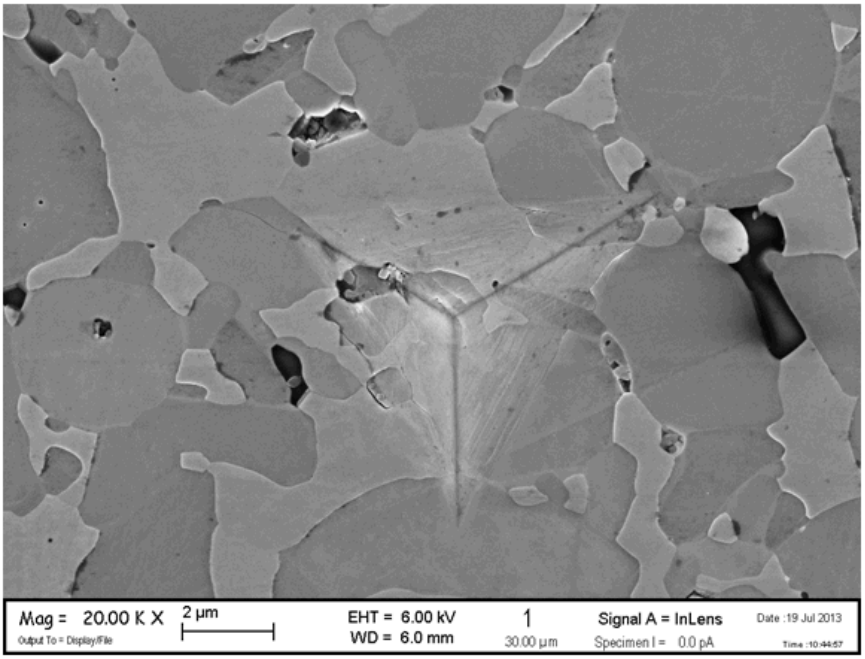

Figure 3: Largest Birkovich indent made with a load of 500 mN, showing activated slip planes in both ZrB_2 and $MoSi_2$ phases. $MoSi_2$ is light gray, ZrB_2 dark gray, and SiO_2 black. Different directions of slip planes can be seen in different ZrB_2 grains. Image taken with a Zeiss Sigma SEM with FE source.

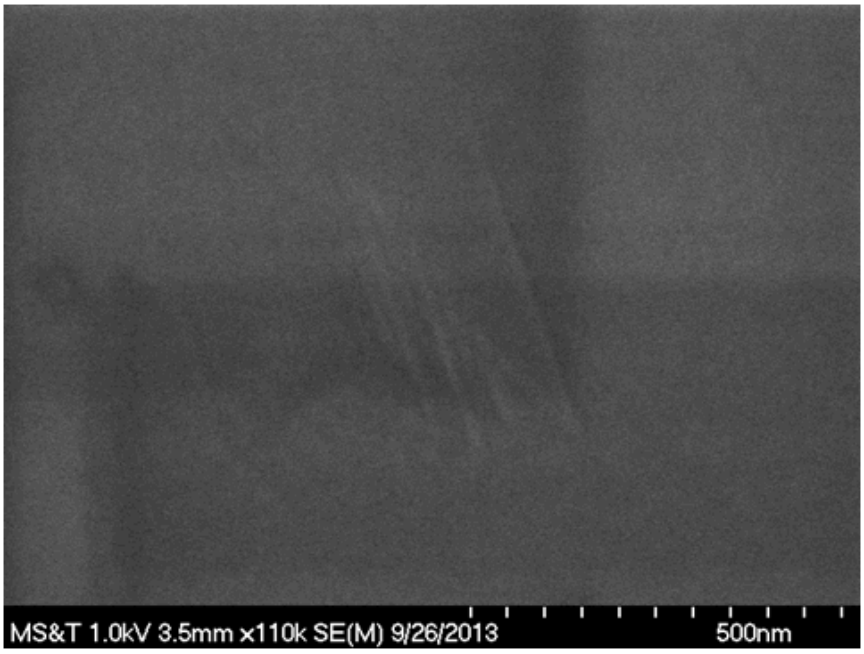

Figure 4: A 5 mN indent in ZrB_2 imaged with the Hitachi S4700 at showing slip planes across the indent.

Figure 5 shows the entire array of sixty 5 mN indents arranged in 6 rows and 10 columns. Difficulty in seeing the microstructure through the optical microscope in the nanoindenter meant that a random are was chosen for the array, which included several silica pockets. The indents were executed automatically and overall, by visual inspection, 30 indents were placed on ZrB_2 grains, 9 were placed on $MoSi_2$ grains, 17 intersected some type of grain boundary or interface, and 4 indents were placed on silica pockets. Therefore, 47/60 indents could be expected to give useful crystallographic information. However, not all of the indents were in the area mapped by EBSD. The dotted quadrangle in Figure 5 shows the area that was mapped; it is distorted because the specimen was tilted at 70°. At sufficient magnification to resolve grains easily, only about 1/3 of the array fit on the screen, and because of the time required to locate the indents on the specimen surface, the SEM time slot was over before more than one map could be completed.

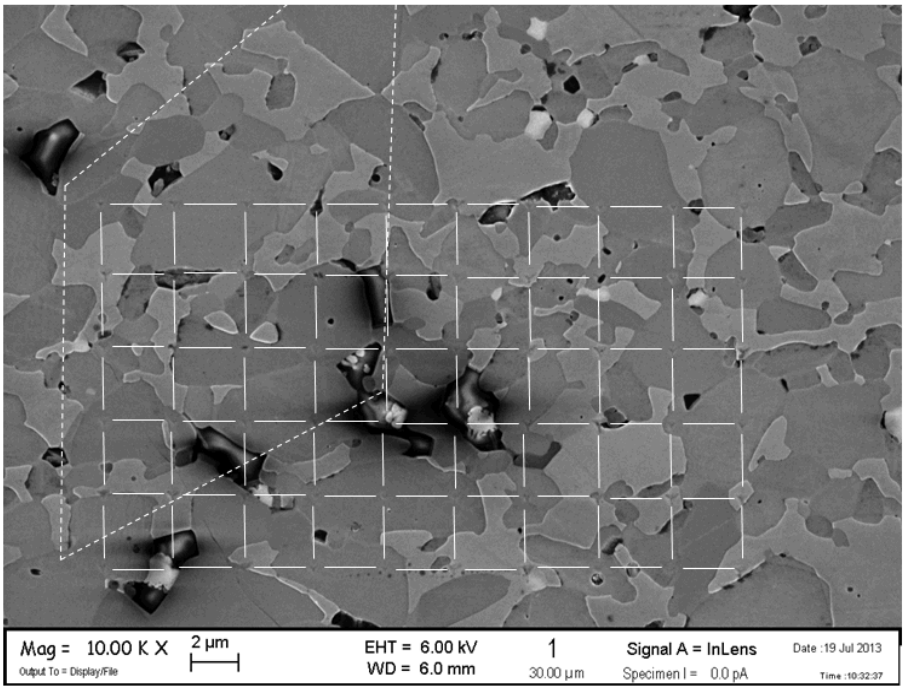

Figure 5: Six-by-ten grid of 5 mN indents at locations indicated by the intersections of solid white grid lines. The quadrangle of dashed white lines shows the area that was mapped with EBSD for this study.

Figure 6 shows the forescatter-backscatter image of the area of the array that was mapped. Individual grains can be recognized from Figure 5, although distorted due to tilt. The surface in Figure 6 slopes away from the viewer from bottom to top at 70°, and this allows for the topographic variability from preferential etching by colloidal silica to be seen.

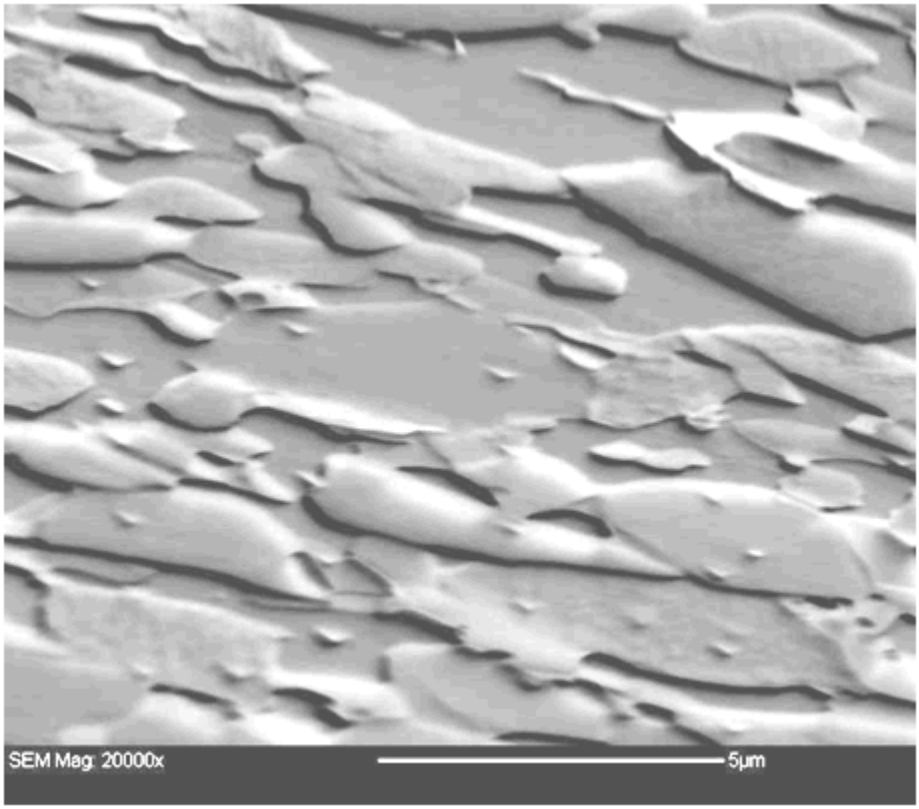

Figure 6: Forescatter-backscatter image at 70° of tilt showing the approximate area mapped with EBSD. 23 of the 5 nM indents are visible. Compare with the untilted specimen area shown in Figure 5.

The initial EBSD map as-collected is shown in Figure 7 overlaid on the forescatter/backscatter image from Figure 6.The software was able to successfully index 74% of the points in the map. It can be seen that areas corresponding to silica pockets in Figure 5 are unindexed due to their amorphous structure, and a substantial area around

grain boundaries is also not indexed. This is possibly due to the preferential etching that was done with colloidal silica, and is not recommended for future EBSD maps.

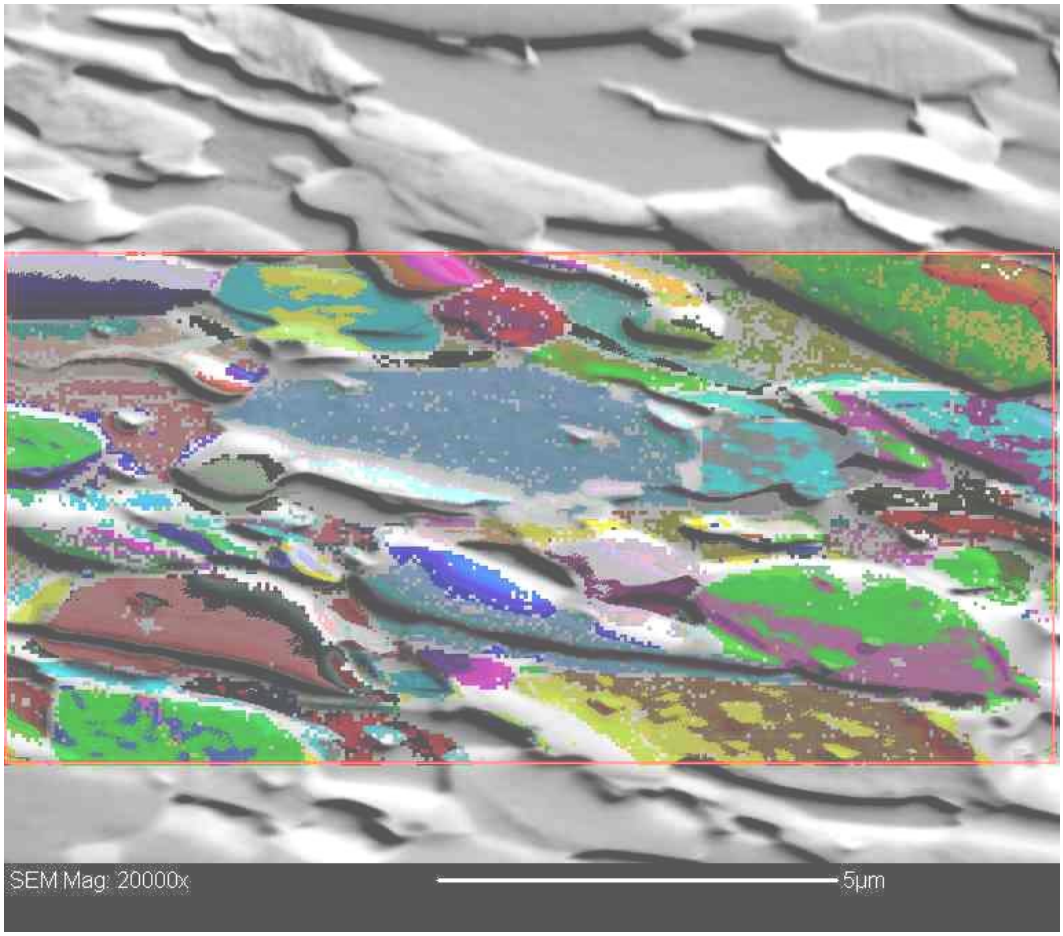

Figure 7: Forescatter-backscatter image showing the initial EBSD map overlaid on the specimen microstructure, 70° tilt. Silica pockets, grain boundaries, and some 5 mN indents are not indexed.

Using the Tango software to extrapolate wild spikes and highlight new grain boundaries generated a suspected index match for the initially unindexed area. This requires some caution on the part of the user, because even areas that were positively identified as amorphous silica have now been assigned crystalline phase identification. This was noted and the locations of the indents were double checked to confirm the phase

indented because the automatically generated data could not necessarily be trusted due to extrapolation by the software which identified amorphous impurities as crystalline phases. Figure 8 is a phase identification map showing the map filled in by the software extrapolation and the grains indexed as ZrB_2 in tints of red and the grains indexed as $MoSi_2$ indexed in shades of blue. Also shown by black dashed lines are two approximate areas that were identified as silica pockets in preliminary images and but which the software has identified as ZrB_2. Table IV shows the results of the extrapolated map.

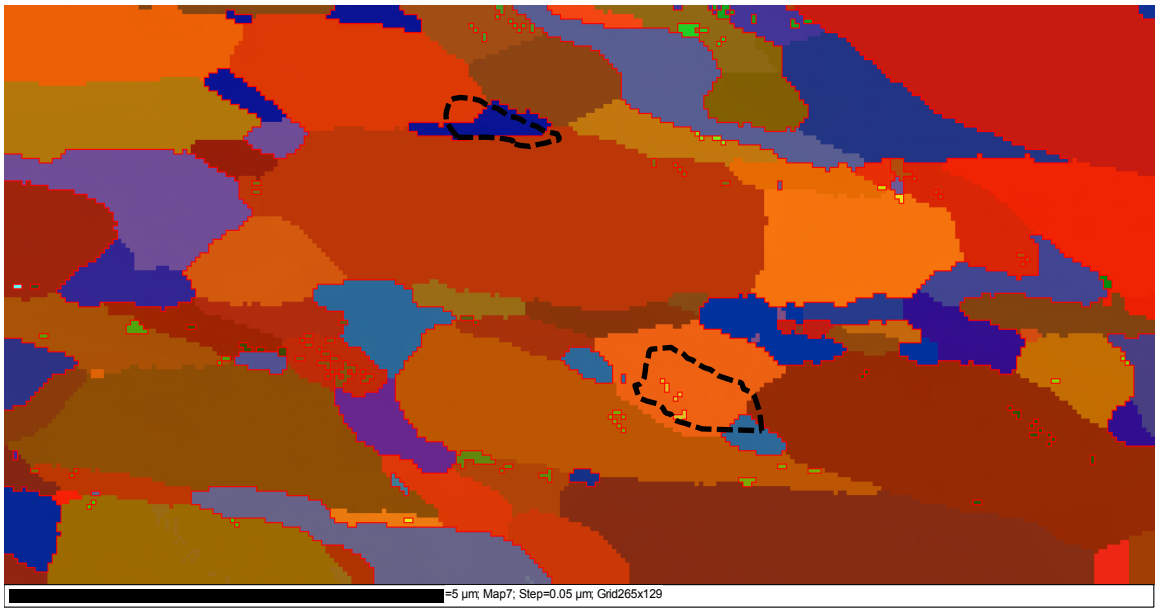

Figure 8: Phase ID map of surface at 70° of tilt showing ZrB_2 in tints of red and $MoSi_2$ in shades of blue. Different shades of color indicate differing crystallographic orientations. Scale bar is 5 µm.

There are many very small SiC grains shown by Table IV, but the majority of them were single pixel points (about 0.05 µm) dispersed across the EBSD map. Until now, such dispersed SiC particles had not been observed in the structure, and most of the SiC was assumed to reside in the SiO_2 pockets. However, this detected SiC may be well-dispersed contamination from the ZrB_2-30%SiC media that was used in ball milling. The average misorientation angle is approximately 90° with a large standard deviation,

indicating that each phase was relatively randomly oriented between 0° and 180°. The author does not understand the relationship between the average grain diameter and the average grain area, which are not compensated for specimen tilt.

Table IV: Summary of the data collected on the grains in the specimen.

Phase:	**Total Area %**	**Number of Grains**	**Avg. Gr. Area (μm^2)**	**Avg. Gr. Diameter (µm)**	**Avg. E2 Angle (°)**	**Mean MAD**
ZrB_2	80.58	62	1.64 ± 2.9	1.07 ± 0.98	94 ± 40	.5118
M	18.64	41	0.59 ± 1.0	0.63 ±0.60	90 ± 44	.5551
ZrO_2	0.0	1	0.005	0.08	173.5	n/a
SiC	0.7	110	0.0063 ±0.008	0.08 ±0.04	96 ± 38	.529
Total:	99.92	214	0.61 ±1.8	0.48 ± 0.7	95 ±40	

Figure 9 shows the map converted to an orientation map showing with grains color coded by crystallographic orientation. The black triangles are overlaid to show the locations of the indents, and several grains are labeled with their numbers to indicate that they were used to confirm that the software used conventional notation for Euler angles when calculating the crystalline orientation. The color keys show that red corresponds to grains which are oriented with their c axis perpendicular to the plain of the specimen surface, green corresponds to grains which have the <010> direction perpendicular to the surface, and blue indicates the (120) plane in hexagonal ZrB_2 and the (110) plane in tetrahedral $MoSi_2$. Thus, red corresponds to a second Euler angle of near 0° or 180° and blue, teal, and green correspond to an angle of near 90°. Table V lists the grains that were used to check this correlation.

Table VI lists the 18 indents within the mapped area, as well as the phase of the grain in which it was placed, the mechanical measurement values recorded by the

nanoindenter, the grain number and average second Euler misorientation angle of the grain.

The data in Table IV are plotted in Figures 11-14, which each show the relationship of modulus, hardness, displacement, and stiffness with the degree of misorientation from the c axis. Because there were only two $MoSi_2$ grains with suitable indents, little information can be gained from their data, except for their relationship to the values of ZrB_2. Only 11 suitable points for ZrB_2 also leave some questions unanswered. Table VII shows the average measured values for each phase at 5 mN.

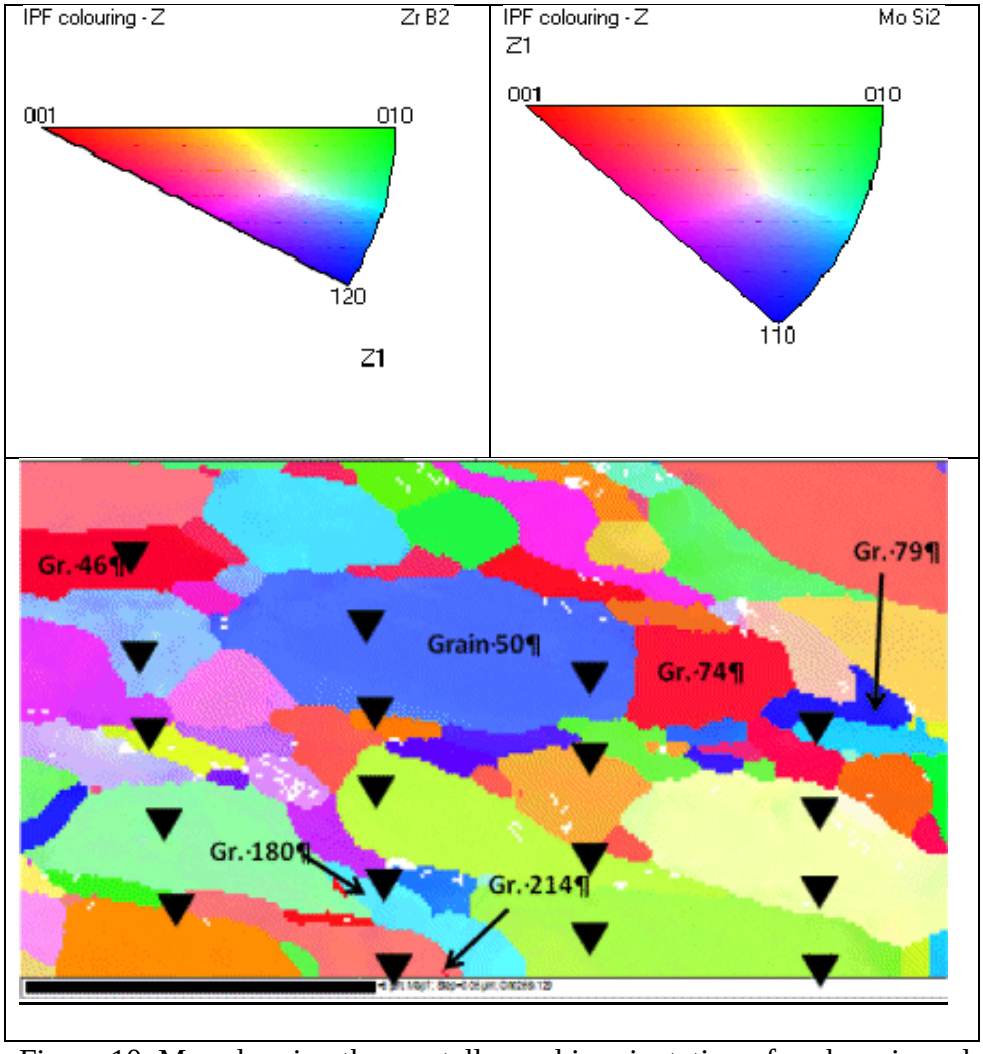

Figure 10. Map showing the crystallographic orientation of each grain coded by the colors in the two keys at top. Locations of the indents are overlaid as enlarged black triangles. Scale bar is 6 μm.

Figure 11 shows Young's modulus with respect to misalignment from the c axis. It is possible that there is a maximum in the modulus when ZrB_2 is loaded perpendicularly to the c axis, or "edge on" to the atomic layers, and a minimum when the alternating layers of Zr and B atoms are being pressed together. It has been suggested in previous research that the zirconium-zirconium bonds are mostly metallic in character, that the boron atomic layer is held together mostly by covalent bonds, and that the primary bond type between the layers and two types of atoms is ionic.

Table V: List of the grains that were used to confirm the second Euler angle color correlation.

Grain Number	**Phase**	**Color**	**Approx. Suspected E2 Angle**	**True E2 Angle**
46	ZrB_2	Red	Near 0° or 180°	168.25°
50	ZrB_2	Blue	Near 90°	77.79°
74	ZrB_2	Red	Near 0° or 180°	162.84°
79	$MoSi_2$	Blue	Near 90°	97.5°
180	ZrB_2	Teal	Near 90°	78.9°
214	$MoSi_2$	Red	Near 0° or 180°	165.61°

Figure 12 shows the variation of Berkovich nanohardness with respect to misalignment from the c axis. $MoSi_2$ is softer than ZrB_2, which is expected. From this plot it is difficult to make any supported conclusions. It may be that there is a hardness maximum when the indentation force is parallel to the c axis. The trend in the data for ZrB_2 is larger than the standard deviation in hardness. More data are needed for this plot especially.

Table VI: Selected measured properties at each 5 mN indent matched with the visually identified phase, the number of the indexed grain, and the mean second Euler angle calculated for that grain.

		Young's Modulus	Birkovich Hardness	Max. Disp.	Stiffness At Max Load	Grain Number	Mean orient. Euler 2
Indent Number	**Phase**	**(GPa)**	**(GPa)**	**(nm)**	**(kN/m)**	**(of 214 total)**	**(°)**
1	ZrB_2	448.781	34.934	81.332	146.0765	46	168.52
2	ZrB_2	530.739	31.74	82.406	173.4144	50	77.79
3	ZrB_2	496.458	30.618	83.825	167.3894	50	77.79
4	GB	446.117	21.19	100.566	187.3991	74/89	
17	ZrB_2	575.867	28.765	84.117	191.2272	131	59.41
18	GB	635.402	35.696	75.087	182.7811	106	
19	Silica	241.393	7.214	174.841	198.9135	50/85/86	
20	$MoSi_2$	493.034	23.016	95.179	192.4185	56	109.11
21	GB	463.937	23.815	94.911	181.6956	80/97	
22	GB	364.978	16.192	116.429	184.8155	85/104	
23	ZrB_2	556.218	29.495	83.526	184.337	104	121.23
24	ZrB_2	454.993	28.753	87.328	162.2818	131	59.41
37	ZrB_2	463.105	28.012	88.376	167.0332	194	61.98
38	ZrB_2	496.982	27.14	88.649	178.5692	194	61.98
39	ZrB_2	511.661	32.143	81.957	167.2146	180	78.9
40	ZrB_2	507.834	31.352	82.978	168.5124	138	109.94
41	GB	498.603	23.461	94.134	191.9606	183/200	
42	$MoSi_2$	467.471	19.18	104.3	203.2795	197	140.41

Table VII: Average values for each phase at an indentation load of 5 mN.

Measurement	**ZrB_2**	**$MoSi_2$**
Young's Modulus (GPa)	520 ± 37	450 ± 36
Berkovich Nanohardness (GPa)	31 ± 2.8	20 ± 1.6
Displacement @ max Load (nm)	83 ± 3	103 ± 4.5
Stiffness at max Displacement (kN/m)	170 ±11	195 ± 8

Figure 13 shows the variability of displacement at maximum load with respect to misalignment from the c axis. Displacement is greater into the $MoSi_2$, which agrees with the relationship seen in the hardness plot in Figure 12. The indenter displacement in the ZrB_2 appears to be fairly constant, no matter the crystalline orientation. However, because of the shallow geometry of the triangular indenter and the fact that hardness values are proportional to the surface area generated during the indent, the linear displacement needs to be exaggerated to see the trend. If the plots are inspected closely, individual data points can be matched between the hardness plot and the displacement plot. This is expected because the hardness is calculated from the displacement.

Figure 14 shows the variability of the stiffness at maximum displacement with respect to misalignment from the c axis. The stiffness relationship between ZrB_2 and M is not understood, and this uncertainty is coupled with a lack of knowledge of how the nano-indentation instrument measures the stiffness. ZrB_2 has a higher elastic modulus on average than $MoSi_2$, yet a lower stiffness value. The stiffness value itself is measured in kN/m, but because the load at maximum displacement should be relatively constant (limited to 5 mN indents) and indenter tip had a higher displacement into $MoSi_2$, these values seem to be backwards. Inquiries have been made to ISTEC about the measurement process of the indenter.

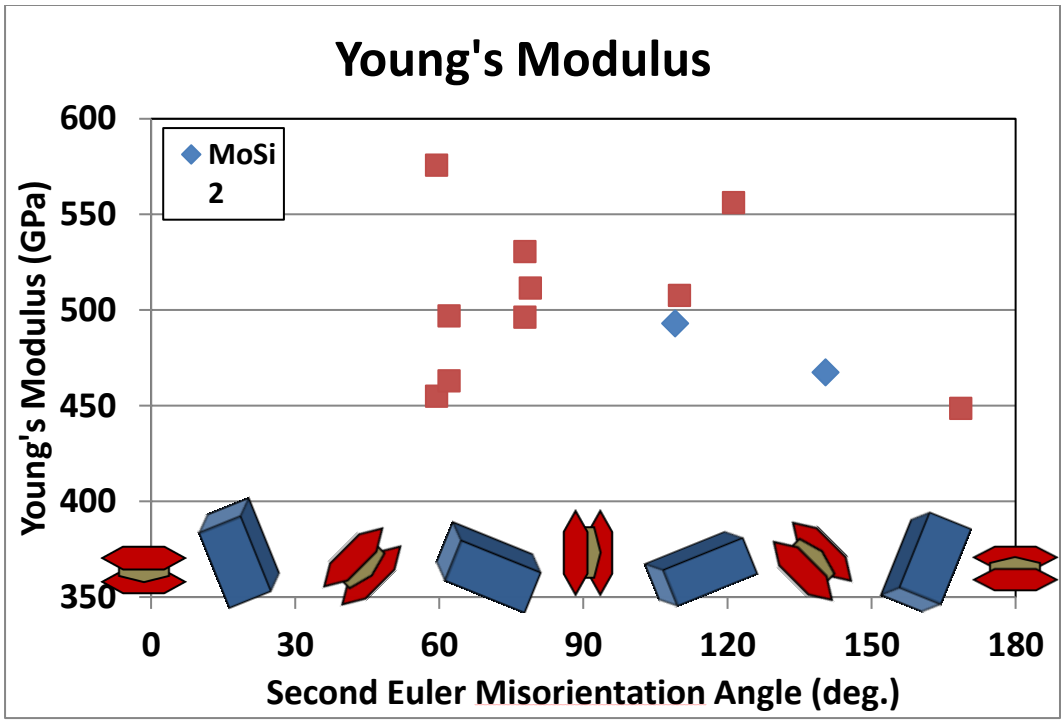

Figure 11: Plot of the Young's modulus with respect to the second Euler misorientation angle. Cartoon representations of rotated unit cells are added for clarification.

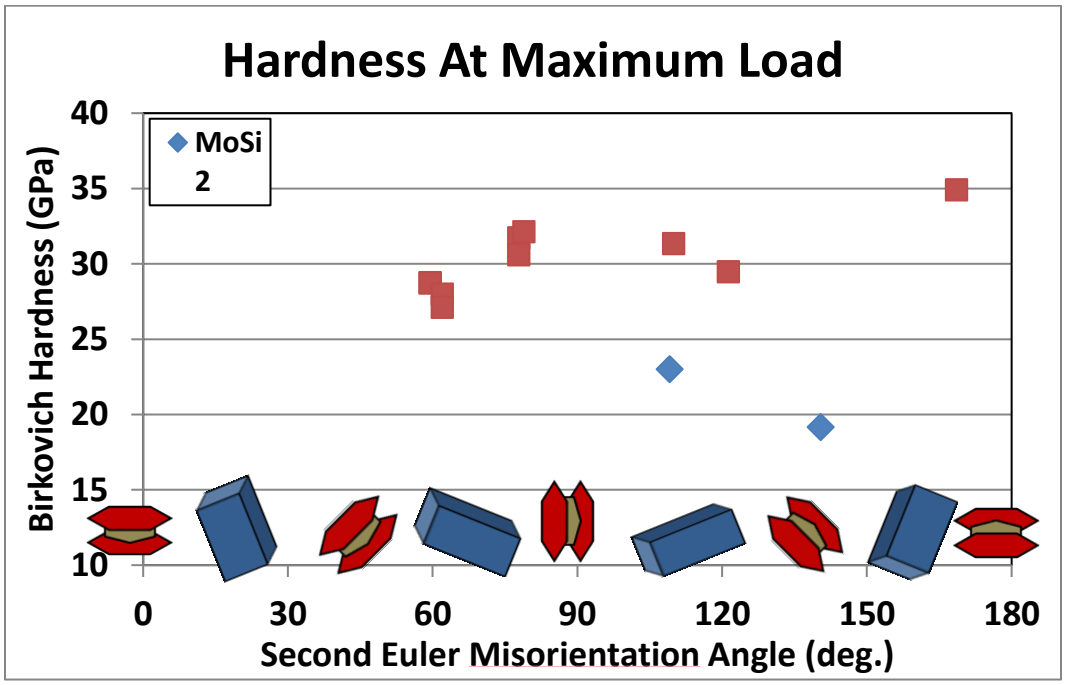

Figure 12: Plot of the Berkovich hardness at maximum load with respect to the second Euler misorientation angle.

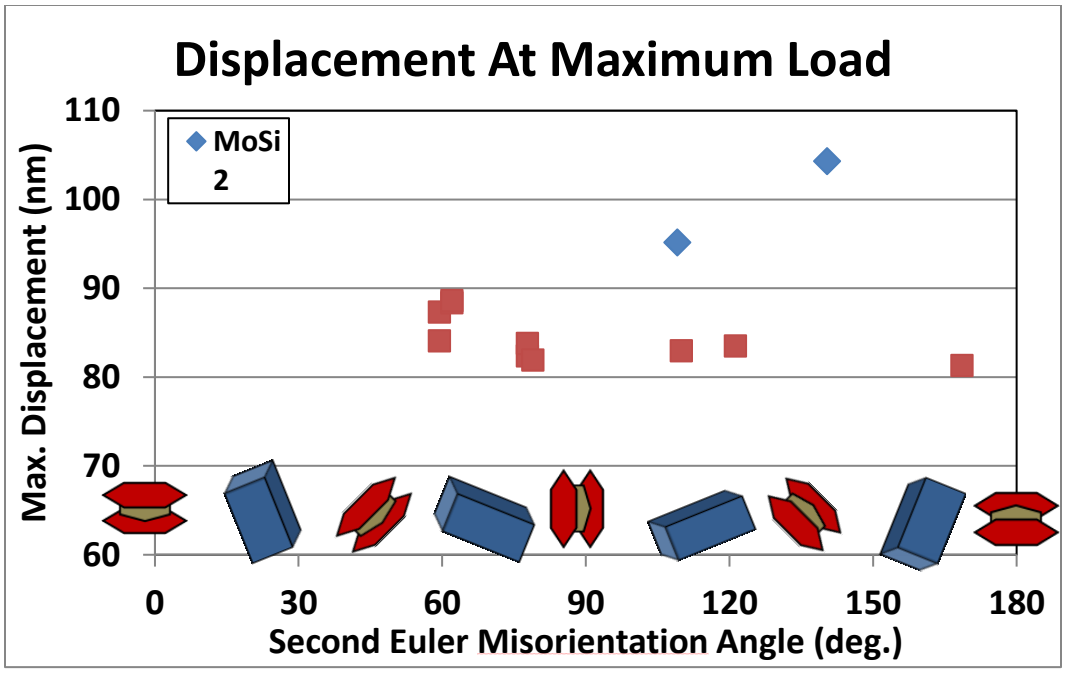

Figure 13: Plot of the displacement into the specimen surface at maximum load with respect to the second Euler misorientation angle.

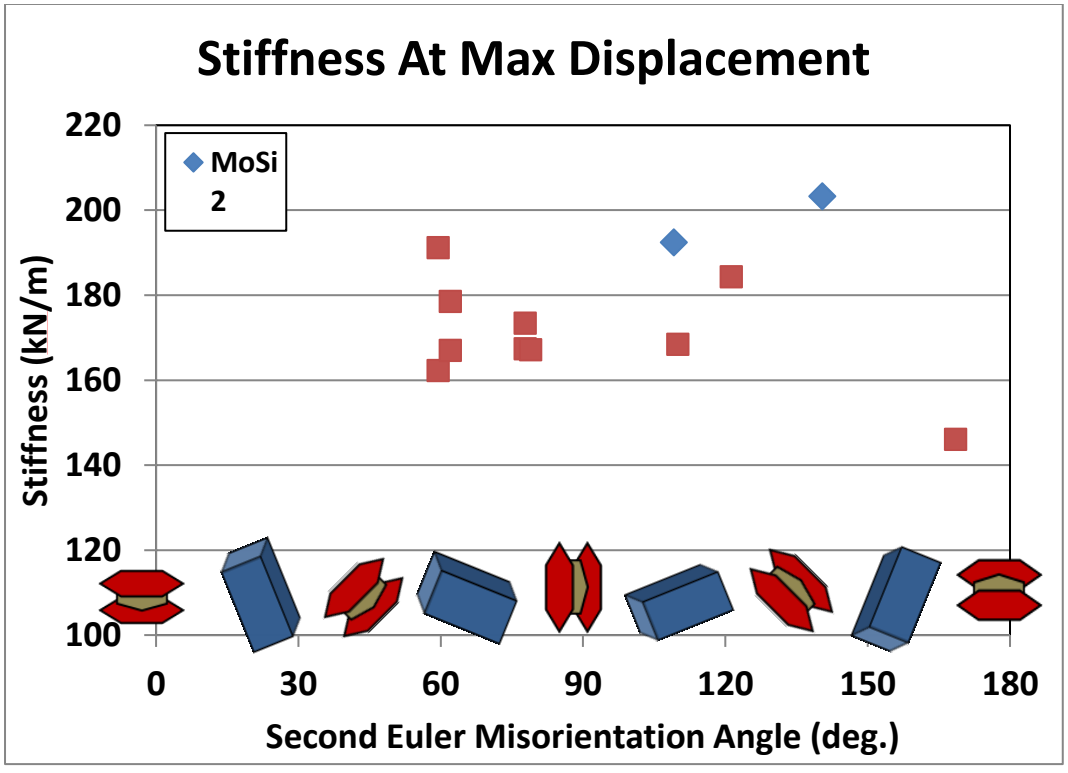

Figure 14: Plot of the stiffness surface at maximum displacement with respect to the second Euler misorientation angle.

CONCLUSIONS

This project was a very educational one. It is obvious that the combination of scanning electron microscopy, energy dispersive spectroscopy, and electron backscattered diffraction can be a very powerful one, and when combined with a technique like nano-indentation can give many kinds of insight into the mechanical behavior of multiphase materials which it would be very difficult to gain in any other way. Several important details were learned about these techniques. First, directly measuring the lattice parameters of the sample mapped by EBSD can be very helpful in achieving higher indexing percentages. Adding topography to a smooth surface by preferential etching is not as helpful. And importantly, users of the EBSD analysis software should be aware that the automatic extrapolation tool can assign crystal structures incorrectly and generate misleading answers.

Based on the eleven indents indexed to ZrB_2 and the two indents indexed to $MoSi_2$, the apparent trend in the Young's modulus follows expected behavior. ZrB_2 has a higher modulus than M, and appears to come to a maximum when the atomic layers are loaded on edge. The data for Berkovich nanohardness are too few to ascertain a definite trend, and the displacement data is a very flattened inverse of the hardness data plot, which is to be expected. The stiffness data are suspect because of questions about the calculation procedure. More data are needed, especially at lower misorientation angles, and because this is a random independent variable in these tests, this means that more indents need indexing and more scans are required.

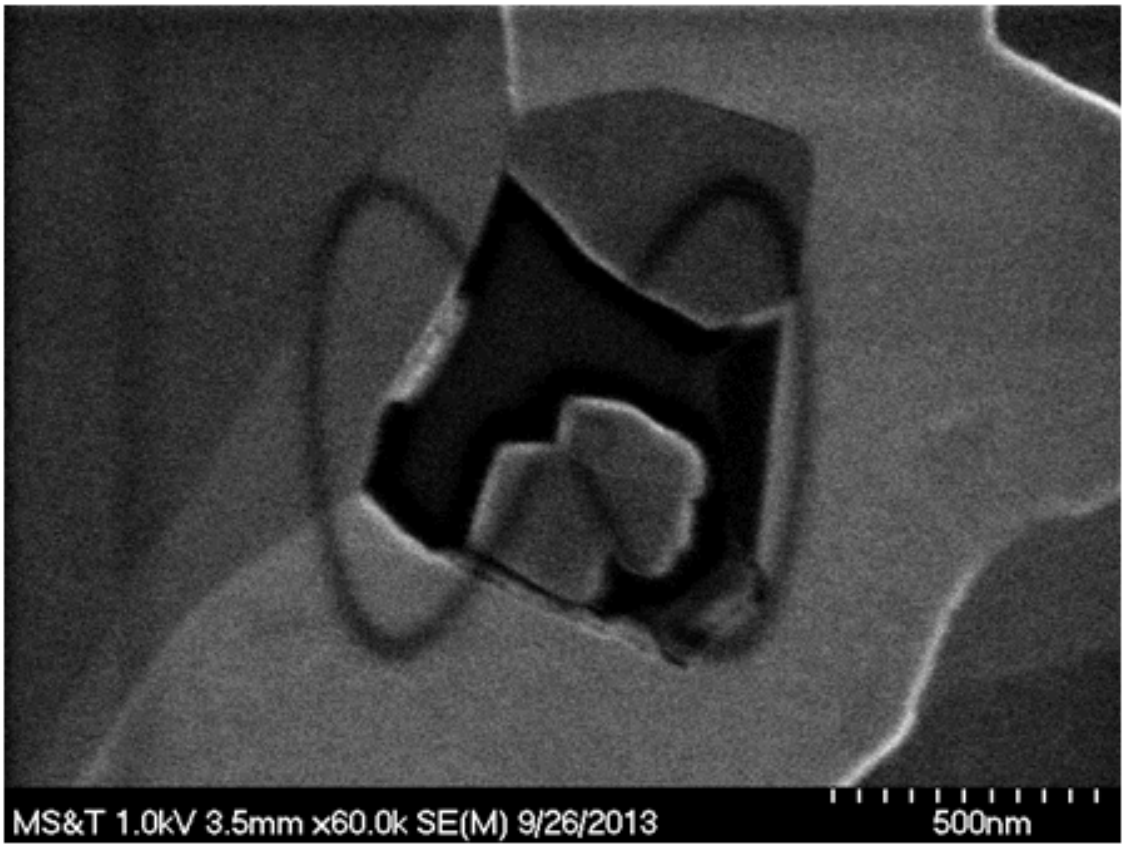

Figure for fun: Carbon deposition after pressing the auto-stigmate button on the Hitachi S4700. Black silica phase containing SiC precipitates and laminar BN contaminants between ZrB_2 and $MoSi_2$ grains.

APPENDIX B.

A ZrB_2-Mo PLANAR DIFFUSION COUPLE

To investigate the interaction between ZrB_2 and Mo in a controlled manner, a planar diffusion couple between densified polycrystalline ZrB_2 and Mo metal sheet was made by hot pressing. Grade B ZrB_2 was ball milled in acetone for 24 hours with ZrB_2 milling media with 1 wt.% boron carbide additions and 1 wt.% carbon additions added as phenolic resin 1 hr before the end of milling. The ZrB_2 powder was dried by rotary evaporation and hot pressed at 1950°C and 32 MPa until no ram travel was detected for ten minutes. Two discs of hot pressed ZrB_2 ~25 mm in diameter and ~6 mm thick were polished with 0.25 μm diamond slurry. A disc of Mo sheet (99.9% basis) was cut by wire EDM and placed between the two polished ZrB_2 surfaces. The ZrB_2-Mo-ZrB_2 stack was hot pressed at 1925°C and 30 MPa for 1 hr, then sectioned by diamond saw and polished with 0.25 μm diamond slurry before investigation by SEM and EDS. The interface is shown in Fig. 1.

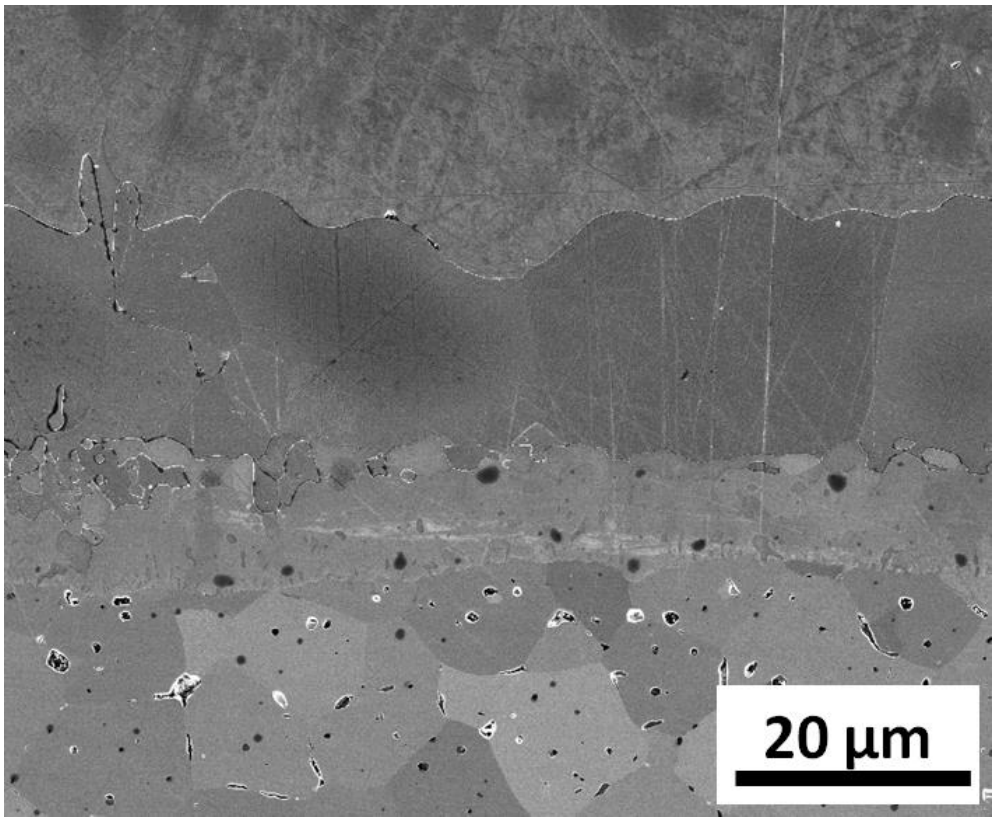

Fig. 1. Secondary electron image of the analyzed interface with Mo at top & ZrB2 at bottom.

EDS mapping (Fig. 2) showed that several layers formed at the interface, all of which have not been identified. Residual carbon impurities were observed in the ZrB_2. Above this in the images and adjacent to the ZrB_2 substrate is a layer that contains Zr, Mo, and appears to contain slightly less B than the ZrB_2 substrate. Above this is a discontinuous layer of what may be ZrC, likely forming via a reaction between ZrB_2 and carbon from the sintering atmosphere or solvents used to clean the polished surfaces before lamination. Between this and the Mo foil substrate is a Mo-rich layer that appears to be distinct from the Mo substrate in the secondary electron image. However, the boundary between this layer and the Mo substrate is not easily visible in the EDS maps. Overall, more analysis is necessary to characterize the phases formed in this diffusion couple.

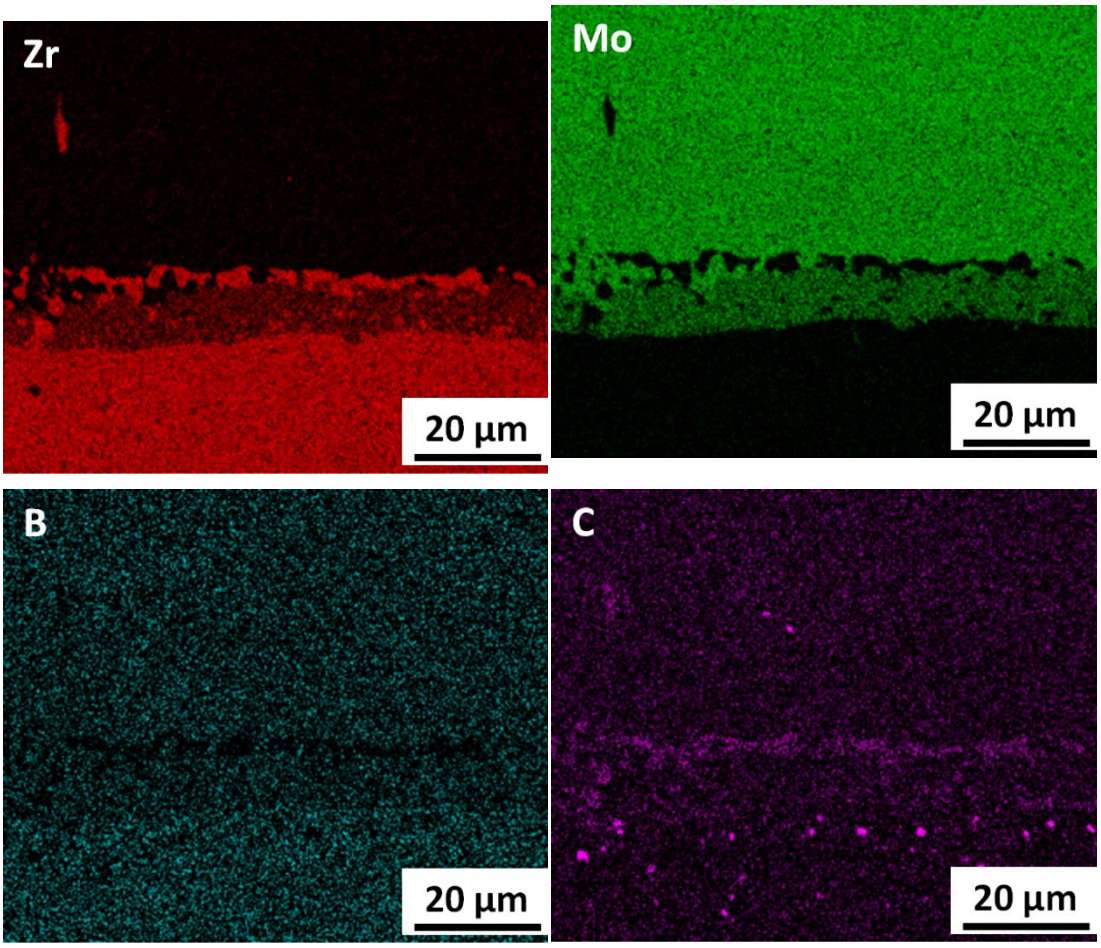

Fig. 2. Elemental EDS maps of a segment of the ZrB_2-Mo interface.

APPENDIX C.

NOTES ON PRECISION SURFACE GRINDING OF DIBORIDE CERAMICS

Flexure specimens tested in this project were based on the “B-bar” geometry nominally 3 mm x 4 mm in cross section as described in ASTM standards C1161 and C1211. The nominal length of the specimens was adjusted from 45 mm recommended by the standard to 43 mm in order to obtain more bar specimens from each hot pressed billet. Early attempts at cutting specimens from billets using a ~1.2 mm thick diamond abrasive blade on a surface grinder resulted in frequent chipping and flaking of the specimens’ lower edges before the blade had cut fully through the billet, usually resulting in <50% yield of usable specimens. This chipping was presumably caused by residual stresses in the specimens combined with their low fracture toughness at room temperature, and downward forces applied by the diamond cutting blade. A machining procedure was developed which combined the use of wire electro-discharge machining (EDM) and longitudinal abrasive surface grinding with resin-bonded diamond grinding wheels. This multi-step procedure allowed consistent machining of specimens with yields typically >95%.

After hot pressing the billets were cleaned (wire brush, wire brush wheel, sandblaster), washed, dried, weighed, and dimensions were measured. Flashing was removed by hand-flattening on an 80-grit metal-bonded diamond pad. Next, billets were bonded with hot-melt adhesive to 410 stainless steel plates, and the top and bottom surface-ground flat and plane-parallel with a 120 grit diamond wheel on a manual surface grinder, as shown in red in the diagram. Following this, specimen blanks were cut from the billet by wire EDM using 0.3 mm diameter 60/40 brass wire, shown in yellow in the diagram. Specimens were cut large enough to allow nominally 100 μm of material removal from the EDM-cut surfaces by surface grinding after EDM. Flexure specimens were thinned in the direction of force application during hot pressing using a 600 grit resin-bonded grinding wheel to within ~200 μm of the final target thickness, shown in brown in the accompanying figure. A downfeed of 2.54 μm (0.0001 in.) per pass and an infeed of ~2.5 mm (~0.1 in.) were used on an automatic surface grinder. NOTE: It was critical that the 600 grit wheel be dressed into full concentricity with its rotational axis every time it was mounted onto the grinder spindle. SiC abrasive dressing sticks mounted in a vise on the grinder chuck were used for this purpose.

Finally, at least 75 µm were removed from all four longitudinal surfaces of the specimens using a 1200 grit resin bonded diamond wheel on the automatic surface grinder, shown in blue. As with the 600 grit wheel, a downfeed of 2.54 µm (0.0001 in.) per pass and an infeed of ~2.5 mm (~0.1 in.) were used. The first ~60 µm were removed after first dressing the wheel into concentricity, after which the wheel was raised and redressed before grinding the final 15 µm from the specimens' surfaces. Redressing before final surface finishing helped to ensure that the entire circumference of the wheel participated in grinding the specimens' surfaces and reduced chatter marks.

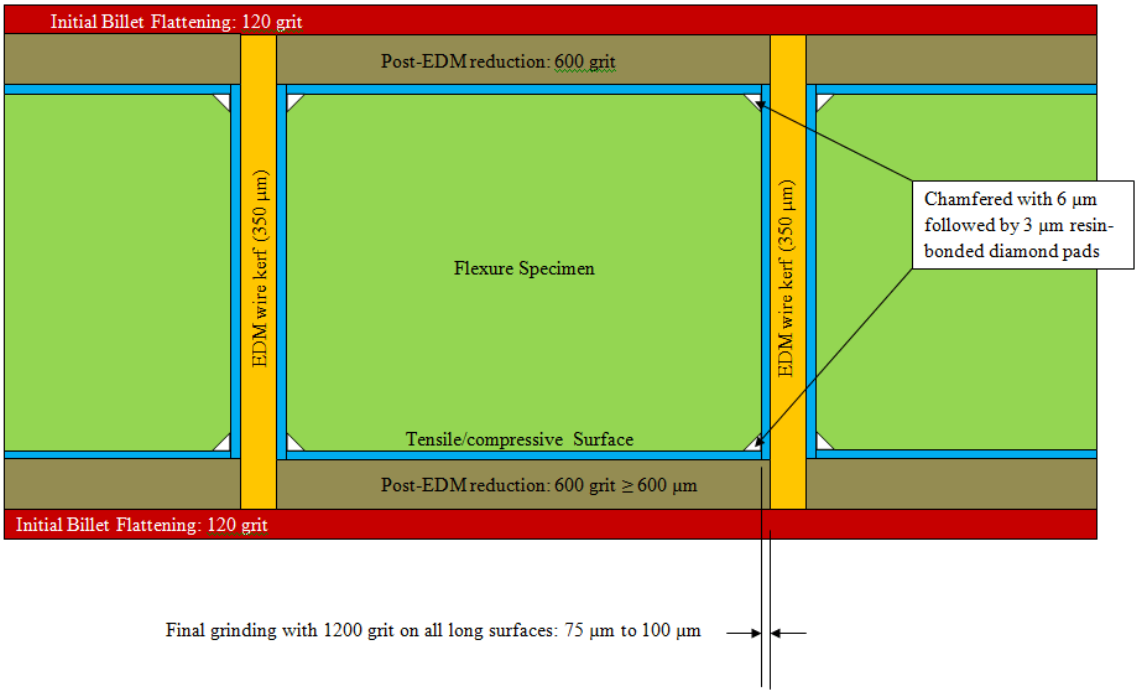

IMPORTANT: it was critical that the 1200 grit wheel be dressed into full concentricity every time it was mounted onto the grinder spindle. Failure to dress the 1200 grit wheel after mounting on the spindle can result in damage or destruction of the specimens. This is possibly due to the fact that the size of the abrasive grit is similar to the minimum downfeed step size, meaning that lack of full circumferential engagement of the wheel may not be sufficient to remove material at a rate as fast as the step-down rate of the grinding head.

Lack of sufficient coolant can also result in destruction of the specimens. Without coolant, frictional heating causes expansion of the specimens and grinding wheel, resulting in more friction and compressive force on the specimens. Coolant level should always be checked before grinding.

REFERENCES

[1] M.P. Harmer, H.M. Chan, G.A. Miller, Unique Opportunities for Microstructural Engineering with Duplex and Laminar Ceramic Composites, Journal of the American Ceramic Society, 75 (1992) 1715-1728.

[2] J.W. Zimmermann, G.E. Hilmas, W.G. Fahrenholtz, Thermal Shock Resistance and Fracture Behavior of ZrB2-Based Fibrous Monolith Ceramics, Journal of the American Ceramic Society, 92 (2009) 161-166.

[3] I. Bogomol, H. Borodianska, T. Zhao, T. Nishimura, Y. Sakka, P. Loboda, O. Vasylkiv, A dense and tough (B_4C-TiB_2)-B_4C 'composite within a composite' produced by spark plasma sintering, Scripta Materialia, 71 (2014) 17-20.

[4] H.X. Peng, Z. Fan, J.R.G. Evans, Novel MMC microstructure with tailored distribution of reinforcig phase, Journal of Microscopy, 201 (2001) 333-338.

[5] X. Deng, B.R. Patterson, K.K. Chawla, M.C. Koopman, Z. Fang, G. Lockwood, A. Griffo, Mchanical properties of a hybrid cemented carbide composite, International Journal of Refractory Metals and Hard Materials, 19 (2001) 547-552.

[6] X. Deng, B.R. Patterson, K.K. Chawla, M.C. Koopman, C. Mackin, Z. Fang, G. Lockwood, A. Griffo, Microstructure/hardness relationship in a dual composite, Journal of Materials Science Letters, 21 (2002) 707-709.

[7] Z. Fang, A. Griffo, B. White, G. Lockwood, D. Belnap, G. Hilmas, J. Butler, Fracture resistant super hard materials and hardmetals composite with functionally designed microstructure, International Journal of Refractory Metals and Hard Materials, 19 (2001) 453-459.

[8] X. Deng, B.R. Patterson, K.K. Chawla, M.C. Koopman, Double Cemented Carbide-A Creative Composite Design Concept, The International Journal of Powder Metallurgy, 37 (2001) 8.

[9] A. Griffo, R. Brown, K. Keshevan, Oil and Gas Drilling Materials, Advanced Materials and Processes, 161 (2003) 59-60.

[10] L. Silvestroni, D. Sciti, Effects of $MoSi_2$ additions on the properties of Hf– and Zr–B_2 composites produced by pressureless sintering, Scripta Materialia, 57 (2007) 165-168.

[11] L. Silvestroni, G. Meriggi, D. Sciti, Oxidation behavior of ZrB_2 composites doped with various transition metal silicides, Corrosion Science, 83 (2014) 281-291.

[12] S.-Q. Guo, T. Mizuguchi, T. Aoyagi, T. Kimura, Y. Kagawa, Quantitative Electron Microprobe Characterizations of Oxidized ZrB_2 Containing $MoSi_2$ Additives, Oxidation of Metals, 72 (2009) 335-345.

[13] H.-T. Liu, W.-W. Wu, J. Zou, D.-W. Ni, Y.-M. Kan, G.-J. Zhang, In situ synthesis of ZrB_2–$MoSi_2$ platelet composites: Reactive hot pressing process, microstructure and mechanical properties, Ceramics International, 38 (2012) 4751-4760.

[14] W.G. Fahrenholtz, G.E. Hilmas, I.G. Talmy, J.A. Zaykoski, Refractory Diborides of Zirconium and Hafnium, Journal of the American Ceramic Society, 90 (2007) 1347-1364.

[15] G.J.K. Harrington, Effect of Solid Solutions and Second Phases on the Thermal Conductivity of Zirconium Diboride Ceramics, Materials Science and Engineering, Missouri University of Science and Technology, Fall 2014.

[16] J.M. Lonergan, W.G. Fahrenholtz, G.E. Hilmas, R. Trice, Zirconium Diboride with High Thermal Conductivity, J. Am. Ceram. Soc., 97 (2014) 1689-1691.

[17] J.W. Zimmermann, G.E. Hilmas, W.G. Fahrenholtz, Thermal shock resistance of ZrB_2 and ZrB_2–30% SiC, Materials Chemistry and Physics, 112 (2008) 140-145.

[18] E.W. Neuman, G.E. Hilmas, W.G. Fahrenholtz, A. Dominguez-Rodriguez., Strength of Zirconium Diboride to 2300°C, Journal of the American Ceramic Society, 96 (2013) 47-50.

[19] H. Mehrer, H.E. Schaefer, I.V. Belova, G.E. Murch, Molybdenum Disilicide - Diffusion, Defects, Diffusion Correlation, and Creep, Defect and Diffusion Forum, 322 (2012) 107-128.

[20] J.J. Petrovic, Mechanical behavior of $MoSi_2$ and $MoSi_2$ composites, Materials Science and Engineering: A, 192/193 (1995) 31-37.

[21] F. Monteverde, The addition of SiC particles into a $MoSi_2$-doped ZrB_2 matrix: Effects on densification, microstructure and thermo-physical properties, Materials Chemistry and Physics, 113 (2009) 626-633.

[22] L. Silvestroni, H.-J. Kleebe, S. Lauterbach, M. Muller, Transmission electron microscopy on Zr- and Hf- borides with $MoSi_2$ addition: Densification mechanisms, Journal of Materials Research, 25 (2010) 828-833.

[23] W.G. Fahrenholtz, E.J. Wuchina, W.E. Lee, Y. Zhou, Ultra-High Temperature Ceramics: Materials for Extreme Environment Applications, Wiley2014.

[24] E.W. Neuman, G.E. Hilmas, W.G. Fahrenholtz, Strength of Zirconium Diboride to 2300°C, Journal of the American Ceramic Society, 96 (2013) 47-50.

[25] E.W. Neuman, G.E. Hilmas, W.G. Fahrenholtz, Mechanical behavior of zirconium diboride–silicon carbide–boron carbide ceramics up to 2200°C, Journal of the European Ceramic Society, 35 (2015) 463-476.

[26] E.W. Neuman, G.E. Hilmas, W.G. Fahrenholtz, Ultra-High Temperature Mechanical Properties of a Zirconium Diboride-Zirconium Carbide Ceramic, Journal of the American Ceramic Society, 99 (2015) 597-603.

[27] L. Silvestroni, H.-J. Kleebe, W.G. Fahrenholtz, J. Watts, Super-strong materials for temperatures exceeding 2000°C, Scientific Reports, (2017).

[28] M.M. Opeka, I.G. Talmy, J.A. Zaykosky, Oxidation-based materials selectioin for 2000°C + hypersonic aerosurfaces: Theoretical considerations and historical experience, Journal of Materials Science, 39 (2004) 5887-5904.

[29] D. Sciti, L. Silvestroni, L. Mercatelli, J.-L. Sans, E. Sani, Suitability of ultra-refractory diboride ceramics as absorbers for solar energy applications, Solar Energy Materials and Solar Cells, 109 (2013) 8-16.

[30] L. Mercatelli, E. Sani, D. Jafrancesco, P. Sansoni, D. Fontani, M. Meucci, S. Coraggia, L. Marconi, J.L. Sans, E. Beche, L. Silvestroni, D. Sciti, Ultra-refractory Diboride Ceramics for Solar Plant Receivers, Energy Procedia, 49 (2014) 468-477.

[31] E. Randich, D.D. Allred, Chemically Vapor-Deposited ZrB_2 as a Selective Solar Absorber, Thin Solid Films, 83 (1981) 393-398.

[32] S. Guo, T. Mizuguchi, M. Ikegami, Y. Kagawa, Oxidation behavior of ZrB_2–$MoSi_2$–SiC composites in air at 1500°C, Ceramics International, 37 (2011) 585-591.

[33] W.G. Fahrenholtz, Thermodynamic Analysis of ZrB_2-SiC Oxidation: Formation of a SiC-Depleted Region, Journal of the American Ceramic Society, 90 (2007) 143-148.

[34] N.L. Okamoto, M. Kusakari, K. Tanaka, H. Inui, S. Otani, Anisotropic elastic constants and thermal expansivities in monocrystal CrB_2, TiB_2, and ZrB_2, Acta Materialia, 58 (2010) 76-84.

[35] J.M. Lonergan, W.G. Fahrenholtz, G.E. Hilmas, W. Lee, Sintering Mechanisms and Kinetics for Reaction Hot-Pressed ZrB_2, Journal of the American Ceramic Society, 98 (2015) 2344-2351.

[36] B. Post, F.W. Glaser, D. Moskowitz, Transition Metal Diborides, Acta Metallurgica, 2 (1954) 20-25.

[37] D.L. McClane, W.G. Fahrenholtz, G.E. Hilmas, D. Smith, Thermal Properties of (Zr, TM)B_2 Solid Solutions with TM = Ta, Mo, Re, V, and Cr, Journal of the American Ceramic Society, 98 (2015) 637-644.

[38] Y.S. Touloukian, R.K. Kirby, E.R. Taylor, T.Y.R. Lee, Thermophysical Properties of Matter, Thermal Expansion - Nonmetallic Solids, Thermophysical and Electronic Properties Information Analysis Center, Purdue University, Lafayette, IN, USA, 1977.

[39] J.L. Watts, G.E. Hilmas, W.G. Fahrenholtz, R. Cutler, Mechanical Characterization of ZrB_2-SiC Composites with Varying SiC Particle Sizes, Journal of the American Ceramic Society, 94 (2011) 4410-4418.

[40] J.J. Cleveland, R.C. Bradt, Grain Size/Microcracking Relations for Pseudobrookite Oxides, Journal of the American Ceramic Society, 61 (1978) 478-481.

[41] E.W. Neuman, Elevated Temperature Mechanical Properties of Zirconium Diboride Based Ceramics, Materials Science and Engineering, Missouri University of Science and Technology, Rolla, MO, USA, 2014.

[42] P. Chantikul, S.J. Bennison, B.R. Lawn, Role of Grain Size in the Strength and R-Curve Properties of Alumina, Journal of the American Ceramic Society, 73 (1990) 2419-2427.

[43] J.B. Wachtman, W.R. Cannon, M.J. Matthewson, Mechanical Properties of Ceramics, 2 ed., J. Wiley and Sons, Inc., Hoboken, NJ, USA, 2009.

[44] M. Taya, S. Hayashi, A.S. Kobayashi, H.S. Yoon, Toughensing of a Particulate-Reinforced Ceramic-Matrix Composite by Thermal Residual Stress, Journal of the American Ceramic Society, 73 (1990) 1382-1391.

[45] R.L. Brett, P. Bowen, Fracture toughness assessment of silicon carbide-based ceramics and particulate-reinforced composites, Composites, 24 (1993) 177-183.

[46] E.W. Neuman, G.E. Hilmas, W.G. Fahrenholtz, M. Cinibulk, Ultra-High Temperature Mechanical Properties of a Zirconium Diboride-Zirconium Carbide Ceramic, Journal of the American Ceramic Society, 99 (2016) 597-603.

[47] J. Watts, G. Hilmas, W.G. Fahrenholtz, D. Brown, B. Clausen, Measurement of thermal residual stresses in ZrB_2–SiC composites, Journal of the European Ceramic Society, 31 (2011) 1811-1820.

[48] S.A. Maloy, J.J. Lewandowski, A.H. Heuer, J.J. Petrovic, Effects of carbon additions on the high temperature mechanical properties of molybdenum disilicide, Materials Science and Engineering: A, 155 (1992) 159-163.

[49] A.L. Chamberlain, W.G. Fahrenholtz, G.E. Hilmas, Characterization of Zirconium Diboride-Molybdenum Disilicide Ceramics, Ceramic Transactions, 153 (2003) 299-308.

[50] R. Mitra, Silicides: Processing and Mechanical Behavior, Structural Intermetallics and Intermetallic Matrix Composites, CRC Press, 2015, pp. 107-165.

[51] E.J.L. Y.-L. Jeng, Review Processing of molybdenum disilicide, Journal of Materials Science, 29 (1994) 2557-2571.

[52] J.J. Petrovic, Toughening strategies for $MoSi_2$-based high temperaure structural silicides, Intermetallics, 8 (2000) 1175-1182.

[53] S.R. Srinivasan, R.B. Schwarz, J.D. Embury, Ductile-To-Brittle Transition in $MoSi_2$, in: I. Baker, R. Darolia, J.D. Whittenberger, M.H. Yoo (Eds.) High-Temperature Odered Intermetallic Alloys V, pp. 1099-1104.

[54] M. Hawgood, J. Hasier, K. Ho, Accumulative Roll Bonding for Bladesmithing: From Book to Burrito to Blade, Journal of Materials, 68 (2016) 3161-3166.

[55] S. Maloy, A.H. Heuer, J. Lewendowski, J. Petrovic, Carbon Additions to Molybdenum Disilicide: Improved High-Temperature Mechanical Properties, J. Am. Ceram. Soc., 74 (1991) 2704-2706.

[56] J.S. Idasetima, J.J. Petrovic, Effects of Carbon Additions on $MoSi_2$ Microstructure and Properties, Philosophical Magazine A, 76 (1997) 271-287.

[57] S.R. Srinivasan, R.B. Schwarz, J.D. Embury, Ductile-To-Brittle Transition in $MoSi_2$, in: I. Baker, R. Darolia, J.D. Whittenberger, M.H. Yoo (Eds.) High-Temperature Ordered Intermetallic Alloys V, Materials Research Society, Boston, MA, USA, 1993, pp. 1099-1104.

[58] W.S. Gibbs, J.J. Petrovic, R.E. Honnel, SiC Whisker-$MoSi_2$ Matrix Composites, Ceramic Engineering Science Proceedings, 8 (1987) 645-648.

[59] A.K. Vasudevan, J.J. Petrovic, A Comparative Overview of Molybdenum Disilicide Composites, Materials Science and Engineering: A, 155 (1992) 1-17.

[60] D. Sciti, L. Silvestroni, M. Nygren, Spark plasma sintering of Zr- and Hf-borides with decreasing amounts of $MoSi_2$ as sintering aid, Journal of the European Ceramic Society, 28 (2008) 1287-1296.

[61] L. Silvestroni, H.-J. Kleebe, S. Lauterbach, M. Muller, Transmission electron microscopy on Zr- and Hf-borides with $MoSi_2$ addition: Densification mechanisms, Journal of Materials Research, 25 (2010) 6.

[62] A.L. Chamberlain, W.G. Fahreholtz, Hilmas, Characterization of Zirconium Diboride-Molybdenum Disilicide Ceramics, Ceram. Trans., 153 (2003) 299-398.

[63] V.O. Lavrenko, A.D. Panasyuk, O.M. Grigorev, O.V. Koroteev, V.A. Kotenko, High-Temperature (to 1600°C) Oxidation of ZrB_2-$MoSi_2$ Ceramics in Air, Powder Metallurgy and Metal Ceramics, 51 (2012) 102-107.

[64] D. Sciti, M. Brach, A. Bellosi, Long-term oxidation behavior and mechanical strength degradation of a pressurelessly sintered ZrB_2–$MoSi_2$ ceramic, Scripta Materialia, 53 (2005) 1297-1302.

[65] D. Sciti, F. Monteverde, S. Guicciardi, G. Pezzotti, A. Bellosi, Microstructure and mechanical properties of ZrB_2–$MoSi_2$ ceramic composites produced by different sintering techniques, Materials Science and Engineering: A, 434 (2006) 303-309.

[66] S.Q. Guo, T. Nishimura, T. Mizuguchi, Y. Kagawa, Mechanical properties of hot-pressed ZrB_2-$MoSi_2$-SiC composites, Journal of the European Ceramic Society, 28 (2008) 1891-1898.

[67] D. Sciti, S. Guicciardi, A. Bellosi, G. Pezzotti, Properties of a Pressureless-Sintered ZrB2-MoSi2 Ceramic Composite, Journal of the American Ceramic Society, 0 (2006) 060427083300081-???

[68] I.G. Talmy, J.A. Zaykoski, M.M. Opeka, High-Temperature Chemistry and Oxidation of ZrB_2Ceramics Containing SiC, Si_3N_4, Ta_5Si_3, and $TaSi_2$, Journal of the American Ceramic Society, 91 (2008) 2250-2257.

[69] L. Silvestroni, D. Sciti, Densification of ZrB_2-$TaSi_2$ and HfB_2-$TaSi_2$ Ultra-High-Temperature Ceramic Composites, Journal of the American Ceramic Society, 94 (2011) 1920-1930.

[70] J.J. Petrovic, Toughening strategies for $MoSi_2$-based high temperature structural silicides, Intermetallics, 8 (2000) 1175-1182.

[71] N. Chawla, B.V. Patel, M. Koopman, K.K. Chawla, R. Saha, B.R. Patterson, E.R. Fuller, S.A. Langer, Microstructure-based simulation of thermomechanical behavior of composite materials by object-oriented finite element analysis, Materials Characterization, 49 (2002) 395-407.

[72] E. Rudy, Ternary Phase Equilibria in Transition Metal-Boron-Carbon-Silicon Systems, Compendium of Phase Diagram Data, Aerojet-General Corporation Technical Report, 1969, pp. 585.

[73] H.E. Çamurlu, Preparation of Single Phase Molybdenum Boride, Journal of Alloys and Compounds, 509 (2011) 5431-5436.

[74] H. Klesnar, T.L. Aselage, B. Morosin, G.H. Kwei, A.C. Lawson, The Diboride Compounds of Molybdenum: MoB_{2-x} and Mo_2B_{5-y}, Journal of Alloys and Compounds, 241 (1996) 180-186.

[75] M. Frotscher, W. Klein, J. Bauer, C.-M. Fang, J.-F. Halet, A. Sensyshyn, C. Baehtz, B. Albert, M_2B_5 or M_2B_4? a Reinvestigation of the Mo/B and W/B System, Z. Anorg. Allg. Chem., (2007) 2626.

[76] R. Kiessling, The Crystal Structures of Molybdenum and Tungsten Borides, Acta Chemica Scandinavica 1, (1947) 893-916.

[77] W. Hayami, A. Momozawa, S. Otani, Effect of defects in the formation of AlB_2-type WB_2 and MoB_2, Inorg Chem, 52 (2013) 7573-7577.

[78] M. Zhang, H. Wang, H. Wang, T. Cui, Y. Ma, Structural Modifications and Mechanical Properties of Molybdenum Borides from First Principles, Journal of Physical Chemistry C, 114 (2010) 6722-6725.

[79] I.R. Shein, K.I. Shein, A.L. Ivanovskii, First-principles study on the structural, cohesive and electronic properties of rhombohedral Mo2B5 as compared with hexagonal MoB2, Physica B: Condensed Matter, 387 (2007) 184-189.

[80] P. Rogl, Boron - Molybdenum - Zirconium, in: G. Effenberg, S. Ilyenko (Eds.) Refrctory Metal Systems: Phase Diagrams, Crystallographic and Thermodynamic Data, Springer Berlin Heidelberg, Berlin, 2010, pp. 72-82.

[81] D.L. McClane, W.G. Fahrenholtz, G.E. Hilmas, D. Smith, Thermal Properties of $(Zr,TM)B_2$ Solid Solutions with TM = Hf, Nb, W, Ti, and Y, Journal of the American Ceramic Society, 97 (2014) 1552-1558.

[82] P.S. Kislyi, M.A. Kuzenkova, Gas-Impermeable Protective Thermocouple Sheaths from Zirconium Boride, Poroshkovaya Metallurgiya, 1 (1965) 32-36.

[83] L. Pauling, B. Kamb, A revised set of values of single-bond radii derived from the observed interatomic distances in metals by correction for bond number and resonance energy, Procedings of the National Academy of Sciences, 83 (1986) 3569-3571.

[84] A. Stanfield, Thermodynamic Calculation of ZrB_2-MoB_2 Solid Solution, Missouri University of Science and Technology, Rolla, MO 65409, USA, 2016.

[85] A. Bellosi, F. Monteverde, D. Sciti, Fast Densification of Ultra-High-Temperature Ceramics by Spark Plasma Sintering, International Journal of Applied Ceramic Technology, 3 (2006) 32-40.

[86] W. Li, X. Zhang, C. Hong, W. Han, J. Han, Microstructure and mechanical properties of zirconia-toughened ZrB_2–$MoSi_2$ composites prepared by hot-pressing, Scripta Materialia, 60 (2009) 100-103.

[87] E.W. Neuman, G.E. Hilmas, W.G. Fahrenholtz, Mechanical Behavior of Zirconium Diboride-Silicon Carbide Ceramics at Elevated Temperature in Air, Journal of the European Ceramic Society, 33 (2013) 2889-2899.

[88] R. Wang, W. Li, Effects of Microstructure and Flaw Evolution on the Fracture Strength of ZrB_2-$Mosi_2$ Composites Under High Temperatures, Journal of Alloys and Compounds, 644 (2015) 582-588.

[89] D. Sciti, M. Brach, A. Bellosi, Oxidation behavior of a pressureless sintered ZrB_2–$MoSi_2$ ceramic composite, Journal of Materials Research, 20 (2011) 922-930.

[90] H.T. Liu, J. Zou, D.W. Ni, J.X. Liu, G.J. Zhang, Anisotropy oxidation of textured ZrB_2–$MoSi_2$ ceramics, Journal of the European Ceramic Society, 32 (2012) 3469-3476.

[91] K.T. Venkateswara Rao, W.O. Soboyejo, R.O. Ritchie, Ductile-Phase Toughening and Fatigue-Crack Growth in Nb-Reinforced Molybdenum Disilicide Intermetallic Composites, Metallurgical Transactions A, 23A (1992) 2249-2257.

[92] E.W. Neuman, G.E. Hilmas, W.G. Fahrenholtz, Mechanical behavior of zirconium diboride–silicon carbide ceramics at elevated temperature in air, Journal of the European Ceramic Society, 33 (2013) 2889-2899.

[93] D. Sciti, M. Brach, A. Bellosi, Oxidation behavior of a pressureless sintered ZrB_2–$MoSi_2$ ceramic composite, Journal of Materials Research, 20 (2005) 922-930.

[94] P.G. Hare, C.D. Thomas, T.N. Topper, R.M. Gotthardt, The Archeology of Yukon Ice patches: New Artifacts, Obsvervations, and Insights, Arctic, 65 (2012) 118-135.

[95] D.R. Clarke, Interpenetrating Phase Composites, Journal of the American Ceramic Society, 75 (1992) 739-759.

[96] X. Deng, B.R. Patterson, K.K. Chawla, M.C. Koopman, Z. Fang, G. Lockwood, A. Griffo, Double Cementec Carbide - A Creative Composite Design Concept, The International Journal of Powder Metallurgy, 37 (2001).

[97] Z. Fang, G. Lockwood, A. Griffo, A Dual Composite of WC-Co, Metallurgical Transactions A, 30 (1999) 3231-3238.

[98] H.X. Peng, Z. Fan, J.R.G. Evans, Novel MMC Microstructure with Tailored Distribution of the Reinforcing Phase, Journal of Microscopy, 201 (2000) 333-338.

[99] M.Y. He, A. Bartlett, A.G. Evans, J.W. Hutchinson, Kinking of a Crack out of an Interface: Role of In-Plane Stress, Journal of the American Ceramic Society, 74 (1991) 767-771.

[100] E.W. Neuman, G.E. Hilmas, W.G. Fahrenholtz, Ultra-High Temperature Mechanical Properties of a Zirconium Diboride-Zirconium Carbide Ceramic, Journal of the American Ceramic Society, (2015) 1-7.

[101] M. Brach, V. Medri, A. Bellosi, Corrosion of pressureless sintered ZrB_2–$MoSi_2$ composite in H_2SO_4 aqueous solution, Journal of the European Ceramic Society, 27 (2007) 1357-1360.

[102] V.A.S. V.O. Lavrenko, V.M. Talash, V.A. Kotenko, T.V.Khomko, Electrochemical Oxidation of ZrB2-MoSi2 Ceramics in a 3% NaCl Solution, Powder Metallurgy and Metal Ceramics, 50 (2011) 749-752.

[103] G.J.K. Harrington, G.E. Hilmas, W.G. Fahrenholtz, Effect of carbon on the thermal and electrical transport properties of zirconium diboride, Journal of the European Ceramic Society, 35 (2015) 887-896.

[104] J.M. Lonergan, W.G. Fahrenholtz, G.E. Hilmas, Zirconium Diboride with High Thermal Conductivity, Journal of the American Ceramic Society, 97 (2014) 1689-1691.

[105] M.M. Opeka, I.G. Talmy, J.A. Zaykoski, Oxidation-based materials selection for 2000°C + hypersonic aerosurfaces: Theoretical considerations and historical experience, Journal of Materials Science, 39 (2004) 5887-5904.

[106] N. Fuhrman, W.J. Bryan, Element with Burnable Poison Coating, in: U.S.P. Office (Ed.), Combustion Engineering, Inc., United States of America, 1987.

[107] M.A. Kuzenkova, P.S. Kislyi, Sintering of Alloys of Zriconium Diboride with Molybdenum Disilicide, Poroshkovaya Metallurgiya, 9 (1966) 11-16.

[108] S.-Q. Guo, T. Nishimura, T. Mizuguchi, Y. Kagawa, Mechanical properties of hot-pressed ZrB_2–$MoSi_2$–SiC composites, Journal of the European Ceramic Society, 28 (2008) 1891-1898.

[109] S.-Q. Guo, Densification of ZrB_2-based composites and their mechanical and physical properties: A review, Journal of the European Ceramic Society, 29 (2009) 995-1011.

[110] W.-M. Guo, Z.-G. Yang, G.-J. Zhang, Microstructural evolution of ZrB_2–$MoSi_2$ composites during heat treatment, Ceramics International, 37 (2011) 2931-2935.

[111] S. Zhu, W.G. Fahrenholtz, G.E. Hilmas, S.C. Zhang, Pressureless sintering of zirconium diboride using boron carbide and carbon additions, Journal of the American Ceramic Society, 90 (2007) 4.

[112] S.C. Zhang, G.E. Hilmas, W.G. Fahrenholtz, Pressureless densification of zirconium diboride with boron carbide additions, Journal of the American Ceramic Society, 89 (2006) 7.

[113] F.T. Monteverde, The addition of SiC particles into a $MoSi_2$-doped ZrB_2 matrix: Effects on densification, microstructure and thermo-physical properties, Materials Chemistry and Physics, 113 (2009) 626-633.

[114] F. Monteverde, A. Bellosi, L. Scatteia, Processing and properties of ultra-high temperature ceramics for space applications, Materials Science and Engineering: A, 485 (2008) 415-421.

[115] Y.S. Touloukian, R.K. Kirby, E.R. Taylor, T.Y. R Lee, Thermophysical Properties of Matter, Thermal Expansion - Nonmetallic Solids, Thermophysical and Electronic Properties Information Analysis Center, Purdue University, Lafayette IN, USA, 1977.

[116] J.L. Watts, G. Hilmas, W.G. Fahrenholtz, R. Cutler, Mechanical Characterization of ZrB_2-SiC Composites with Varying SiC Particle Sizes, Journal of the American Ceramic Society, 94 (2011) 4410-4418.

[117] J.J. Cleveland, R.C. Brandt, Grain Size/Microcracking Relations for Pseudobrookite Oxides, Journal of the American Ceramic Society, 61 (1978) 478-481.

[118] M. Nakamura, S. Matsumoto, T. Hirano, Elastic constants of $MoSi_2$ and WSi_2 single crystals, Journal of Materials Science, 25 (1990) 5.

[119] N.L. Okamoto, M. Kusakari, K. Tanaka, H. Inui, M. Yamaguchi, S. Otani, Temperature dependence of thermal expansion and elastic constants of single crystals of ZrB_2 and the suitability of ZrB_2 as a substrate for GaN film, Journal of Applied Physics, 93 (2003) 88.

[120] V.O. Lavrenko, V.A. Shvets, V.M. Talash, V.A. Kotenko, T.V. Khomko, Electrochemical Oxidation of ZrB_2-$MoSi_2$ Ceramics in a 3% NaCl Solution, Powder Metallurgy and Metal Ceramics, 50 (2011) 749-752.

[121] R.J. Grohsmeyer, G.E. Hilmas, F.T. Monteverde, W.G. Fahrenholtz, A. D'Angio, D. Sciti, L. Silvestroni, ZrB_2-$MoSi_2$ Ceramics with Varying $MoSi_2$ Content and ZrB^2 Powder Particle Size: Processing and Microstructure, Journal of the European Ceramic Society, TBD (2017a) TBD.

[122] R.G. Munro, Material Properties of a Sintered α-SiC, Journal of Physical Chemistry Reference Data, 26 (1997) 9.

[123] I.R. Shein, A.L. Ivanovskii, Elastic properties of mono- and polycrystalline hexagonal AlB_2-like diborides of s, p and d metals from first-principles calculations, Journal of Physics: Condensed Matter, 20 (2008) 415218.

[124] P.K. Yadawa, S.K. Verma, G. Mishra, R.R. Yadav, Effect of Elastic Constants on the Ultrasonic Properties of Group VIB Transition Metal Diborides, Journal of Nanotechnology & Advanced Materials, 2 (2014) 1-9.

[125] W.G. Fahrenholtz, G.E. Hilmas, S. Zhang, S. Zhu, Pressureless Sintering of Zirconium Diboride: Particle Size and Additive Effects, J. Am. Ceram. Soc., 91 (2008) 1398-1404.

[126] J.L. Watts, G. Hilmas, W.G. Fahrenholtz, Mechanical Characterization of ZrB_2-SiC Composites with Varying SiC Particle Sizes, J. Am. Ceram. Soc., 94 (2011) 4410-4418.

[127] F.T. Monteverde, L. Silvestroni, Combined Effects of WC and SiC on densification and thermo-mechanical stability of ZrB_2 ceramics, Materials & Design, 109 (2016) 396-407.

[128] T. Cutard, T. Viatte, G. Feusier, W. Benoit, Microstructure and High Temperature mechanical Properties of $TiC_{0.7}N_{0.3}$-Mo_2C-Ni Cermets, Materials Science and Engineering: A, 209 (1996) 218-227.

[129] M. Mallik, S. Pan, H. Roy, Fracture Toughness Measurement of Hot Pressed ZrB_2-$MoSi_2$ Composite, International Journal of Current Engineering and Technology, 3 (2013) 1647-1652.

[130] R. Jenkins, R.L. Snyder, Introduction to X-Ray Powder Diffractometry, John Wiley and Sons, Inc., New York, 1996.

[131] M.N. Rahaman, Ceramic Processing and Sintering, 2nd ed., Taylor and Francis Group, LLC, Boca Raton, FL, USA, 2003.

[132] J.M. Lonergan, D.L. McClane, W.G. Fahrenholtz, G.E. Hilmas, R. Orru, Thermal Properties of Hf-Doped ZrB_2 Ceramics, Journal of the American Ceramic Society, 98 (2015) 2689-2691.

[133] T.J. Whalen, A.T. Anderson, Wetting of SiC, Si3N4, and Carbon by Si and Binary Si Alloys, Journal of the American Ceramic Society, (1975) 396-399.

[134] H.-T. Liu, J. Zou, D.-W. Ni, J.-X. Liu, G.-J. Zhang, Anisotropy oxidation of textured ZrB_2–$MoSi_2$ ceramics, Journal of the European Ceramic Society, 32 (2012) 3469-3476.

[135] V.O. Lavrenko, V.A. Shvets, V.M. Talash, V.A. Kotenko, T.V. Khomko, Electrochemical Oxidation of ZrB_2-$MoSi_2$ Ceramics in a 3% NaCl Solution, Powder Metallurgy and Metal Ceramics, 50 (2012) 749-753.

[136] D.J. Evans, S.A. Court, P.M. Hazzledine, H.L. Fraser, Deformation Mechanisms in the Intermetallic Compound $MoSi_2$, in: I. Baker, R. Darolia, J.D. Whittenberger, M.H. Yoo (Eds.) High-Temperature Ordered Intermetallic Alloys V, Materials Research Society, Boston, MA, USA, 1993, pp. 567-572.

[137] Y.Q. Liu, G. Shao, P. Tsakiropoulous, On the Oxidation Behavior of $MoSi_2$, Intermetallics, 9 (2001) 125-136.

[138] M. Kazemzadeh Dehdashti, W.G. Fahrenholtz, G.E. Hilmas, Effects of transition metals on the oxidation behavior of ZrB_2 ceramics, Corrosion Science, 91 (2015) 224-231.

[139] R.J. Grohsmeyer, G.E. Hilmas, F.T. Monteverde, W.G. Fahrenholtz, Densification Process and Formation of Solid Solution Shell in ZrB_2-$MoSi_2$ Ceramics with Varying $MoSi_2$ Content and ZrB_2 Powder Particle Size, Journal of the European Ceramic Society, TBD (2017) TBD-TBD.

[140] H.J. McSkimin, Measurement of Elastic Constants at Low Temperatures by Means of Ultrasonic Waves–Data for Silicon and Germanium Single Crystals, and for Fused Silica, Journal of Applied Physics, 24 (1953) 988.

[141] C.F. Smith, W.B. Crandall, Calculated High-Temperature Elastic Constants for Zero Porosity Moniclinic Zirconia, Journal of the American Ceramic Society, 47 (1964) 624-627.

[142] ASM Engineered Materials Reverence Book, 2 ed., ASM International, Materials Park, OH, USA, 1994.

[143] E.W. Neuman, Elevated Temperature Mechanical Properties of Zirconium Diboride Based Ceramics, Ceramic Engineering, Missouri University of Science and Technology, Rolla, MO, USA, 2014, pp. 278.

[144] G. Pezzotti, On the Actual Contribution of Crack Deflection in Toughening Platelet-Reinforced Brittle-Matrix Composites, Acta Metallurgica et Materialia, 41 (1993) 1825-1839.

[145] R.P. Kusy, Influence of Particle Size Ratio on the Continuity of Aggregates, Journal of Applied Physics, 48 (1977) 5301-5305.

[146] F.-Z. Dai, Y. Zhou, Effects of transition metal (TM=Zr, Hf, Nb, Ta, Mo, W) elements on the shear properties of TMB_2s: A first-principles investigation, Computational Materials Science, 117 (2016) 266-269.

[147] I. Bogomol, H. Borodianska, Y. Sakka, A Dense and Tough (B_4C-TiB_2)-B_4C 'Composite Within a Composite' Produced by Spark Plasma Sintering, Scripta Materialia, 71 (2014) 17-20.

[148] X. Deng, Double Cemented Carbide - A Creative Dual Composite, The International Journal of Powder Metallurgy, 37 (2001).

[149] X. Deng, B.R. Patterson, K.K. Chawla, M.C. Koopman, Z. Fang, G. Lockwood, A. Griffo, Mechanical Properties of a Hybrid Cemented Carbide Composite, International Journal of Refractory Metals and Hard Materials, 19 (2001) 547-552.

[150] A. Griffo, R. Brown, K. Keshavan, Oil and Gas Drilling Materials, Advanced Materials and Processes, 161 (2003) 59-60.

[151] Z.Z. Fang, A. Griffo, B. White, G. Lockwood, D. Belnap, G. Hilmas, J. Bitler, Fracture Resistant Super Hard Materials and Hardmetals Composite with Functionally Designed Microstructure, International Journal of Refractory Metals and Hard Materials, 19 (2001) 453-459.

[152] H. Ming-Yuan, J.W. Hutchinson, Crack Deflection at an Interface Between Dissimilar Elastic Materials, International Journal of Solids and Structures, 25 (1989) 1053-1067.

[153] R.J. Grohsmeyer, G.E. Hilmas, F.T. Monteverde, W.G. Fahrenholtz, A. D'Angio, D. Sciti, L. Silvestroni, Mechanical Property Relationships in ZrB_2-$MoSi_2$ Ceramics with Varying $MoSi_2$ Content and ZrB_2 Powder Particle Size at Room Temperature and 1500°C in Air, Journal of the European Ceramic Society, TBD (2017d) TBD-TBD.

[154] B.W. Rosen, Z. Hashin, Effective Thermal Expansion Coefficients and Specific Heats of Composite Materials, International Journal of Engineering Science, 8 (1970) 157-173.

[155] J. Watts, G. Hilmas, W.G. Fahrenholtz, D. Brown, B. Clausen, Measurement of Thermal Residual Stresses in ZrB_2-SiC Composites, Journal of the European Ceramic Society, 31 (2011) 1811-1820.

[156] Y.Q. Liu, G. Shao, P. Tsakiropoulos, On the Oxidation Behavior of $MoSi_2$, Intermetallics, 9 (2001) 125-136.

VITA

Ryan Joseph Grohsmeyer was born in March, 1990, in Monterey, California. In 1996, he and his family moved to Southern Maryland, where Ryan enjoyed spending time at Historic St. Mary's City and playing in the woods with his sister, Irene. In 2004 Ryan began two hobbies: making and throwing darts with an atlatl, and learning from professional blacksmith and farrier Pat Fulcher, who helped initiate Ryan's interest in metallurgy. In 2007, Ryan worked as a summer counselor at Colonial Camp Flintlock, LLC, and also attended the ASM Materials Camp at University of Missouri-Rolla by the recommendation of Dr. Klaus Zwilsky (President of American Society for Metals International 1989–1990), which solidified Ryan's interest in materials science. In 2008, he attained the rank of Eagle Scout and graduated from St. Mary's Ryken High School.

For the next five summers, he worked as a civilian engineering technician at the Robert N. Becker Laboratory at the Naval Air Test Center at NAS Patuxent River, machining and mechanically testing primarily steel, titanium, and aluminum alloy specimens in fatigue and custom profiles. From 2008–2012, he attended the Inamori School of Engineering at Alfred University in NY, graduating cum laude with honors in his field of study with a Bachelor of Science in materials science and engineering. At Alfred, he met his fiancée, Alexandra Beall, and many great friends.

Ryan began his PhD research in Fall 2012 at the Missouri University of Science and Technology under the advisement of Dr. Gregory E. Hilmas and Dr. William G. Fahrenholtz. During the summers of 2013, 2014, and 2015 Ryan was a visiting student at the Consiglio Nazionale delle Ricerche, Istituto di Scienza e Tecnologia dei Materiali Ceramici in Faenza, Italy, where he worked with Andrea D'Angio under the tutelage of Dr. Frederic Monteverde, Dr. Laura Silvestroni, Dr. Diletta Sciti, and Cesare Melandri. Ryan's PhD research focused on ZrB_2-$MoSi_2$ ceramics and dual-scale composite architectures for use at elevated temperature. He presented work at eight conferences nationally and internationally, and wrote five manuscripts for publication. In May 2017 he received his PhD in materials science and engineering from Missouri University of Science and Technology. He continued his career at Corning Incorporated in Painted Post, New York.